HIGH MASS X-RAY BINARIES AT EXTREME ENERGIES WITH VERITAS

by

Payel Kar

A dissertation submitted to the faculty of
The University of Utah
in partial fulfillment of the requirements for the degree of

Doctor of Philosophy

in

Physics

Department of Physics and Astronomy

The University of Utah

December 2017

The University of Utah Graduate School

STATEMENT OF DISSERTATION APPROVAL

The dissertation of **Payel Kar**
has been approved by the following supervisory committee members:

David B. Kieda ,	Chair(s)	**September** 14^{th} **2017** Date Approved
Andrew W. Smith ,	Member	**July** 10^{th} **2017** Date Approved
Anil C. Seth ,	Member	**September** 14^{th} **2017** Date Approved
Shanti Deemyad ,	Member	**September** 14^{th} **2017** Date Approved
Sarah E. Bush ,	Member	**September** 14^{th} **2017** Date Approved

by **Benjamin C. Bromley** , Chair/Dean of
the Department/College/School of **Physics and Astronomy**
and by **David B. Kieda** , Dean of The Graduate School.

ABSTRACT

Out of the numerous high-mass X-ray binaries, only 6 are detected above 100 GeV, all of which host a massive Be/O type star and a compact star. The nature of the compact star in majority of these TeV binaries is unknown. The emission mechanisms in these systems may hold key information about their population scarcity in our galaxy. VERITAS has been instrumental in unraveling the physics of TeV binaries. This dissertation takes a closer look at the well-known TeV binary LS I $+61^\circ$ 303 and a TeV binary candidate SS 433.

LS I $+61^\circ$ 303 has a compact star revolving around a giant optical Be star which is rapidly losing mass due to its fast rotational speeds. The binary exhibits modulated emission from radio to TeV wavelengths dependent on its orbital and superorbital periods. This dissertation presents three new key aspects of this TeV binary, a correlation between X-ray and TeV emission from the source over multiple orbits that is sampled over 3 y, quiescent TeV emission around the entire orbit and probable subtle spectral changes dependent on the positions of the binary components in the 26.5-day orbit. The X-ray/TeV correlation hints at the origin of emission at these two wavebands from a single particle population. The TeV base emission and spectral variations may be indicative of a neutron star in the system which flip-flops between its accretor and propeller phases along the orbit.

SS 433 is a high-mass X-ray binary consisting a stellar microquasar with dual relativistic jets orbiting a massive star once every 13.1 days. The binary is embedded in the W50 nebula and the precessing jets are shaping the morphology of the surrounding medium. The eastern and western jet termination regions have long been predicted to be potential sources of high-energy gamma rays, produced due to the interaction of the jets with surrounding interstellar medium. SS 433 is not detected at TeV energies from $\sim$ 70 h of VERITAS data, 99% confidence level flux upper limits are calculated on multiple regions along the jets and at the location of the blackhole that were selected based on previous X-ray observations. The upper limits can be used to constrain the energetics in this microquasar system.

For Ma and Baban.

CONTENTS

LIST OF FIGURES

LIST OF TABLES

ABBREVIATIONS

CO	Compact Object
Dec	Declination
FOV	Field of View
GeV	Giga electron Volt
HAWC	High-Altitude Water Cherenkov
HE	High Energy
HMXB	High-Mass X-ray Binary
IACT	Imaging Air Cherenkov Telescope
IC	Inverse Compton
keV	kilo electron Volt
LAT	Large Area Telescope
LMXB	Low-Mass X-ray Binary
MAGIC	Major Atmospheric Gamma-ray Imaging Cherenkov
MJD	Modified Julian Day
MeV	Mega electron Volt
NSB	Night Sky Background
PMT	Photo Multiplier Tube
RA	Right Ascension
SED	Spectral Energy Distribution
TeV	Tera electron Volt
U.L.	Upper Limit
VERITAS	Very Energy Radiation Imaging Telescope Array System
VHE	Very High Energy
XRT	X-ray Telescope

ACKNOWLEDGEMENTS

'There is no such thing as a "self-made man". We are made up of thousands of others. Everyone who has ever done a kind deed for us, or spoken one word of encouragement to us, has entered into the makeup of our character and of our thoughts, as well as our success.

- George Matthew Adams

First of all I would like to thank my supervisor and mentor Prof. Dave Kieda, I could not have done this without his constant guidance and encouragement. For all the stimulating conversations not only about physics but about life. His advise "to show up is half your work done" is something which helped me immensely on difficult days when I thought it is impossible to do this. I am sincerely grateful to him. The biggest thank you would not be enough to express my gratitude for my advisor, mentor, and friend Dr. Andrew Smith. He helped me find my passion for gamma-ray astronomy, he pushed me to stand up for my work and defend it and he always lended an ear when I was overwhelmed.

I would like the thank the entire VERITAS Collaboration for their help, support, and guidance. I am especially grateful to Prof. Gernot Maier, Prof. Jamie Holder, Prof. Scott Wakely, Prof. Abe Falcone, and Prof. Reshmi Mukherjee for their advice and perspective. Special thanks to Prof. Stephan LeBohec for all those engaging discussions on science, philosophy, God, and numerous pitchers of beer.

To my friends Nolan and Ahron, thank you for all the physics discussions and listening to my rants. To Mei Hui without whom I could not have written my dissertation, you put up with me on my worse days and for that I will be always be thankful. I would like to thank my friends in Salt Lake City, Apratim, Aishwaryadev, Sayan, Niladri, Palash Da, Rambo, and Tinni who never let me miss home. To Farhana who is like a sister to me, our shenanigans are what fueled me through long days in school, thank you for being my friend. To my friends Arjun, Dodo, Ratul, and Avik for being constant companions and helping me push my limits, a big thank you.

I would like to thank my family. First and foremost my parents, they are the guiding force of my life. They sat with me through all those nights when I studied for exams or when I rehearsed for a presentation even if it was on Skype. Even though they were thousands of miles away, their unwavering support was with me everyday. Huge thanks to my brother Subhro who pushed me to step outside my boundaries, when everyone else was opposed, he secretly supported me to follow my dreams and constantly reminds me even today not to give up, just because it is difficult. Thank you to my sister-in-law Reema who always kept my chin up.

Last of all, I would like to thank my husband and best friend Dipanjan. For believing in me when I did not believe in myself, for taking care of me, for counseling me, and so many other things that I cannot fit in here. I could not have done this without you, you are what keeps me going.

CHAPTER 1

HIGH-ENERGY ASTRONOMY

Astronomy is one of the oldest branches of the natural sciences. Humans throughout history have tried to understand how changing patterns of the night sky influence their everyday lives. What we see with our eyes is only a part of the larger picture.

The universe seen in thermal and nonthermal radiation, at various wavelengths appears quite different. The electromagnetic spectrum stretches from radio wavelength (comparable to the size of a building) to gamma-ray wavelengths (comparable to the size of atomic nuclei). Most of the radiation seen from the universe is thermal in nature coming from the matter at a temperature of a few Kelvin to 10,000,000 K, beyond which atoms are ionized. The magnetic forces take over and the ionized matter in the form of electron and other charged particles are accelerated along the magnetic field lines. The accelerated charged particles further interact with matter, magnetic fields, and radiative fields to produce X-ray and gamma-ray radiation. Figure 1.1* shows the Crab Nebula at various wavelengths. While the X-ray image of the nebula clearly shows the jets and spiraling matter around the pulsar, the gamma-ray image appears as a point source and the morphology is distinctively different at other wavelengths. In this chapter, the production mechanisms of gamma-ray photons are discussed along with the description of gamma-ray binaries which emit it.

1.1 Physics of High-Energy Radiation

Nonthermal high-energy (HE) and very-high-energy (VHE) photons are produced in various astrophysical sources like blazars, pulsar wind nebula (PWN), supernova remnants (SNR), etc. with power-law distributions. Charged particles are accelerated to relativistic velocities by the powerful electromagnetic fields present within these astrophysical

*Image from http://www.wikiwand.com/en/Crab_Nebula

sources. HE and VHE photons are produced by those relativistic charged particles through various radiative processes like synchrotron radiation, inverse Compton scattering, and hadronic interactions. The next section describes processes that accelerate ions to ultra-relativistic energies followed by an overview of the radiative processes.

1.1.1 Particle Acceleration

Charged particles can be accelerated by an astrophysical electric or magnetic field. In pulsars, acceleration of charged particles by the electric field is seen in the vacuum gaps. Three different models are used to describe the origin of the emission based on different locations of the vacuum gaps. Particle acceleration and emission can occur from the gap above the magnetic pole of the pulsar (Polar Gap model) or from a region away from the surface of the pulsar surface where the co-rotation velocity of the surrounding plasma approached the speed of light (Out Gap model). The third model suggests particle acceleration and radiation at the outward asymptotically extending narrow gap from the magnetic pole (Slot Gap model).

A different acceleration mechanism, proposed by Enrico Fermi, uses magnetic fields in the plasma at astrophysical shock sites. Astrophysical shocks are collisionless, i.e., the mean free path of the colliding particles are much larger than the size of the system due to low ambient density. The shocks are driven by plasma instabilities. The *second-order Fermi acceleration* explains the acceleration of relativistic particles by reflection off randomly moving 'magnetic mirrors' within the plasma. Stochastic head-on collisions with the magnetic mirrors increase the energy of the particle whereas a tail-on collision reduce its energy. The former is more probable than the later. The average energy gain (ΔE) per collision is given by

$$\left\langle \frac{\Delta E}{E} \right\rangle = \frac{8}{3}\left(\frac{v}{c}\right)^2 \tag{1.1}$$

where v and c are velocity of the plasma and light respectively and E is the particle energy before collision. The name *second-order* is based on the exponent. The energy spectrum $N(E)$, a function of the characteristic time of confinement of the particle in the accelerating region τ_{esc} is given by

$$N(E)dE = const. \times E^{1+\frac{\tau_{acc}}{\tau_{esc}}} dE \tag{1.2}$$

where τ_{acc} is the timescale for acceleration of the particles. This mechanism is much slower and less efficient than the *first-order Fermi acceleration* mechanism.

First-order Fermi acceleration is expected when relativistic charged particles collide with strong shock waves like those produced in supernova explosion and jets of active galactic nuclei (AGN). The velocity of expanding plasma could reach 1000 times that of the interstellar cloud. Physical properties like pressure, velocity, temperature are different on two side of the shock front. The charged particles do not interact directly with the shock front but are assumed to interact with the plasma. Hence, their directions are always isotropic with respect to their surroundings. The relativistic particles energy in its stationary frame increases at each shock crossing, independent of the direction in which it crosses the shock. Every time the charged particles cross the shock front it gains energy give by

$$\left\langle \frac{\Delta E}{E} \right\rangle = \frac{4}{3}\left(\frac{v}{c}\right) \tag{1.3}$$

The energy spectrum the particle is given by

$$N(E)dE = const. \times e^{-2}dE \tag{1.4}$$

Fermi acceleration processes are only part of the story. It is still unclear how the particles are initially accelerated to relativistic energies before the first-order and second-order mechanisms take over further pushing them up to ultra-relativistic velocities.

One of the more recent theories of particle acceleration uses *magnetic reconnection* which is the breaking and reconnection of oppositely directed field lines within the plasma. At extremely high temperatures matter is ionized and exists as a cloud of electrons and positive ions referred to as the plasma state. The plasma has it own magnetic field lines trapped within the material. Charged particles are guided by magnetic fields within the plasma and they, in turn, change the magnetic field, both maintaining a dynamic equilibrium. If two magnetic field lines come too close to each other the entire pattern is disrupted and the field lines break and reconnect into an entirely new configuration in plasma releasing enormous amount of energies. *Magnetic reconnection* converts the stored magnetic field energy into heat and kinetic energy imparting exorbitant energy to charged particles thereby accelerating them to high energies. Magnetic reconnection may produce a power-law particle distribution following

$$\frac{dN}{dE} \propto E^{-p} \tag{1.5}$$

where p may reach 1 for highly magnetized plasma (*1*). This is considerably harder than the first-order Fermi process, where the particle distribution with a spectral index of $\gtrsim 2$ may be achieved. It is possible the shocks and magnetic reconnection to contribute towards particle acceleration in the same source like it is seen in Earth's magnetosphere. There are other acceleration mechanisms which are been proposed as well like *shear acceleration* (*2*), *wakefield acceleration* (*3*), etc.

1.1.2 Radiative Processes

Most of the radiation from the universe is thermal radiation given off of stars, dust, gas, and other galaxies. Above absolute zero temperature, all matter emits thermal radiation. Thermal energy generated by the random movements of atoms and molecules in the matter is converted to electromagnetic energy resulting in the emission of photons. Exotic sources in the universe like supernova remnants, active galactic nuclei, gamma-ray bursts, pulsar wind nebulae, nova, etc. emit nonthermal radiation that extends from X-ray energies to gamma-ray energies, the furthest end of the electromagnetic spectrum. Charged particles accelerated to relativistic energies produce the nonthermal radiation via a multitude of processes which are described in the following sections.

1.1.2.1 Relativistic Bremsstrahlung

Bremsstrahlung, translated from German, means 'breaking radiation' and is referred to radiation from an electron when it is decelerated in a Coulomb field of atomic nuclei. A schematic diagram of the process is shown in Figure 1.2. If the electron was initially traveling at relativistic energies then it may also radiate photons of similar energy. This implies that the electron power-law energy distribution will be echoed in the energy spectrum of the emitted photons, with the same spectral index. It is an important phenomenon occurring in the development of cosmic-ray induced particles showers in the atmosphere, and in that context will be discussed in Section 2.4.2.

1.1.2.2 Inverse Compton Scattering

A photon interacting with an electron may transfer energy by scattering the electron and changing its direction in the process known as Compton scattering. The inverse mechanism happens commonly in astrophysical sources, where a charged particle (mostly

electron) may interact with a 'seed' low-energy photon, transferring a bulk of its energy, to the photon, raising it to gamma-ray energies. This process is called inverse Compton scattering and is one of the most common production mechanisms for VHE gamma rays (*4*). A parallel schematic comparison for both the process is diagrammatically shown in Figure 1.3. The low-energy seed photons may be from the cosmic microwave background (CMB), local infrared (IR) photons from dust and clouds, optical and ultraviolet (UV) photons from stars or X-ray photons from accretion discs, etc.

If E_p is the initial energy of the photon then after collision the energy of relativistic electron (E'_p) is given by:

$$E'_p \sim \gamma^2 E_{seed} \tag{1.6}$$

where $\gamma = 1/\sqrt{1 - v^2/c^2} = E_p/m_e c^2$ is the Lorentz factor (*5*). The rate of energy lost by the electron (dE_e/dt) while interacting with an isotropic seed photon field with energy density U_p is given by

$$\frac{dE_e}{dt} = -\frac{4}{3}\sigma_T c \beta^2 \gamma^2 U_p \tag{1.7}$$

where σ_T is the Thomson cross section and $\beta = v/c$. The above equation holds only in the Thomson regime where $\gamma h\nu \ll m_e c^2$, ν being the frequency. The resulting spectrum of the scattered photon follows a power-law of index $(1 + \alpha/2)$ if the electron spectrum itself also follows a power-law of spectral index α. Above this limit, the full Klein-Nishina cross section must be used so that the probability of the interaction is suppressed (*6*). In the Klein-Nishina regime, the electron loses a major fraction of its energy in a single interaction.

1.1.2.3 Synchrotron Emission

Photons produced by synchrotron radiation hardly reach gamma-ray energies yet it is one of the dominant processes producing nonthermal radiation and provided important information about the cosmic ray population in the source. Radiation produced by relativistic charged particles spiraling along strong magnetic fields is called synchrotron radiation. The emission is beamed into a cone of angle $\alpha \approx m_e c^2/E_e$ shown in Figure 1.4 and it is emitted in a continuous spectrum with a characteristic peak.

The continuum falls off exponentially above the critical gyration frequency $\omega_c = 3c\gamma^3/2\rho_c$, where γ and ρ_c are Lorentz factor and radius of curvature of the magnetic field, respec-

tively. The higher particle energies gives more polarized and more collimated synchrotron beams. Often the energetic electron population may upscatter the synchrotron photons they produced themselves while travelling in the magnetic fields, a process called synchrotron self-Compton (SSC). If SSC radiation can be identified by comparing morphologies, emission region, etc. at the source, then the ratio of radiative losses from inverse Compton and synchrotron radiation (η) can be used to estimate the magnetic field in the region (B) using the following equation:

$$\eta = \frac{\left(\frac{dE}{dt}\right)_{IC}}{\left(\frac{dE}{dt}\right)_{sync}} = \frac{U_{rad}}{\frac{B^2}{2\mu_0}} \tag{1.8}$$

where U_{rad} is the energy density of the radiation and μ_0 is permeability of free space.

1.1.2.4 Curvature Radiation

Extremely strong magnetic fields $\sim 10^{12}$ G dampen the gyration of the relativistic charged particles due to synchrotron losses. In this case, the particles propagate along the magnetic field line instead of a moving in a helical path around it, producing curvature radiation. A diagram of the process is shown in Figure 1.5. When curvature radiation is beamed in the forward direction it may reach gamma-ray energies. This is one of the most important gamma-ray production mechanisms of pulsars.

The maximum Lorentz factor of curvature photons is given by

$$\gamma_{max} = \frac{E_e^{max}}{m_e c^2} \simeq \left(\frac{3\rho_c^2 E_{\parallel}}{2e}\right)^{\frac{1}{4}} \tag{1.9}$$

where $E_{\parallel}$ is the electric field strength parallel to the magnetic field, ρ_c is the radius if curvature of the magnetic field and E_e^{max} is the maximum energy of the electron. The electrons reach the *radiation-reaction* limit when its gain in energy from acceleration in the magnetic field is equal to its loss due to curvature radiation. The photon spectrum at this point has a break given by

$$E_\gamma^{break} = \rho_c^{1/2}(hc)\left(\frac{3}{2}\right)^{7/4}\left(\frac{E_{\parallel}}{e}\right)^{3/4} = \gamma_{max}(hc)\left(\frac{3}{2}\right)^{7/4}\left(\frac{E_{\parallel}}{e}\right)^{3/4}. \tag{1.10}$$

Above the break energy an exponential cutoff is seen in the energy spectrum, a common feature in all the *Fermi*-LAT pulsars (7).

1.1.2.5 Neutral Pion Decay

Hadrons could contibute significantly to the gamma-ray emission observed from the different sources via decay of neutral pions. Cosmic rays (primarily protons but also helium and other heavy elements) are accelerated at shocks via *Fermi acceleration* mechanisms. These accelerated cosmic rays collide with other hadrons from the ambient matter (interstellar medium, decretion / accretion discs, stellar winds, etc.), produce new mesons and baryons, some of which decay to produce gamma rays. The most likely production processes are:

$$\text{Cosmic Ray} + \text{Ambient Matter} \rightarrow p + p \rightarrow \begin{bmatrix} \pi^0 & \rightarrow & \gamma + \gamma \\ \pi^+ & \rightarrow & \mu^+ + \nu_\mu \\ \pi^- & \rightarrow & \mu^- + \bar{\nu}_\mu \end{bmatrix} \tag{1.11}$$

The π^0 decays into two gamma-ray photons 98.8% of the time and the π^+ and π^- decay into muons and neutrinos 99% of the time with a lifetime of 10^{-16} s (*8*). Neutrinos are seen by detectors like IceCube (*9*), neutrino observations could assist in identifying hadronic vs leptonic models of gamma-ray emission from a source.

1.2 Astrophysics of Gamma Ray Binaries

Gamma-ray binary is a broad definition for binary systems detected at HE and/or VHE regimes. They are a subset of X-ray binaries and their distinguishing feature is that their main power output is at gamma-ray wavelengths. The nonthermal radiated power of a gamma-ray binary dominates the spectrum in comparison to the thermal component from the optical star (*10*). X-ray binaries have a compact object (either stellar blackhole or a neutron star) accreting matter from a companion star. Based on the mass of the companion star ($M_\star$), they are characterized as *Low Mass X-ray Binaries* (LMXB) where $M_\star < 2 - 3\ M_\odot$ or *High Mass X-ray Binaries* (HMXB) where $M_\star > 10\ M_\odot$. Only 6 of the HMXB binaries are detected at VHE energies and all of them host a giant O or Be type star. They are listed in Table 1.1. In the HE energy range, a lot more variety is seen with LMXB, microquasars (μQ) and two giant main sequence stars with colliding winds. A brief overview of each of the different types of gamma-ray binaries is presented in the next section along with a diagrammatic representation of each type in Figure 1.6. The last section focuses of HMXB which are detected at TeV energies.

1.2.1 Microquasars Binaries

As suggested by the name, microquasars (μQ) are mini versions of AGNs with an accreting blackhole expelling powerful jets. Similar to AGNs, the relativistic jets of μQ exhibits emission from radio to X-ray energies supporting the presence of TeV electrons which, in turn, could result in HE and VHE emission. At present, two μQs are known emitters of HE emission both detected by *AGILE* and *Fermi*-LAT . They are Cygnus X-1 (*11*, *12*) and Cygnus X-3 (*11*, *13*, *14*), both systems harbor blackhole candidates orbiting massive stars. The spectral state of a μQ is its key feature; μQs generally show the presence of HE emission only when radio emission is seen. Thermal emission up to MeV energy range may be seen in the spectrum but the observed GeV emission is unrelated to the MeV spectral tail. While the MeV thermal emission may be coming from the corona of the accretion disc, the GeV emission is produced further out from the disc (*15*). Small pressure differences within the jet itself may give rise to shocks. These shocks cause recollimated jets and are the probable sites of particle acceleration that result in the observed GeV emission. In AGNs, these recollimated shocks give rise to knots of observed HE / VHE emission (e.g., M87 (*16*)).

The Cyg X-3 binary system has a massive Wolf-Rayet star in a 4.8 h tight orbit with a black hole candidate (*14*). The high mass loss rate of the optical star exerts extreme ram pressure on the companion due to close proximity (only one stellar radius distance), which would be sufficient to recollimate the jets of the blackhole, a possible explanation for the HE emission seen from the system. This system has not been detected at VHE wavelengths.

Cyg X-1 has been observed at VHE wavelengths and only one time came close to being detected by MAGIC in 2006 with a 4.9 σ pretrials (*17*). The VHE excesses by MAGIC was observed during an X-ray flaring state contemporaneously detected by *RXTE*, *Swift* and *INTEGRAL*. Cyg X-1 was detected $\sim 8\sigma$ significance level using 7.5 years of *Fermi*-LAT data and a gamma-ray luminosity of 5.5×10^{33} erg s^{-1} above 60 MeV was calculated(*18*). The origin of HE emission could be either leptonic or hadronic. The most likely explanation of the HE emission is the upscattering of seed photons by inverse Compton processes by energetic particles produced in the relativistic jets. The seed photons could be thermal photons from the optical star and/or accretion disc. Strong polarization in the 0.2-1 MeV

tail provides evidence of synchrotron emission in the jets, which could also explain the HE emission produced by Synchrotron-Self-Compton processes.

No VHE emission has been seen from extensive searches of other microquasar X-ray binaries either with a high-mass or a low-mass companion (*19–21*). Deeper observations of our galaxy by *Fermi*-LAT and the next generation Cherenkov telescope, Cherenkov Telescope Array (CTA) will further constrain the emission models of μQ and may help in finding gamma ray emitting μQ X-ray binaries. For now, the VHE emission from a μQ binary remains unconfirmed.

1.2.2 Pulsar Binaries

Pulsars are abundant in the HE sky and a lot of them have companion stars which overfill their Roche lobe and transfer the matter to the pulsar. Depending on the mass of the companions the pulsar binaries could be a Low-Mass X-ray Binary (LMXB) with $M_\star \lesssim 1.5\ M_\odot$ or a High-Mass X-ray Binary (HMXB) with $M_\star \gtrsim 10\ M_\odot$. While HMXB with a pulsar have an O or B type massive companion star the LMXB may have main sequence stars of 1.5-5 $M_\odot$ from which matter has been stripped away by the pulsar or white dwarf. LMXB are concentrated in the direction of the galactic center and are progenitors of the majority of observed millisecond radio pulsars. Rotation-powered pulsars drive tenuous highly relativistic winds of charged particles (e^+e^-) and electromagnetic energy beyond its light cylinder. In pulsar wind nebulae (PWN), the pulsar is isolated, and its energetic wind travels far out interacting with the shell left behind by the supernova explosion (which created the pulsar) creating shocks. In binary systems, the pulsar wind interacts with the wind of the optical companion, a much denser environment and forms a shock structure at a much smaller scale than a PWN. Equating the pulsar wind ram pressure to the surrounding ram pressure of the isotropic, coasting stellar wind, we can estimate the distance traveled by the pulsar wind

$$\frac{R}{d} \approx \frac{1}{1+\eta^{1/2}} \text{ where } \eta = \frac{\dot{M}_w v_w}{\dot{E}/c} \tag{1.12}$$

where the orbital separation is 'd', $\dot{E}$ is the pulsar wind power, $\dot{M}_w$ and v_w are the stellar wind mass loss rate and velocity, respectively. A strong stellar wind would generate a strong 'thrust', $\dot{M}_w v_w$ would constrain the pulsar wind close to the pulsar itself ($\eta \gg 1$) which implies $R/d \ll 1$. The opposite is true when the strong pulsar wind pushes back

a weaker stellar wind to its surface ($\eta \ll 1$) implying $R/d \approx 1$. HE and VHE gamma rays may be produced by energetic particles accelerated at the shock via diffuse shock acceleration (*Fermi acceleration*) or shock-driven reconnection. For details see (*22*) and references therein.

Besides PSR B1259-63, only 4 other pulsar binaries with massive companions have been detected: PSR J1740-3052, PSR J1638-4725, PSR J0045-7319, and PSR J2032+4127 (*22*). While the first three may be too faint to detect at HE due to low spin down power and larger distances, the last one is a very promising candidate. PSR J2032+4127 is a 143 ms pulsar in a super eccentric orbit ($e = 0.95$) possibly associated with 15 $M_\odot$ star with a 45-50 year orbital period (*23*, *24*). The pulsar is approaching periastron in November 2017 and providing a once in a lifetime opportunity by current generation telescopes to observe any variable HE / VHE emission from the associated (yet unidentified) source TeV J2032+4130 (*25*, *26*). The brightening X-ray emission seen by *Chandra* and *Swift* (by a factor of 70 since 2002 (*24*)) currently during pulsar approach towards periastron may be due to the collision of the pulsar wind and the Be star wind similar to that seen in PSR B1259-63. This makes PSR J2032+4127 / TeV J2032+4130 one of the most interesting multiwavelength targets of opportunity.

1.2.3 Other Binaries

Two other types of binaries have been detected at HE by *Fermi*-LAT . A *nova* explosion in 2010 from V407 Cygni located in the Cygnus region by *Fermi*-LAT was a surprising event. It was the first time that HE gamma rays were detected from such a binary (*27*). V407 Cygni and other nova binaries are composed of a white dwarf and an aging star (red giant or red dwarf). The outer shell of an aging star expands from which matter (mostly hydrogen) is captured by the white dwarf and accumulates on its surface. When the density of matter reaches above a critical limit, fusion of hydrogen into helium begins resulting in a powerful explosion. The thermonuclear runaway event blasts the accumulated gas creating shocks in the expanding envelope around the white dwarf star. At the shock front, particles may be accelerated by *Fermi acceleration* processes resulting in the observed HE emission. As the nuclear burning ceases after a few days the pressure falls and the envelope around the white dwarf fades away. Most of the energy in a nova

is released in the optical band but the detection of multiple nova events by *Fermi*-LAT establishes another class of gamma-ray binaries (*28*). Nova events have not been detected at VHE energies yet, which places limits on the highest energies to which particles can be accelerated in such systems (*29*).

HE gamma rays > 100 MeV were detected from η Carina, a colliding wind binary system by *AGILE* during July 2007 - January 2009 (*30*). The η Carinae system has a luminous blue variable star (LBV) of $\sim 90 M_{\odot}$ in a highly eccentric orbit $(e = 0.9)$ with a O star of $\sim 30\ M_{\odot}$. Powerful dense winds from both the massive stars collide producing X-rays during its $\sim$ 2023 days orbital period (*30*) and is an ideal laboratory to study theories of particle acceleration and radiation under extreme conditions. There are multiple recipes of HE photon production that may be used to explain the observed HE flux. The collision of supersonic winds from the massive stars creates efficient shock fronts where charged particles are accelerated through *first-order Fermi* and other acceleration mechanisms (*31*). Seed photons from nearby stars and thermal photons arising from collision of the winds could be inverse Compton scattered by the energetic particles producing HE emission that dominates the HE spectrum up to GeV energies. If the shocks accelerate protons efficiently, they may interact with protons from the dense stellar outflows and produce neutral pions which decay to produce HE gamma-ray photons. While *AGILE* had seen flares in η Carinae at gamma-ray energies (*30*) similar to X-rays, *Fermi*-LAT observed steady gamma-ray emission. The binary has now been intensely observed over three periastron passages, each time exhibiting an X-ray flare followed by a dip and then gradual recovery of the emission, but with slight differences each time. This may indicate structural changes in the colliding winds. η Carinae is the sole member of the colliding wind gamma-ray binary class and remains undetected at VHE.

1.2.4 TeV Binaries

TeV Binaries are a special class of HMXB that consistently has been detected by VHE instruments. Currently, there are only 6 such systems. Most of the TeV binary systems exhibit modulated emission over a broad range of wavelengths tied to their orbital periods (P_{orb}). While all of them have a compact object in orbit around a massive star (O or Be type) their periods can extend from a few days to a few years. PSR B1259-63 is the only

TeV binary known to host a *ms* pulsar, for the others the nature of the compact object is still unknown. The next section takes a closer look at three of the TeV binaries PSR B1259-63, LS 5039 and HESS J0632+057 which will help us understand different aspects of these systems. Since LS I $+61^{\circ}$ 303 is the principle source of interest for this dissertation, its relevant background is discussed in later chapters of the dissertation in the context of observations, analysis, and results.

- PSR B1259-63: In the PSR B1259-63 binary system, a luminous Be star SS 2883 of 30 $M_{\odot}$ is orbited by a 48 ms radio pulsar once every 1236 days. An artist impression is shown the system in Figure 1.7. The equatorial disc of the Be star is inclined to the eccentric orbit of the pulsar. Intense HE and VHE emissions are observed from the system when the pulsar crosses the dense decretion disc of the Be star. At periastron the pulsar is only 0.9 AU away from its companion and its radio pulses are eclipsed. The colliding winds of the pulsar and the Be star wind results in a bow shock where $e^{+}e^{-}$ may be accelerated and produce gamma rays by IC processes. Several mechanisms of HE gamma-ray production via synchrotron radiation, bremsstrahlung radiation, and pion decay may also be at play (*32*–*34*). The HE emission seen by *Fermi*-LAT a month after periastron was almost 30 times brighter than what has been observed preperiastron (*35*). Studies of PSR B1259-63 provide crucial understanding of the emission mechanisms in other TeV binaries.

- LS 5039: Emission is observed from LS 5039 from radio to TeV energies. The compact object orbits the 23 $M_{\odot}$ O type star once every 3.9 days. VHE emission was first observed from the system by H.E.S.S. (*36*). The geometry of the binary system is shown on the *left* panel of Figure 1.8 where Superior Conjunction (SUPC) is the orbital position of the CO when its eclipsed by the bigger optical star and Inferior Conjunction (INFC) when it is in the foreground of the optical star. While the X-ray and VHE emission show similar characteristics the HE emission seems to be anticorrelated with TeV emission. Maxima and minima is observed at inferior and superior conjunction, respectively, for both X-ray and TeV energies, but the trend is opposite for Mev-GeV energy range. A spectral evolution from a harder to a softer state is seen between inferior and superior conjunction at TeV energies, this is also inverted

in the MeV-GeV energy range. Spectral energy distribution (SED) in the VHE range is shown on the *right* panel of Figure 1.8. While a simple power law for SUPC phase range (in blue) fits the spectral points, an exponential cutoff around 6 TeV is seen in the spectrum for INFC passage (*37*). The seperation between the star and the CO the binary system varies between 2-6 $R_\star$, immersing the accelerated charged particle in a dense photon field continuously. The stellar photons are boosted to gamma-ray energies very efficiently by inverse Compton processes on account of shorter radiative timescales compared to the escape timescale. Proton-proton interaction in the dense stellar wind resulting in neutral pions and their decay into gamma rays may also contribute to the observed flux (*38*).

- HESS J0632+057: Observations by H.E.S.S of the Monoceros Loop SNR in 2004 resulted in the serendipitous discovery of HESS J0632+057 (*39*). It is the only gamma-ray binary which is not detected by *Fermi*-LAT at HE (*40*, *41*), but is detected by other VHE instruments (*42*, *43*). Observation with *Swift* confirmed the binary nature of HESS J0632+057, identifying the X-ray source XMMU J063259.3+054801 and Be star MWC 148 as the two components of the binary system. The period of the binary is about 315 days, and it exhibits modulated X-ray and TeV emission around the orbit. The VHE and X-ray emissions were found to be correlated (*44*). HESS J0632+057 exhibits two distinct maxima in the flux at both X-ray and VHE wavebands with a X-ray minima in between at apastron (*45*). A simple one-zone leptonic model, where relativistic electrons lose energy by synchrotron emission and inverse Compton emission resulting in the X-ray and VHE emission, respectively, can explain the observed correlation between the two wavebands. The alternating maxima and minima in the emission observed may arise due to geometry of the sytem and/or mass accretion rate from the stellar disc onto the compact object. For extended discussion on the missing MeV-GeV emission and the peculiar light curve, see (*45*) and references therein.

Table 1.1: Catalog of gamma-ray binaries.

Name	Binary Components		P_{orb} [d]	HE	VHE
High Mass X-ray Binaries					
LS 5039	?	O	3.9	✓	✓
HESS J1018-589 A	?	O	16.6	✓	✓
LS I +61° 303	?	Be	26.5	✓	✓
HESS J0632+057	?	Be	315	✗	✓
PSR B1259-63	47.7 ms pulsar	Be	1236.7	✓	✓
HESS J1832-093 (*47*)	?	?	?	?	✓
Low Mass X-ray Binaries (selected few)					
XSS J12270-4859	1.7 ms pulsar	red dwarf	0.29	✓	✗
PSR J1023+0038	1.7 ms pulsar	red dwarf	0.20	✓	✗
2FGL J0523.3-2530	?	red dwarf	0.69	✓	✗
PSR B1957+20	3.8 ms pulsar	brown dwarf	0.38	✓	✗
Microquasars					
Cyg X-3	blackhole ?	Wolf-Rayet	0.20	✓	✗
Cyg X-1	blackhole	O	5.60	✓	?
Novae					
V407 Cyg	white dwarf	red dwarf	14000 ?	✓	✗
V1324 Sco	white dwarf	red dwarf	0.07 ?	✓	✗
V959 Mon	white dwarf	red dwarf	0.30	✓	✗
V339 Del	white dwarf	red dwarf	0.13 ?	✓	✗
V1369 Cen	white dwarf	red dwarf	?	✓	✗
Colliding Wind Binaries					
η Carinae	LBV	O/WR	2023	✓	✗

Table is updated from (*22*), see references therein

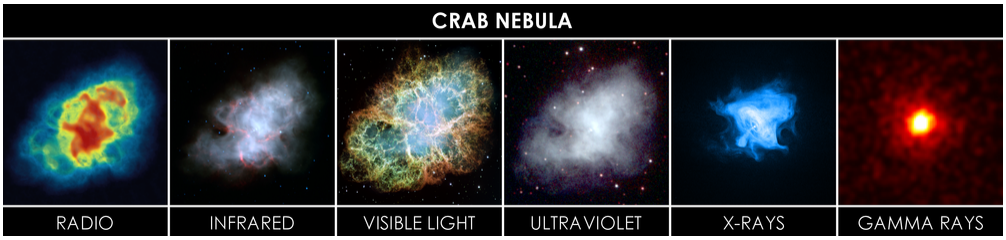

Figure 1.1: The Crab Nebula seen is radio, infrared, visible light, ultraviolet, X-rays, and gamma rays.

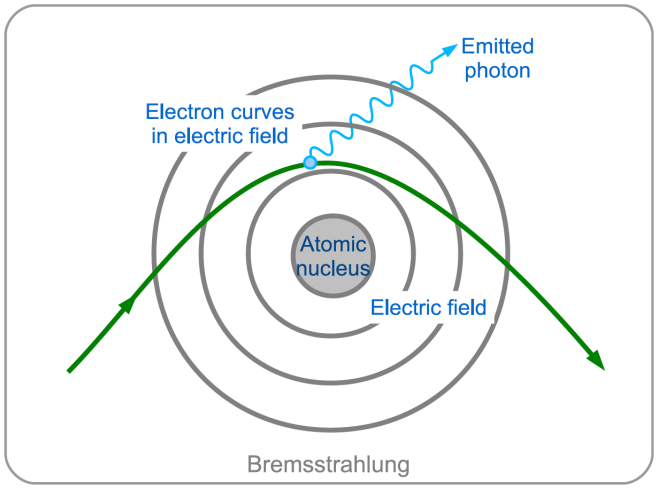

Figure 1.2: Bremsstrahlung radiation. Figure from (*46*).

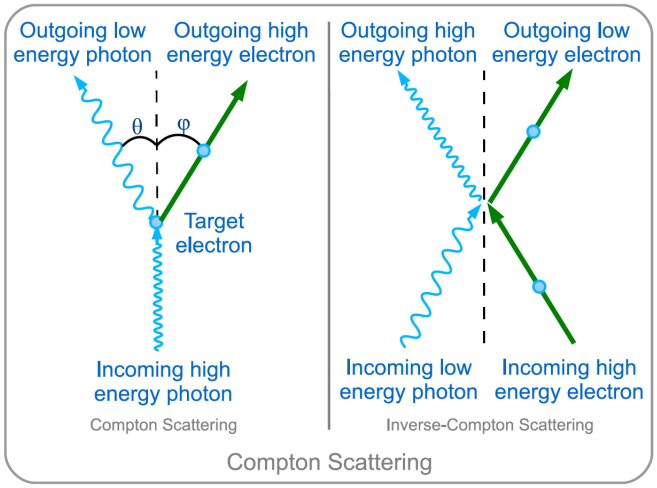

Figure 1.3: Compton scattering and Inverse Compton scattering. Figure from (*46*).

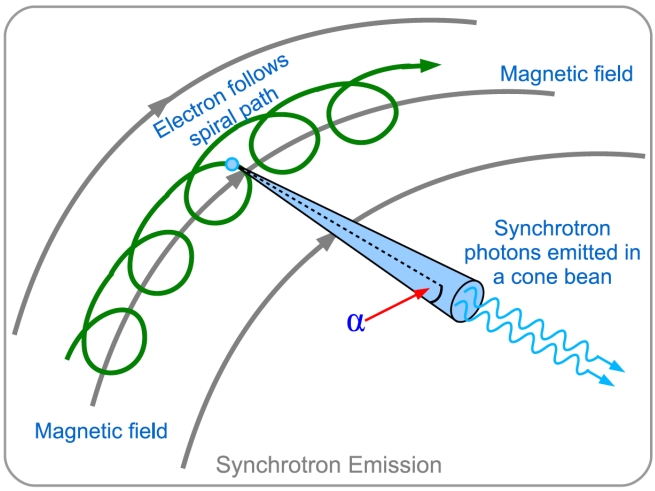

Figure 1.4: Synchrotron radiation. Figure from (*46*).

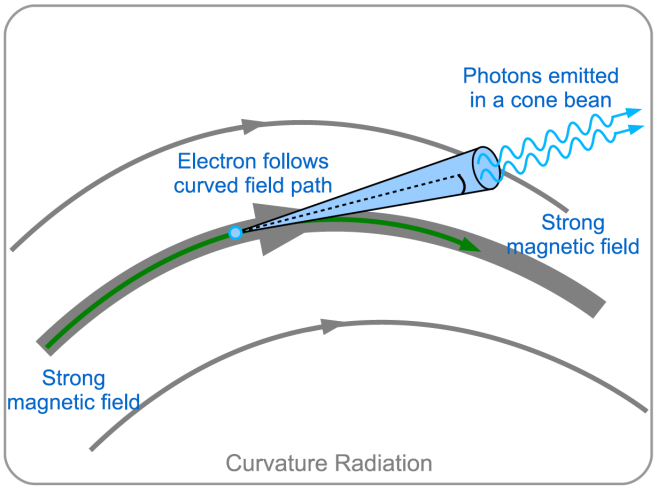

Figure 1.5: Curvature radiation. Figure from (*46*).

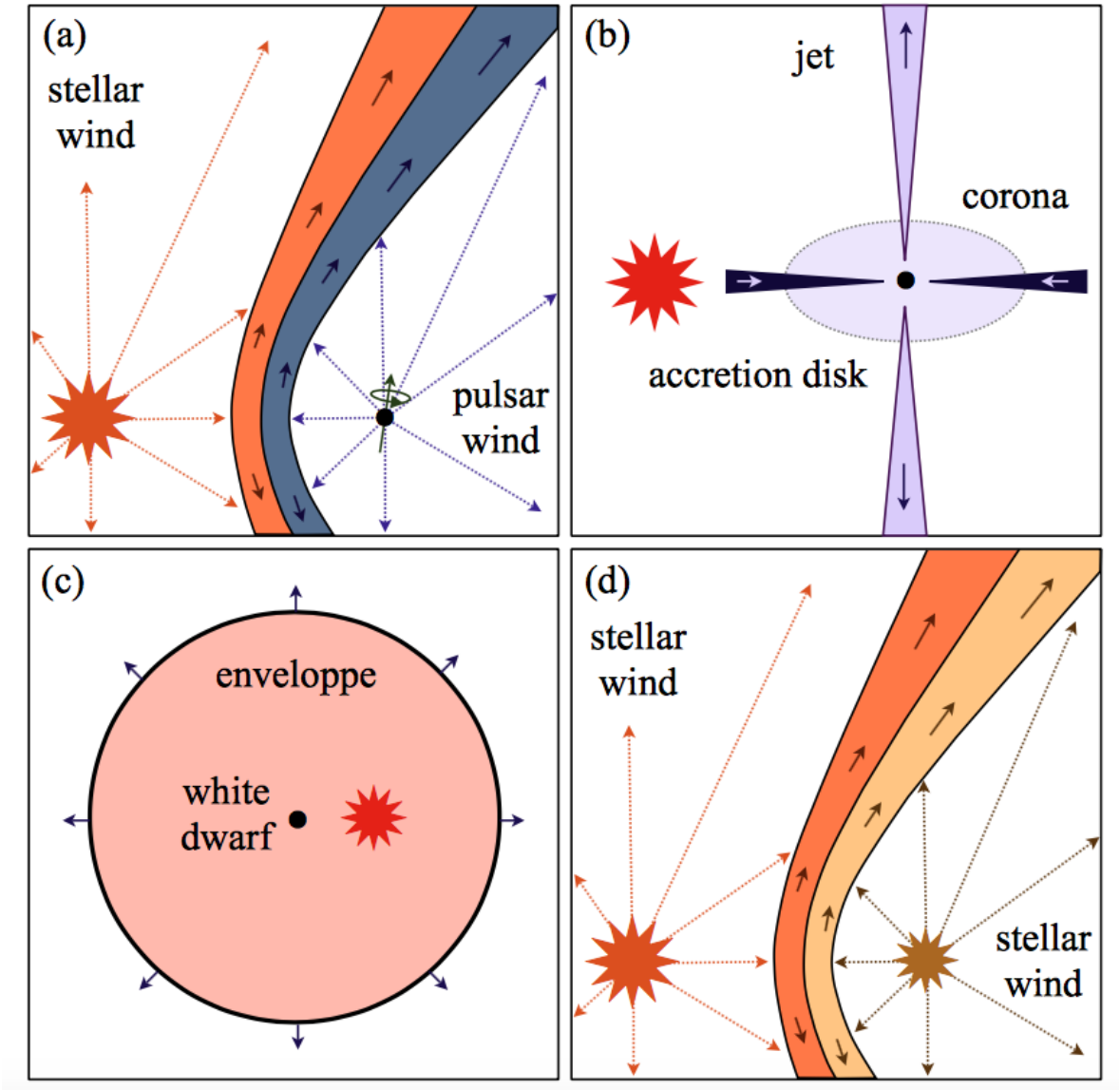

Figure 1.6: Different types of gamma-ray emitting binary systems. (a) A giant star in association with a rotation powered pulsar. (b) An optical star in association with a stellar black hole with accretion disc and jet. (c) A white dwarf enveloped in the expanding exterior of the associated nova. (d) Colliding wind binary with interacting stellar winds from two optical stars. Figure from (22).

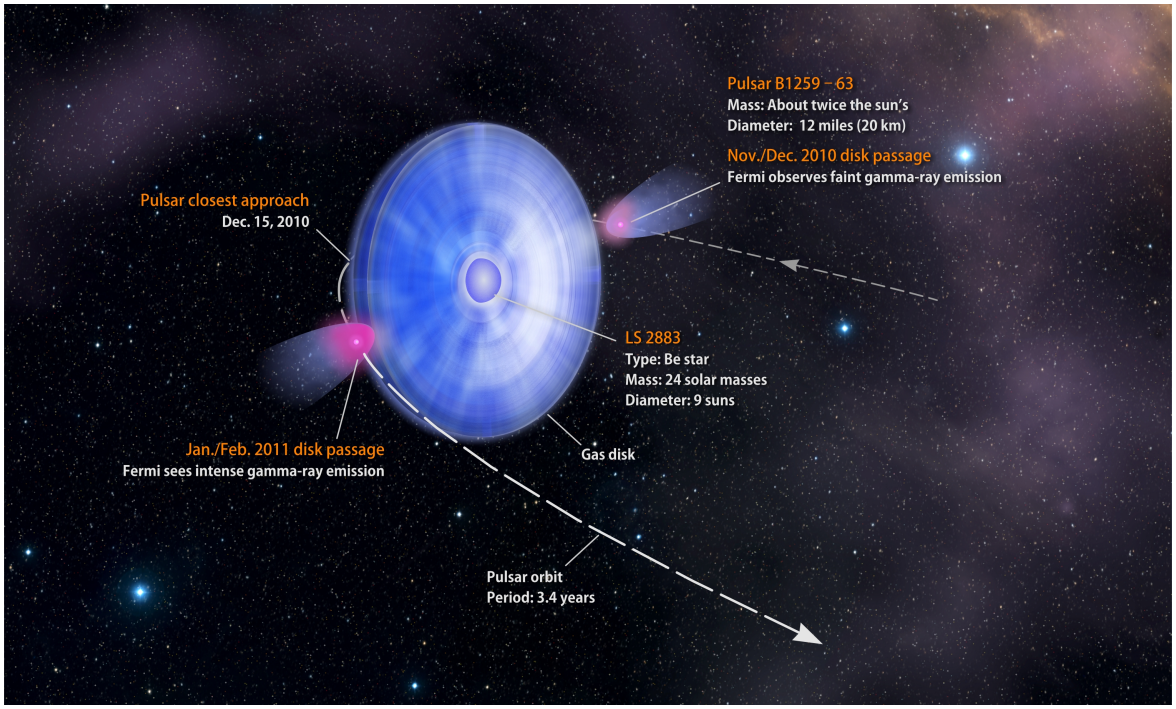

Figure 1.7: Anatomical diagram of unique binary system PSR B1259-63. It is the only TeV Binary where the compact object has been confirmed to be a pulsar from its pulsed emissions. The pulsar has an orbital period of 3.4 years and emits high-energy gamma rays twice during its passage through the equatorial disc of the star. (Credit: NASA's Goddard Space Flight Center/Francis Reddy)

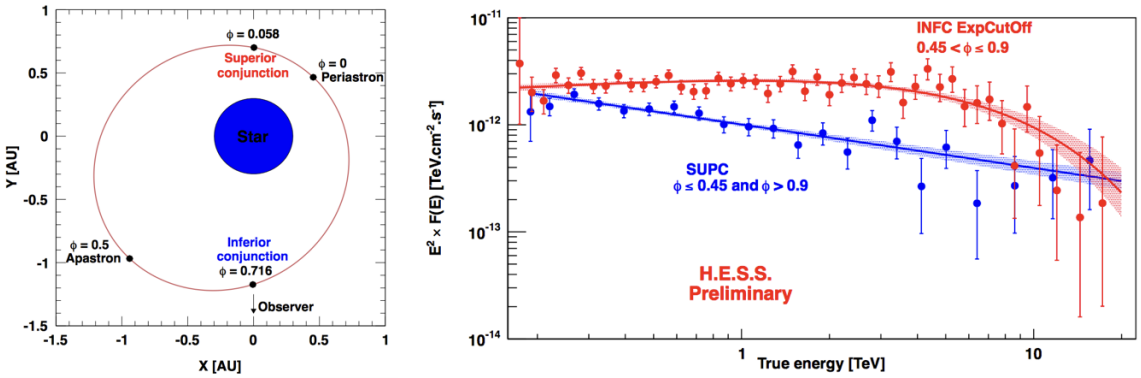

Figure 1.8: *Left:* Orbital geometry of LS 5039 binary system. *Right:* Spectral energy distribution for two different phase ranges during Superior Conjunction (blue) and Inferior Conjunction (red). Both figures are reproduced from (37).

CHAPTER 2

OBSERVING HIGH-ENERGY RADIATION

Observation at extreme energies comes with many challenges. High energy photons (from far UV to gamma-ray energies) do not reach the earth's surface like photons in the optical or radio energy range. HE photons have to be imaged in space or imaged with indirect techniques on the ground. Some of the leading telescopes observing the farthest end of the electromagnetic spectrum are discussed with special focus on *Swift*, *Fermi*, *VERITAS*, which are instruments relevant to this research.

2.1 X-ray Telescopes (keV energies)

The earth's atmosphere is opaque to X-rays, they have to be observed from space-based instruments. The first imaging X-ray telescope Einstein Observatory was launched in 1978. Since then many successful X-ray telescopes like EXOSAT, Ginga, RXTE, ROSAT, ASCA XMM-Newton, and Chandra have detected thousands of X-ray sources both in and outside the galaxy. In this particular dissertation, data from the Swift X-ray telescope are extensively used. A description of the instrument is given below.

2.1.1 Swift - XRT

The Swift Gamma-Ray Burst Explorer (*48*) is a pioneer transient astronomy instrument primarily dedicated to observing Gamma-Ray Burst and their afterglows in multiwavelength. Three instruments are carried by Swift, the Burst Alert Telescope (BAT(*49*), energy range 15-150 keV) which detects bursts and autonomously slews the instrument rapidly in that direction to observe it with the X-ray Telescope (XRT(*50*), energy range 0.2-10 keV) and Ultra Violet Optical Telescope (UVOT (*51*), 170-600 nm band). The satellite was launched in 2004 and has observed more than 1000 GRBs, the farthest one being 13 billion lightyears away from earth occurring at the dawn of star formation in the universe.

Swift has a flexible Target of Opportunity program using which the XRT is pointed

at interesting sources by other instruments to perform multiwavelength studies. The XRT uses a grazing incidence Wolter I telescope to focus X-rays onto a focal plane camera, which contains a single e2v CCD-22 detector. It has a 23.6 $\times$ 23.6 arcminute FoV and positional accuracy of 3 arcseconds. Is has an effective area of $\sim$ 125cm^2 at 1.5keV and had originally 4 readout modes (Image, Photodiode, Windowed Timing, and Photon Counting). The modes are designed to avoid saturation of the detector during various phases of observations and switches autonomously based on instantaneous count rates in each CCD frame. The Swift Gamma-Ray Burst satellite is shown in Figure 2.1 and the schematic diagram of the onboard X-ray Telescope(XRT) is shown in Figure 2.2

2.2 Space Based Gamma-Ray Telescopes (MeV-GeV energies)

High-energy photons cannot be focused like optical or even X-ray photons. Above 20 MeV gamma-ray photons are detected by electron-positron (e^-e^+) pair produced from their interaction with matter. The direction and energy of the photons in determined from the e^- tracks in the detector and the energy deposited in the calorimeter. COS-B and EGRET were pioneers on gamma-ray astronomy and discovered many HE galactic and extragalactic sources. With the launch of Fermi Gamma-Ray Space Telescope (formerly GLAST) in 2008, gamma-ray astronomy stepped into an era of unprecedented growth and discovery.

2.2.1 Fermi Gamma-Ray Telescope

Fermi observes the high-energy sky in the energy range 20 MeV to >300 GeV (*52*). It has two instruments on board, the Large Area Telescope (LAT) which is the primary imaging gamma-ray detector and the Gamma-ray Burst Monitor (GBM) consisting 14 scintillation detectors dedicated to detecting transient phenomenon. The LAT lies under the plastic anticoincidence detector shown in Figure 2.3 which helps in determining the background of cosmic rays. The gamma rays entering the instrument interact it one of the 18 tungsten converter layers producing e^-e^+ pairs. The e^-e^+ pairs further produce ions interacting with the thin silicon strip detectors, interleaved with the tungsten layers. The particles are tracked in Si strips alternating in X and Y directions used in reconstructing the energy of the incident gamma ray. The particles are absorbed in the cesium iodide calorimeter from

which the energy of the incident gamma ray is calculated from the energy deposited in the calorimeter. The GBM covers the energy range of 8 keV - 30 MeV and detects GRBs and other transient phenomena, for details of this instrument see (*53*).

Fermi has made many discoveries over it 8+ years of operations and boasts of 3000+ sources in its catalog (*54*). One of the most intriguing discoveries by *Fermi*-LAT are the Fermi Bubbles, two giant structures above and below the plane of the Milky Way connected at the galactic center, perhaps a remnant of the activity of the supermassive black-hole in the center of the galaxy. It has detected more than 1000 GRBs and the most distant gamma-ray blazar. Recently *Fermi*-LAT detected the most extreme gamma-ray binary in another galaxy called LMC P3. Residing in the Large Magellanic Cloud, a galaxy 163,000 light-years away, the binary has a 10.3 day orbit composed of a giant star accompanied by a compact crushed stellar core and it is the most luminous gamma-ray binary known.

2.3 Ground Based Gamma-Ray Telescopes (TeV energies)

Astrophysical objects produce gamma rays with a steeply falling power-law spectrum resulting in lower photon flux at higher energies. The Crab Nebula shows $\sim 10^{-3}$ γs m^{-2} s^{-1}above 100 MeV when observed above 1 TeV yields only ~ 6 $\gamma s \mathrm{m}^{-2}\mathrm{year}^{-1}$ (*55*). Larger light collectors or detectors are required to compensate for the lower flux of photons. While space-based instruments have a distinct advantage of directly imaging gamma rays with exceptional angular and energy resolution, they are limited in the size of the detector (collection area $\sim 1m^2$), hence, they cannot probe highest energy range of the spectrum. Ground-based gamma-ray telescopes with effective collection areas of $> 10^5 m^2$ measure VHE gamma rays indirectly from the Cherenkov radiation produced by gamma-ray-driven particle cascades in the detector medium (atmosphere and/or water).

2.3.1 Imaging Atmospheric Cherenkov Telescopes

The first detection of the very first VHE gamma-ray source, the Crab Nebula by Whipple Observatory in 1989 marks the beginning of the VHE gamma-ray astronomy field. Since then many imaging Cherenkov telescopes has operated like HEGRA, CAT, CANGAROO, CELESTE, STACEE. HEGRA for the first time demonstrated the benefit of stereo imaging technique using 5 telescopes. The three currently operational new generation of

Imaging Atmospheric Cherenkov Telescopes (IACTs) H.E.S.S, MAGIC, and VERITAS has improved sensitivities an order of magnitude than the previous generation discovering hundreds on VHE sources. A short description of H.E.S.S. and MAGIC are presented below followed by detailed description VERITAS and it analysis technique at the end of the chapter.

- H.E.S.S.: The High-Energy Stereoscopic System or H.E.S.S. shown on the top panel of Figure 2.4 is an array of 5 IACTs located in the Khomas Highland of Namibia at 1800 m a.s.l. 23°16′ S, 16°30 E. In phase I, H.E.S.S. began operations with 4 telescopes in December 2003. A much larger 5th telescope was incorporated in the center of the array and began the phase II operation in July 2012. The H.E.S.S. II telescope lowered the energy threshold to 30 GeV (*56–58*). The 12 m sized smaller telescopes have 5° field of view and Davies-Cotton optical reflectors whereas the 28 m large telescope has a parabolic mirror with 3.2° field of view. The galactic plane survey conducted by H.E.S.S. provided an unprecedented glimpse at inner part of the Milkyway galaxy at very high energies. Numerous new sources were identified which were associated with SNRs, PWNs, binaries, star forming regions, starburst galaxy, active galactic nucleus, and unidentified sources (*59*). H.E.S.S. has discovered more than 80 VHE gamma-ray sources from it 10,000+ h of observations and continues observing the non-thermal VHE southern sky.

- MAGIC: The Major Atmospheric Gamma Imaging Cherenkov Telescope or MAGIC, shown on the bottom panel of Figure 2.4 is an array of 2 telescopes with 17 m diameter observing the VHE sky from 30 GeV to a tens of TeVs. It is located at a height of 2200 m a.s.l. on the Roque de Los Muchachos European Northern Observatory on the Canary Island of La Palma (28°N, 18°W). Initially, its started operations with 1 telescope in 2004 and later an identical telescope was added in 2009 for stereoscopic mode, improving the sensitivity significantly due to better background rejection. MAGIC detected two of the most distant blazars PKS 1441+25 and QSO B0218+357 at VHE energies (*60*), light from these blazars has been traveling for over half the age of the universe. Gamma rays are freely attenuated while traveling through the universe due to the interaction with diffuse emission, the extragalactic background

light. Detection of VHE emissions helped in improving the models for extragalactic background light that is created by all stars and dust throughout the history of the universe. MAGIC has made many important discoveries like pulsed VHE emission from the Crab pulsar and delayed signal from QSO B0218+357 confirming deflection of VHE photons by gravitational lenses in agreement with General Relativity (*61*, *62*).

2.3.2 Water Cherenkov Telescopes

The Milagro detector that operated between 2000 and 2008 was the first particle detector using water tanks. It detected the Crab Nebula, MRK 421, MRK 501 and a number of extended sources in the galactic plane including the Geminga PWN. Milagro was the predecessor of the current water Cherenkov telescope, HAWC briefly described below.

The High Altitude Water Cherenkov Telescope or HAWC observes gamma rays at the highest energies between 100 GeV and 100 TeV. It is situated at the base of Sierra Negra volcano in Puebla, Mexico (altitude = 4100m, location N $18^{\circ}59'48''W97^{\circ}18'34''$) (*63*). The completed detector started operations in November 2014 and has a 1-year sensitivity of 5-10% (variation dependent on the declination of the source) of the flux from the Crab Nebula. It has a wide field of view $>$ 1.5 sr and a high duty cycle $>$ 90% continuously surveying the VHE sky. The unique detector uses 300 commercial water storage tanks each with 4 upward facing photomultiplier tubes (PMTs) embedded in 190,000 liters of ultra-purified water. The array of water tanks is shown in Figure 2.5. The basic principle of operations is similar to IACTs except water is used as an additional cascading medium. VHE photon that produces EAS reaching the ground produces further cascades in the water. The detector acts as a calorimeter estimating the EM energy deposited from the cascade particles. Larger transverse momentums are expected from cosmic ray cascade particles, illuminating PMTs further from the shower core than from gamma-ray showers. The patterns of illuminated PMTs are used to differentiate cosmic ray showers and gamma-ray showers. A total of 39 sources were detected by HAWC from it 275 days of operations, some of which are known VHE gamma-ray sources and a host of new unassociated source. For details of the instruments and its outstanding discoveries see (*64*, *65*).

2.3.3 Future of Very High-Energy Astronomy

The Cherenkov Telescope Array or CTA, the next generation of IACTs promises to increase the number of VHE sources by an order of magnitude. Three classes of telescopes in the array will cover an energy range from 20 GeV to 300 TeV. The CTA Observatory will host 8 Large Size Telescopes (LSTs), 40 Medium Size Telescopes (MSTs) and 70 Small Sized Telescopes (SSTs) shown on *left* of Figure 2.6. While the northern site at La Palma, Spain will be consists of fewer telescopes (15 MSTs and 4 LSTs) aimed at an energy range 20 GeV - 20 TeV, the larger southern site at Chile will cover the entire energy range with 4 LSTs, 25 MSTs, and 70 SSTs. On the *right* of Figure 2.6, the expected sensitivity of CTA is shown in comparison to the current generation of IACTs. For an overview of the CTA concept, see (*66*).

2.4 Terrestrial Observations of Very High-Energy Radiation

The atmosphere acts as a barrier between earth and high-energy radiation from the universe, which while protects life on earth, also makes direct observation of VHE radiation difficult. Relativistic cosmic ray particles and VHE gamma-ray photons on striking air molecules initiates cascades of particle called *Extensive Air Showers* which emit *Cherenkov* radiation. IACTs like VERITAS detect the faint ultraviolet Cherenkov light flashes and reconstruct the incident primary cosmic-ray particle or photon. The following sections explore the production of Cherenkov radiation in the atmosphere, the developments of extensive air showers, and fundamentals of the detection technique employed by IACTs.

2.4.1 Cherenkov Radiation

The maximum velocity that can be achieved by a particle is that of the speed of light in the vacuum (c). Light itself slows down in a medium like air or water which has a refractive index greater than 1. In such a medium, a particle can travel faster than light and in the process emits *Cherenkov radiation*. When a charged particle travels through a dielectric medium it polarizes the surrounding medium. Once the charged particle has passed the polarized molecules relax by emitting radiation (a pulse of light lasting tens of nanoseconds). If the charged particle has low velocities, i.e., less than the speed of light in the medium, the polarization is symmetrical along the path of the particle. The

radiation produced during relaxation is not coherent and does not travel long distances. If the charged particle, on the other hand, is traveling with ultrarelativistic speeds greater than that of light in the medium, the polarization is asymmetric along the path of the particle. The radiation produced during relaxation in this case called Cherenkov radiation is coherent. Both these scenarios are shown in Figure 2.7. Cherenkov pulses are produced along the track of the charged particle and they constructively add up according to Huygens's principle at a given angle from the particle trajectory as shown in Figure 2.8. The Cherenkov angle (θ_C) is given by:

$$\cos\theta_C = \frac{c/n}{\beta c} = \frac{1}{\beta n} \tag{2.1}$$

The threshold speed to produce Cherenkov radiation is given by $\beta_{th} = 1/n$ as $\cos\theta_C \leq 1$. According to Einstein's relativity principle for a particle of rest mass, m the energy threshold of the particle for the production of Cherenkov radiation is:

$$E_{C,th} = \gamma mc^2 = \frac{mc^2}{\sqrt{a - n^2}} \tag{2.2}$$

Depending on the height of the atmosphere it density changes which in turn affects the refractive index. The refractive index increases on approaching the sea level which changes the Cherenkov angle and energy threshold. At sea level, the refractive index at visible wavelengths is 1.00029, so the maximum Cherenkov angle $\theta_{C,max} = 1.4^\circ$ at sea level, and about 0.8° at an altitude of $\sim$ 810 km, where VHE gamma-ray showers typically reach their maximum development. Similarly, the threshold energies at sea level for electrons and protons are 21 MeV and 39 GeV, respectively.

2.4.2 Extensive Air Showers

The cascades induced by charged particles are called *hadronic showers* and those by VHE gamma-ray photons are called *electromagnetic showers*. There are some distinctive features between the two showers which are key to separating the gamma-ray signal from the cosmic ray background. The two types of showers and their key differences are shown in Figure 2.9 and discussed in the following two sections.

2.4.2.1 Hadronic Shower

When a cosmic ray enters the Earth's atmosphere it strikes nucleus of an atmospheric molecule like nitrogen or oxygen and initiates a cascade of particles. The dominant particle

produced in these interactions are π mesons which also collide with air molecules generating cascades. There are three components in a hadronic shower, the electromagnetic component, the hadronic component and the muonic component. The electromagnetic component is driven by electrons, positrons, and photons produced in subcascades that have been initiated by immediate decays of neutral pions into photons ($\approx 10^{-16}$ s). The charged pions and kanons have larger decay times ($\approx 10^{-8}$ s) and collide with more atmospheric molecules continuing the hadronic cascades. The multiplication will continue until the energy of each secondary drops below the pion production threshold. Those remaining nucleons and other high-energy hadrons belong to the hadronic component of the shower. Secondaries with smaller energies decay into muons and neutrinos which are the third component. Different components of the hadronic cascade are shown in Figure 2.10.

2.4.2.2 Electromagnetic Shower

When a high-energy photon enters the atmosphere it initiates an electromagnetic cascade. The photon creates an electron-positron pair (e^+e^+) within the Coulomb field of an atmospheric nucleus. The e^- and e^+ loses energy by emitting bremsstrahlung radiation. The photon from the bremsstrahlung radiation further produces e^+e^+pairs and the cascade continues. In a simple model, the alternating processes continue with the energy being equally distributed in each iteration (although in reality multiple photons may be produced by a single lepton). Hence, energy of the particles halves while the number of particle doubles as shown in Figure 2.11. As the shower advances the energy of particles reaches a critical value of $\approx$ 83 MeV where energy losses through ionization become the dominant process for electrons which rapidly cool and thermalize. The shower has a maximum number of particles at this point after which it rapidly decreases. As also the energy of the bremsstrahlung photons falls below the pair production threshold, no new leptons will be produced and the shower dies out. The cosmic ray flux entering the earth's atmosphere is about 4 orders of magnitude greater than gamma-ray flux. Rejection of the cosmic ray background is essential to extract a pure gamma-ray signal which is done by exploiting subtle differences seen in the extensive air showers the create. These differences are:

- Cosmic ray showers have large transverse momentum in the cascade particles. They create a broader light pool and have significant contributions from muons which reach the Earth's surface. The Cherenkov light density is nonuniform unlike gamma ray-induced air showers.
- In electromagnetic showers, all Cherenkov photons are emitted from a single shower. This results in a constant temporal profile where photons emitted later are closer to the ground arrive earlier than those emitted earlier during the shower. The hadronic showers have irregular time profiles where muons being deeply penetrating reach earlier than the Cherenkov photons from the main shower.
- Since hadrons penetrates the atmosphere further their showers are brighter due to less atmosphere that the shower traverses.

2.4.3 Imaging Atmospheric Cherenkov Technique

Space-based telescopes like *Fermi*-LAT although extremely successful in detecting gamma rays in the GeV energy range, struggle at higher energies because of their small effective areas. The lower flux of VHE gamma rays requires much larger effective areas. As explained in the previous section, the VHE gamma rays create light pools on the ground, if a detector is located within the lightpool, it could detect the Cherenkov flashes. The ground-based observatories would have a much larger effective area with the atmosphere itself acting like a calorimeter (*67*).

IACT telescopes employ large optical mirrors to reflect and focus light onto a camera. The current generation of IACT telescope cameras is highly pixelated where each pixel is a photomultiplier tube (PMT). For the next generation of telescopes, Geiger-mode avalanche photodiode (G-APDs) as photo sensors are being tested (*68*). PMTs efficiently detect single photons ($\sim$ 25%) with fast response times of a few nanoseconds. Due to the high gain of the vacuum electron multiplier and low noise, PMTs are sensitive single photoelectrons detectors which coupled with fast timings are capable of imaging the faint optical flashes against the night-sky background.

Cherenkov light from the elongated air shower is projected on the camera as an ellipse as shown in Figure 2.9. The distribution of light in the elliptical image of the shower holds key properties of the shower development, like a more energetic primary particle would

penetrate deeper in the atmosphere and generate of Cherenkov photons, thereby creating a brighter image. Since electromagnetic showers are much tighter and well-behaved compared to hadronic showers, the images of electromagnetic showers are regularly shaped elongated ellipses compared to hadronic showers which are broader. This property was studied extensively through simulations and a list of empirical parameters pertaining to the image (parameters are described in detail in Section 2.5.2.2) was calculated by Hillas and are named after him (*69*). The Hillas parameters are instrumental in identifying the signal (gamma ray-induced showers) from the background (hadronic showers, which are much more numerous). Detailed analysis of image and reconstruction of the event is described in Section 2.5.2 in the context of VERITAS.

Stereoscopic imaging by multiple telescopes further enhances effective background rejection. An air shower has to trigger simultaneously at least two telescopes to be registered as an event candidate, significantly reducing background from accidental triggers by NSB or rogue muons created in hadronic showers. Currently, opperational stereoscopic telescope arrays like VERITAS and H.E.S.S. also has superior angular and energy resolutions compared to mono telescopes like Whipple. The biggest disadvantage of an IACT is their low duty cycle (only $\sim$ 1000 h in a year for VERITAS) since they can only operate during clear good-weather nights with the moon illuminated $\leq$ 80%. They are limited in their field of view compared to space-based gamma-ray telescopes like *Fermi* and ground-based water Cherenkov telescopes like HAWC.

2.5 VERITAS: An Imaging Atmospheric Cherenkov Observatory

The Very Energetic Radiation Imaging Telescope Array System or VERITAS, successor of the Whipple 10 m telescope is an array of 4 IACTs of 12 m diameter located at the Fred Lawrence Whipple Observatory, Arizona, USA (31°40N, 110°57W, 1.3km a.s.l.). The current operational array is shown in Figure 2.12.

It uses the Imaging Atmospheric Cherenkov Technique discussed in the following section to detect gamma rays in the 85 GeV to $>$ 30 TeV energy range (*70*, *71*). It has been upgraded twice, first was relocating one of the telescope (T1) in 2009 to a more symmetrical position in the array to increase sensitivity by 30% (*72*, *72*). The second upgrade in 2012

was replacing the PMTs in the camera to a higher quantum efficiency ones (*73*, *74*) and an improvement of the trigger system (*75*). Currently VERITAS detects a source with 1% flux of the Crab Nebula in less than 25 h. With reduced high voltages in the PMTs, the array can now observe in bright moonlight ($\sim$ 80% moon illumination) increasing its duty cycle by 30% (*76*). The lifetime of the instrument is divided in 3 epochs, V4 (Sep 2007 - July 2009) initial array with all 4 telescopes, V5 (Sep 2009 - July 2012), after the relocation of telescope 1 (T1) and V6 (Sep 2012 - present) post-PMT and trigger upgrades. Details about the instrument and its data processing and analysis is presented Section 2.5.1 and Section 2.5.2, respectively.

2.5.1 VERITAS: Hardware

Each of the 4 identical telescopes in VERITAS has 3 major hardware units, the optical support structure with the mirrors and camera, the trigger system, and the data acquisition system. The following subsections describe in brief each of the 3 units with references for in-depth information.

2.5.1.1 Optics and Camera

The telescope has altitude-azimuth mount using a commercially made positioner on a steel custom-made optical support structure (OSS). The spherical OSS with a radius of curvature r on each telescope features 345 mirrors with a radius of curvature $2r$ according to the Davies-Cotton segmented mirror design. Each hexagonal mirror facet has a surface area of 0.322 m^2 with totals to a $140m^2$ for the composite reflector. The Davies-Cotton reflectors are relatively inexpensive and easy to align compared to parabolic mirrors and have superior on-axis and off-axis aberrations. The only disadvantage to this design is that the asynchronous nature of the mirrors broadens the arrival window of Cherenkov light to $\sim$ 4 ns in the case of the VERITAS reflectors (*77*). The 12-m diameter composite reflector focusses light onto a camera supported by quad arm structure which uses a mechanical bypass to direct the camera load onto a set of counterweights at the back of the OSS. The segmented reflector, quad arms and the camera box can be seen in Figure 2.13

The camera is pixelated with 499 photo-multiplier tubes (PMTs) each of 28.6 mm diameter. The PMTs are UV sensitive and have fast rise times coupled with high quantum efficiency. The camera has a 3.5° field of view (FoV). The PMTs are housed inside light

concentrators (modified Winston Cones (*78*)) to maximize collecting area and reducing dead space between adjacent pixels. The Winston Cones restrict stray off-axis light from hitting the PMTs and limit to those photons reflected off the mirrors. A multichannel power supply controls the power to individual PMTs. The postupgrade Hamamatsu PMTs (model R10560-100-20 MOD) have a higher quantum efficiency of 37% at 330 nm compared to the preupgrade Photonics PMTs (model XP2970/02) with 20% quantum efficiency at 320 nm. The pulse width is also reduced from 6.8 ns from preupgrade to 4.2 ns in postupgrade. The upgraded PMTs gains are approximately 1.5 times the gain of the original PMTs, both operational with a nominal gain of 2×10^5 (*79*). A high-bandwidth preamp at the base of each PMT further provides an additional gain of 6.6 and monitors the DC output for anode current to protect the PMTs from sudden light flashes (from car headlights, airplane, lightning, bright stars, and the moon)

2.5.1.2 Trigger System

The VERITAS trigger system identifies gamma-ray signals from background fluctuations. The trigger has three hierarchical conditions which have to be satisfied for an event to be classified and recorded as a gamma ray in the data acquisition system. A simple flowchart of the trigger logic is shown in Figure 2.14.

The three stages of the trigger are as follows:

- L1: The Level 1 trigger or L1 is a pixel-wise trigger which fires when the signal in a single PMT crosses a certain threshold. The out from L1 is sent to Level 2 trigger.
- L2: The Level 2 trigger or L2 fires when adjoining pixels receive a signal within a designated narrow time window. The L2 trigger passes on its output signal to Level 3 trigger.
- L3: The Level 3 trigger or L3 is an array-wise trigger. When L2 signals from 2 or more telescopes are received within a required time window, it fires the L3 trigger. The VERITAS readout and data acquisition system (DAQ) finally processes and records the event information from each telescope and writes it in the database.

For a detailed description of the triggering system, associated electronics, and the upgraded triggering system see (*75*, *80*)

2.5.1.3 Data Acquisition

The VERITAS data acquisition system (DAQ) uses 500 megasample/sec flash analog-to-digital converters (FADCs) (*81*). Analog signals from the PMTs are continuously digitized at 2ns/sample rate by the FADCs which is then stored in a ring buffer for 32 μs waiting for the L3 trigger. On receiving the L3 trigger the standard operation of DAQ reads out a section of the buffer for each PMT signal. Following this, a telescope level event builder assimilates all event information and sends it to an array-level data harvester. The job of the harvester is then to combine events information like event numbers, GPS timing, etc. from all the telescope and saves it in a custom VERITAS data format (VBF) in the database. Additional information from weather monitors, high voltage values, trigger settings, source pointing detail, etc. is also written to the database along with the target, observation mode, and manual reports from observers. The database is accessed by Data Quality Monitoring (DQM) and offline analysis software to reconstruct the events.

2.5.2 VERITAS: Data Analysis

VERITAS has a simplified realtime analysis that is handy in detecting 'flaring' sources. The *Quicklook* analysis package (*82*) looks at individual runs as well as combines runs from the same night for a source to give an estimate of its flux. Using predetermined flowcharts for individual sources *Quicklook* helps observers on site decide Targets of Opportunity observations for transients.

The detected signal is the starting point in the analysis from which the original gamma ray is back calculated using simulations. From the moment the gamma ray strikes the top of the atmosphere up to it being recorded as traces, many processes affect them. There is a multitude of variables affecting the initial interaction height of the gamma ray, the volume of the atmosphere, reflectivity of the mirrors, quantum efficiency of the cameras, the NSB, loss in electronics, etc. Many of these variables cannot be measured directly and details about the original gamma ray cannot be obtained by simply solving an equation with these variables. The EAS are compared with simulations to identify gamma ray-induced showers from a hadron induced background, reconstruction of air shower direction, energy of the incident gamma ray and significance of source.

There are two offline analysis packages *EventDisplay* (ED) and *VEGAS* (VEritas Gamma-

ray Analysis Suite) which are capable of more detailed analysis. The flowchart for the *EventDisplay* package is shown in Figure 2.15. Both analysis packages are similar but use independent techniques. Any results which are published are verified by both analysis packages. This work is entirely done using ED.

2.5.2.1 Calibration and Image Cleaning

The charge from each PMT is digitized by the FADC as traces which along with all trigger and time stamp information are stored in the database. The traces are characteristic of the digital counts (d.c.) associated with the amplitude of the Cherenkov light pulse. the d.c. is also related to the number of photoelectrons (pe). The response of PMTs are complex, dependent on the wavelength and each one is different. They also have different gains and varying length of cables which affects the arrival time of the pulses at the FADCs. The idiosyncrasies of the PMTs require them to be calibrated. Laser pulses are fired at the camera with a 337nm nitrogen laser through an opal diffuser for 2 min every night (called a flasher run) illuminating the PMTs at the same time with similar intensity. The laser is pulsed at about 10Hz and the intensity over the entire camera varies within a 10-15% range. The flasher runs accounts for the changes in the PMTs gains over the period of operation.

The fluctuations from night sky background (NSB) affects individual PMT rates. The NSB changes rapidly with pointing position. It is continuously monitored by recording at regular intervals the fluctuation in all PMTs. PMT outputs are negative voltages which are then AC coupled and adjusted to a baseline voltage. The baseline voltage is selected such to log small positive fluctuations but also has an adequate range to account for large negative pulses. In the absence of a Cherenkov light signal, the output from the PMTs is called the *pedestal*. The charge in each pedestal event is determined for individual pixels or PMTs by summing the waveform data over a set period and plotting on a histogram. The mean pedestal value is calculated from the histogram and the RMS value about the mean is called *pedvar*. This process is repeated over several time slices during a single 'data run'. The pedestals are subtracted from a real event and pedvar accounts for the noise in the system. The integrated charges are then corrected for relative differences in PMT gains using the flasher calibration for the particular night. Figure 2.16 shows the stages

of calibration and image cleaning from left to right. The image on the left shows a raw image of the charges in the camera pixel and the one in the center is after subtraction of the pedestal.

Following the above calibration, there might still be pixels with substantially integrated charge residue due to single electrons or the NSB. These are isolated colored pixels seen in the center image on Figure 2.16. Pixels with integrated charge more than 5 times its pedestal RMS is called a 'picture pixel' and those with more than 2.5 times adjacent to the picture pixels are called 'boundary pixels'. Pixels which can neither qualify as picture pixels or boundary pixel are considered as noise and are further removed from the image. The image of the right in Figure 2.16 is that of a final cleaned image of the shower.

2.5.2.2 Image Parameterization

As explained in Section 2.4.2 gamma ray-induced air showers are much more compact and regularly shaped compared to cosmic ray induced air showers. The image on the camera also translates this property, gamma-ray shower appears elliptical whereas cosmic ray showers are broad and irregularly shaped. Specific parameters suggested by A. M. Hillas is used to demarcating gamma-ray showers from cosmic ray showers (*69*). These parameters now called *Hillas parameters* were formulated using Monte Carlo simulations of air-shower development and atmospheric Cherenkov production in 1985 and were used by the Whipple 10m telescope to detect the first gamma rays from the Crab Nebula in 1989(*83*). Hillas parameters of the image are calculated which is fundamental in reconstructing the arrival direction and energy of the incident gamma rays. A diagram depicting the Hillas parameters are shown in Figure 2.17 followed by the definition of the parameters and the property of the shower that each one measures.

2.5.2.3 Event Reconstruction

The gamma-ray event can now be reconstructed from the image based on the calculated Hillas parameters from the previous step. There are three fundamental properties of the incident gamma ray that is calculated during event reconstruction. These are:

- The direction of arrival of the gamma ray. Since gamma-ray photons do not interact with magnetic fields, the direction of arrival would trace it back straight to its source in the sky.

- The location of the air shower core which would extrapolate to the point on the ground where the gamma ray would have hit in the absence of atmospheric absorption.

- The energy of the incident gamma ray.

1. Arrival Direction Reconstruction: The elliptical image of the air shower from each telescope is now overlaid on a single camera plane and the intersection of their major axes gives the arrival direction of the incident photon similar to shown in Figure 2.18. In reality, however, each pair of telescope images have their own intersection point. For N images there are $N.(N-1)/2$ intersection points.The intersection point is a weighted average where weight W_{ij} for a telescope pair i and j is given by

$$W_{ij} = \left(\frac{1}{s_i} + \frac{1}{s_j}\right)^{-1} \times \left(\frac{w_i}{l_i} + \frac{w_j}{l_j}\right)^{-1} \times \sin\theta_{ij} \tag{2.3}$$

   The weight is dependent on the size of the image s_i, the ratio of width to the length of the image w_i/l_i and the sine of the angle between the two axes. Greater weight is assigned to assigned to higher quality images that are brighter and more elongated. Once the position in the camera coordinates for the source is determined it is converted into astronomical coordinates (equatorial coordinates J2000 right ascension RA and declination DEC).

2. Arrival Shower Core Reconstruction: Determination of the shower core location (i.e., the point on the ground where the gamma ray would have stricken had it not interacted with the atmosphere) is essential in determining the relative position of the shower with respect to the telescopes. This reconstruction is similar to the arrival direction reconstruction where instead of the analysis in camera coordinates it is done in spatial coordinates. The reconstructed shower core is used to calculate the *impact parameter 'r'*, the distance between a particular telescope and the shower core in a plane perpendicular to the shower arrival direction (distance between point Ti and P in Figure 2.19). The impact parameter is needed to calculate the height of the shower maximum which is the point where maximum particles are produced or

the brightest part of the shower. The height of shower maximum can be calculated using the equation

$$H_i = \frac{r_i}{\tan\theta_i} \tag{2.4}$$

where r_i is the impact parameter and θ_i is the angle between the image centroid and reconstructed arrival direction of the gamma-ray photon each calculated for the i^{th} telescope. Lines joining each telescope and the shower core intersects each other and similar to direction reconstruction the shower core is also reconstructed by weighted intersection points from pairs of telescopesas shown in Figure 2.20. The height of shower maximum is a differentiating parameter between gamma rays and background cosmic ray showers or muons of similar energies since the latter two reach deeper in the atmosphere and have a lower height for their shower maximum.

3. Arrival Energy Reconstruction: The energy of the incident gamma-ray photon is proportional to the amount of Cherenkov photons emitted in the air shower which, in turn, is related to the total charge contained in the shower image (*size*). But the amount of Cherenkov light seen by the camera depends on many factors like the distance of the air shower core, the direction of the air shower core (zenith angle, azimuthal angle, wobble offset), the NSB level, etc. Since there is no easy way to measure the instrumental response directly (like using a test beam), Monte Carlo simulations are employed covering a large parameter space. Millions of incident gamma rays are simulated from a variety of zenith angles and a scattered in a random isotropic manner over and area ($\sim$ 750 m radii) around the telescopes. The events are in the 50 GeV to 250 TeV energy range and follow a power law spectrum with an index of -2. The Cherenkov light from the simulated air showers is used as an input to a model of the detector and the resultant. Histograms are constructed for median shower energies E required to produce an image of a given size at a given core impact distance which is called look-up tables. One histogram is produced for each combination of noise level, telescope number, offset between source and the pointing direction, zenith angle, and azimuthal angle, resulting in the production of a 7-dimensional lookup table for the reconstructed energy. For actual observational data, these parameters are used as 'address' to find the correct corresponding energy

of incident gamma ray. The reconstructed energy is weighted as follows:

$$E = \frac{\sum_{i=1}^{N_{Tel}} E_i/\sigma_{E_i}^2}{\sum_{i=1}^{N_{Tel}} 1/\sigma_{E_i}^2} \tag{2.5}$$

where E_i is the estimate of energy for telescope i and σ_i is the standard deviation of the energy obtain from the look-up table. Examples of look-up table are shown in Figure 2.21 and Figure 2.22.

2.5.2.4 γ-Hadron Seperation

The next point in the analysis after all pertinent information about the air shower has been obtained is to determine which of them have been created by gamma rays and which by cosmic rays. An effective procedure to identify gamma ray-induced showers versus cosmic ray induced showers was using the *width*, the *length* and other discriminating parameters of the shower image. This was the older method called 'box cut' analysis where cuts on individual parameters were made to retain the gamma-ray signal.

Cosmic ray-induced showers are wider, longer, and irregular compared to gamma ray-induced ones. The two parameters *mean scale length* (MSL) and *mean scale width* (MSW) of the observed shower image is compared to that of their simulated value. Using the same Monte Carlo simulation that generated energy look-up tables, MSCW and MSCL are now used to calculate expected values. For an event observed by N_{Tel} number of telescopes with *sizes* s_i, zenith angles z_i, impact parameters r_i and noise level n_i (i is the index of telescope), the two parameters are calculated as:

$$MSL = \frac{1}{N_{Tel}} \sum_{i=1}^{N_{Tel}} \frac{L_i}{L_{sim}(s_i, z_i, r_i, n_i)} \tag{2.6}$$

$$MSW = \frac{1}{N_{Tel}} \sum_{i=1}^{N_{Tel}} \frac{W_i}{W_{sim}(s_i, z_i, r_i, n_i)} \tag{2.7}$$

With multiple telescopes these parameters can be averaged as *reduced mean scale length* and *reduced mean scale width* calculated as:

$$MSCL = \frac{1}{N_{Tel}} \sum_{i=1}^{N_{Tel}} \frac{L_i - \hat{l}(s_i, r_i)}{\sigma_{l,MC}(s_i, r_i)} \tag{2.8}$$

$$MSCL = \frac{1}{N_{Tel}} \sum_{i=1}^{N_{Tel}} \frac{W_i - \hat{w}(s_i, r_i)}{\sigma_{w,MC}(s_i, r_i)} \tag{2.9}$$

where L_{sim} and W_{sim} are the expected values of length and width found by interpolation in the appropriate look-up table, derived from simulated data. $\hat{l}$ and $\hat{w}$ are median val-

ues of length and width respectively from the simulations and $\sigma_{l,MC}$ and $\sigma_{w,MC}$ are their standard deviations. The observed gamma-ray events parameters are distributed around 1.0 whereas for cosmic-ray events, the parameters are more broadly distributed around larger values. The distributions are seen in Figure 2.23. Another parameter used in the gamma-hadron separation is the θ^2. The angle between the reconstructed event and the direction of a candidate source is called the θ parameter. A predetermined value of θ^2 is used to define the source region and for an event, if θ^s is less that the predetermined value it is counted as a signal event. Placing cut-off values for these three parameters MSCL, MSCW and θ^2 it is possible to reject 99% of cosmic-ray events and retaining 85% of gamma-ray events (*84*).

Recently an advanced analysis method was developed by the Boosted Decision Tree (BDT) machine learning technique improving the sensitivity of the analysis. Discrimination of gamma rays from the background is achieved by a multivariate analysis. Several variables are combined into a single variable which indicates the degree to which an event is gamma-ray-like or cosmic-ray-like. For a detailed description of the method and the improvement in sensitivities compared to standard analysis of VERITAS data see (*85*).

2.5.2.5 Background Estimation and Significance Calculation

Even with best gamma-hadron separation methods that reject of the majority of cosmic ray some background still remain. They may be positron or electron-induced showers or hadronic shower which look similar to gamma-ray ones. A purer gamma-ray signal can be obtained by further subtracting the background. A region of interest around the gamma-ray candidate source (ON) is defined along with a signal free background region (OFF). The size of the ON region is defined by the parameter θ^2 which for point-like sources is $\leq 0.008 deg^2$ and for extended source could be up to $0.02 deg^2$. A simple way to select an OFF region that was used by the Whipple 10m telescope was to point at a blank patch of sky with no expected gamma-ray signal at about similar azimuth and elevation as the ON observation on the source. But this method resulted in only 50% of the observational time to actually observe the source. This was solved using the *wobble* observation mode where the source was placed at a slight offset from the camera center and the background is sampled from same offsets in the camera from other directions. The observation is

averaged out by placing the source in 4 different offset positions, north, south, east, and west. There were two methods used in the wobble observations modes for background estimation which are the *Ring Background* method and the *Reflected Region* method. In the *Ring Background*, method the OFF region is defined as a ring around the ON region with the definition of radius and width from the user. In the *Reflected Region* method OFF regions, the same size as the ON region are placed in a ring arrangement around the pointing position with the ON region as a part of the ring. Both the methods of selecting OFF regions for a particular ON regions with the source are shown in Figure 2.24

The number of excess events is obtained by using the number of events in the OFF region (N_{OFF}) and in the ON region (N_{ON}) as follows

$$N_{excess} = N_{ON} - \alpha N_{OFF} \tag{2.10}$$

where α is a normalization parameter. For *Ring Background* method α is the ratio of the solid angle subtended by the ON region to that of the OFF region. For *Reflected Region* method α is the ratio of the time spent of On region to OFF region. The uncertainty of N_{excess} is given by

$$\Delta N_{excess} = \sqrt{\Delta N_{ON}^2 + \alpha^2 \Delta N_{OFF}^2} \tag{2.11}$$

where ΔN_{ON} and ΔN_{OFF} are errors on the number of events in ON and OFF region respectively. Considering Poissonion distribution for the counts the error on excess counts can be rewritten as:

$$\Delta N_{excess} = \sqrt{\Delta N_{ON} + \alpha^2 \Delta N_{OFF}} \tag{2.12}$$

The significance σ on the counts is hence given by

$$\sigma = \frac{N_{excess}}{=} \frac{\Delta N_{excess}}{\sqrt{N_{ON} + \alpha^2 N_{OFF}}} \tag{2.13}$$

The above method was demonstrated by Li and Ma insufficient due to uncertainity in the number of background counts (*86*). They proposed a more robust method following log-likelihood test of the null hypothesis, that all counts come from the background distribution. This equation takes the form

$$\sigma = \sqrt{2}\Big\{ N_{ON} \ln\Big[\frac{1+\alpha}{\alpha}\Big(\frac{N_{ON}}{N_{ON}+N_{OFF}}\Big)\Big] + N_{OFF} \ln\Big[(1+\alpha)\Big(\frac{N_{OFF}}{N_{ON}+N_{OFF}}\Big)\Big]\Big\}^{\frac{1}{2}} \tag{2.14}$$

Typically a source is 'detected' when the N_{excess} is large enough to lead to a Significance $\geq 5\sigma$.

2.5.2.6 Spectral Reconstruction and Flux Calculation

When a source is significantly detected from its excess counts a spectral distribution can be reconstructed. A spectral distribution examines how the measured energy is distributed throughout the excess counts. This is vital in understanding the spectral energy distribution of the gamma-ray source. Before spectral reconstruction the *effective area* of the detector has to be determined. *Effective area* defines the efficiency of the telescope in detecting and measuring gamma rays. It is a complicated function of zenith angle, *pedvar*, cuts of *size*, MSL and MSW, etc. The *effective area* is also determined from Monte Carlo simulations of showers scattered over a radius of 750 m on the ground within energy range 50 GeV to 250 TeV with a spectral index of -2. Only 2-3% of the showers trigger the simulated detector out of millions and only 0.5-2% passes the quality cuts. The *effective area* is obtained as:

$$A_{eff}(E) = \frac{S(E)}{N(E)} A_{thrown} \tag{2.15}$$

where $N(E)$ $S(E)$ are the number of events thrown and the number of events which pass the cuts respectively and A_{thrown} is the area on the ground over which the simulated events were thrown.

Using the *effective area* the differential energy spectrum can be determined. The differentialenergy spectrum is the number of detected excess events detected per unit area per unit times per energy interval given by

$$\frac{dF(E)}{dE} = \frac{N_{excess}(E)}{A_{eff}(E) T_{obs} dE} \tag{2.16}$$

where T_{obs} is the dead-time corrected observation time of the data sample and dE is the width of the distribution binning. The excess in each observation is weighted by the time and area over which the excess was accumulated, given by

$$\frac{dF(E)}{dE} = \frac{\sum_{i=0}^{n} N^{i}_{excess}(E)}{\sum_{i=0}^{n} A^{i}_{eff}(E) T^{i}_{obs} dE} \tag{2.17}$$

where i is the index and n is the number of observation runs.

Due to the interdependence of the *effective area* and the differential energy spectrum, the bias in the energy reconstruction will change the shape of the effective area (an index of -2 was assumed for simulated events), depending on the shape of the simulated spectrum.

Table 2.1: Hillas parameters used for identifying gamma-ray showers, highlighted parameters are the original 6 from (*69*).

Size	Sum of all digital counts in the image, measures brightness of the shower
Frac2	Fraction of the total image contained between two brightest pixels, measures concentration of the image brightness
Length	Approximate length of image along the major axis
Width	Approximate length of image along the minor axis, measure shape of the image along with length
Azimuth	The RMS spread of light along a line perpendicular to the line connecting the image centroid to the center of FoV, measures shape and orientation of image
Miss	Perpendicular distance between the major axis of the image and the center of FoV, measures orientation of the image
Distance	Distance between centroid of image and center of FoV
Alpha	Angle beween major axis and a line joining centroid of image to center of FoV, measures the orientation of the image
Length/Size	Measure of the compactness of the image in comparison to its total light content, helps eliminate local muon background
Loss	Fraction of the image contained within the camera
NTubes	Number of pixels that forming the image, an estimation of the quality of the image

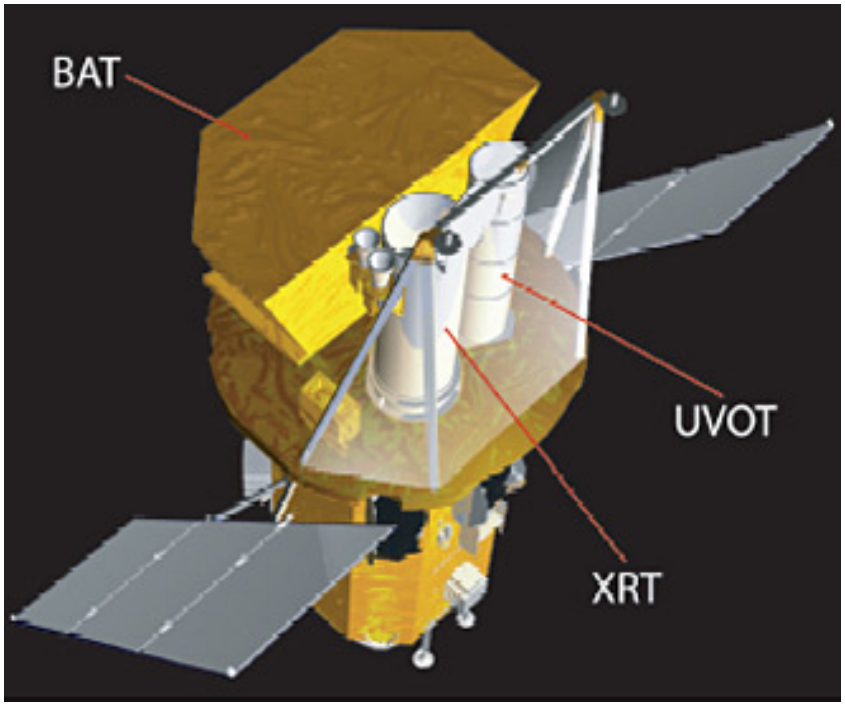

Figure 2.1: The Swift Gamma-Ray Burst Mission Telescope. Photo courtesy of NASA.

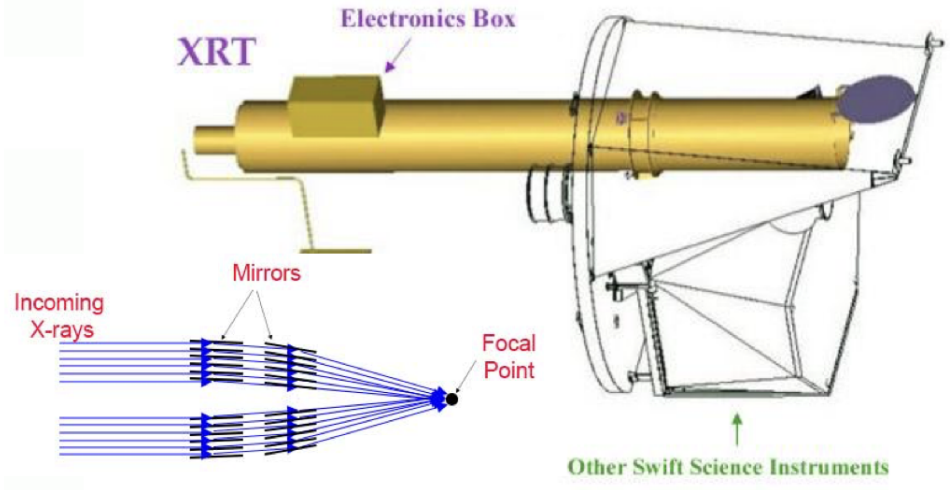

Figure 2.2: X-ray telescope schematic diagram with an inset diagram of grazing incidence used for focussing X-rays. Photo courtesy of NASA.

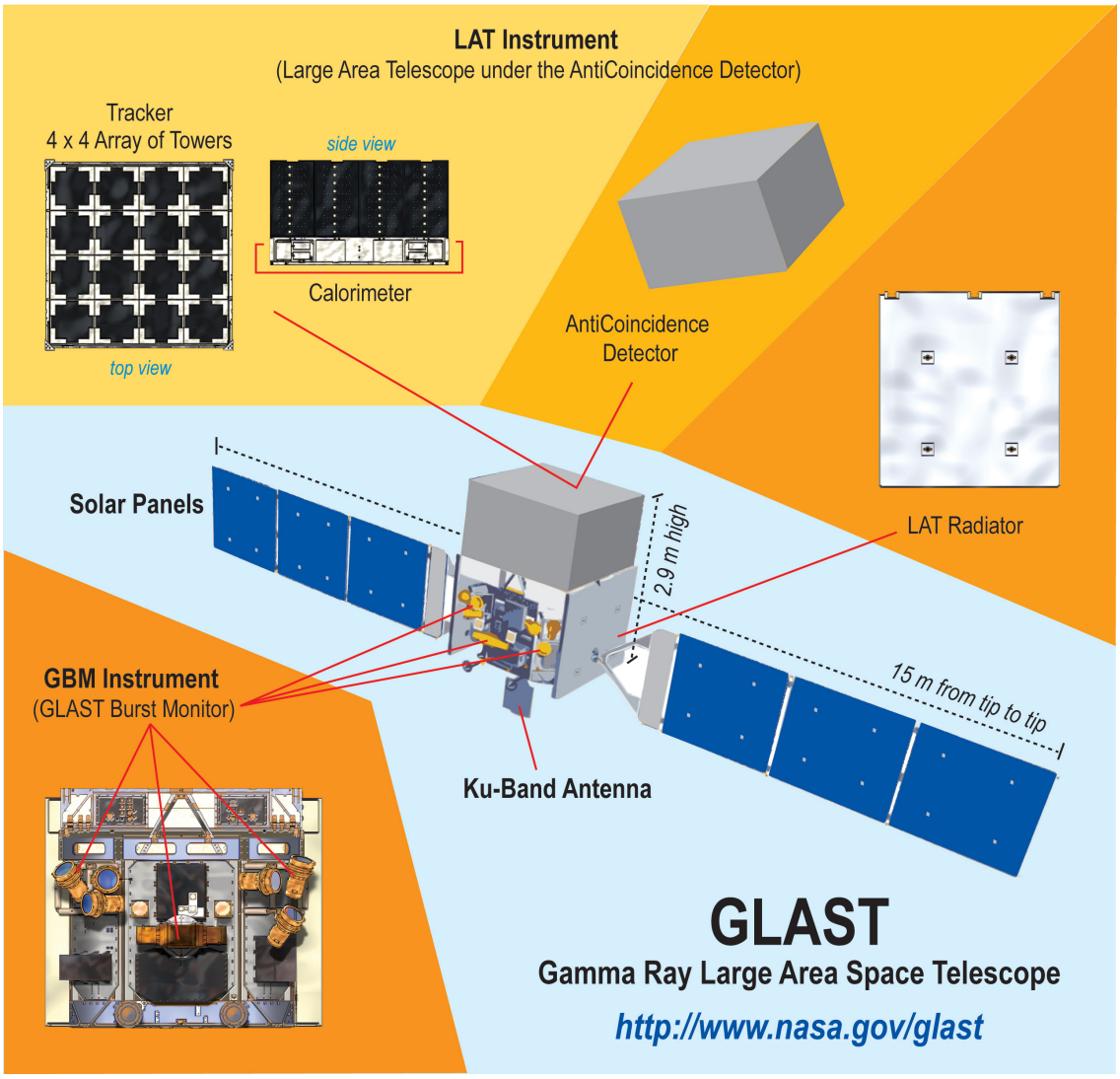

Figure 2.3: The Fermi Gamma-Ray Space Telescope.

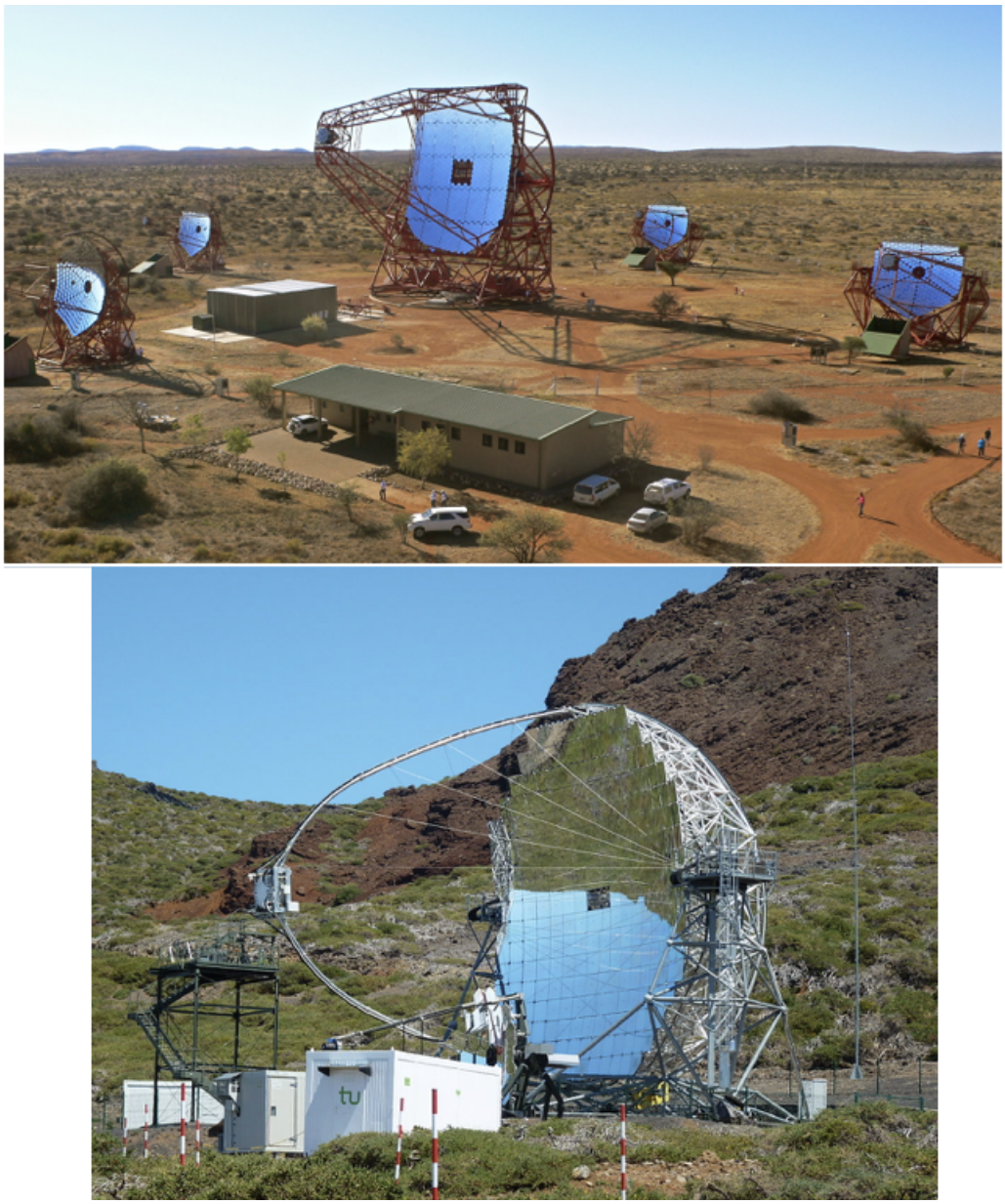

Figure 2.4: *Top:* High-Energy Stereoscopic System II telescope (H.E.S.S. II) located in Namibia, near the Gamsberg mountain. *Bottom:* Major Atmospheric Gamma Imaging Cherenkov telescope (MAGIC) located in the Canary Island of La Palma, Spain.

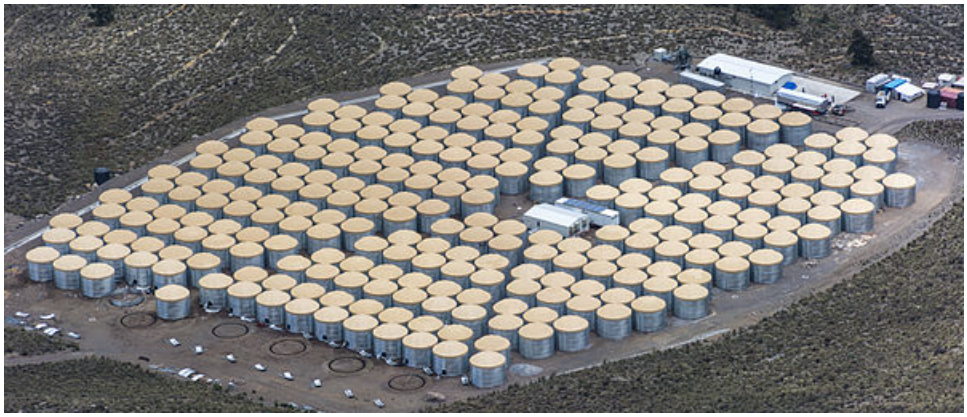

Figure 2.5: High Altitude Water Cherenkov Observatory (HAWC), located on the flanks of the Sierra Negra volcano near Puebla, Mexico.

This is solved by iterating the above equation and correcting the weight on the effective area with each iteration using the measured energy spectrum(*87*).

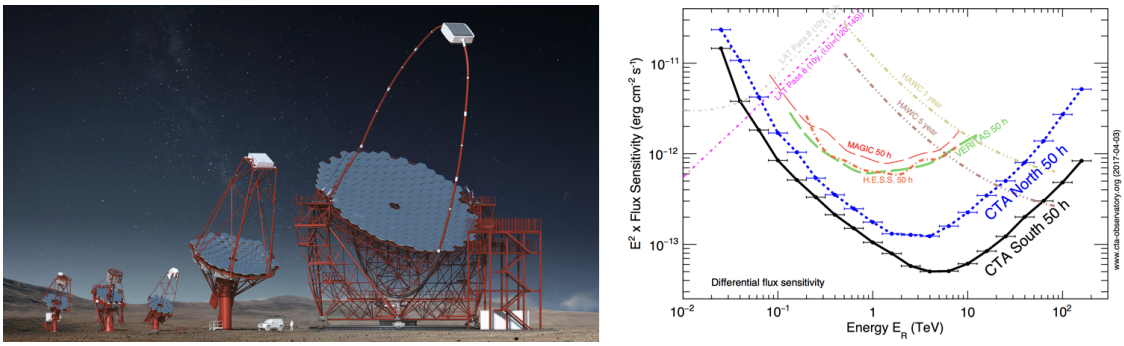

Figure 2.6: *Left:* Artist impression of the three classes of telescopes in Cherenkov Telescope Array (CTA). From right to left in the picture, the Large-Size Telescopes (LST) with 23m diameter for lower energy range, the Medium Size Telescope (MST) of 12m diameter for medium energy range and three different Small Size Telescopes (SST) which are being tested with 1-2m diameters for the highest energy range. Credit: G. Pérez, IAC, SMM *Right:* A comparison of the performance of CTA with the currently operational gamma-ray instruments in the same energy range, image courtesy CTA Consortium.

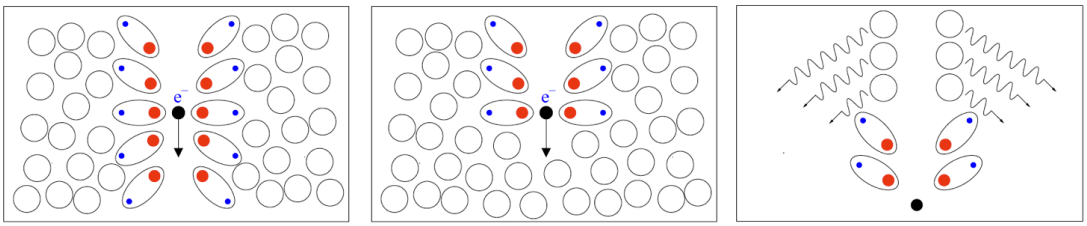

(a) $v < c/n$ (b) $v > c/n$ (c) $v > c/n$

Figure 2.7: Production of Cherenkov radiation. (a) When a charged particle travels slower than light in the dielectric medium the radiation during relaxation is random and cancels out. (b) When charged particles travel faster than speed of light in the medium there is directional polarization (c) When particles relax from directional polarization they emit *Cherenkov radiation* (*46*).

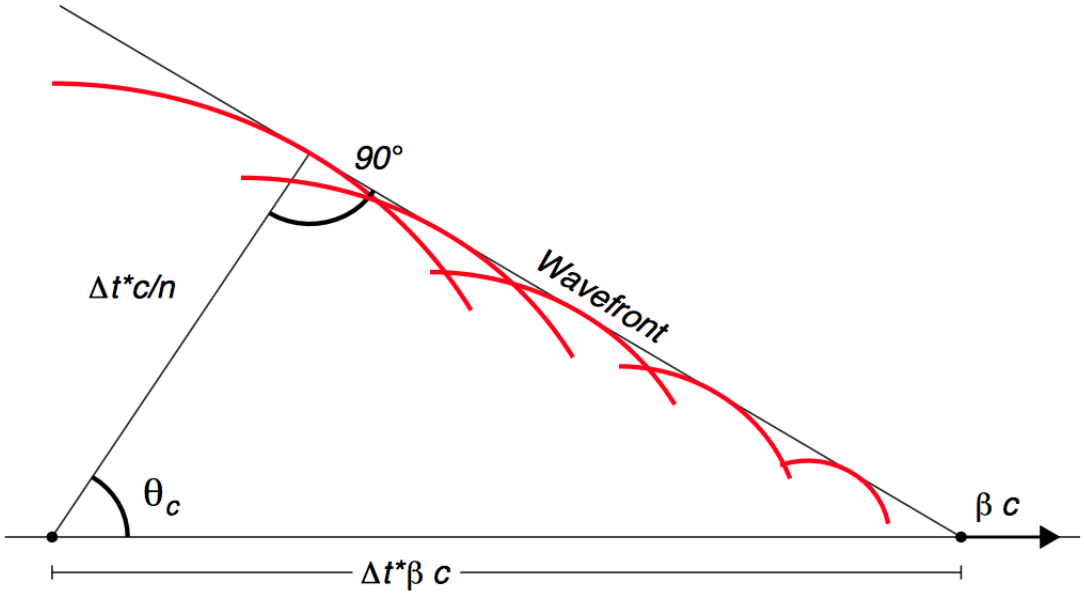

Figure 2.8: Schematic of the Cherenkov radiation emitted along the path of a fast moving particle.

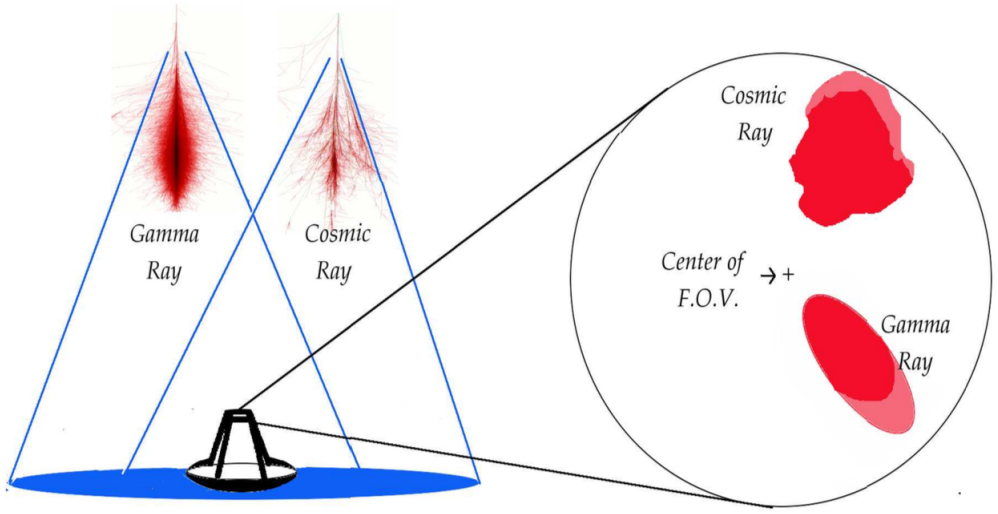

Figure 2.9: Diagrammatic representation of image created on the telescope camera by a gamma ray-induced shower and cosmic ray induced shower. The gamma-ray shower being more temporally and spatially coherent produce compact ellipsoidal images compared to cosmic ray shower which are randomly irregular in shape. Image credit A. W. Smith (*88*).

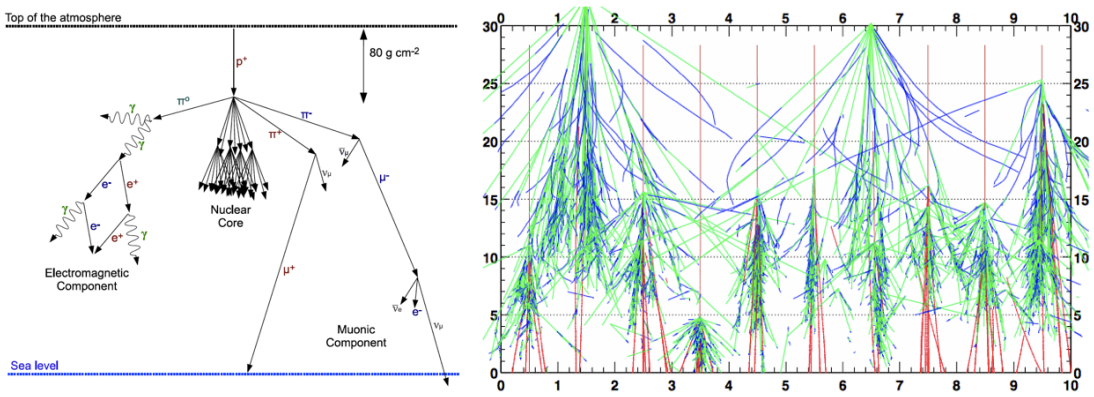

Figure 2.10: Particle cascades created by an incident cosmic ray is shown on *left* with simulation of 10 showers produced by 300 GeV protons on *right*. Simulation image from (*89*), cascade image from (*46*).

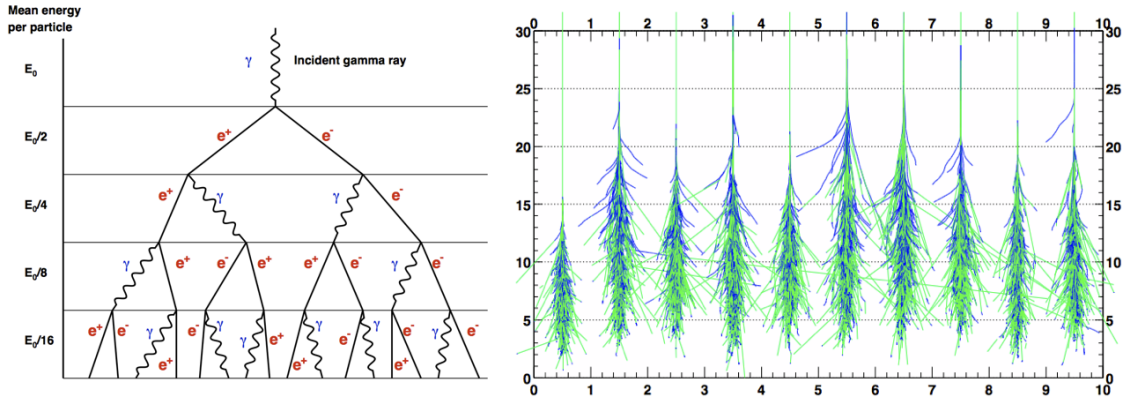

Figure 2.11: Particle cascades created by an incident gamma ray is shown on *left* with simulation of 10 showers produced by 300 GeV gamma ray on *right*. Simulation image from (*89*), cascade image from (*46*).

Figure 2.12: The Very Energetic Radiation Imaging Telescope Array System Observatory located at the Fred Lawrence Whipple Observatory at the base of Mt. Hopkins, southern Arizona, USA.

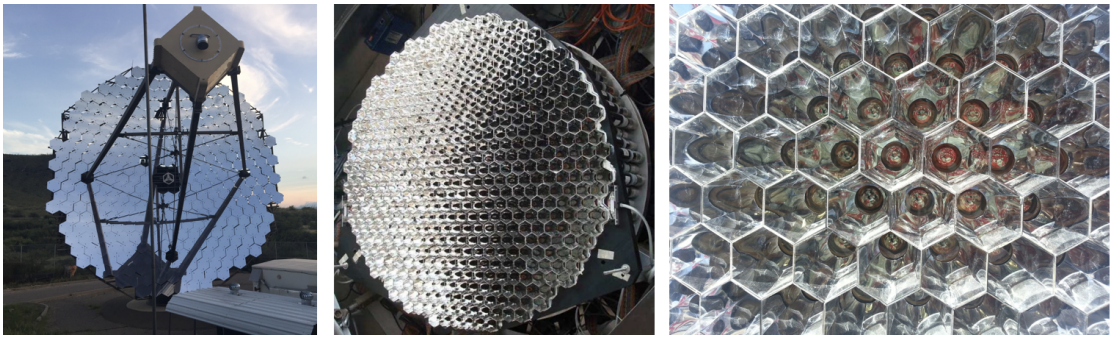

Figure 2.13: *Left:* Davies-Cotton tessellated mirror of the VERITAS telescope (T2) with camera box supported on the quad arms. *Center:* 499 pixel PMT camera of VERITAS *Right:* PMTs housed inside the lightcones.

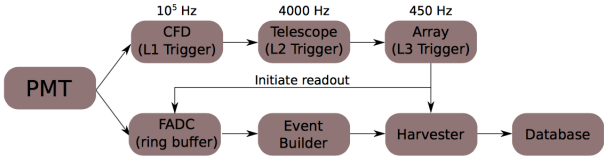

Figure 2.14: A simplified flowchart of the VERITAS trigger system by R. Bird.

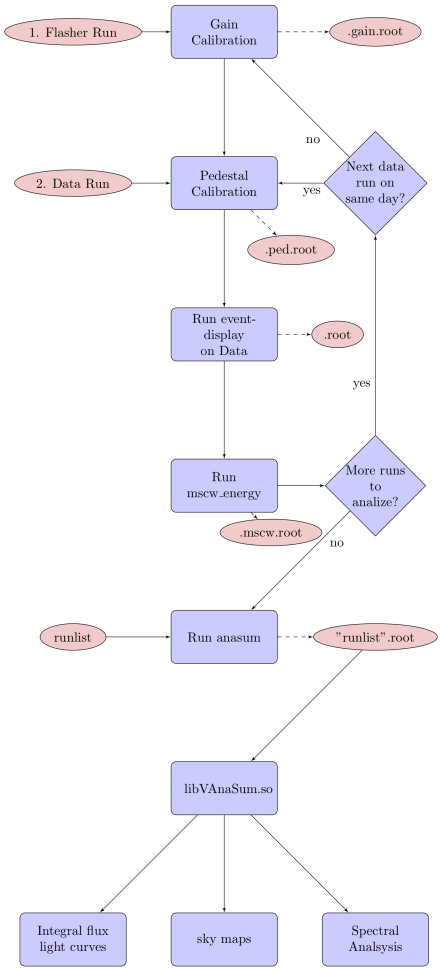

Figure 2.15: VERITAS data analysis flowchart for *EventDisplay* package.

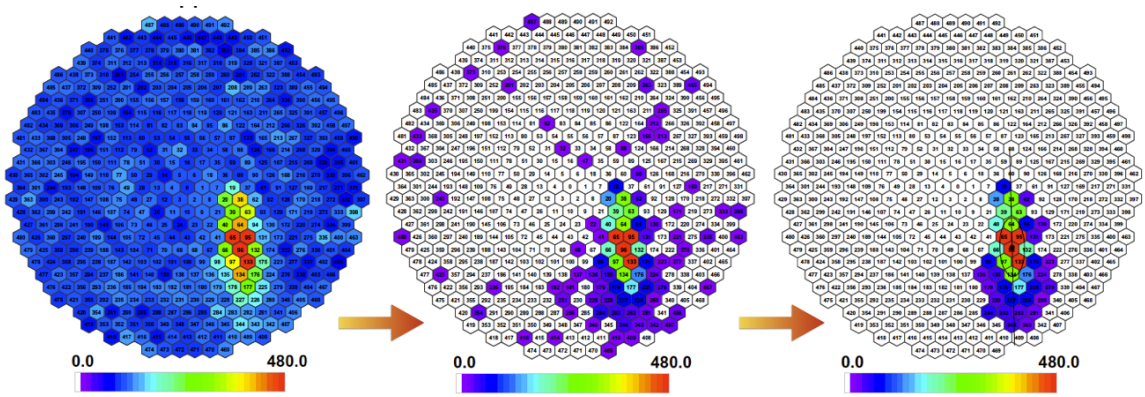

Figure 2.16: The stages of calibration and image cleaning. *Left:* Raw image *Center:* Raw image after pedestal subtraction *Right:* Cleaned image (*46*).

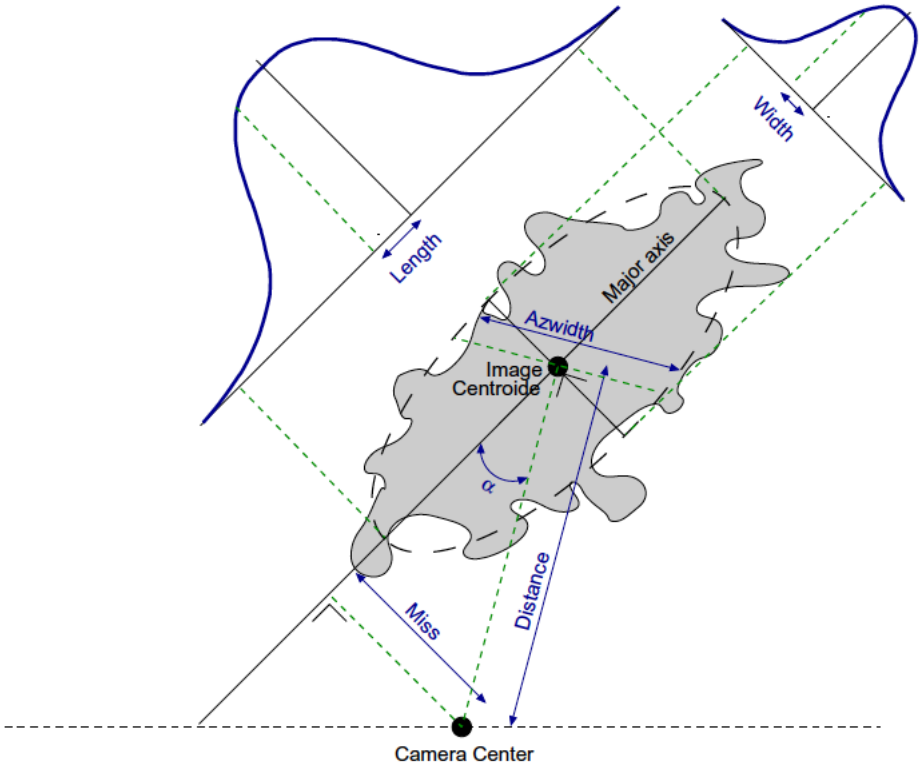

Figure 2.17: Hillas parameters. Image from (*46*).

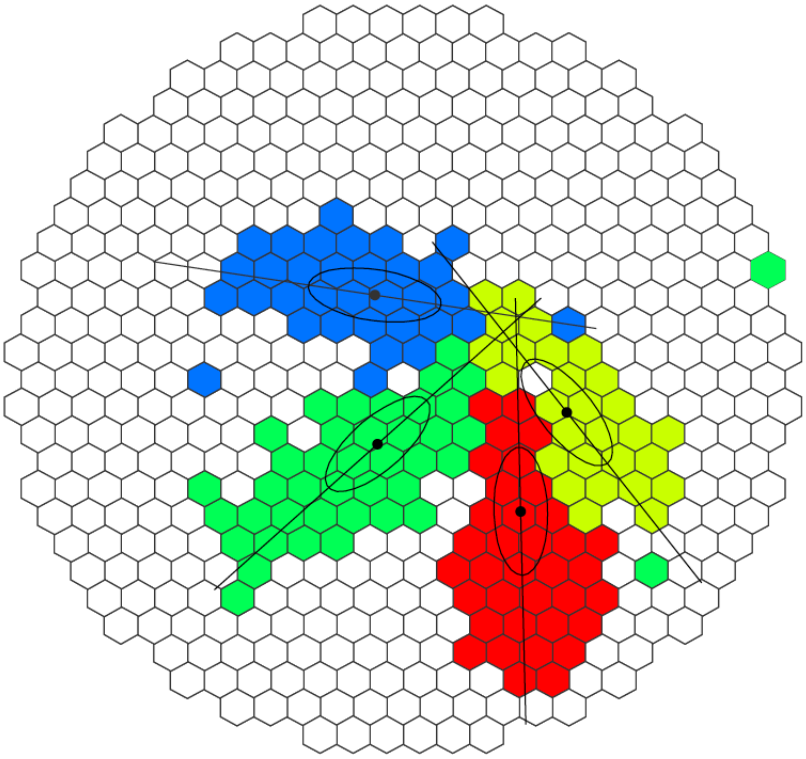

Figure 2.18: Direction reconstruction by VERITAS array from images in the camera. Image from (*46*)

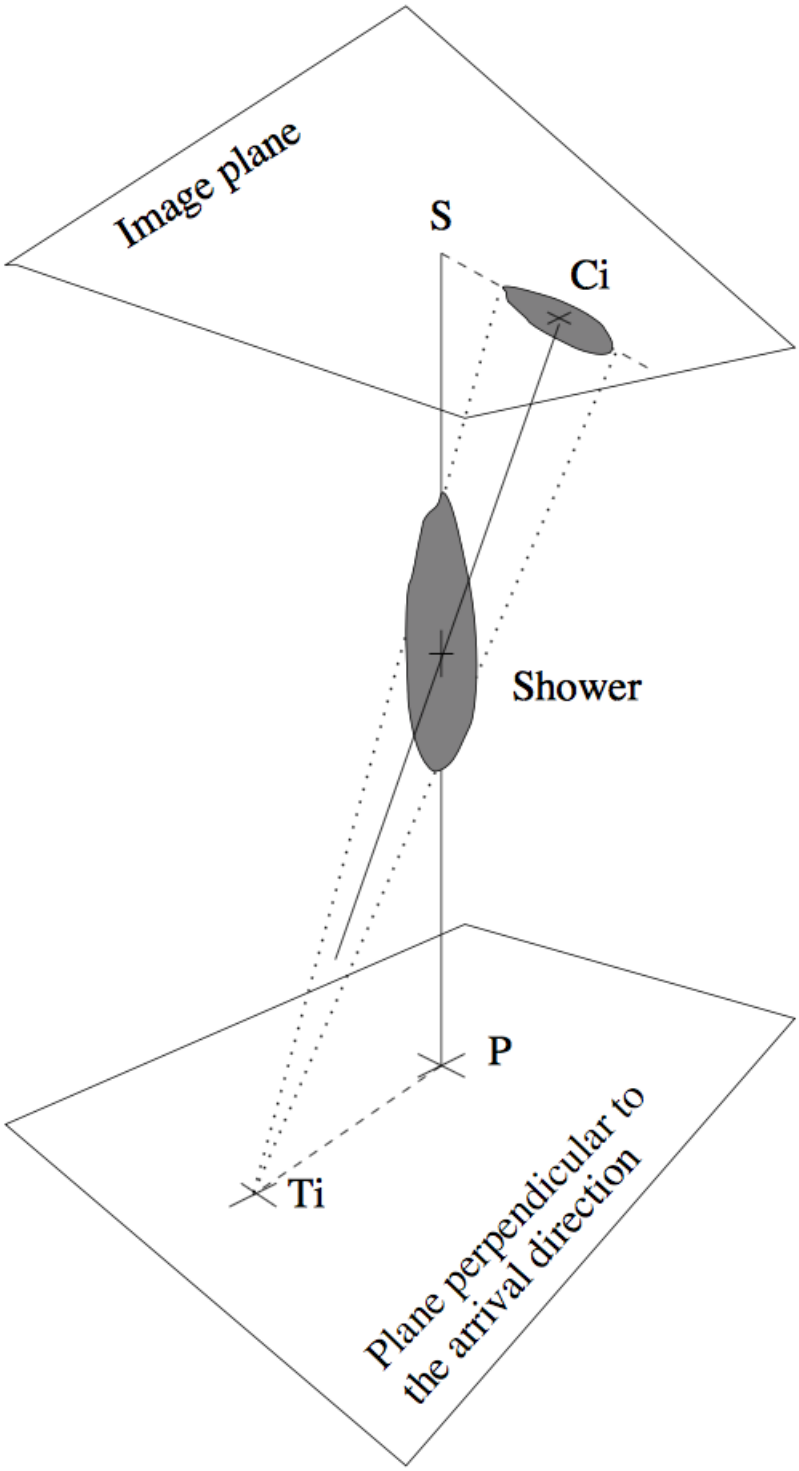

Figure 2.19: Schematic diagram of the projection of a air shower on image plane of telescopes. The labels are as follows, S → Source location, P → Shower core location on ground, Ci → Centroid of image, Ti → Location of i^{th} telescope. Figure reproduced from (*90*).

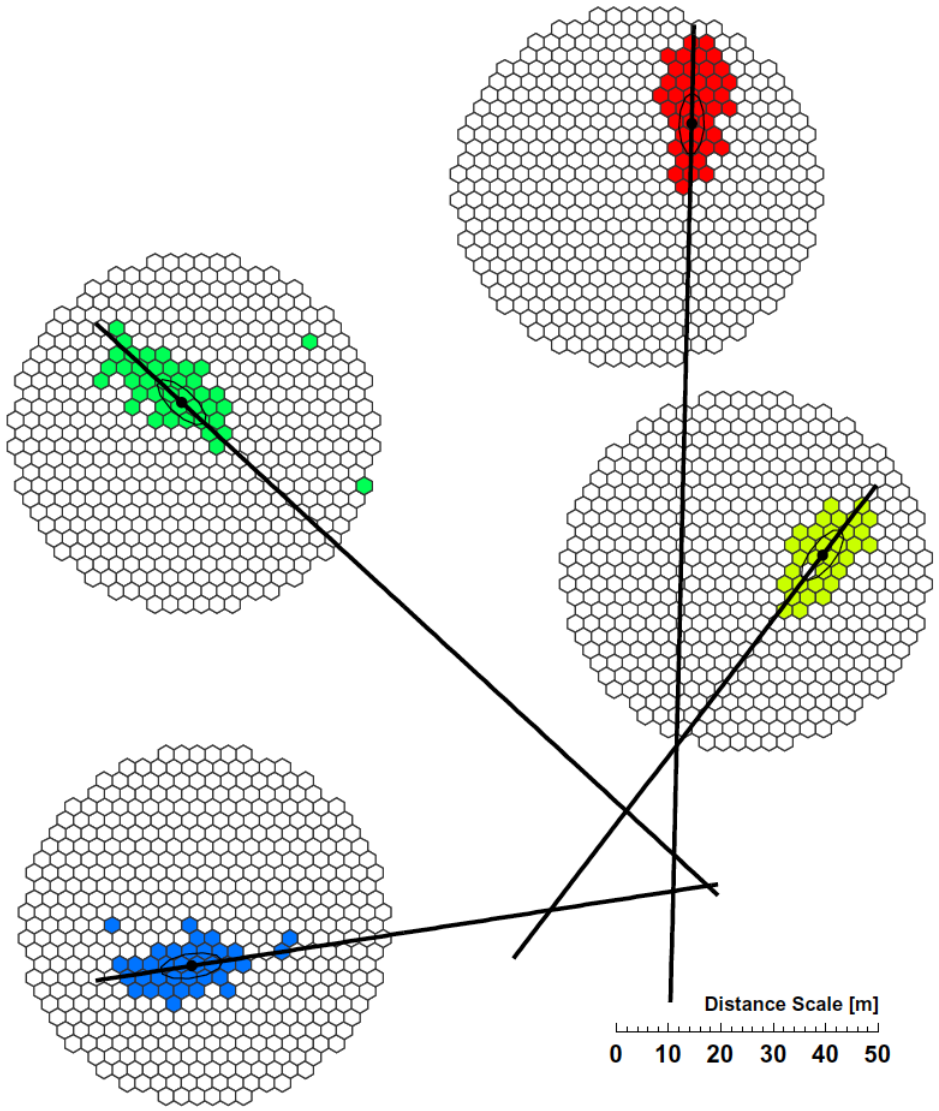

Figure 2.20: Schematic diagram of air shower core location reconstruction. Solid line along major axis of the shower images on the camera joins to the location of shower core for the particular camera. Intersection between each pair of telescopes are weighted to obtain a final location of the shower core, the point on ground where the incident gamma ray would have hit in the absence of atmosphere (*46*).

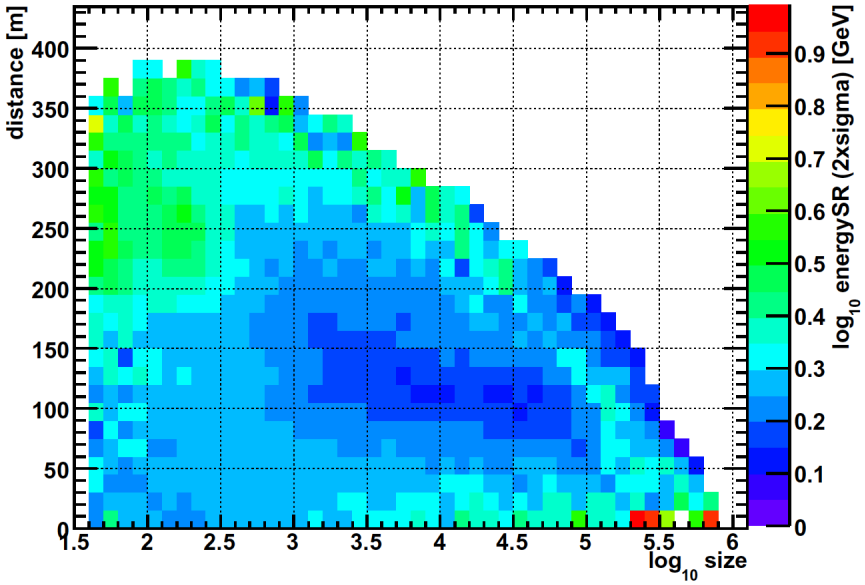

Figure 2.21: Example of look-up table with the x-axis represnting the *size* and y-axis the distance of the shower core for a 20° and camera *pedvar* 5 d.c. Using these two parameters the z-axis i.e. the median energy of the shower is obtained. Image from (*46*).

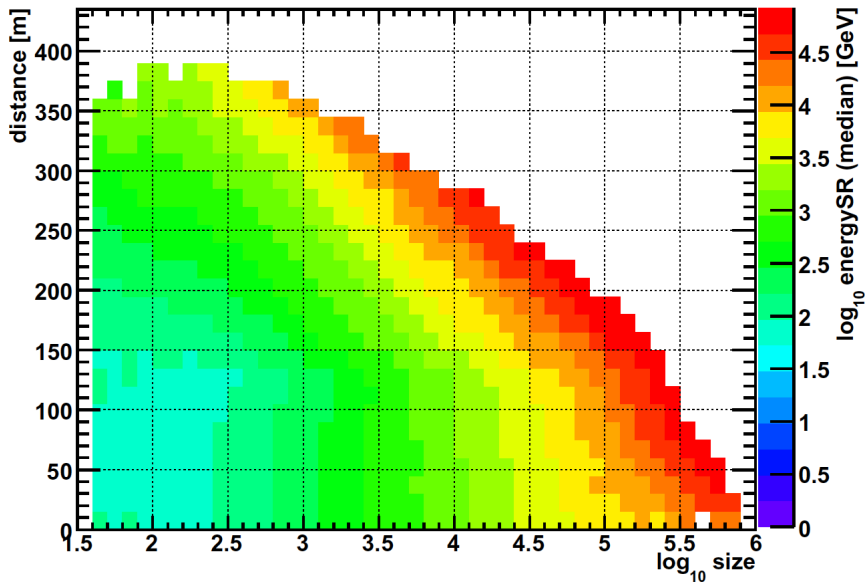

Figure 2.22: Distribution of the standard deviations corresponding to the distribution of energies from the top look-up table. Image from (*46*).

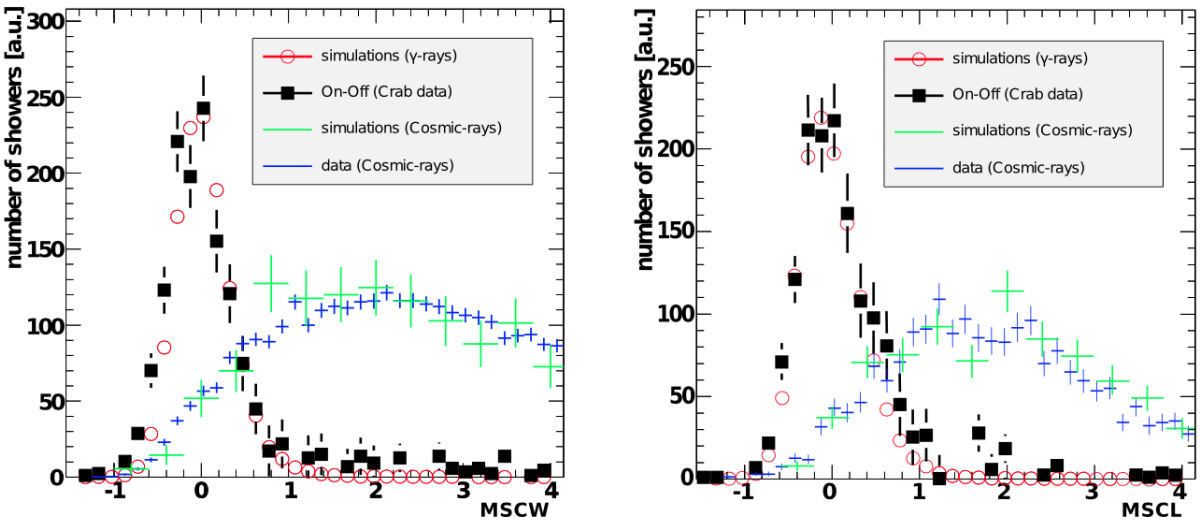

Figure 2.23: Distribution of MSCL on *left* and MSCW on *right* for observed data and Monte Carlo simulations for signal and background regions. The ON-OFF distribution is background-subtracted data for Crab Nebula. Image provided by G. Maier.

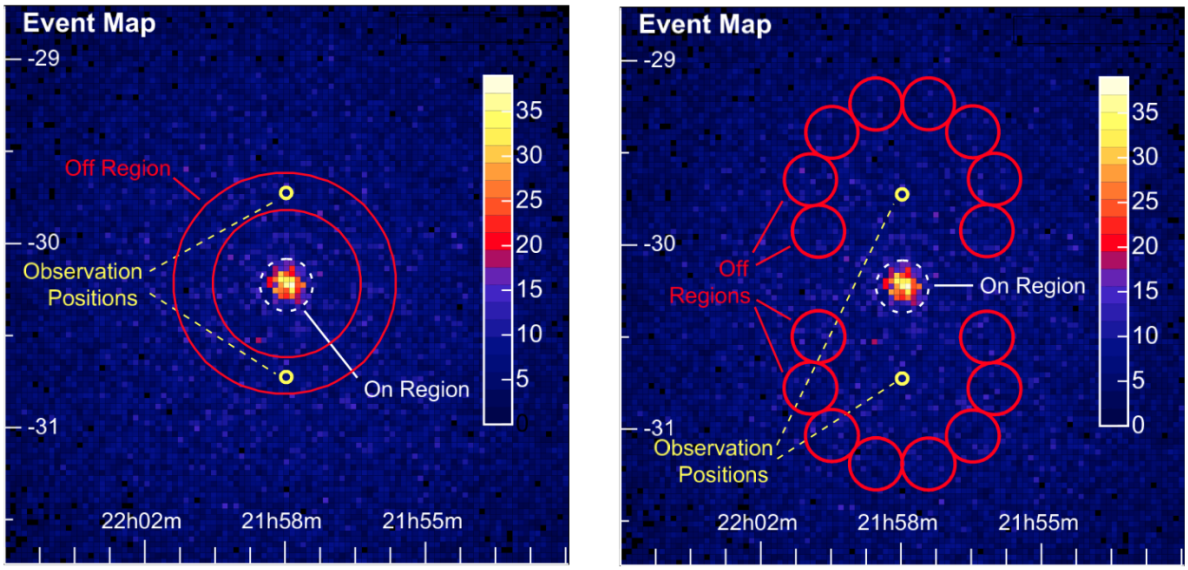

Figure 2.24: (a) Ring Background and (b) Reflected Background methods used for background estimation. Figure reproduced from (*91*).

CHAPTER 3

DECADAL STUDY OF LS I $+61^\circ$ 303 WITH VERITAS (2007-2016)

The TeV binary LS I $+61^\circ$ 303 located 2 kpc away from Earth has a compact object (CO) in an eccentric orbit around a giant Be type 10-15 $M_\odot$ star (*92*). LS I $+61^\circ$ 303 exhibits modulated gamma-ray emission around its 26.5 days orbit, mostly detectable at TeV energies around its apastron passage, with maximum flux during $\phi = 0.55 - 0.65$ phase range. Multiple flaring episodes at TeV energies have been observed since its detection in 2006 with nightly flux variability. Significant TeV emission was also detected in late 2010 from the source close to its periastron passage at superior conjunction. VERITAS has observed LS I $+61^\circ$ 303 for over a decade, accruing 200+ h of data during different parts of its orbit. The TeV spectrum is well fitted by a power law with small variations of spectral index of ~ 2.6 over year long timescales. Emission from the entire orbit detected from radio to GeV wavelengths enables detailed studies of the modulation pattern, super-orbital period, and orbit-to-orbit variabilities. Previously, such studies were difficult at TeV energies since the source was detectable only for a fraction of the orbit during its apastron passage. For the first time, TeV emission from LS I $+61^\circ$ 303 is now detected by VERITAS almost entirely around the binary's 26.5 day orbit. We have analyzed all available data for LS I $+61^\circ$ 303 since Fall 2007 in 10 individual phase bins of width $\Delta\phi = 0.1$. The source was detected at $> 5\sigma$ significance level for 9 out of 10 phase bins. A spectral analysis for two different parts of the orbit revealed subtle variation of the spectral index between them. The implication of these results is discussed.

3.1 LS I $+61^\circ$ 303 , an Exceptional TeV Binary

LS I $+61^\circ$ 303 (=V615 Cas) was identified as a variable radio emitter in 1977, discovered during a galactic plane survey and later identified as the radio counterpart of Cos B

gamma-ray source CG135+01 (*93*). It is a member of one of the most sparsely populated source class of TeV binaries with only 5 other known members: HESS J0632+57, LS 5039, PSR B1259-63, HESS J018-589, and HESS J1832-093. All of them exhibit modulated TeV emission tied to their orbital periods ranging from a few days to a few years. The orbital parameters of LS I $+61^\circ$ 303 are shown in Figure 3.1.

LS I $+61^\circ$ 303 has a rapidly spinning Be star, spectral type B0Ve (*94*) in a binary association with a companion CO of unknown nature. The much debated CO (either a neutron star (NS) or a microquasar (μQ) revolves around the main sequence star in an eccentric orbit ($e = 0.54 \pm 0.03$) with a period $P_{orb} = 26.4960$ days (*95*). A diagram of the orbit is shown in Figure 3.1. The solid black line marks the orbit of the compact object around the Be star (in orange) with the circumstellar disc wind (in yellow). The different phases (ϕ) are marked in the orbit: periastron(P) occurs at $\phi = 0.23$ when the CO is closest to the star, and apastron(A) occurs at $\phi = 0.73$ when the CO is farthest away from the star. Superior conjunction(SUPC) and inferior conjunction(INFC) are two positions in the orbit with respect to the observer when the giant star in front of or behind the CO, respectively. Periodic emissions are observed from LS I $+61^\circ$ 303 in radio, X-ray, GeV, and TeV wavelengths, modulated by its orbital period (P_{orb}) (*93*, *96–99*). The optical and IR radiation from the Be star is also modulated by P_{orb} (*100*), where the modulation occurs due to the shock produced by the transit of the CO through the dense gaseous envelope of the star.

3.2 The Compact Object of LS I $+61^\circ$ 303

Out of the known TeV gamma-ray binaries, PSR B1259-63 is the only one definitively known to host a neutron star (a 48 ms radio pulsar). The nature of the CO in LS I $+61^\circ$ 303 and other binaries is unknown. The CO in LS I $+61^\circ$ 303 has been both modeled as a NS and μQ . TeV gamma rays are produced by either the shock front of the colliding pulsar and Be star's winds or by the relativistic precessing jets which are powered by accreting matter from the Be star onto the blackhole. Neither models adequately explain all observed features of this system. An overview of the NS vs μQ debate is presented in the following sections.

3.2.1 Accretion-Ejection / Microquasar Model

It was proposed in 1982 that the nonthermal emission from LS I $+61^\circ$ 303 may be due to an accretion-ejection mechanism of a μQ (*93*) and this model has been developed extensively in the last few decades. Based on the leptonic or hadronic production mechanism of the HE emission, there are two viable scenarios of the accretion-ejection μQ model.

According to the μQ model in (*101*), the CO moving in an orbit along the equatorial plane of the Be star accretes matter from its circumstellar disc and then partially ejects it as a jet. The jet then interacts with the surrounding matter from the stellar wind forming shocks, accelerating electrons to relativistic energies. These accelerated electrons lose energy via synchrotron and IC processes where radiation produced by the latter is heavily attenuated in certain phases due to γ - γ annihilation. The HE photons produced by leptonic processes interact with low-energy photons from the star or its circumstellar disc. The rate of accretion by the CO depends on the relative velocity between the CO and the material of the circumstellar disc of the star and its density profile. The authors of the above model have assumed as a constant magnetic field of B = 1G and a photon density (U) with contributions from the star ($U_\star$) and its circumstellar disc (U_{CD}) where the former dominates except around periastron passage. Higher rates of accretion at periastron (where there is the greatest density of matter) would result in greater HE emission. According to the model, there would be increased HE emission at apastron where the CO moving at slower velocities would also accrete matter at a higher rate (the slower velocity of CO compensating for the lower density of matter from the stellar wind).

The generalized hadronic model for galactic μQ binaries described in (*102*) and adopted specifically for LS I $+61^\circ$ 303 (*103*) has a jet (containing relativistic electrons and protons) ejected by the BH perpendicular to the accretion disc plane. The jet would have an appreciable relativistic proton flux which collides and interacts with strong, dense winds of the star. Following the reaction channel

$$p + p \rightarrow p + p + \xi_{\pi^0}\pi^0 + \xi_{\pi^\pm}(\pi^+ + \pi^-)$$

where ξ_π is the corresponding multiplicity. The pions then decay to produce neutrinos and GeV-TeV gamma rays. Acceleration efficiency of protons are low but so are its radiative losses. A leptonic scenario alone is unable to explain gamma rays of energies greater than

10 TeV that have been observed from LS I $+61^\circ$ 303 , as they predict a spectral break around a few TeV (*104*). Electrons cool very fast through IC processes in the ambient photon field of the optical star and its decretion disc. Contrary to electrons, protons can be accelerated to much higher energies, resulting in harder TeV spectrum. Hence, a hadronic component to the VHE emission mechanism is a necessary inclusion. For details and development of the μQ model see references (*101–106*). Neither the μQ model nor the colliding wind NS model (description in following Section 3.2.2) are successful in explaining all aspect of this system. Some additional intrinsic properties of the μQ model and the evidence supporting the accretion - ejection μQ model for LS I $+61^\circ$ 303 are summarized below.

1. Consecutive radio observations by MERLIN in 2004 revealed a double sided 200 AU structures from the CO (*107*). The left image of in Figure 3.2 shows a bent S-shaped structure similar to a well know galactic microquasar SS433 with precessing jets (inset). The image on the right of the same figure shows the disappearance of one side of the jet. The authors have interpreted that the jet suffers large rotations on daily time scales, calculating a displacement of 0.6×24 h for the eastern side of the jet resulting in its disappearance. A series of observations performed with VLBA in 2006 revisited in (*108*) show both single-sided and double-sided structures of LS I $+61^\circ$ 303 which the authors concluded to be precessing jets of a μQ . The observations supported a Doppler-boosted elliptical core precession with the counter-jet attenuated or deboosted, making it appear for large angles and disappear for smaller values. Based on the astrometric shift of the core of this alleged jet, a 27-28 day period of precession was calculated.

2. The orbital period (P_{orb}) of LS I $+61^\circ$ 303 modulates its emission along the entire electromagnetic spectrum. A second longer modulation period of the peak flux of the radio outburst was observed (*95*). It had a periodicity of 1667 ± 8 days (will be referred to as superorbital period (P_{sup}) now onwards). The peak of the radio outburst in each orbit was also found to shift within phase range $\sim 0.4 - 0.9$. Each P_{sup} period commenced at phase $\phi_{superorbital} = 0.6$ when the peak radio flux occurred close to periastron, gradually delaying the occurrence in each orbit later until reaching apastron at $\phi_{superorbital} = 0.4$. Another period claimed to be the precessional

period of the μQ jet P_{pre}= 26.92 $\pm$ 0.07 days, was derived analyzing radio data from Green Bank Interferometer (GBI) (*109*). This newly discovered periodicity P_{pre} along with P_{orb} and P_{sup} was used to formulate a theory of astronomy beat (*106*).

- $\frac{1}{\nu_{orb}-\nu_{pre}}$ = 1667 days matched P_{sup}, where $\nu_{orb} = \frac{1}{P_{orb}}$ and $\nu_{pre} = \frac{1}{P_{pre}}$
- $P_{avg} = \frac{2}{\nu_{orb}+\nu_{pre}} = 26.70 \pm 0.05$ days was used to explain the delayed radio flux peak observed in each superorbital period. It appeared that the radio modulation was not according P_{orb}but due to P_{avg}, which was first empirically calculated in (*110*).

In (*106*), it is demonstrated that the light curve from three consecutive radio outburst (Figure 3.3 *Top*) demonstrated better periodicity when folded using P_{avg} as seen in Figure 3.3 *Bottom* frame rather than when folded using the orbital period P_{orb} as seen in *Center* panel of the figure (*106*). The authors in (*111*) claimed LS I $+61^{\circ}$ 303 to be an exception to the majority of HMXB, where the compact object is known to harbor a precessing jet have a jet precessional period an order of magnitude longer than its orbital period as predicted here (*112*).

3. A 6.7-years' data set from GBI revealed periodic radio flares were actually two consecutively occurring optically thick and thin outbursts (*113*). This double outburst was modeled to be shock-in-jet model commonly used in the context of AGNs, where a relativistic plasma traveling within a steady jet creates shocks. A steady, low-velocity, conical jet centered on the system produces an optically thick emission with $\alpha > 0$ (for flux density $S \propto \nu^{\alpha}$ where ν is the frequency). This is followed by optically thin outbursts, i.e., $\alpha < 0$ by a 'transient jet' where isolated components, so-called knots or plasmoids, are moving at relativistic speed away from the binary (*114*).

4. Using $\sim$ 36.8 years of data from multiple instruments it is demonstrated in (*106*) that P_{orb} and P_{pre} were the dominating periods driving the emission patterns of the LS I $+61^{\circ}$ 303 binary system. Their model of synchrotron emission from a precessing jet of period P_{pre} refilled every orbit with period P_{orb} matched the observed 36.8 year radio data over 8 consecutive superorbital cycles.

5. The one-sided structure to be interpreted as a cometary pulsar tail would require the Be star wind to overwhelm the pulsar wind, forcing the interaction cone to be wrapped around the pulsar. A modest power from the pulsar wind in the order of $\sim 10^{36}$ erg s^{-1} would force quite a wide interaction cone even for strong Be wind parameters assuming velocity $V_{Be} = 10^3$ km $s^{-1}$and mass loss rate $\dot{M}_{Be} = 10^{-8}\, M_\odot\, yr^{-1}$, making the CO as a neutron star candidate unlikely (*104*).

6. Finally the strongest argument presented against the NS model is the absence of pulsed emission from LS I $+61^\circ$ 303 in any wavelength. The complete attenuation of the pulsed signal at all wavelengths would require high column density throughout the entire orbit (including apastron where elevated flux is noted in other multiple wavebands), or a previously undetected special geometry between the rotational and magnetic axis of the neutron star (*115*).

3.2.2 Colliding Wind Neutron Star Model

The second popular theory about the CO of LS I $+61^\circ$ 303 assumes it to be a young energetic pulsar with spindown power $\sim 10^{36} erg\ s^{-1}$ generating a strong relativistic wind extending beyond its light cylinder. The isotropic 'pulsar wind' is composed of electrons and positrons radially flowing outwards with most of the spindown power being transferred to the leptons and a small fraction being transferred to the magnetic field (*32*, *116*–*120*). The stellar wind forms an envelope for the pulsar wind (similar to the remnant of Crab supernova confining its pulsar wind). A collisionless shock forms between the pulsar wind and the stellar wind, accelerating electrons to energies sufficient to produce X-ray radiation via synchrotron processes. The shock is shaped like a 'bow' or 'comet' pointing away from the stellar companion. The X-ray producing electrons also transfer energy to low energy stellar photons via IC processes, resulting in high-energy TeV photons. Most of the emission occurs at the pulsar standoff distance R_s (where the pressure from the stellar wind and pulsar wind are at equilibrium):

$$\frac{\dot{E}}{4\pi R_s^2 c} = \rho_w (V_w - V_p)^2 \tag{3.1}$$

where $\dot{E}$ is the pulsar spin-down rate, ρ_w is the density of stellar wind, V_w and V_p are wind speeds for the pulsar and the star, respectively. The distance of standoff, orbital separation,

pulsar wind energy and magnetization are what determine the physical condition of the shock, where the magnetic field varies with R_s as

$$B \propto \frac{1}{R_s^2} \tag{3.2}$$

At periastron, closest to the star, the stellar wind is the most dense causing a smaller standoff distance R_s resulting in a higher magnetic field B. The higher magnetic field drives up the synchrotron emission rate, thereby reducing the maximum electron energy available to low-energy photons. This lowers inverse-Compton production, resulting in a decrease in TeV emission. At apastron, the density of the stellar wind is low due to larger orbital separation resulting in larger R_s, thereby lowering the magnetic field. A lower magnetic field reduces synchrotron losses and inverse-Compton losses dominate producing greater TeV emission. For details of the model, refer to (*88*, *119*)

An additional factor to be considered in the NS model is the composition of the wind from the Be star. The stellar wind has a fast, radiation-driven isotropic component and a slower equatorial component which forms a thin decretion disc. The fast wind is clumpy and slows down the escape of HE electrons from the system. Plasma instabilities also help in retaining the relativistic electrons within the clumps and are carried away with them. The short time-scale X-ray variability reported in (*121*) is accounted to the time-dependent emission of X-rays from these clumps. The relativistic electron in the clumps loses energy via IC, synchrotron, and Coulomb channels, where the first two dominate in the 1 keV - 10 GeV energy range, as demonstrated by the strong cutoff seen in *Fermi*-LAT data. A diagram of the clumpy Be star wind and its interaction with the pulsar wind is shown in Figure 3.4; the interaction region is irregularly shaped (shown by the dark gray circle) instead of a smooth bow shock (dashed curve) dues to the clumpiness of the stellar wind.

For details of the clumpy pulsar wind model and associated arguments against the microquasar model, see (*120*) and references therein. Top arguments in favor of the pulsar wind binary are summarized as follows:

1. In the absence of detected pulsation from LS I $+61^\circ$ 303 , the most convincing evidence presented to support the colliding Be-pulsar wind binary model were the 10 images observed every 3 days by VLBA covering one full orbit; the observations indicated a cometary 'tail' structure pointning away from the massive star (*122*). Study

of the tail indicated a synchrotron gradient opacity, with highest energy particles at the head. Figure 3.5 shows a composite picture from this observation.

2. A simple calculation using Kepler's third law estimates the mass range of the CO in LS I $+61^\circ$ 303 to be $1.27 < M_{CO} < 1.98 M_\odot$ with a most likely value of $M_{CO} \approx 1.6 M_\odot$ (*123*),

$$P_{orb}^2 = \frac{4\pi^2 (a_1 + a_2)^3}{G(M_\star + M_{CO})} \tag{3.3}$$

where a_1 is the semi-major axis, a_2 is the semi-minor axis, $M_\star$ is the mass of the Be star (estimated to be $12.17 M_\odot < M_\star < 17.83 M_\odot$, typical for similar spectrally similar Be stars). The range of values for the mass of the CO was calculated varying the orbital inclination angle (i_{orb} between $65^\circ - 75^\circ$) which was assumed to be within a few degrees of the inclination angle of the Be star equatorial plane ($i_{Be} \sim 70^\circ$) with respect to the line of sight. A more significant misalignment than assumed in this calculation would have resulted in considerable variability in the $H\alpha$ emission twice when the CO would have crosses the circumstellar disc in its orbit. Compact stars in binary association within a mass between $1.4 M_\odot$ (Chandrashekhar limit) and $2.8 M_\odot$ are most likely neutron stars (*124*, *125*). This makes a NS a good candidate for the CO of LS I $+61^\circ$ 303 .

3. The broadband spectra of LS I $+61^\circ$ 303 seen in Figure 3.6 does not look like a typical accreting microquasar binary at low Eddington ratio like Cygnus X-1, as seen in (*126*). There is no cutoff seen in the LS I $+61^\circ$ 303 spectrum at $\sim$ 100 keV, generally seen in other microquasars. On the other hand, LS I $+61^\circ$ 303 has a striking resemblance with the broadband spectrum on PSR B1259-63, the only confirmed pulsar wind binary (*127*).

4. The orbital orientation of the CO in the LS I $+61^\circ$ 303 system may be uncertain but there is no doubt that we do not view the system face-on like a blazar; hence, even if a jet is present its emission would not dominate the spectrum. The aforementioned jet has been also propounded to be fast precessing, changing orientation on daily time-scale in (*107*), which implies during times when the jet is misaligned with its axis, the spectrum would be dominated by the accretion emission. No such resemblance

between the spectrum of LS I $+61^\circ$ 303 and a standard accreting black hole binary has been found yet.

5. LS I $+61^\circ$ 303 exhibited a strong magnetar-like $\sim 0.2s$ flare event, observed by *Swift*-Burst Alert Telescope (BAT) with a flux of $\simeq 5 \times 10^{-8}$ erg cm^{-2} s^{-1} peaking in 15-150 keV range (*128*, *129*). The flux was higher than the average flux by $\sim 10^3$, with similarities to a blackbody spectrum, typical of soft gamma repeaters (SGR) or anomalous X-ray pulsars (*130*). Such behavior may be indicative of strong magnetic fields in LS I $+61^\circ$ 303 , similar to other in magnetars which sometimes are known to emit pulsar winds (*131*).

6. The authors in (*120*, *132*, *133*) also point out that most Be binaries with resolved CO have neutron star companions, with a few exceptions containing hard-to-find dwarf companions. This may be due to the unique evolutionary path of the binary system. Initially, the more massive companion transfer mass to the B star during a period of Roche lobe overflow powering rapid rotation and converting them to Be stars. The rapid mass loss of the massive companion converts them to small Helium stars with few solar masses, eventually exploding as a supernova and leaving behind a neutron star but not a blackhole (see (*134*, *135*), and references therein). The authors in (*133*) calculated a very small fraction ($\sim 1/30$) may result in a blackhole following different method of Be star formation which equates to $\leq$ 2 blackholes among the known galactic Be X-ray binaries.

3.3 VERITAS Observations and Analysis

VERITAS started observing LS I $+61^\circ$ 303 in 2006 (when MAGIC discovered it) and has continued its campaign every year, accumulating nearly 240 h of data over 10 years. The data used in this dissertation were collected between October 5, 2007 and November 23, 2016 covering three different epochs of the telescope operations. A summary of the observations is listed in Table 3.1. The orbit of LS I $+61^\circ$ 303 is divided into 10 phase bins of width $\Delta\phi = 0.1$, setting $\phi = 0$ on **JD 2443366.775**, the date of discovery of LS I $+61^\circ$ 303 as a variable radio source. The entire dataset covers all the phases with maximum exposures during the phases around apastron. Data was recorded in wobble mode with a

0.5° offset, a standard technique for point sources. Due to the declination of the source, it transits the sky at medium elevations; observations are in $29° - 42°$ zenith angle range. The data used in the analysis are quality-selected to remove minutes affected due to weather and hardware problems. Standard analysis for a point source using BDT technique is performed using methods described in Section 2.5.2 at energy threshold $E_{thresh} > 300$GeV. Except for three individual seasons 2008/2009, 2009/2010, and 2010/2011, the source is detected every season with significance varying between 5.6σ and 21σ generally near its apastron passage of the orbit. There was a single instance of detection of significant emission (5.6σ) from LS I $+61°$ 303 during its superior conjunction closer to its periastron passage (*136*).

3.4 Results

VERITAS observations have yielded many interesting results over the years leading to understanding the physical mechanisms at work in LS I $+61°$ 303 . A long-term monitoring program by VERITAS has been successfully observing LS I $+61°$ 303 for more than a decade, acquiring at least 10 h of data every season. A study of the entire dataset (240+ h) recorded since 2007 has new discoveries in store which could possibly help address a few unanswered questions about this unique TeV binary. Flux-based lightcurves for the entire data set is shown in Figure 3.7 with individual exposures for the years and their significance of detections. In the first two sections, we take a closer look at individual seasons when TeV outbursts occurred and when the source was in a quiescent state. In the next section, we focus on the discovery of quiescent TeV emission from LS I $+61°$ 303 almost around the entire orbit. The final section is a study of the spectral energy distribution in the TeV range at different parts of the orbit.

3.4.1 Seasons with TeV Outbursts

TeV outbursts are generally observed from LS I $+61°$ 303 close to its apastron passage in the phase range $\phi = 0.6 - 0.7$ when flux observed can be well above 15% of the Crab Nebula. Photons with energy of 10 TeV or more has been observed during these flaring states implying existence of energetic particles with tens of TeV energy in the binary system. We take a closer look at 4 such occurrences during the 2011/2012, 2014/2015, 2015/2016 and

2016/2017 observing seasons.

- **2011 / 2012:** VERITAS recorded $\sim$ 24 h of quality-selected live-time data on LS I $+61^{\circ}$ 303 during the 2011/2012 season between December 16, 2011 (MJD 55911) and January 21, 2012 (MJD 55947). The source was active during its 2 orbits in apastron phase with flux between $10 - 20 \times 10^{-12} \gamma s$ cm^{-2} s^{-1}above 300 GeV with maximum flux of $>$ 15% of the Crab Nebula. Using the advanced BDT analysis techniques the number of 'ON' events at the source location were N_{ON} = 584 and 'OFF' events were N_{OFF} = 307, corresponding to a significance of 13.6σ detection. For this same data set the previously published significance is 11.9σ (*137*). The previously published results fit the SED with a power-law fit of the form $(1.37 \pm 0.14_{stat}) \times 10^{-12} \times ((E/1\text{TeV}))^{-2.59 \pm 0.15}$. The advanced BDT technique also improved the SED and the current fit is listed in Table 3.2. LS I $+61^{\circ}$ 303 was also found to be variable at TeV energies on a much shorter nightly timescales. Daily flux variability was seen in these data where flux change at the significance level of 2.7σ and 3.6σ were calculated. Using simultaneous / contemporaneous data from *Fermi*-LAT and Swift XRT , these data were also tested for correlation between TeV fluxes and X-ray and GeV fluxes but the emissions were found to be independent of each other. A GeV-TeV joint SED using simultaneous data from *Fermi*-LAT and VERITAS exhibited an exponential cuttoff of the GeV emission at $\sim$ 4GeV, a characteristic generally seen in *Fermi*-LAT pulsars.

- **2014 / 2015:** In the 2014 / 2015 observing season, VERITAS acquired $\sim$ 23 h of quality-selected livetime data recorded between October 16, 2014 (MJD 56946) and December 12, 2014 (MJD 57003) sampling 3 different orbits of the binary. Above a threshold of 300GeV, the number of 'ON' events at the source location were N_{ON} = 841 and 'OFF' events were N_{OFF} = 364, corresponding to a detection of 21.4σ significance level (after trials). The TeV flux was found inconsistant to a constant flux model at the level of 10σ and was tested for variability on nightly timescales. For each flux pair (f_1, f_2) separated by a day with statistical errors (σ_1, σ_2), the probability that $f_1 \neq f_2$ in terms of standard deviation (assuming fluxes and errors are normally distributed) is obtained as:

$$S(f_1 \neq f_2) = \frac{|f_1 - f_2|}{\sqrt{\sigma_1^2 + \sigma_2^2}} \tag{3.4}$$

Although the data were sparsely recorded having only a few pair of observations recorded on consecutive nights, variability at 5.15σ (pretrials) significance level was found between a pair of consecutive nights. Spectral study for individual orbits exhibited similar spectral shapes and indices. The TeV fluxes reaching more than 30% of the Crab Nebula that were observed during the first orbit is the highest ever recorded from LS I $+61^\circ$ 303 . This historically bright flare confirmed the presence of 10-20TeV electrons in the system. Following a model independent method proposed in (*138*) a magnetic field was obtained in the range (0.02-0.03)G. A detailed analysis (Box cut method), results and interpretation of this exceptional flaring episode of LS I $+61^\circ$ 303 was published with significant contributions from the author of this thesis (*139*).

- **2015 / 2016:** The following observing season 2015 / 2016 about 19 h of quality-selected live time data were recorded by VERITAS between December 01, 2015 (MJD 57357) and January 14, 2016 (MJD 57401). Above energy $>$ 300GeV the number of 'ON' events at the source location were N_{ON} = 456 and 'OFF' events were N_{OFF} = 194, corresponding to a significance of 15.4σ detection (after trial). These data sample two different orbits with some coverage around periastron passage leading up to the TeV flaring phases. All the data in this season are in the phase range $\phi = 0.031 - 0.69$.

- **2016 / 2017:** In the current observing season of 2016 / 2017 LS I $+61^\circ$ 303 was monitored between October 01, 2017 (MJD 57662) and November 23, 2016 (MJD 57715) by VERITAS for nearly 14 h, out of which 12.6 h is good quality data and unaffected by weather. The source was detected at a significance level of 11.8σ. The data sample three different orbits in the phase range $\phi = 0.54 - 0.84$. The phase binned lightcurves of all the above discussed 4 years are shown in Figure 3.8, with the fluxes in the $\phi = 0.6 - 0.7$ range 15-30% of the Crab Nebula and during rest of the of the orbit at the quiescent flux $<$ 5% of the Crab Nebula.

The TeV spectrum is from all the years including outbursts and are fitted with a power law of the form:

$$\frac{dN}{dE} = N_0 \left(\frac{E}{E_0} \right)^{-\Gamma} \tag{3.5}$$

The results on the power law fit for individual years are summarized in Table 3.2 and the SEDs are shown in Figure 3.9. The spectral index remains more or less stable during the flaring activity except in the most recent season when it appears to be softer but still within error limits. In the last three observational seasons, LS I $+61^\circ$ 303 has consistently been in its elevated flux state near apastron. This type of consistency at TeV energies is seen for the first time; whether it is a manifestation of a long term modulation is still unclear.

3.4.2 Seasons with Quiescent / Low TeV emission

- **October 2008 - December 2010:** Following the first detection of LS I $+61^\circ$ 303 with the full VERITAS array in the 2007/2008 observing season, the source entered a phase of low TeV emission over the next three seasons (*136*). In the next three seasons 2008/2009, 2009/2010, and 2010/2011, VERITAS acquired 38.4 h, 20.1 h, and 15.5 h of good quality livetime data, respectively. The 2008/2009 data were recorded between October 21, 2008 (MJD 54760) and February 01, 2009 (MJD 54863) in the original configuration of the array (V4). The next two seasons were in V5 configuration after the relocation of one of the telescopes and were observed between October 15, 2009 (MJD 55119) and December 12, 2009 (MJD 55177) for 2009/2010 and between September 16, 2010 (MJD 55455) and November 06, 2010 MJD 55506 for 2010/2011 season. Phases covered during these three seasons were $\phi_{'08-'09} = 0.03 - 0.91$ (sampled over 2 orbits), $\phi_{'09-'10} = 0.58 - 0.78$ (sampled over 2 orbits) and $\phi_{'10-'11} = 0.0565 - 0.4312$ (sampled over 3 orbits). The integrated data set of 70+ h over all phases gave a significance $< 5\sigma$, below the required significance level to claim detection. Above the 300 GeV threshold nightly observations gave a flux upper limit of 3%-8% of the steady flux of Crab Nebula. During its periastron passage (near $\phi \sim 0.1$) LS I $+61^\circ$ 303 was detected one time from the data recorded between September 17, 2010 (MJD 55455) and November 7, 2010 (MJD 55507) it was detected at 5.6σ significance level. The source deviated from its known behaviour of outburst during apastron passage as seen in 2007, and was not detected during the expected $\phi = 0.6 - 0.7$ phase interval. The correlation between X-ray and TeV gamma-ray emission that

was found previously by the MAGIC Collaboration during a single orbit in 2007 (*140*) was used to estimate an expected flux of nearly 10% of the Crab Nebula using simultaneous Swift XRT data. But the 2008-2010 upper-limit was found 4.6 times lower than the expected flux.

- **October 2012 - January 2014:** In 2012/2013 observing season, VERITAS sampled the tail of one orbit and the beginning of the next orbit covering phase range $\phi < 0.81$ & $\phi < 0.46$. The data recorded between December 05, 2012 (MJD 56266) and December 21, 2012 (MJD 56282) was targeted at the phase where TeV emission is generally not detected but the source was detected in a quiescent state. In the 13.4 h data set 111 excess events were detected resulting in a 8.1σ significance level. The flux above 300GeV was $(4.36 \pm 0.62) \times 10^{-12}$ γ cm^{-2} s^{-1}corresponding to 4.1% of the Crab Nebula. In 2013/2014 observing season, VERITAS sampled 1 orbit covering phase range $\phi = 0.26 - 0.72$ recorded the data between November 25, 2013 (MJD 56621) and December 07, 2013(MJD 56633). From the 8.6 h of quality-selected livetime exposure an excess of 70 events above the background was detected corresponding to a 6.0σ significance level. The flux above 300GeV was $(3.29 \pm 0.70) \times 10^{-12}$ γ cm^{-2} s^{-1} corresponding to 3.1% of the Crab Nebula.

The observations during the previously mentioned two seasons were mostly targeted to inspect emission at other parts of the orbit. We are not ruling out the near-apastron TeV emission during this above timeframe. TeV observations are very time limited with observations taking place separated by days and for integrations lasting only few h. The orbital period of LS I $+61^\circ$ 303 is close to the lunar cycle which hinders observation covering the entire orbit since IACTs have limited exposure during bright moon phases. This also results in sparse sampling. During the 2 years, observations covered only 2 partial orbits out of 20 total, leaving a possibility that the source was active in some of the unobserved periods.

3.4.3 Discovery of Base TeV Emission Around the Orbit

Using the full VERITAS observational data set recorded during September 2007 - December 2016, covering 10 observing seasons and three epochs of the instrument operations revealed that TeV emissions from LS I $+61^\circ$ 303 are seen around its entire orbit. Setting

the orbital phase $\phi_0 = MJD$ 43366.775 and using an orbital period P_{orb}=26.4960 days, the entire data set is divided into 10 phases with width $\Delta\phi = 0.1$. Each phase bin is individually analyzed and except for 1 bin the source is detected at $\geq 5\sigma$ significance in all the phase bins. A summary of the results from each phase bin is shown Table 3.3. Integral flux estimates from each phase bin is shown in Figure 3.10 and in Table 3.3.

- Phase bin $\phi = 0.0 - 0.1$: A total of $\sim$ 16.6 h of quality-selected live time data was available for this phase bin. An excess of 97 events from the source above the background was obtained (excess map shown on top right of Figure 3.11) which corresponds to detection at the 5.6σ significance level. The significance skymap is shown along with the significance distributions on the left panel of Figure 3.11 on the top and bottom, respectively. On the bottom right of the figure, we see the cumulative significance. The flux corresponding to this phase is $(2.906 \pm 0.6184) \times 10^{-12}\ \gamma$ cm^{-2} s^{-1}, which is about 2.8% of the Crab Nebula flux.

- Phase bin $\phi = 0.1 - 0.2$: A total of $\sim$ 11.1 h of quality-selected live time data was available for this phase bin. An excess of 76 events from the source above the background was obtained (excess map shown on top right of Figure 3.12) which corresponds to detection at the 5.4σ significance level (pretrial). The significance skymap is shown along with the significance distributions on the left panel of Figure 3.12 on the top and bottom, respectively. On the bottom right of the figure, we see the cumulative significance. The flux corresponding to this phase is $(4.03 \pm 0.82) \times 10^{-12}\ \gamma$ cm^{-2} s^{-1}, which is about 3.8% of the Crab Nebula flux.

- Phase bin $\phi = 0.2 - 0.3$: A total of $\sim$ 19.8 h of quality-selected live time data was available for this phase bin. An excess of 92 events from the source above the background was obtained (excess map shown on top right of Figure 3.13) which corresponds to detection at the 5.1σ significance level (pretrial). The significance skymap is shown along with the significance distributions on the left panel of Figure 3.13 on the top and bottom, respectively. On the bottom right of the figure, we see the cumulative significance. The flux corresponding to this phase $>$ 300GeV is $(2.77 \pm 0.60) \times 10^{-12}\ \gamma$ cm^{-2} s^{-1}, which is about 2.6% of the Crab Nebula flux.

- Phase bin $\phi = 0.3 - 0.4$: A total of $\sim$ 19.8 h of quality-selected live time data was available for this phase bin. An excess of 110 events from the source above the background was obtained (excess map shown on top right of Figure 3.14) which corresponds to detection at the 6.1σ significance level (pretrial). The significance skymap is shown along with the significance distributions on the left panel of Figure 3.14 on the top and bottom, respectively. On the bottom right of the figure, we see the cumulative significance. The flux corresponding to this phase is $(3.35 \pm 0.61) \times 10^{-12}$ γ cm^{-2} s^{-1}, which is about 3.2% of the Crab Nebula flux.

- Phase bin $\phi = 0.4 - 0.5$: A total of $\sim$ 9.1 h of quality-selected live time data was available for this phase bin. An excess of 46 events from the source above the background was obtained (excess map shown on top right of Figure 3.15) which corresponds to 3.8σ significance level. The low significance is due to the limited exposure resulting in low photon statistics. Since a minimum of 5σ significance is required to claim detection, only upper limit on the flux are available for this phase bin. The flux corresponding to this phase is $< (4.59) \times 10^{-12}$ γ cm^{-2} s^{-1}. The significance skymap is shown along with the significance distributions on the left panel of Figure 3.15 on the top and bottom, respectively. On the bottom right of the figure, we see the cumulative significance.

- Phase bin $\phi = 0.5 - 0.6$: A total of $\sim$ 26.8 h of quality-selected live time data was available for this phase bin. An excess of 330 events from the source above the background was obtained (excess map shown on top right of Figure 3.16) which corresponds to detection at the 15.5σ significance level. The significance skymap is shown along with the significance distributions on the left panel of Figure 3.16 on the top and bottom, respectively. On the bottom right of the figure, we see the cumulative significance. The integral flux corresponding to this phase is $(6.57 \pm 0.54) \times 10^{-12}$ γ cm^{-2} s^{-1}, which is about 6.2% of the Crab Nebula flux.

- Phase bin $\phi = 0.6 - 0.7$: A total of $\sim$ 46.1 h of quality-selected live time data was available for this phase bin. An excess of 598 events from the source above the background was obtained (excess map shown on top right of Figure 3.17) which corresponds to detection at the 20.8σ significance level (pretrial). The significance

skymap is shown along with the significance distributions on the left panel of Figure 3.17 on the top and bottom, respectively. On the bottom right of the figure, we see the cumulative significance. The integral flux corresponding to this phase is $(7.40 \pm 0.44) \times 10^{-12}\ \gamma\ \mathrm{cm}^{-2}\ \mathrm{s}^{-1}$, which is about 7% of the Crab Nebula flux. This phase range corresponds to period of highest TeV outbursts.

- Phase bin $\phi = 0.7 - 0.8$: A total of $\sim$ 29.3 h of quality-selected live time data was available for this phase bin. An excess of 196 events from the source above the background was obtained (excess map shown on top right of Figure 3.18) which corresponds to detection at the qqσ significance level (pretrial). The significance skymap is shown along with the significance distributions on the left panel of Figure 3.18 on the top and bottom, respectively. On the bottom right of the figure, we see the cumulative significance. The flux corresponding to this phase is $(3.69 \pm 0.46) \times 10^{-12}\ \gamma$ $\mathrm{cm}^{-2}\ \mathrm{s}^{-1}$, which is about 3.5% of the Crab Nebula flux. This phase range corresponds to the apastron passage.

- Phase bin $\phi = 0.8 - 0.9$: A total of $\sim$ 15.2 h of quality-selected live time data was available for this phase bin. An excess of 94 events from the source above the background was obtained (excess map shown on top right of Figure 3.19) which corresponds to detection at the 6.1σ significance level (pretrial). The significance skymap is shown along with the significance distributions on the left panel of Figure 3.19 on the top and bottom, respectively. On the bottom right of the figure, we see the cumulative significance.The flux corresponding to this phase is $(3.53 \pm 0.62) \times 10^{-12}\ \gamma$ $\mathrm{cm}^{-2}\ \mathrm{s}^{-1}$, which is about 3.3% of the Crab Nebula flux.

- Phase bin $\phi = 0.9 - 1.0/0.0$: A total of $\sim$ 9 h of quality-selected live time data was available for this phase bin. An excess of 58 events from the source above the background was obtained (excess map shown on top right of Figure 3.20) which corresponds to a 5.0σ significance level (pretrial). The significance skymap is shown along with the significance distributions on the left panel of Figure 3.20 on the top and bottom, respectively. On the bottom right of the figure, we see the cumulative significance. The flux corresponding to this phase is $(3.81 \pm 0.85) \times 10^{-12}\ \gamma\ \mathrm{cm}^{-2}\ \mathrm{s}^{-1}$, which is about 3.6% of the Crab Nebula flux.

3.4.4 Orbital Spectral Evolution of LS I $+61^\circ$ 303

The spectrum of LS I $+61^\circ$ 303 around the apastron passage has been stable over the duration of this study. The spectral index for a power law fit to the TeV data has been in the range $-2.5 \sim -2.6$. Integrating 10 years of data into 10 phase bins, we can take a closer look at the progression of the spectrum around other phases in the orbit. Initially, we consider two separate sections of the orbit, first covering the apastron passage where the TeV outbursts are generally seen in the phase range $\phi = 0.5 - 0.8$, second covering the rest of the orbit of CO around the optical star in the phase range $(0.8 < \phi \,\&\, \phi < 0.5)$, including the periastron passage. A summary of the spectral fit information in the different parts of the orbit of LS I $+61^\circ$ 303 is shown in Table 3.4.

- **Apastron Passage ($\phi = 0.5 - 0.8$):** Half of VERITAS observations are focussed during these three phases bins, with a total of $\sim$ 102 h of quality-selected livetime data acquired during three epochs of the instrument's operation. The SED is shown in Figure 3.21.

  An excess of 1123 events over the background is seen from the source corresponding to a detection at 27σ significance level. A skymap of all recorded apastron passage is shown on the *left* panel of Figure 3.21 with an inset of the pertaining section of the orbit. The power law fit to this data is shown on the *right* panel of Figure 3.21 along with the parameters of the fit. The spectral index is $\Gamma = -2.63 \pm 0.06_{stat}$ with a reduced $\chi^2 = 1.1$. It is to be noted that we see a number of events in the highest energy bin (center of the bin at 16.788) and no break in the spectrum is seen. The VHE photons at energies above 10 TeV are indicative of the presence of relativistic electron with energies above 10 TeV. The spectral index is consistent with previously reported numbers from this LS I $+61^\circ$ 303 (*98*, *99*, *141*, *142*, *142*)

- **Rest of the Orbit ($\phi > 0.8$ & $\phi < 0.5$):** VERITAS has extensively observed the rest of the orbital phase for 100.8 h. The SED is shown in Figure 3.22. At the source location an excess on 570 events were recorded corresponding to a detection at 13.9σ significance level.

  The difference in flux level from this much longer orbital coverage of the periastron passage compared to the shorter apastron passage is clearly seen with similar h of data. The shape of the spectral energy distribution for this part of the orbit is

shown in the *right* panel of Figure 3.22 along with the power-law fit parameters. The spectral index for the fit is $\Gamma = -2.81 \pm 0.16_{stat}$ showing good evidence for a much softer spectrum compared to the apastron passage. The phase range covers both periods when the CO is behind the equatorial disc of the optical star and in its front, i.e., inferior conjunction and superior conjunction passage, respectively. This is the softest spectrum seen for LS I $+61^{\circ}$ 303 . A point to be noted is that there are systematics involved due to three different epochs of the array and we have only few differential flux points on the SED resulting in a reduced $\chi^2 = 0.3$. No spectral break is seen up to 3 TeV, above which this energy only upper limits can be computed due to limited statistics. The possibility of a spectral break above 3 TeV cannot be ruled out. A similar spectral break above 6 TeV is seen in the spectrum of LS 5039 during the binary's INFC (*37*).

The data from the section of the orbit containing periastron passage are further divided to take a closer look at the spectrum. The first part is before periastron occurs containing superior conjunction point, i.e., in the phase range ($\phi > 0.8$ & $\phi < 0.2$) which will be referred to as 'just before.' The second part is in the phase range ($\phi > 0.2 \& \phi < 0.5$) containing both the periastron point (at $\phi = 0.223$) and the inferior conjunction which will be referred to as 'just after.'

- **Just before periastron ($\phi > 0.8$ & $\phi < 0.2$):** During this part of the orbit LS I $+61^{\circ}$ 303 is detected at 10.9σ significance level from 323 excess events. The spectrum is fit with a power law shown on the *left* panel of Figure 3.23 along with the fit parameters and an inset of the relevant part of the orbit.

  The fit shows evidence for a softer spectrum than that seen at apastron ($\Gamma = -2.86 \pm 0.21$). The fit has a decent quality with a reduced $\chi^2 = 1.2$. The slightly larger error on the spectral index is due to lower statistics and systematics arising from the three different epochs. The softer spectrum could be attributed to higher absorption due to the CO being behind the dense equatorial disc of the optical star and may not be an intrinsic property of the system.

- **Just after periastron ($\phi > 0.2 \& \phi < 0.5$):** The second part of the periastron passage orbit has similar exposure of $\sim$ 48.8 h as the first part described above. An excess

of 247 events is doung at the source location of LS I $+61^\circ$ 303 compared to the background corresponding to a detection at 8.8σ significance level. The power law fit to the spectrum for just after section of the orbit is show on the *right* panel of Figure 3.24 along with an inset marking the pertaining section of the orbit.

The spectral index obtained from the fit is $\Gamma = -2.61 \pm 0.22_{stat}$ consistant with the observed spectrum during apastron. The larger limits of the spectral index is again attributed to low statistics as well as systematics arising from three different epochs. Since the CO is the the foreground of the optical star and its disc, we see similar spectral indices as apastron passage when the CO is furthest from the influence of the optical star. This hints towards a constant interaction between the CO and its companion as the origin of the detected constant TeV emission seen around the entire orbit.

3.5 Discussion

The decadal study of all VERITAS data on LS I $+61^\circ$ 303 yields a set of observations that can constrain the nature of the CO in LS I $+61^\circ$ 303 . The μQ model (Section 3.2.1) and NS model (Section 3.2.2) match certain observations but neither models can comprehensively explain all observations. The nature of the compact object is likely more complicated than presented in these simple models. A third model for LS I $+61^\circ$ 303 , with a neutron star transitioning between its ejector and propeller regimes, is presented here in context of these new results seen from the VERITAS decadal study.

A neutron star can be classified into categories based on the interaction between its electromagnetic fields and the surrounding plasma as the compact star evolves through its lifetime. The structure of a neutron star and its surrounding magnetic fields are shown in Figure 3.25. A table of the the different classes are summarized in Table 3.5 followed by short descriptions of the relevant classes.,

- **Ejector (E)**: In the ejector phase, the pressure of the electromagnetic radiation and expelled relativistic particles is high enough to sweep away the surrounding matter beyond the capture radius, i.e., radius of the light cylinder. In the ejector regime, the neutron star is spun down, its rotation frequency is decreased and the power of the relativistic wind is reduced as a result.

- **Propeller (P)**: In the propeller phase the outward pressure of electromagnetic radiation and expelled relativistic particles is more balanced with the inward pressure from the surrounding medium. The rapidly rotating strong magnetic field of the neutron star hinders the accretion of matter onto its surface. Until the necessary condition of Keplerian velocity $>$ velocity of Alfvén surface * is reached, accretion cannot take place. The magnetic field throws back the plasma beyond the capture radius, matter may not be completely shed away like the ejector phase and accumulates in the vicinity of the NS but stationary accretion is also not possible. The time-dependent stresses associated with the rotating magnetic field of the spinning neutron star deposit energy and angular momentum into the surrounding plasma. This loss of energy results in spinning down the neutron star and drives plasma outflows. The propeller phase is one of the least observed states in the evolution of neutron stars.

- **Accretor(A), Georotator(G), and Magnetor(M)**: When the co-rotating radius R_c is smaller than the stopping radius R_{st}, matter accretes onto the NS, a stage known as the *Accretor*. This is the most well-studied phase of a NS. A *Georotator* is a slowly rotating NS in which the Alfvén radius is larger than capture radius R_G hindering matter falling onto the surface of the star. *Magetors* are NS in tight binary systems where the Alfvén radius $R_A > a$, the semi-major axis of the system. The optical star then lies within the Alfvén surface of the magnetic star.

The flip-flop model for LS I $+61^\circ$ 303 assumes the neutron star transitions between its Ejector and Propeller phases along its orbit (*143*). At periastron the neutron star is surrounded by dense material of the decretion disc of the Be star. The neutron star is in the propeller regime when its radiation pressure tries to push out the surrounding matter. As the neutron star travels further away from the optical star along its elliptical orbit, the density of matter decreases and the outward radiation pressure overcomes the inward pressure from enveloping matter. The neutron star transitions to the ejector regime, expelling the enveloping matter gathered during propeller phase. The ejector phase con-

*Alfvén surface is the surface of the region surrounding a neutron star from which ionized gas is pulled around by the star's magnetic spinning field

tinues until all the matter is exhausted and somewhere following apastron the changeover to propeller ensues. A diagram of the flip-flop model is shown in Figure 3.26.

The flip-flop model seems like a plausible explanation for the base TeV emission seen continuously around the orbit for LS I $+61^\circ$ 303 . At $\sim \phi_{0.5}$, the NS transitions to the ejector phase following which TeV outbursts are seen until it returns to its quiescent TeV flux at $\sim \phi_{0.8}$. Past apastron point at $\sim \phi_{0.8}$, the enveloping matter has been exhausted and the NS switches back to its propeller regime as it gradually advances towards region of dense stellar material. In the propeller state, the neutron stars's magnetosphere grows beyond the co-rotation radius. The centrifugal force prevents the surrounding co-rotating matter from reaching the magnetic poles. In contrast, the strong magnetic fields of X-ray pulsars in the accretor phase disrupts the accretion flow and funnels matter onto the magnetic poles (*144*). The ram pressure of the flow exerted on the magnetosphere is balanced by the magnetic pressure. The accretion rate is so high that the intense ram pressure shrinks the Alfv́en radius (magnetosphere of NS) making it smaller than the co-rotation radius. This results in accretion of matter onto the magnetic poles creating X-ray hotspots. The emission from the X-ray hotspots is beamed and produces regular pulsations when passing the line of sight as the NS rotates (given the magnetic axis and rotational axis are misaligned) (*145*). Since there is no in-falling matter during the propeller regime no X-ray pulsation is expected in this phase (*146*), this also explains the absence of X-ray pulsation from LS I $+61^\circ$ 303 (*147*).

In the propeller regime, high mass capture rate at periastron translates to high X-ray luminosity and is estimated to be $\sim 2 \times 10^{34}$ erg s^{-1}. At ejector phase high efficiency($1 -$ 10% (*148*)) of conversion of spin-down energy would result in HE emission and expected X-ray luminosity $2 \times 10^{33} - 2 \times 10^{34}$ erg s^{-1}. These calculated values (*149*) are close to the observed value from the system. There is a hint of slightly elevated TeV flux in phase $\phi_{0.1-0.2}$, just before periastron similar to the elevated X-ray flux also seen during this period (*149*). During Ejector phase the gamma-ray emissions are thought to originate at the shock front where the stellar winds are interacting with the relativistic wind of the pulsar. At Propeller the plasmon accumulated near the NS could spiral around like a vortex and the high voltages and shocks between the layers of the plasma vortex could be responsible for the quiescent TeV emission that is observed (*149*).

The plasmon mass accumulated by the propeller NS would appear after periastron passage (*150*). After the transition of propeller $\rightarrow$ ejector an outburst in multiple wavelengths is expected. The radio peak of outburst is always delayed from the X-ray peak by $\Delta\phi \simeq 0.2$. The delay is accounted for by the time of flight of HE particles in the plasmon close to the binary to the radio emitting region (at a distance 10 times more than seperation distance of the NS and optical star) (*151*). This behaviour is also predicted in the flip-flop model for LS I $+61^{\circ}$ 303 (*149*). The X-ray outburst shift in the phase range $\phi = 0.35 - 0.75$ based on the superorbital period $P_{sup}$of the system. Hα observations have hinted that cyclical changes in some characteristics of the Be star is the origin of the superorbital period. Based on 7 years of *Fermi*-LAT observations, the circumstellar disc of the Be star is now suggested to be elliptical in shape and its major axis rotates at the superorbital period of 1667 days (*152*). Estimated spin period of the NS from the flip-flop model is P_{spin} = 0.15 s - 0.20 s (*149*, *150*). This also fits well with the idea of a slow spinning highly magnetized star responsible for the magnetar like flares that were seen from LS I $+61^{\circ}$ 303 (*143*, *153*).

The spectral energy distribution at TeV energies around the orbit is quite stable with an index $\Gamma = (-2.5) \sim (-2.6)$ except during superior conjunction passage, just before periastron $\phi > 0.8$ & $\phi < 0.2$ when the neutron star is behind a dense equatorial decretion disc of the optical star. The softer spectrum extends upto 3 TeV beyond which there could be a spectral cutoff. Similar effect is seen in LS 5039 which shows a spectral cutoff at 6 TeV during its INFC passage. Attenuation at VHE energies are common due to absorption and pair production mechanisms which results into a softer spectrum (similar to spectrums of blazars).

Table 3.1: VERITAS dataset of LS I $+61^\circ$ 303 observations.

Observing Season	Instrument Epoch	Quality Selected Livetime [mins]	Detection Significance (σ)
2007 / 2008	V4	1518	6.2
2008 / 2009	V4	2305	3.8
2009 / 2010	V5	1207	0.7
2010 / 2011	V5	933	4.6
2011 / 2012	V5	1551	14.0
2012 / 2013	V6	490	6.5
2013 / 2014	V6	522	5.6
2014 / 2015	V6	1746	21.4
2015 / 2016	V6	1137	16.0
2016 / 2017	V6	703	12.4
All	V4, V5, V6	12112	29.2

Table 3.2: Comparison of the 4 flares from LS I $+61^\circ$ 303 .

Observing Season	σ	N_0	Γ	Integral Flux $\times 10^{-12}$ cm^{-2} s^{-1}	Highest Flux $\times 10^{-12}$ cm^{-2} s^{-1}
2011-2012	13.6	1.46 ± 0.14	-2.48 ± 0.10	5.87 ± 0.52	18.79 ± 2.90
2014-2015	21.4	2.00 ± 0.13	-2.56 ± 0.08	8.27 ± 0.50	37.79 ± 4.04
2015-2016	15.4	1.77 ± 0.15	-2.50 ± 0.11	7.72 ± 0.58	22.63 ± 3.10
2016-2017	11.8	1.71 ± 0.19	-2.81 ± 0.18	6.45 ± 0.70	16.87 ± 2.86

Table 3.3: LS I $+61^\circ$ 303 phase binned results.

Phase bin (ϕ)	Pre-trial Significance (σ)	Flux [$\times 10^{-12}$ cm^{-2} s^{-1}]	% of Crab	Exposure [min]
$0.0 \rightarrow 0.1$	5.6	2.90 ± 0.61	2.8	992
$0.1 \rightarrow 0.2$	5.4	4.03 ± 0.80	3.8	663
$0.2 \rightarrow 0.3$	5.1	2.77 ± 0.60	2.6	1186
$0.3 \rightarrow 0.4$	6.1	3.35 ± 0.61	3.2	1178
$0.4 \rightarrow 0.5$	3.8	< 4.59	< 4.3	547
$0.5 \rightarrow 0.6$	15.9	6.57 ± 0.54	6.2	1289
$0.6 \rightarrow 0.7$	18.8	7.40 ± 0.44	7	2517
$0.7 \rightarrow 0.8$	8.0	3.69 ± 0.46	3.5	1630
$0.8 \rightarrow 0.9$	5.2	3.53 ± 0.62	3.3	731
$0.9 \rightarrow 0.0$	5.0	3.81 ± 0.85	3.6	543

Table 3.4: LS I $+61^\circ$ 303 apastron versus periastron.

Phase bin (ϕ)	Significance (σ)	Flux [$\times 10^{-12}$ cm^{-2} s^{-1}]	% of Crab	Spectral Index	Exposure [min]
$0.5 \rightarrow 0.8$	27.0	6.10 ± 0.27	5.8	-2.63 ± 0.06	6143
$0.8 \rightarrow 0.5$	13.9	3.27 ± 0.25	3.1	-2.81 ± 0.16	6048
Just Before $0.8 \rightarrow 0.2$	10.9	3.57 ± 0.35	3.4	-2.86 ± 0.21	3120
Just After $0.2 \rightarrow 0.5$	8.8	2.96 ± 0.37	2.8	-2.62 ± 0.22	2928

Table 3.5: Classification of neutron stars.

Notation	Name	Relation between characteristic distance s	Accretion rate
E	Ejector	$R_{st} > max[R_G]$	$\dot{M}_c \leq \dot{M}_{cr}$
P	Propeller	$R_c < R_{st} \leq max[R_G]$	$\dot{M}_c \leq \dot{M}_{cr}$
A	Accretor	$R_{st} \leq min[R_c, R_G]$	$\dot{M}_c \leq \dot{M}_{cr}$
G	Georotator	$R_G < R_{st} \leq R_c$	$\dot{M}_c \leq \dot{M}_{cr}$
M	Magnetor	$R_{st} > a, R_c > a$	$\dot{M}_c \leq \dot{M}_{cr}$
R_G	Gravitational capture radius of NS, radius of a cylindrical region where plasma kinetic energy is less then gravitational potential		
R_{st}	Stopping radius is the distance where electromagnetic field of NS balances gravitational field of accreting plasma		
R_c	Co-rotation radius is the distance at which NS rotation velocity matches the Keplerian velocity surrounding plasma, making it rotate like a solid mass		
$\dot{M}_c$	Accretion rate		
$\dot{M}_{cr}$	Critical accretion rate $(\frac{4\pi c}{\kappa} R_{st})$		

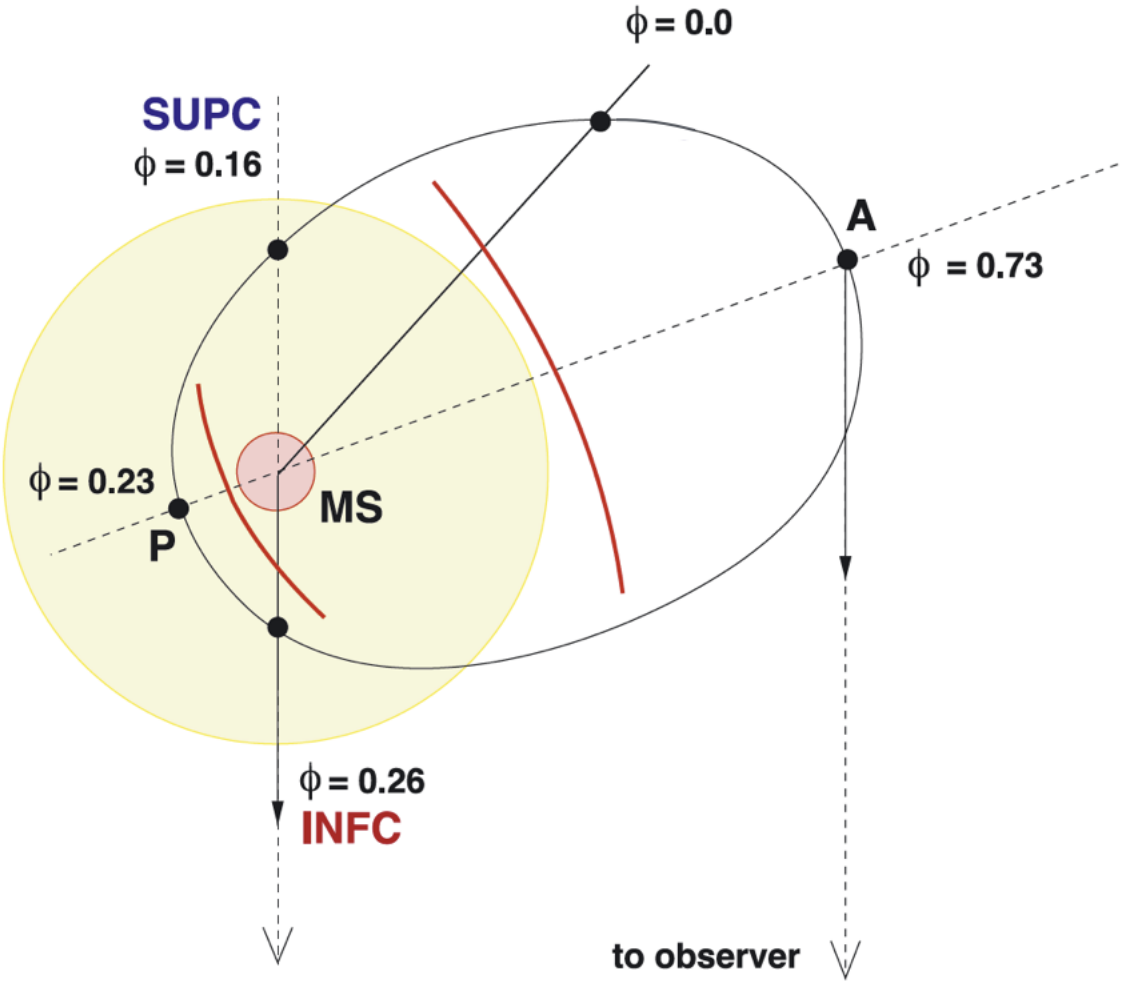

Figure 3.1: Orbital geometry of LS I +61° 303 without considering inclination. Locations of periastron(P), apastron(A), superior conjunction(SUPC), and inferior conjunction(INFC) in the orbit(solid black line) are marked. The giant massive star (MS, orange) and it equatorial disc (yellow) are also shown. Figure reproduced from (*154*).

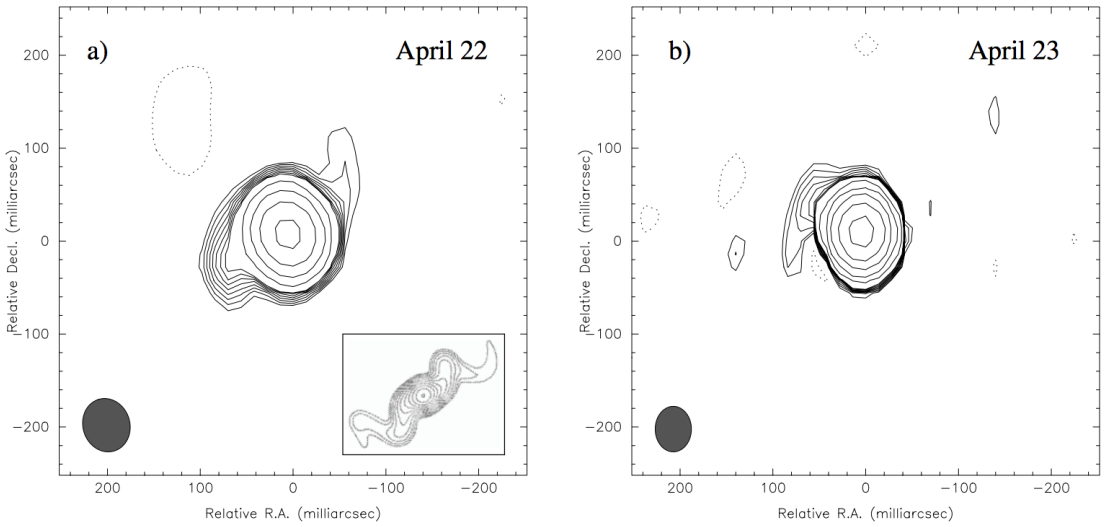

Figure 3.2: MERLIN self-calibrated image of LS I +61° 303 on 2 different days at 5GHz showing S-shaped morphology, similar to precessing jets of SS433 inset in figure. Absence of the asymmetric extension was considered evidence for precessing jet. Figures reproduced from (*107*).

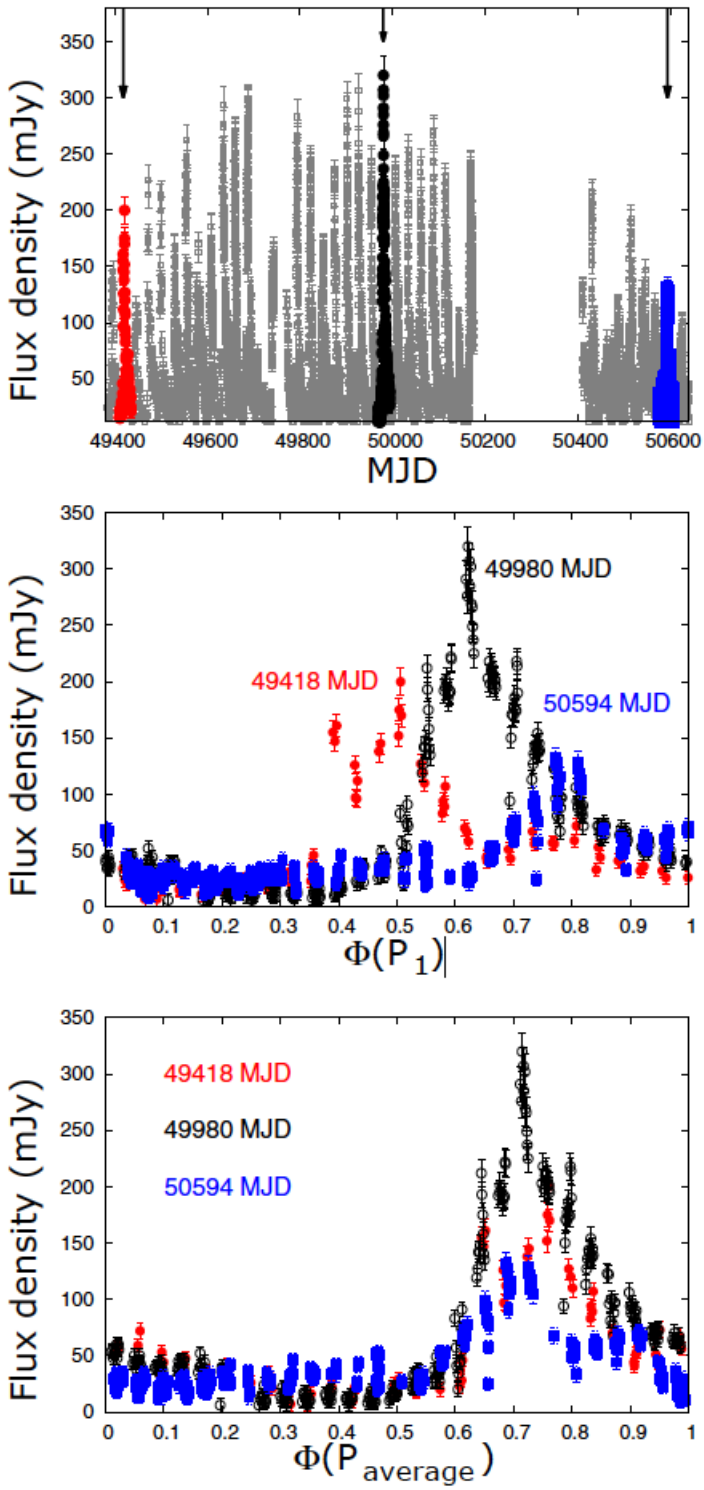

Figure 3.3: *Top*: Consecutive radio outburst from LS I +61° 303 , *Center*: Lightcurve folded using periodicity P_{orb}, *Bottom*: Lightcurve folded using periodicity P_{avg}, figure reproduced from (*106*).

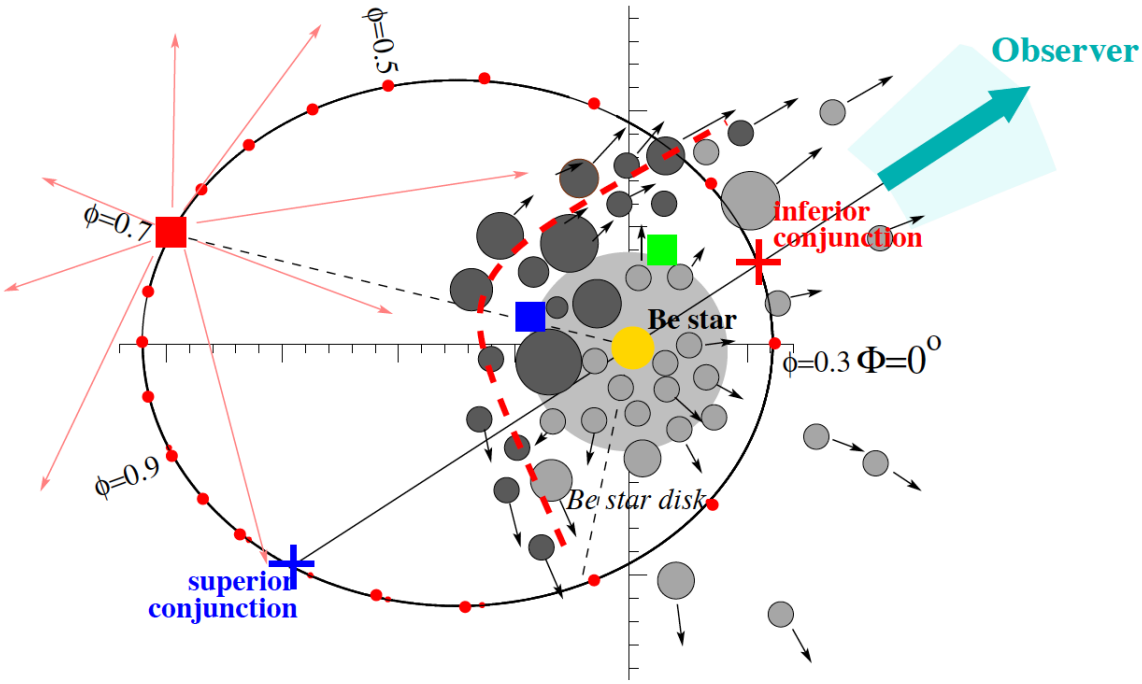

Figure 3.4: Schematic diagram of interaction between the pulsar wind and clumpy stellar wind from Be star. Radius of Be star (in yellow) corresponds to smallest tick on the coordinate axes. Red dots are $\Delta\phi = 0.05$ phase intervals, uncertainty in observer angle is $\pm 9^{\circ}$. Figure reproduced from (*120*).

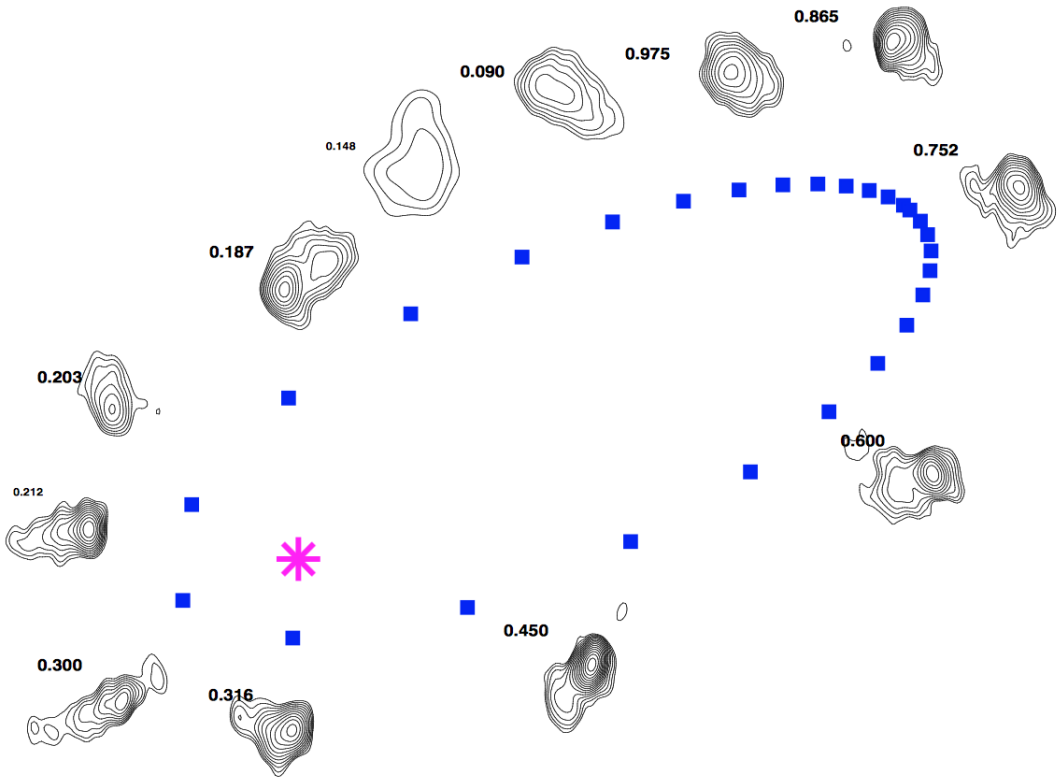

Figure 3.5: VLBA image of LS I +61° 303 at 8.3GHz sampling entire orbit. The cometary tail-like structure pointing away from the central giant star reproduced as strong evidence for binary pulsar model. Blue squares are location of compact object one day apart, magenta star is location of Be star. The orbit is exaggerated to fit all images, figure reproduced from (*122*).

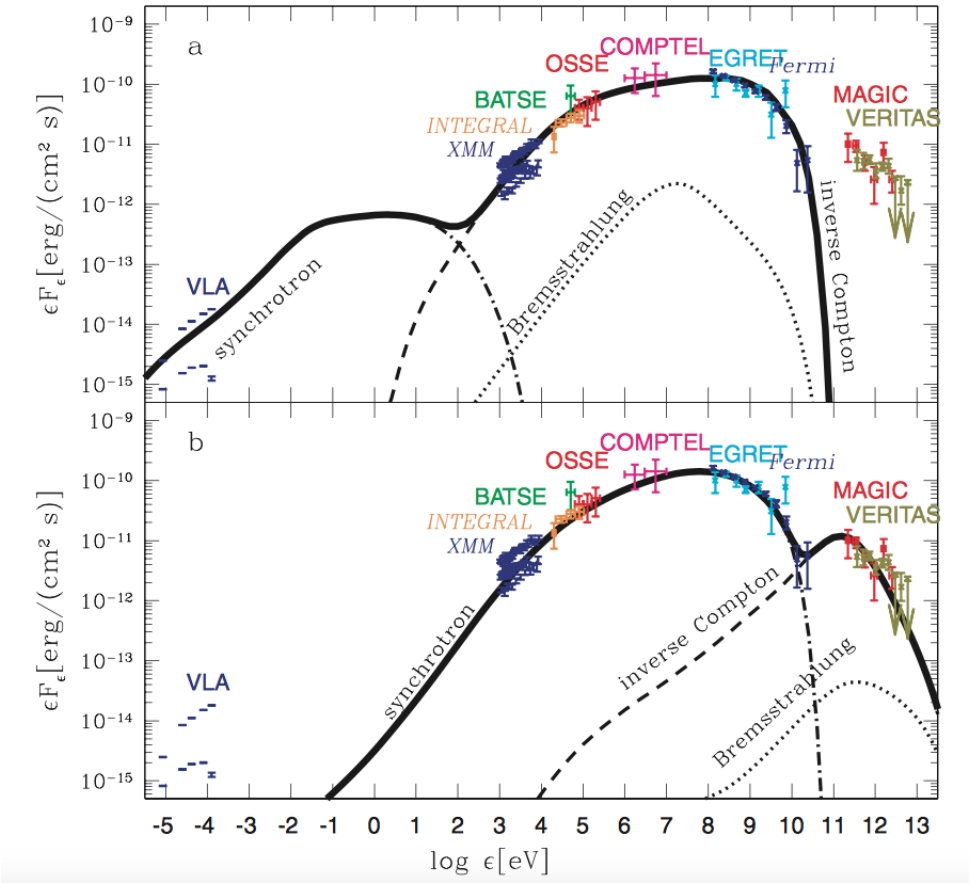

Figure 3.6: Model spectra of LS I +61° 303 overlaid with observed data. Solid line represents sum of individual spectral components in dashed, dot-dashed and dotted curves. *Top*: Model where X-ray dominated by IC processes *Bottom*:Model where X-ray dominated by synchrotron process. Figure reproduced from (*120*).

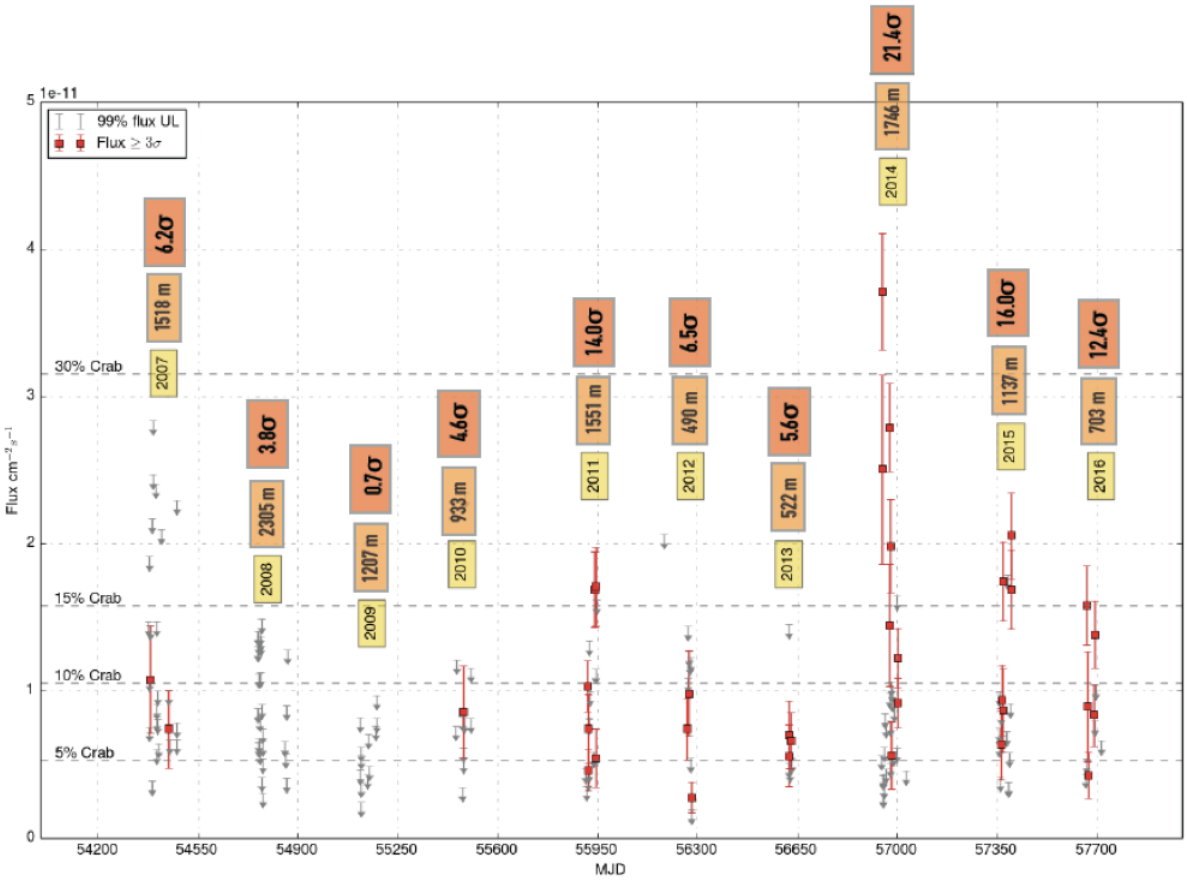

Figure 3.7: TeV lightcurve of LS I +61° 303 September 2007 - December 2016.

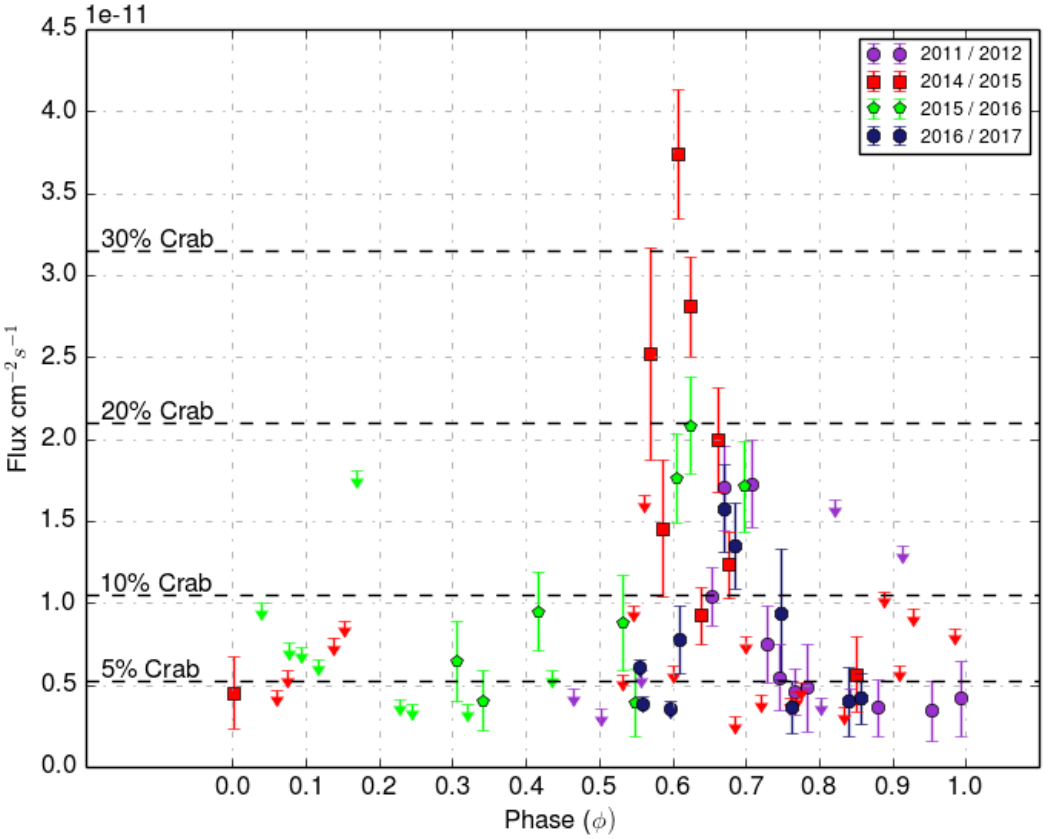

Figure 3.8: Phase binned fluxes from LS I +61° 303 during the 4 flaring season, 2011/2012 in black, 2014/2015 in red, 2015/2016 in green, and 2016/2017 in blue.

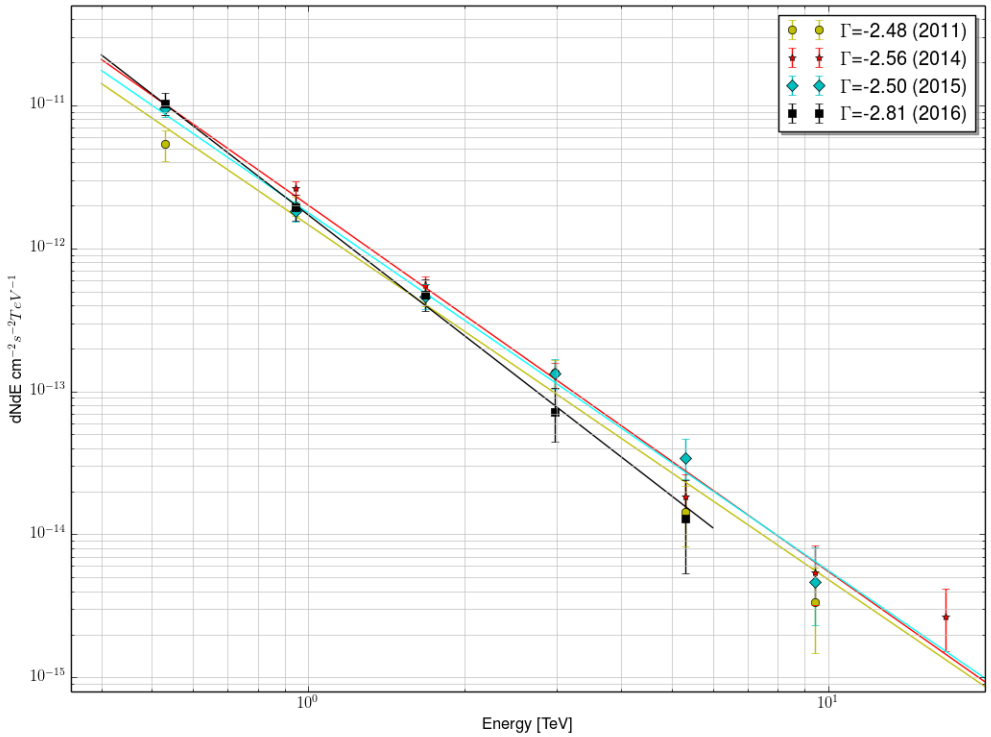

Figure 3.9: TeV spectral energy distributions for years 2011, 2014, 2015, and 2016.

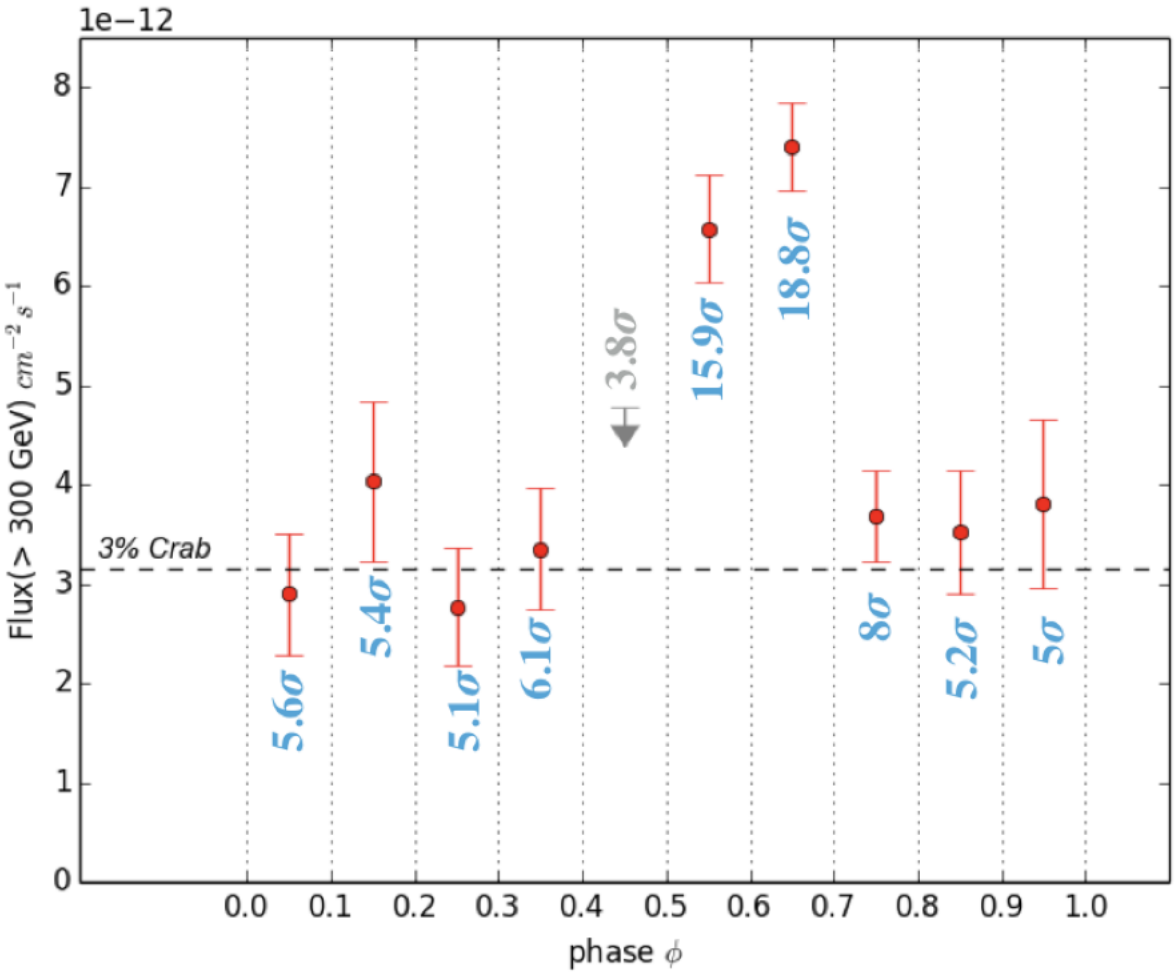

Figure 3.10: Phase binned flux of LS I +61° 303 for decadal data.

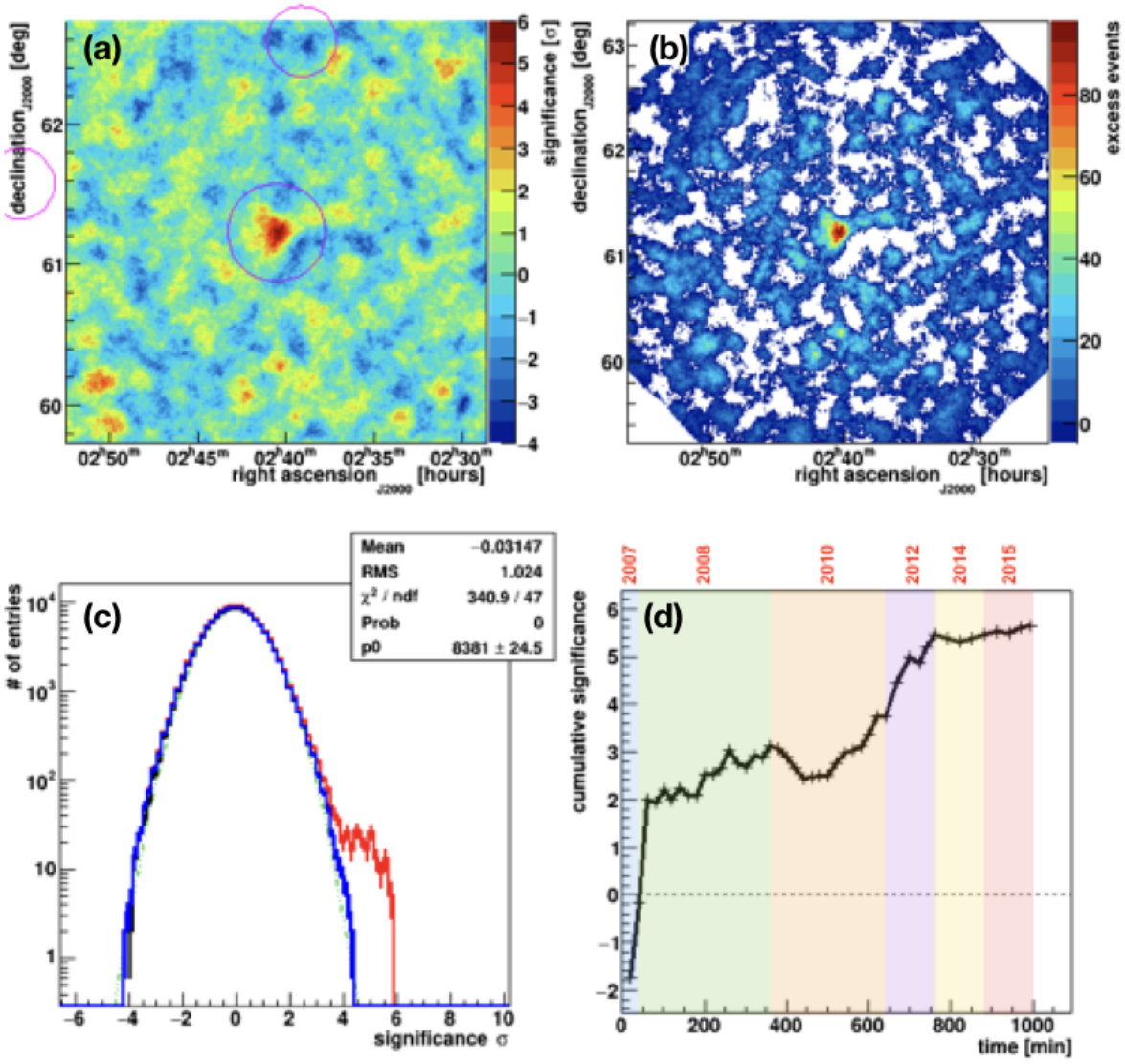

Figure 3.11: Results for phase $\phi = 0.0 \rightarrow 0.1$ (a)Significance skymap (b)Excess map (c)Significance distribution (d) Cumulative significance.

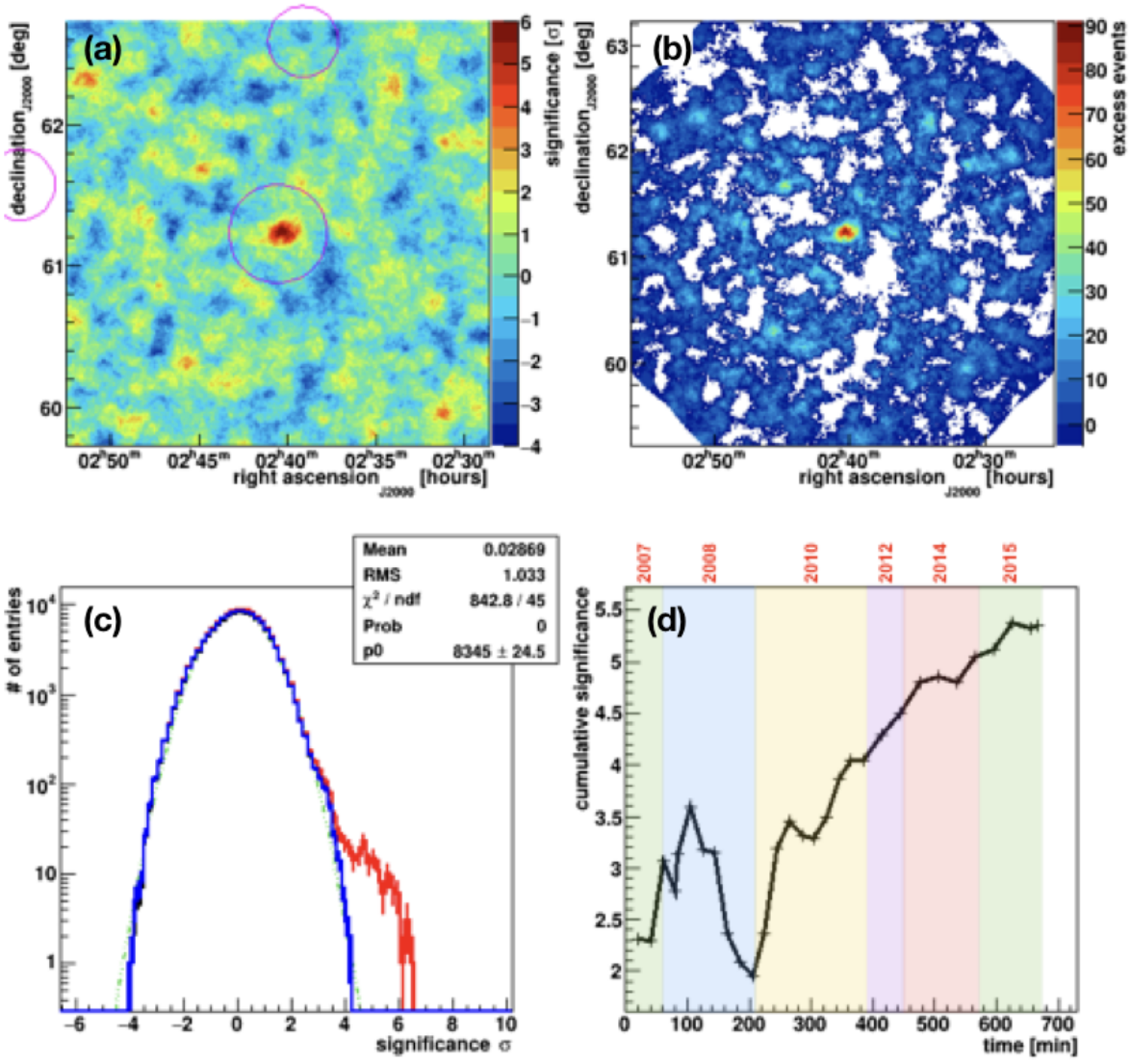

Figure 3.12: Results for phase $\phi = 0.1 \rightarrow 0.2$ (a)Significance skymap (b)Excess map (c)Significance distribution (d) Cumulative significance.

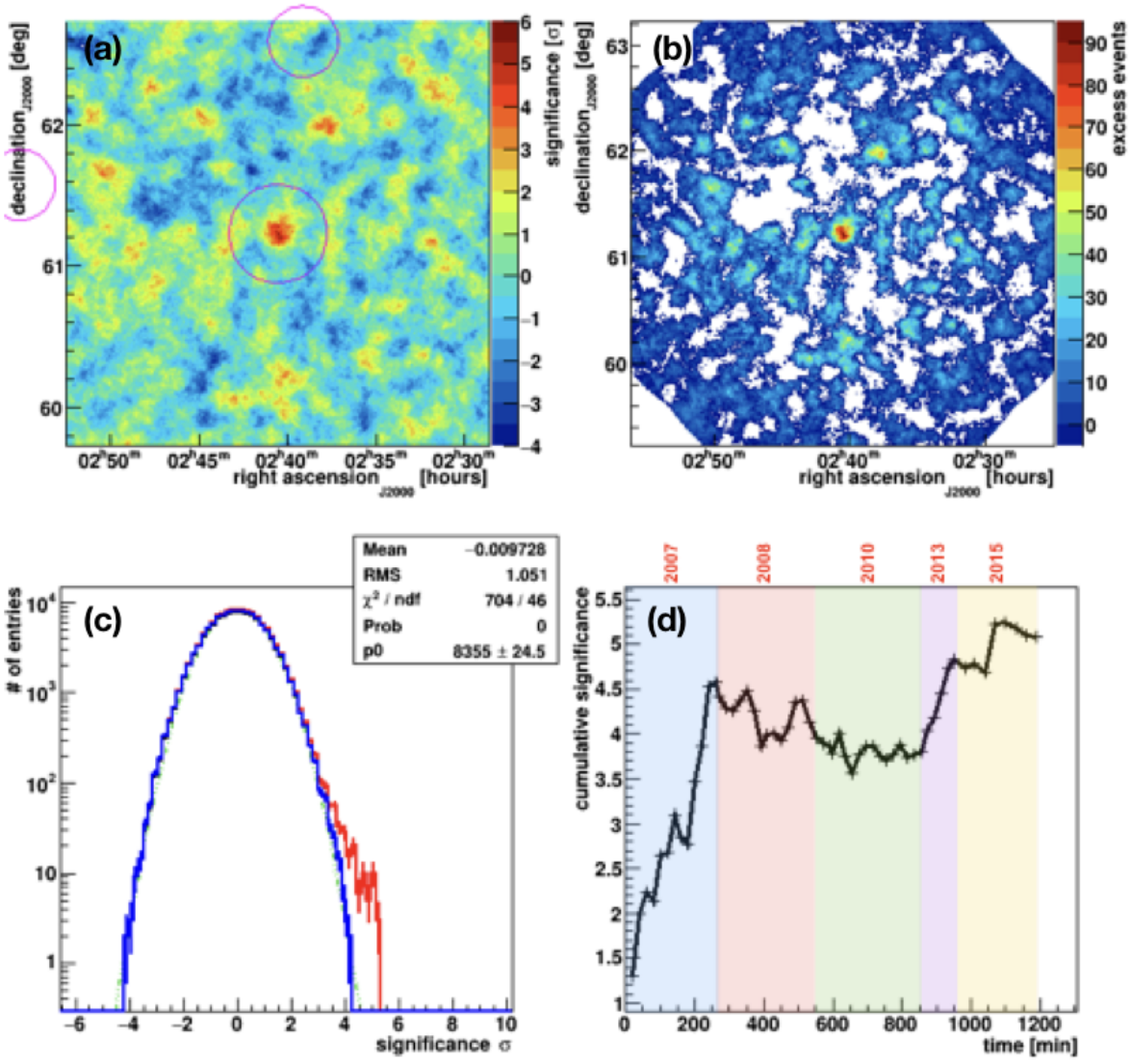

Figure 3.13: Results for phase $\phi = 0.2 \rightarrow 0.3$ (a)Significance skymap (b)Excess map (c)Significance distribution (d) Cumulative significance.

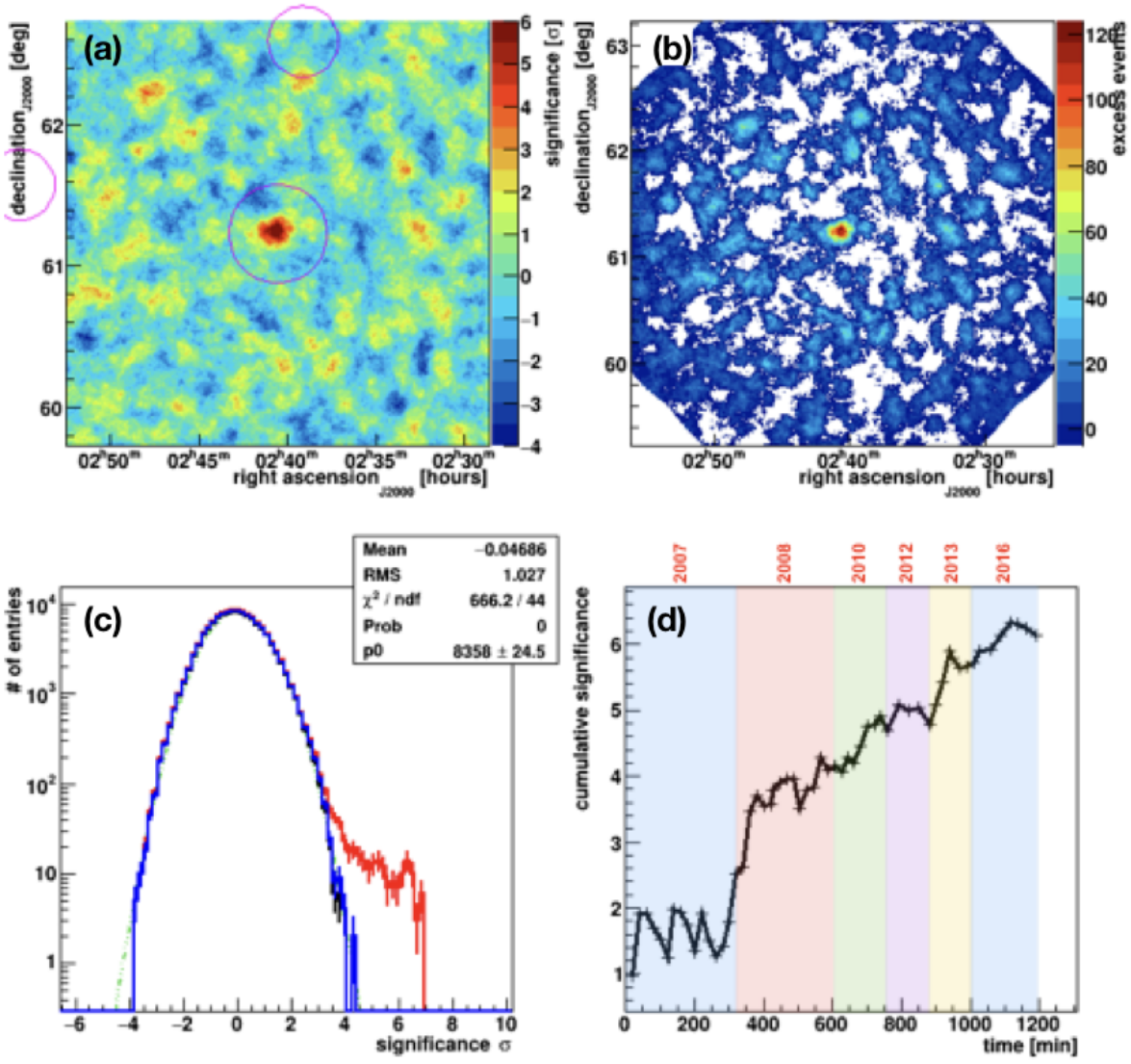

Figure 3.14: Results for phase $\phi = 0.3 \rightarrow 0.4$ (a)Significance skymap (b)Excess map (c)Significance distribution (d) Cumulative significance.

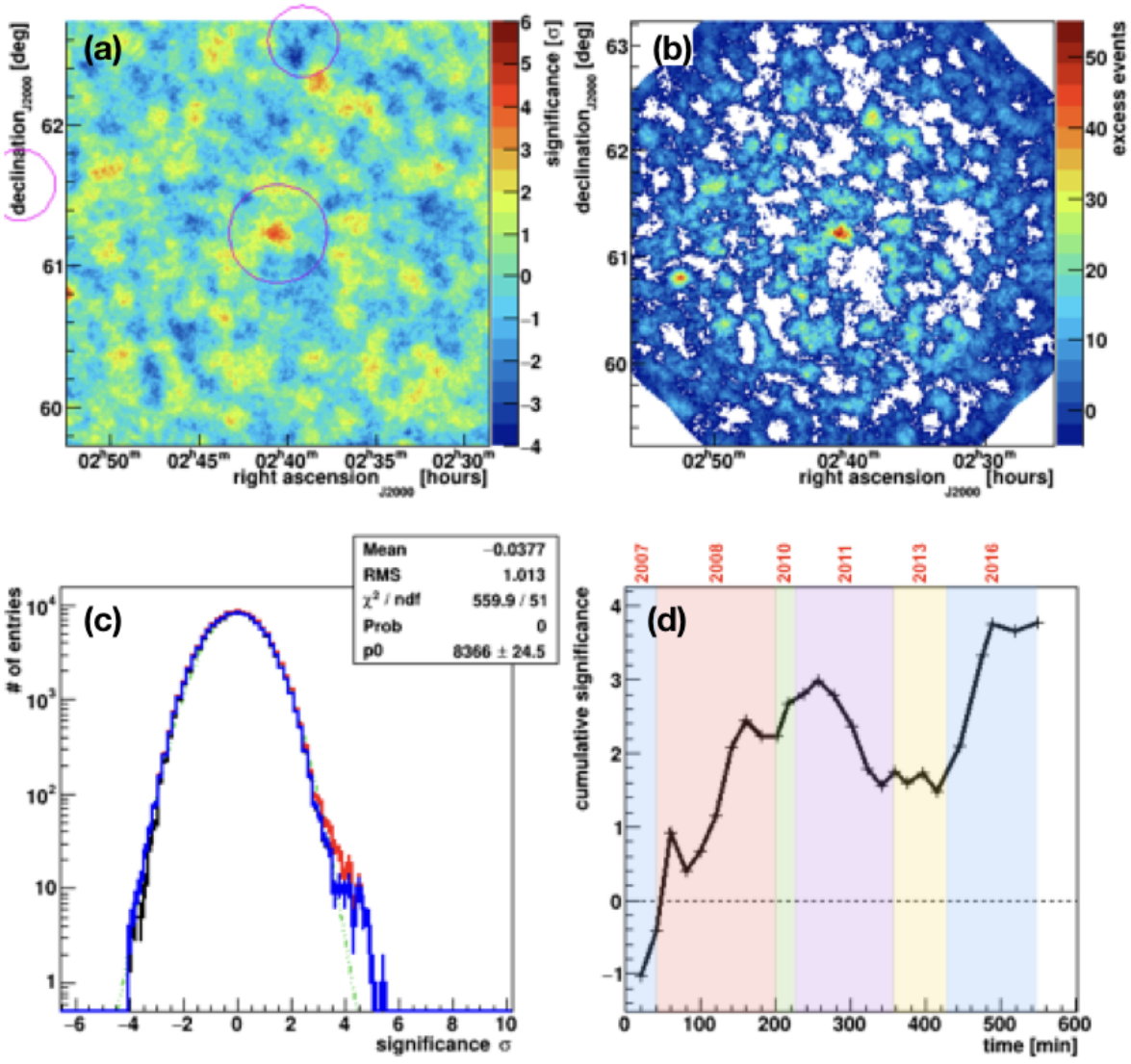

Figure 3.15: Results for phase $\phi = 0.4 \rightarrow 0.5$ (a)Significance skymap (b)Excess map (c)Significance distribution (d) Cumulative significance.

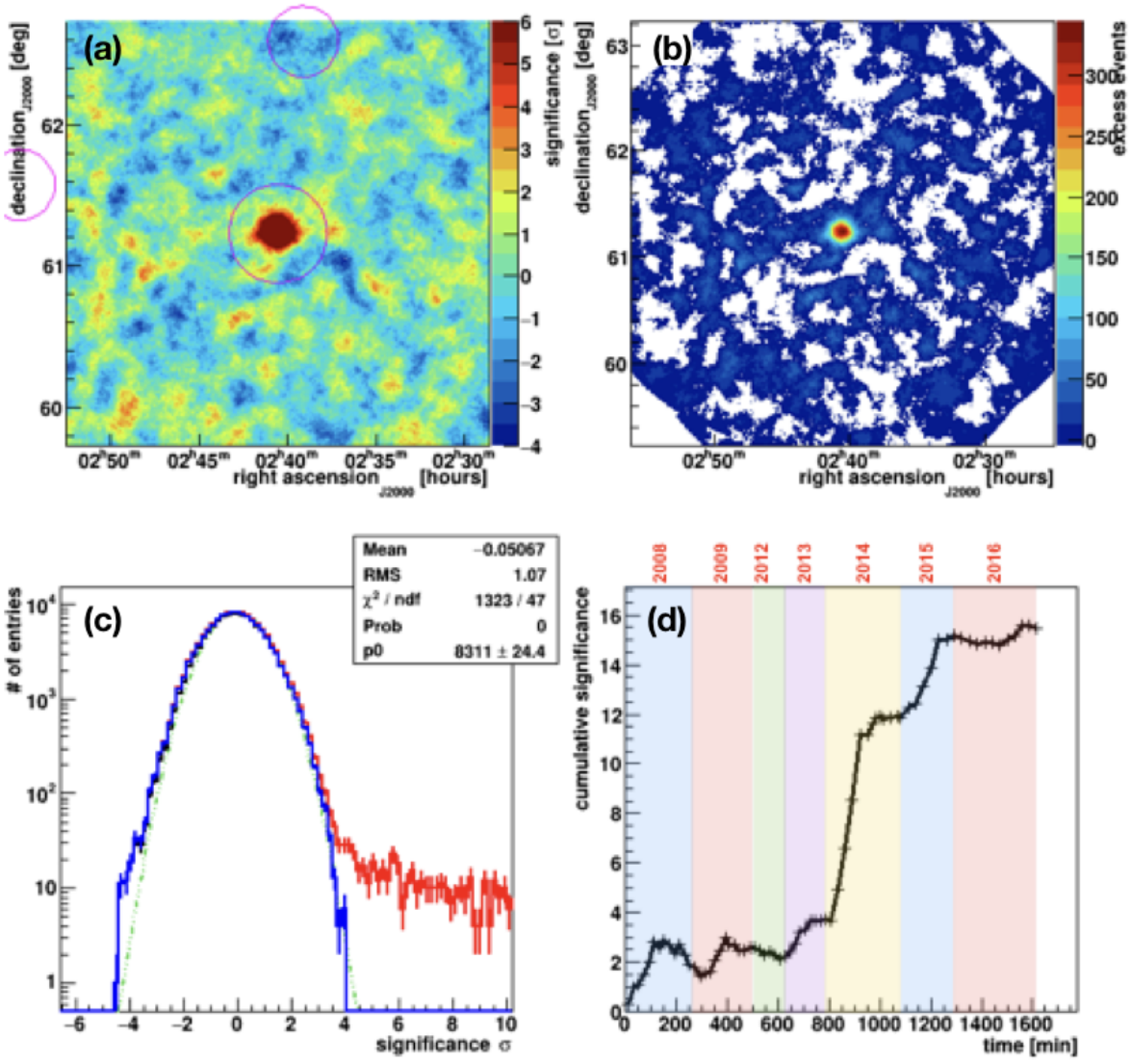

Figure 3.16: Results for phase $\phi = 0.5 \rightarrow 0.6$ (a)Significance skymap (b)Excess map (c)Significance distribution (d) Cumulative significance.

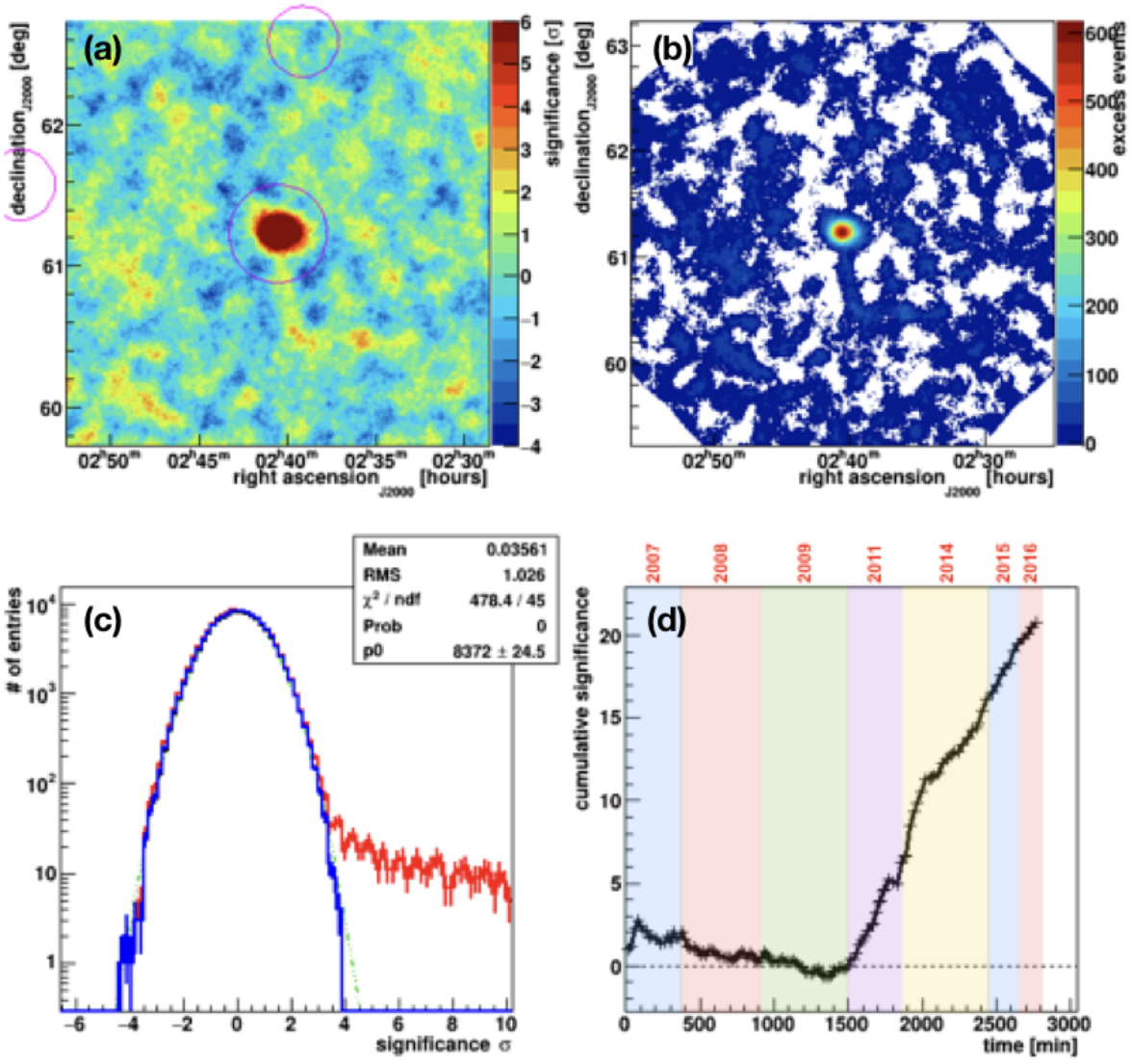

Figure 3.17: Results for phase $\phi = 0.6 \rightarrow 0.7$ (a)Significance skymap (b)Excess map (c)Significance distribution (d) Cumulative significance.

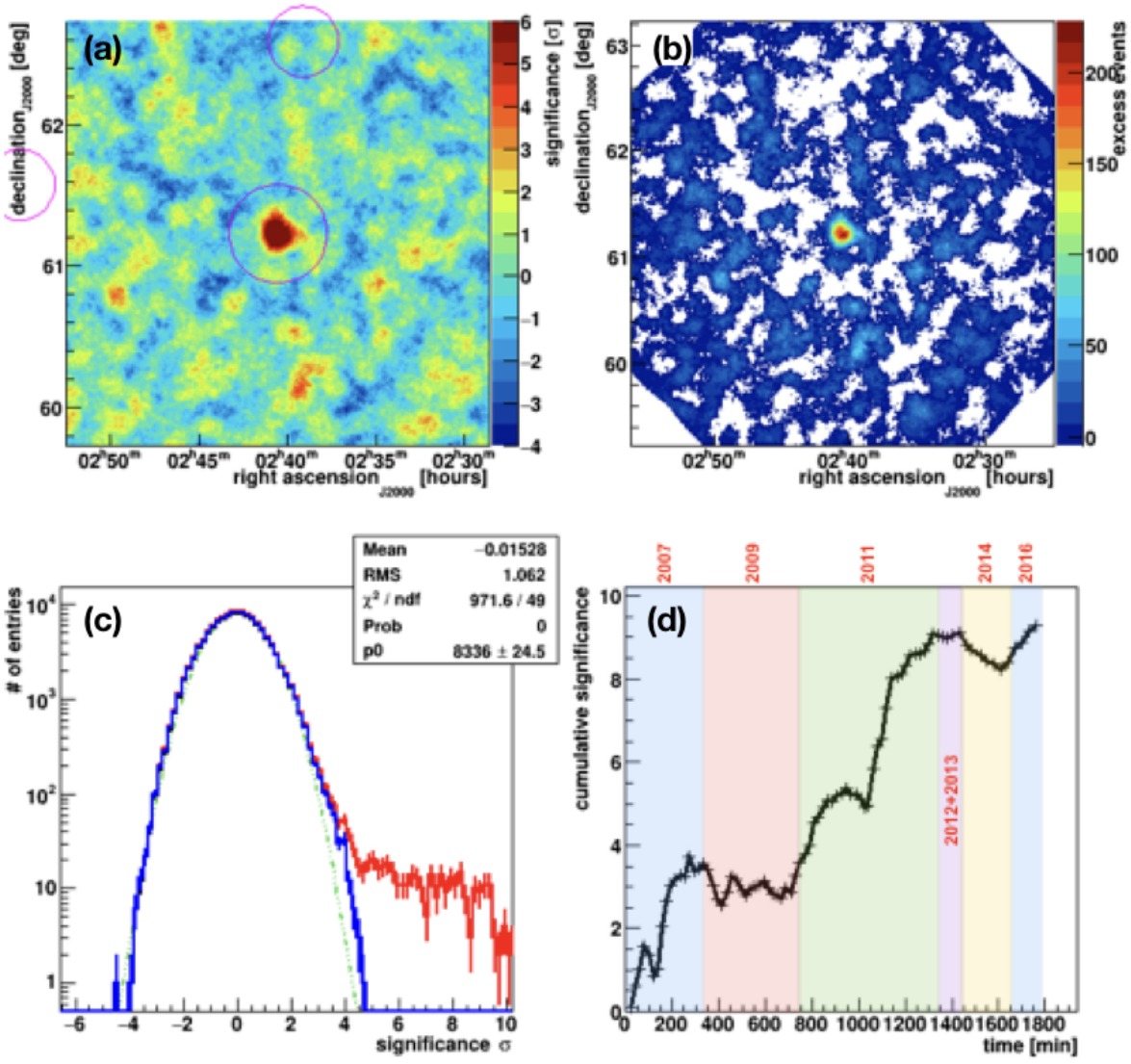

Figure 3.18: Results for phase $\phi = 0.7 \rightarrow 0.8$ (a)Significance skymap (b)Excess map (c)Significance distribution (d) Cumulative significance.

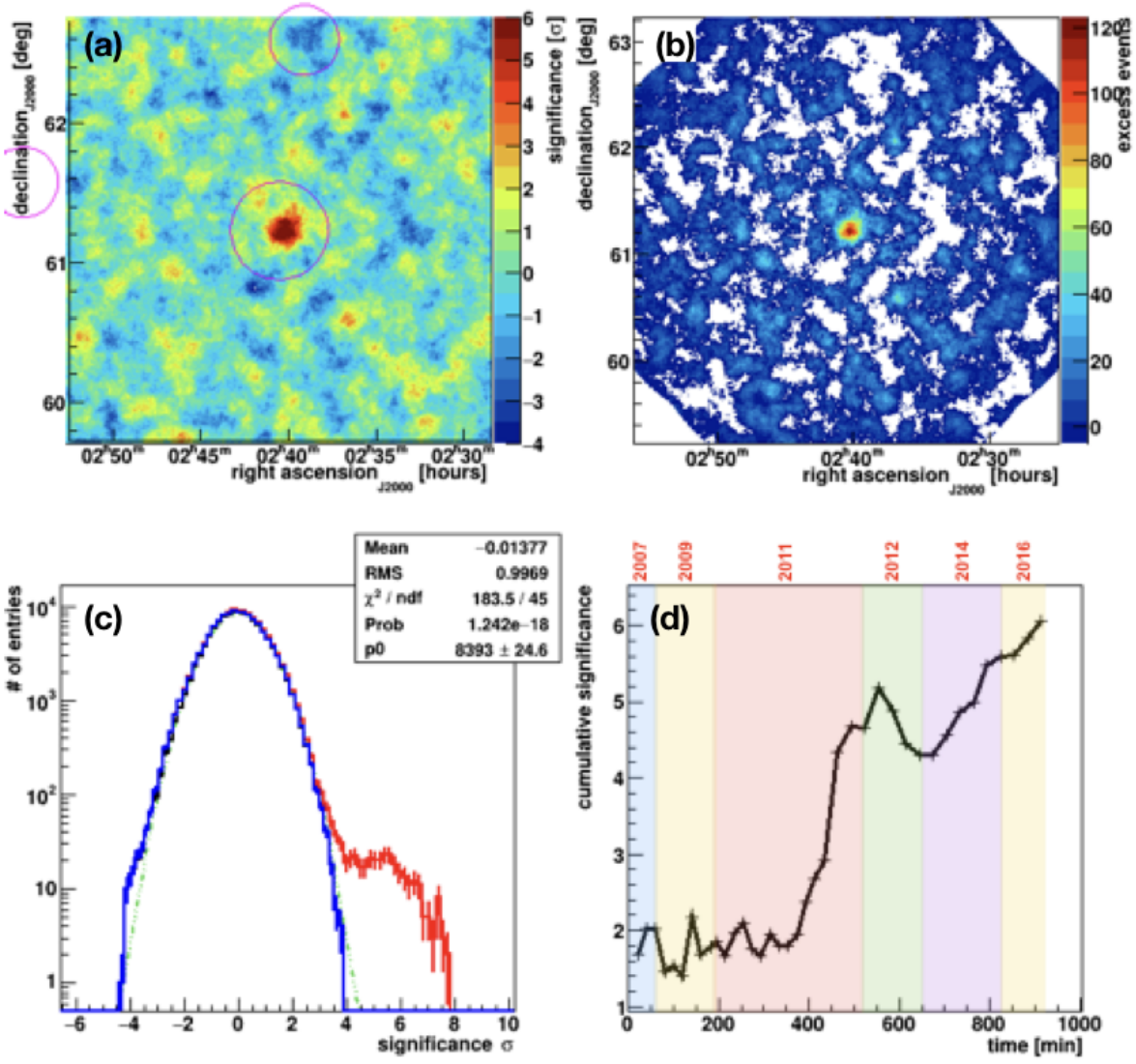

Figure 3.19: Results for phase $\phi = 0.8 \rightarrow 0.9$ (a)Significance skymap (b)Excess map (c)Significance distribution (d) Cumulative significance.

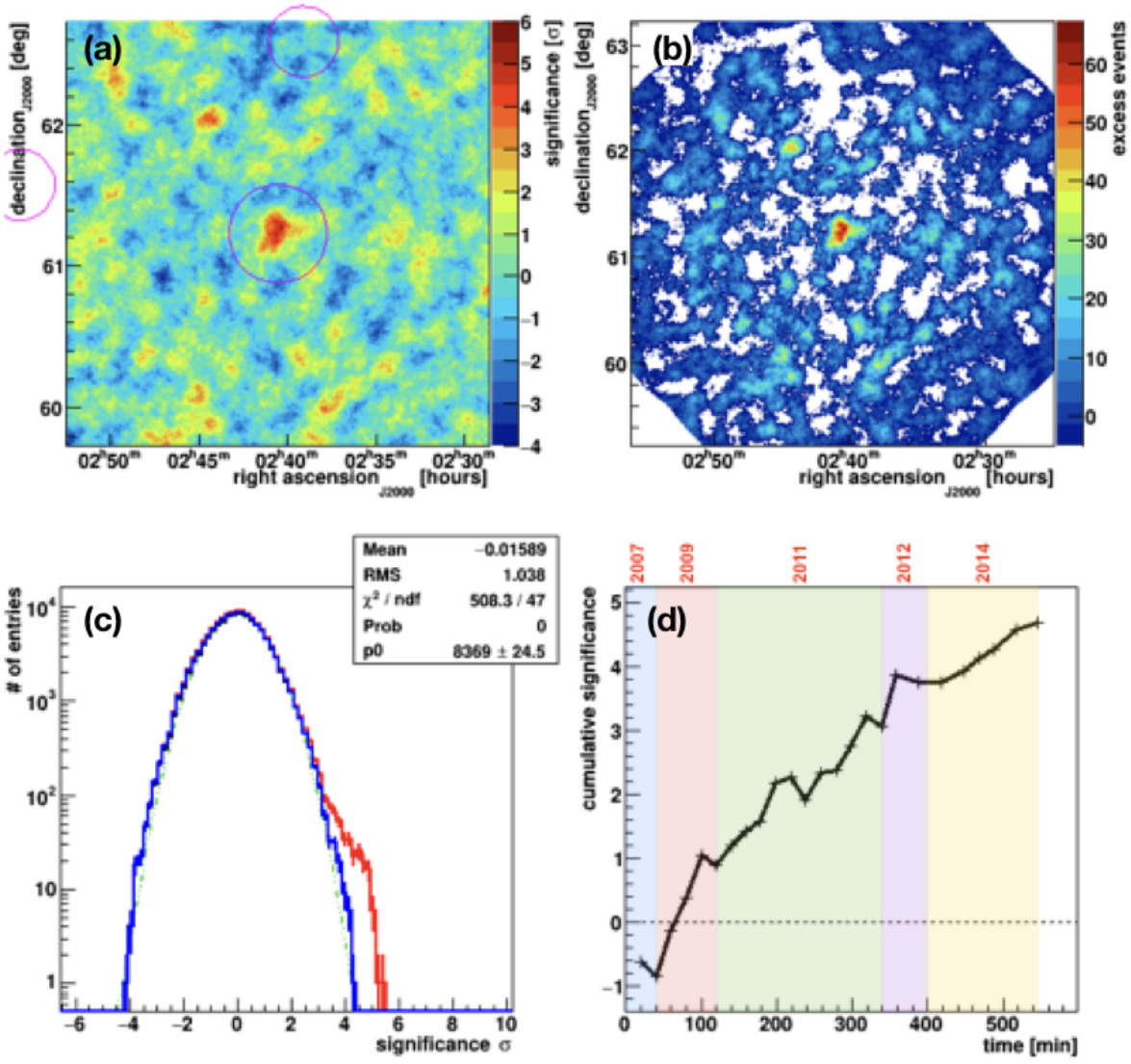

Figure 3.20: Results for phase $\phi = 0.9 \rightarrow 1.0$ (a)Significance skymap (b)Excess map (c)Significance distribution (d) Cumulative significance.

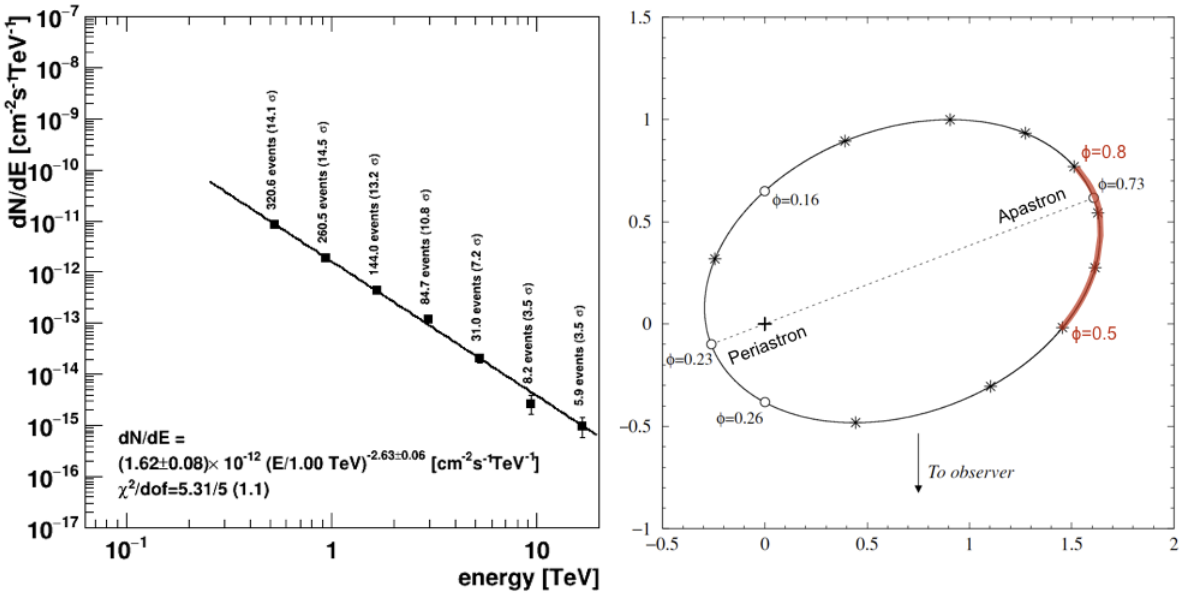

Figure 3.21: SED of apastron passage for phase 0.5 → 0.8 on *left*, the part of the orbit is marked on the figure on the *right* from (92).

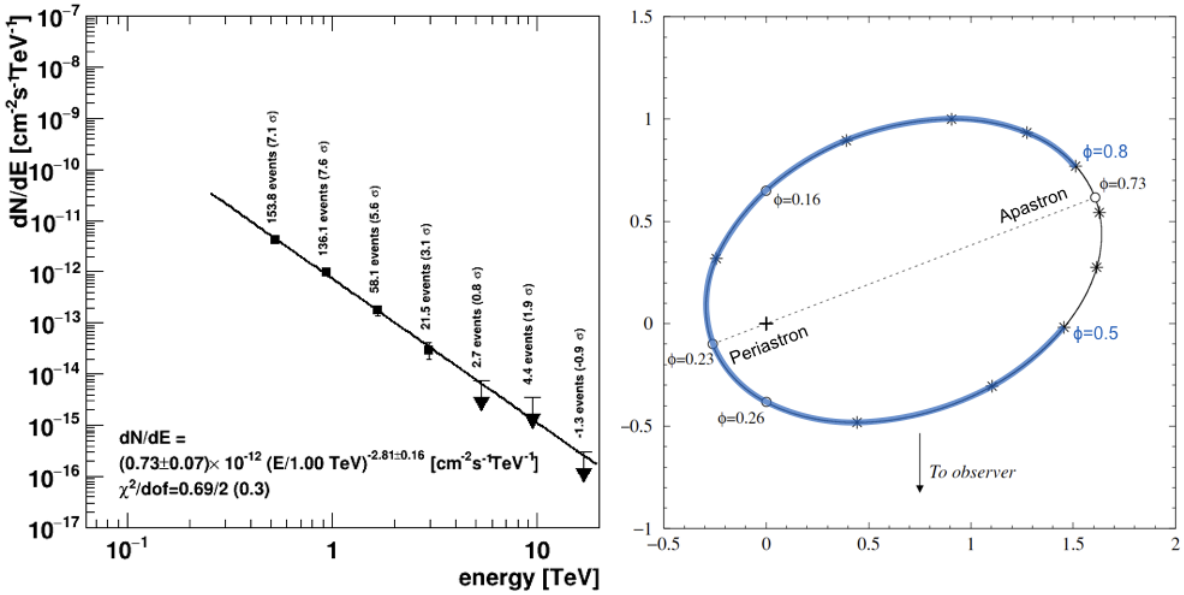

Figure 3.22: SED of periastron passage for phase 0.8 → 0.5 on *left*, the part of the orbit is marked on the figure on the *right* from (92).

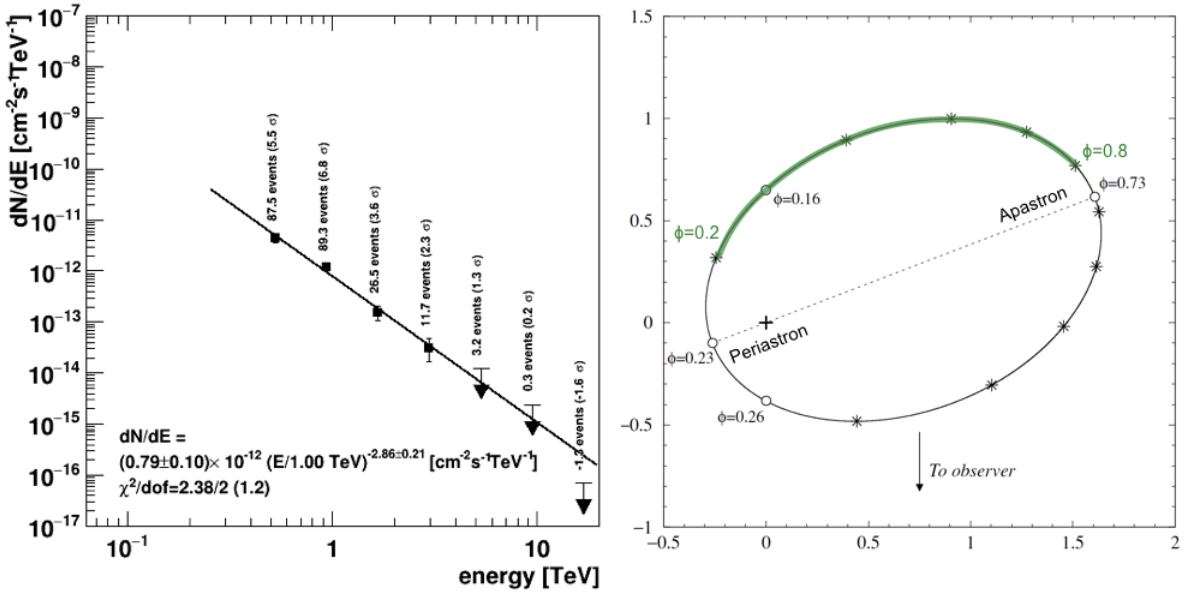

Figure 3.23: SED of periastron passage just before closest approach for phase 0.8 → 0.2 on *left*, the part of the orbit is marked on the figure on the *right* from (*92*).

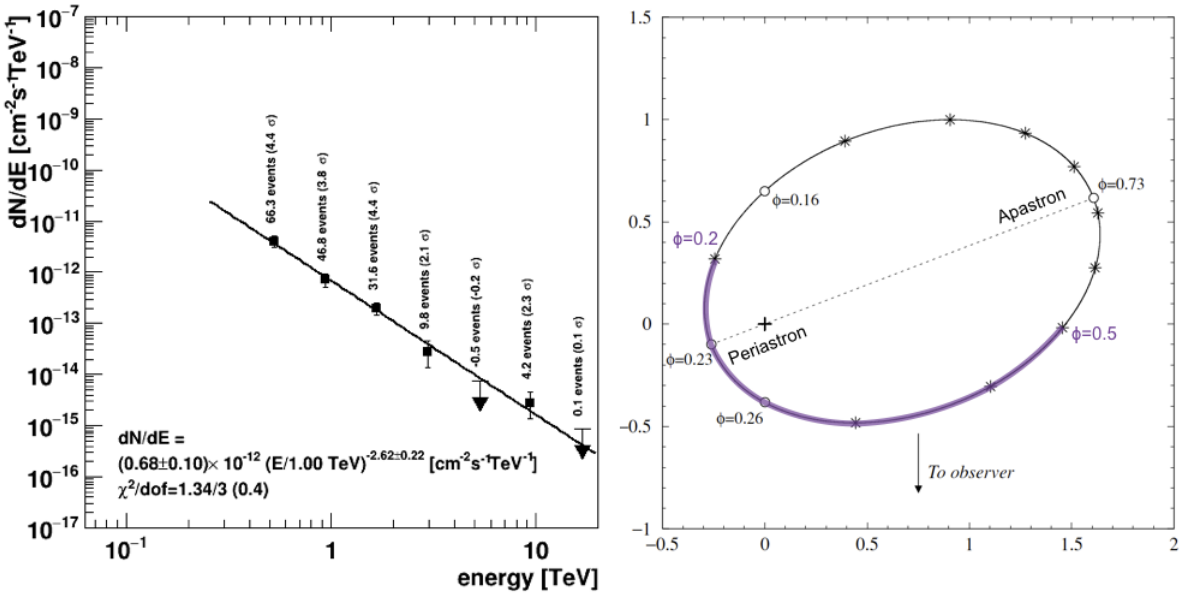

Figure 3.24: SED of periastron passage Just after closest approach for phase 0.2 → 0.5 on *left*, the part of the orbit is marked on the figure on the *right* from (*92*).

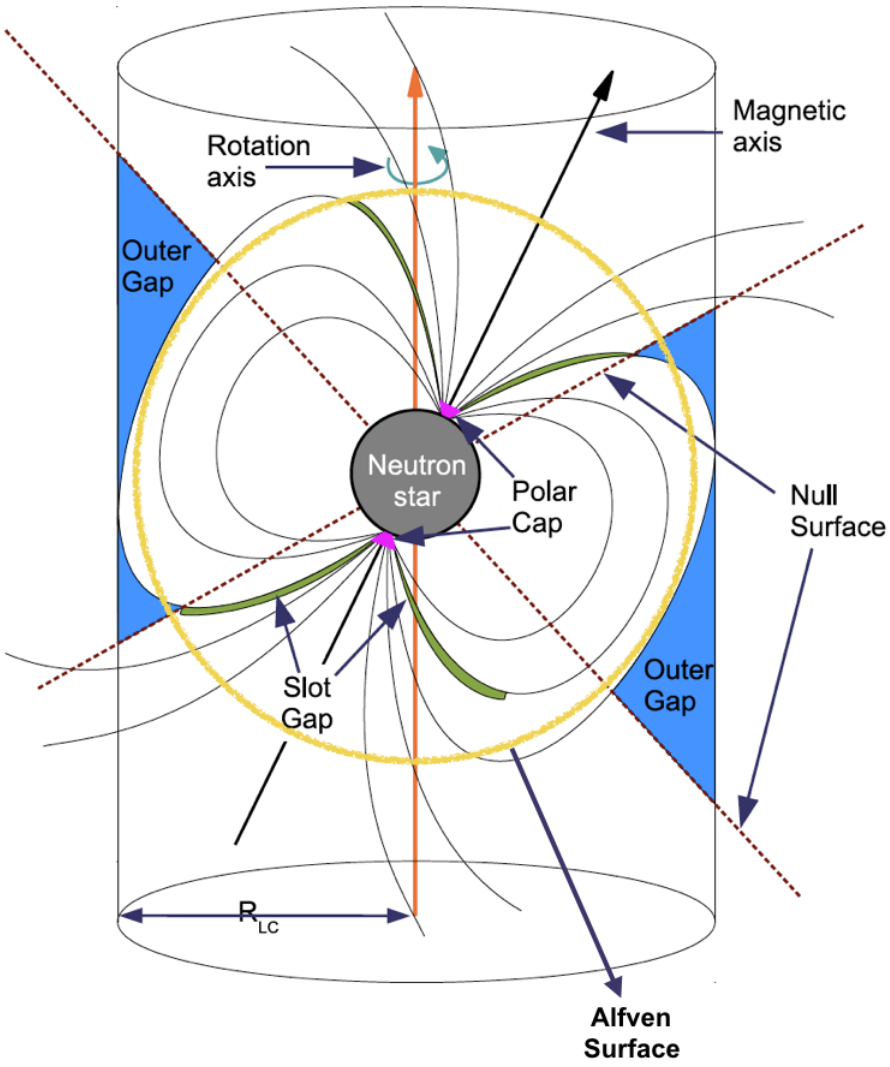

Figure 3.25: Diagram of emission zones of a pulsar. The last closed magnetic field line defines the boundary of the light cylinder of radius R_{LC}. Surface of the sphere centered at the pulsar with radius R_{LC} is known as the Alfvén surface. Figure modified from (*46*).

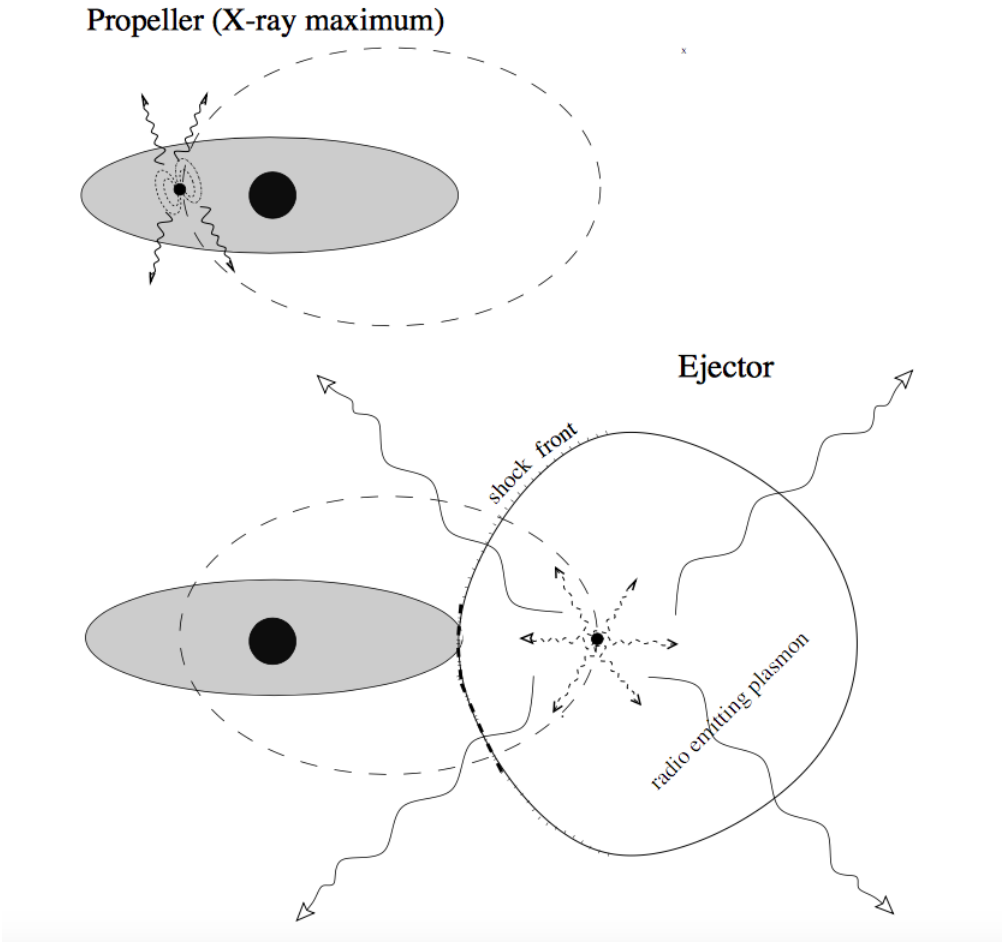

Figure 3.26: The Ejector-Propeller flip-flip model for LS I $+61^{\circ}$ 303 , dashed ellipse represent the orbit of the neutron star and shaded ellipse is the equatorial disc of the Be star. Figure adapted from (*149*).

CHAPTER 4

LS I +61°303: A MULTIWAVELENGTH CORRELATION STUDY

Emission from LS I +61° 303 extends from low radio frequencies of 150 MHz (*155*) to more than 13 TeV at gamma rays (*139*). Only a handful of galactic sources the emit over the entire electromagnetic spectrum. The cosmic interplay of a fast rotating Be star and its companion compact object (CO) drives the thermal and nonthermal emission from this binary system. The 26.5 day orbit of the CO around the massive star modulates emission at radio (*93*), infrared (*156*), optical (*157*, *158*), X-ray (*159*), HE gamma-ray (*160*), and VHE gamma-ray (*98*, *99*) wavelengths. A second important period associated with this system is 1667 days, known as the super-orbital period and its modulation effects are also seen at radio(*155*), X-ray(*151*, *161*), HE gamma-ray (*162*), and VHE gamma-ray (*163*) wavelengths. A brief overview of important characteristics of LS I +61° 303 brought to light by observations in different wavebands are presented in the following section followed by observations, results and their implications from multiwavelength campaign performed by VERITAS and its partners *Fermi* Gamma-Ray Space Telescope and *Swift* X-ray Telescope.

4.1 Multiwavelength Picture of LS I +61° 303

The variable nature of LS I +61° 303 was discovered in 1978 by the NRAO 91m transit telescope (*164*) and was suggested as a counterpart of CG135+1, one of the ten unidentified the gamma-ray sources discovered in the previous year by the Cos B satellite (*165*). Although no optical variability was initially found, it gradually became clear that this high mass X-ray binary has a highly periodic nature and its variability ranges on the timescales of a few hours to a few years. In the following subsections, we look at some of the major conclusions backed by observational data in multiwavelength.

4.1.1 Radio Observations

Decades of radio observations of LS I $+61^\circ$ 303 have helped narrow down the geometry of the system and other parameters associated with it. The orbital and superorbital phase $\phi = 0$ was set at $T_0 = MJD43366.775$ for historical reasons when the source was first detected at radio wavelengths (*95*). A mass constraint for the optical giant star is 10 - 15 $M_\odot$ with the inclination $25^\circ \lesssim i \lesssim 60^\circ$ for a neutron star and $i \lesssim 25^\circ$ for a blackhole (*92*). Spectral line radio observation places LS I $+61^\circ$ 303 at a distance of $2.0 \pm 0.2 kpc$ with a total line-of-sight neutral hydrogen column density of about $10^{22}\ cm^{-2}$(*166*). The orbital period was also precisely defined from radio observation P_{orb}= (26.4960 $\pm$ 0.0028) days by (*95*) and so was the superorbital period P_{sup}= (1667 $\pm$ 8) days. A third period P_{pre}= 26.92 $\pm$ 0.07 was associated with the binary system which was claimed to be the precessional period of the μQ jets (*109*). Using these three periods obtained P_{orb}, P_{pre} and $P_{sup}$from various radio observations, an intriguing theory of astronomical beats was presented which assert that the system harbors a μQ with dual precessing jets. See Section 3.2.1 for theories supporting the μQ model for this sources from radio observations. Ten images from observations made at 3-day intervals covering the 26.5-day orbit of the binary with VLBA revealed an elongated 'tail'-like structure pointing away from the optical star. The rapid morphology change at periastron of radio emission resolved at AU scales slows down at apstron was interpreted as the wind of the pulsar supporting the neutron star model. Details of the above model and other theories supporting the NS model are discussed in Section 3.2.2. Despite extensive searches, no pulsations have been found at radio wavelengths from LS I $+61^\circ$ 303 (*115*).

Using 36.8 years of radio data shown in top panel of Figure 4.1, two new periods were found, $P_{average} = 26.704 \pm 0.004$ days was seen to fit the periodic radio outburst data modulated by $P_{long} = 1628 \pm 49$ days where $P_{average}$ is the average of the P_{orb} and P_{pre}. P_{long} and $P_{average}$ were the beat frequencies of P_{orb} and P_{pre}. A synchrotron emission model for μQ with precessing jets was able to reproduce the multiple periodicities observed over 36.8 years of observations. In the bottom panel of Figure 4.1, the model data points in red are fitted to entire radio data shown in the top panel. For more details on the astronomical beat phenomenon for LS I $+61^\circ$ 303 , refer to Section 3.2.1 and (*106*).

4.1.2 Optical and Hα Observations

The optical star in LS I $+61^{\circ}$ 303 also exhibits light variation which follows the radio light curve (*167*). The amplitude of the optical light curve was 0.1 magnitude with errors bars a decade smaller indicative of definite variation. The maximum of optical light was found to occur as phase $\phi = 0.6$ decaying to half the maximum intensity in 2 days. The correlation between radio and optical variability was tied to the accretion model suggested in (*168*)

The 26.5 day orbital period (P_{orb}) was detected in the Hα emission as was the superorbital period of $\sim$ 4.5years (P_{sup}) (*169*) pointing to a relation with the evolution of circumstellar disc. The correlation between Hα peak seperation ΔV and equivalent width (EW) is given by

$$log\left[\frac{\Delta V}{2v\ sini}\right] = -a\ log\left[\frac{EW(H\alpha)}{\mathring{A}}\right] + b \tag{4.1}$$

where the constants $a \simeq 0.4$ and $b \simeq -0.1$ for EW(Hα)$> 3\mathring{A}$ and $v\ sini$ corresponds to projected rotational velocity. Dense envelopes could require b = +0.2. Assuming $v\ sini =$ 360 km s^{-1} for LS I $+61^{\circ}$ 303 , a plot of $log(\Delta V/2v\ sini)$ against EW(Hα) is shown in Figure 4.2.

Best fit to the data is depicted as solid black line corresponding the a = 0.38 and b = 0.07 and the average behaviour of Be stars and their upper limits in dashed lines. The plot clearly shows the circumstellar disc of LS I $+61^{\circ}$ 303 is much denser than average Be stars (almost double). The disc is probably also smaller in size than isolated Be stars, as it would be tidally truncated by the wind of the neutron star in tight orbit.

According to the authors in (*169*) the $P_{pre} \simeq$ 4.5 years is an intrinsic characteristic of the optical star related to its mass loss rate which, in turn, affects the mass accretion rate onto the neutron star. The changing accretion rate onto the magnetosphere of the neutron star alters the position of the shockfront and alters. The ejector-propeller model explains the shift in radio peak based on the changing accretion rate. When the mass loss rate is lower the ejector scenario occurs earlier, consequently, this intiates an earlier radio outburst than when the mass loss rate is higher.

4.1.3 X-ray Observations

The X-ray counterpart of LS I $+61^\circ$ 303 was first identified by *Einstein* Observatory in 1981 (*170*). No variability was observed but its low X-ray luminosity compared to high gamma-ray luminosity did not go unnoticed. The possibility of an extra power source - a young pulsar associated with the giant star was theorized. The variable nature was of the source was discovered by ROSAT followed by ASM/RXTE (*159*, *171*). The skymap of LS I $+61^\circ$ 303 is seen on the left panel of Figure 4.3 with a quasar in the field of view. The X-ray flux from LS I $+61^\circ$ 303 peaks in the phases range $\phi = 0.35 - 0.75$ along the superorbital period, routinely leading the peak radio flux by $\Delta\phi = 0.2$. The right panel of Figure 4.3 shows the light curve from Swift / BAT at hard X-ray wavelengths (15-150keV). *INTEGRAL* (18-60keV) and *Swift/BAT*(15-150keV) both found superorbital variability in the hard X-ray energy band and a power-law spectrum with no high-energy cutoff (*172*, *173*).

Temporal analysis using the Lomb-Scargle periodogram technique revealed a third period of 26.93 days in the X-ray data that was previously seen in radio data. This period was interpreted as the jet precession period (P_{pre}) of the LS I $+61^\circ$ 303 microquasar (*111*). Fast flux variations are seen at X-ray wavelengths from *Chandra* data where the count rate varies by $\sim$ 25% within a timescale of few hours (*174*).

Perhaps one of the most interesting X-ray events seen from LS I $+61^\circ$ 303 was a magnetar-like short burst lasting only 0.2 - 0.3 s that was detected by Swift-BAT (*128*, *129*). The X-ray image using 165 ks data from Swift-XRT overlaid with error circle of the event from Swift/BAT is shown in Figure 4.4. Although a magnetar in binary association with a Be star is unprecedented, it is not an impossibility, and a flip-flop accretor - propeller model outlined in (*143*) might be a feasible model for the observed behavior. According to this model, the CO object flip-flops between an rotationally powered accretion regime during apastron passage to a propeller decretion regime during periastron passage. The possibility of a soft gamma repeater or a faraway line-of-sight magnetar could also be the origin of the event recorded by Swift/BAT, but the probability of these two rare galactic source types (TeV binary and a magnetar within 1.4") is extremely low. The probability of occurrence these two types of galactic sources within a few arcseconds of each other cannot be accurately calculated without further assumptions like the population distribution of

the sources and a total number of sources. Even with these assumptions, it would still be impossible to rule out a single chance probability of occurrence. So far no other X-ray sources have been found within the error circle.

4.1.4 GeV Observations

Observations of LS I $+61^\circ$ 303 from *Fermi Gamma Ray Space Telescope* within a few months from its 2008 launch, cleared up questions raised by observations by Cos B, EGRET and other previous observatories. Unambiguous modulated emission was seen by *Fermi*-LAT at GeV energies due to its orbital period $P_{orb} = 26.49$ days and 2CG 135+01 was clearly identified as the gamma-ray counterpart of LS I $+61^\circ$ 303 . The peak of the phase folded light-curve observed by *Fermi*-LAT was at phase $\phi = 0.3$ (*97*). The spectrum fits a power-law with an exponential cut-off at $\sim$ 6GeV. The orbit-to-orbit flux variability observed by *Fermi*-LAT around $\phi = 0.3$ was consistent with the interaction of the dynamic Be star wind with the CO. The modulation based on the superorbital period P_{sup}= 1667 days previously observed at radio and X-ray wavelengths was also established at GeV energies using *Fermi*-LAT data. A sinusoidal fit to the GeV flux variation in phases during apastron passage is extremely likely with a chance probability mostly less than 10^{-7}. The left panels of Figure 4.5, depicting the periastron passage phases ($\phi = 0.0 - 0.5$), do not demonstrate the superorbital modulation. The circumstellar disc of the Be star undergoes a quasi-cyclical expansion and shrinkage and the observed superorbital modulation was tied to this phenomenon. Both X-ray and GeV gamma-ray emission were enhanced around superorbital phase $\phi_{sup} = 0.2$ (see Figure 4.5), where maximum values of the Hα EW point towards the role of the Be star's disc. Inconsistent variability of the power spectrum found in the data also hinted at a quasi-cyclical evolution of equatorial decretion disk of the Be star (*162*).

Inverse Compton radiative processes are mostly likely driving the HE emission from LS I $+61^\circ$ 303 where stellar photons are upscattered to GeV energies by accelerated electrons originating near the compact object. Maximum flux should be expected where the density of seed photons are at a maximum (i.e., closest to the star at periastron) as seen in *Fermi*-LAT data. The cutoff that is seen at GeV energies could be due to a number of reasons such as radiative losses, changing energy profile of the accelerated electrons, pair

production on interaction with stellar photons, hadronic interactions of the photons during passage through the stellar disc, absorption, etc. Any of the above reasons could also help explain the phase mismatch seen in peak flux between HE and VHE wavebands where maximum flux occurs near apastron passage for the later. For details of observations and results in the GeV energy range described above see (*97*, *162*) and references therein.

4.1.5 TeV Observations

LS I $+61^\circ$ 303 was first discovered in the VHE energy range in 2006 by the MAGIC Collaboration and later confirmed by VERITAS (*98*, *99*). The source exhibits its highest VHE flux states just before apastron ($\phi = 0.775$) in the phase range $\phi = 0.55 - 0.65$. When it was first discovered the TeV peak flux was $\sim$ 15% of the Crab Nebula. In the following years in October 2008 - January 2010, the source was barely detected by MAGIC above 300GeV threshold at a 5.4% Crab Nebula flux level (*142*). During this same period the entire integrated VERITAS data set yielded a 3.3σ significance level for constant emission around the orbit, but surprisingly the source was detected at 5.6σ significance in the sections of data where the CO was approaching periastron near it inferior conjunction passage (*136*). This was contradictory to the binary's expected behavior of maximum flux near apastron. Nightly variability was seen be VERITAS during TeV outbursts in both 2011 and 2014 (*137*, *139*) with posttrials significances $\sim$ 4σ at a 99% confidence level. Although fast X-ray variability on $\sim$second timescales (X-ray flux doubling in 2 s) have been seen (*175*), such fast timescales are hard for current IACTs to detect photostatistics. These fast variabilities could be important observational tools to provide constraints on the size of X-ray/TeV emission zones (referred to as 'clumps' in the wind) for the neutron star model (see Section 3.2.2). The orbit-to-orbit variability measured by other wavelengths that are associated with the superorbital modulation was finally confirmed from MAGIC and VERITAS data (*163*). The sinusoidal fit to MAGIC and VERITAS data demonstrating the superorbital variability of TeV flux is shown in Figure 4.6.

The dynamic, complex variability of LS I $+61^\circ$ 303 makes it an ideal candidate for multiwavelength study by VERITAS. For the first time, our analysis has detected a correlation between X-ray and TeV emission over multiple orbits spanning several observational seasons. A detailed study of these observations is presented in the rest of this chapter.

4.2 VERITAS Observations and Data Analysis

The VERITAS observations used for this multiwavelength correlation study are a subset of the data set used in the previous chapter in Section 3.3. VERITAS made 19 simultaneous / contemporaneous observations with Swift during the 2014 - 2016 period. The results of the data analysis from dates corresponding to simultaneous / contemporaneous observations from Swift XRT are listed in Table 4.1. In this table, negative significance and negative flux arise from greater number off-counts in the background region than on-counts in the source region. The data is unevenly sampled mostly in the orbital phase range $\phi = 0.4 - 0.9$ from 7 different orbits of the binary.

4.3 Swift-XRT Observations and Data Analysis

The XRT is the focussing X-ray telescope for the Swift Gamma Ray Burst Observatory. Refer to Section 2.1.1 for details of the instrument and technical description. Swift has a flexible Target of Opportunity program which supports multiwavelength observations. VERITAS coordinated its observations with Swift XRT and obtained 19 simultaneous / contemporaneous data pairs which are used for the multiwavelength correlation study. The Swift XRT data are analyzed using the webtools available from the UK Swift Science Data Center [*]. X-ray light curves and spectra are constructed based on HEAsoft v6.16 package [†] available from NASA's HEASARC (High Energy Astrophysics Science Archive Research Center). The source spectrum for the complete data set is best fit by a simple power-law model with photoelectric absorption, shown in Figure 4.7. The soft X-ray spectral index is found to be $1.58^{+0.08}_{-0.07}$ with $\chi^2/n.d.f. = 0.953$ and neutral hydrogen density $n_H = (8.5 \pm 0.8) \times 10^{21}$ cm^{-2} . Analysis results of individual observations for dates corresponding to VERITAS observations are listed in Table 4.2. Photon index is found to vary between $1.31^{+0.28}_{-0.27}$ and $2.1^{+0.6}_{-0.5}$ with reduced-χ^2 varying in the range 0.657 to 1.004 for individual observations.

[*] http://www.swift.ac.uk/user_objects/

[†] https://heasarc.nasa.gov/lheasoft/

4.4 Fermi Observations and Data Analysis

The Large Area Telescope (LAT), the primary instrument on the Fermi Gamma-Ray Space Telescope has a large field of view ($>$ 2 sr, one fifth of the sky). *Fermi*-LAT continuously observes the sky, except during instrument calibrations. This makes *Fermi*-LAT an ideal instrument to track variable sources like LS I $+61^\circ$ 303 , as it acquires continuous data spanning its entire mission operation (beginning in 2008). For this correlation study, three intervals of *Fermi*-LAT data (10.16.2014 - 01.10.2015, 12.01.2015 - 01.14.2016 and 10.01.2016 - 11.23.2016), have been used. Each interval covers a corresponding VERITAS observing season. The corresponding MJD format for these intervals are 56946-57032, 57357-57401, and 57662-57715, respectively. The data are publicly available from Fermi Science Support Center website [‡] and analyzed using Fermi Science Tools v10r0p5. We used spacecraft file (pointing and livetime history) and events data file in Pass 8 data format corresponding to instrument response function 'P8R2_SOURCE_V6'. We selected these files for the above interval for a ROI 20° centered around coordinated of LS I $+61^\circ$ 303 , RA: 40.1319 Dec: 61.2293.

gtselect source class photons (option evclass=128) from both front and back of the spacecraft were selected (option evtype=3) within a radius of 10° from the position of LS I $+61^\circ$ 303 . Next, we used *gtmktime* to select Good Time Interval (GTI) data (time ranges when the data can be considered valid based on spacecraft parameters of pointing, livetime, etc.) contained in the spacecraft file. Time intervals when the ROI was observed at a zenith angle greater that 90° were excluded to eliminate contamination arising from the Earth's limb. The *gtlike* tool was used to perform maximum unbinned likelihood analysis for all the 3FGL catalog sources (gll psc v16.fit) that are within 20° of the ROI, the galactic diffuse emission (gll_iem_v06) and the isotropic diffuse emission (iso_P8R2_SOURCE_V6_v06). Parameters of all nonvariable sources 5° away from LS I $+61^\circ$ 303 were fixed to their 3FGL catalog values. For sources located within 5° of the ROI, the normalization parameter was left free and using a log-parabola spectral model (as prescribed in 3FGL catalog), the light curve of LS I $+61^\circ$ 303 with 1 day binning was constructed. The value of fluxes on the days corresponding to VERITAS observations along with their Test Statistic (TS) are listed

[‡]https://fermi.gsfc.nasa.gov/ssc/data/

in Table 4.3.

Spectral analysis was performed on the data for the first interval 10.16.2014 - 01.10.2015, (MJD 56946-57032) using the likeSED (a user contributed tool) from FSCC [§]. The spectral form of LS I $+61^\circ$ 303 was modeled by a power-law with exponential cutoff of the form

$$\frac{dN}{dE} = N_0 \left(\frac{E}{E_0} \right)^{\Gamma} \exp\left(-\frac{E}{E_{cut}} \right) \tag{4.2}$$

where N_0 is the normalization constant, E_0 is the scale factor of energy, Γ is the spectral index and E_{cut} is the cut-off energy. The best-fit parameters obtained from an unbinned likelihood fit are $N_0 = (9.5 \pm 3.1) \times 10^{-5}\ \gamma s\ \mathrm{MeV}^{-1}\mathrm{cm}^{-2}\ \mathrm{s}^{-1}$, $\Gamma = 1.97 \pm 0.05$ and $E_{cut} = 4.00 \pm 0.69$ GeV for $E_0 = 1$ MeV

4.5 Results of Correlation Studies

The nature of the compact object in LS I $+61^\circ$ 303 is debatable. Neither the microquasar model (see Section 3.2.1) nor the neutron star model (see Section 3.2.2) explain the observed variabilities across different wavebands. Decades of observations had made it clear that neither models can adequately fit all of the historical observations. In the absence of detected pulsations or accretion-like X-ray spectrum, simultaneous multiwavelength observations may help in establishing a comprehensive physical model for this source. The following sections discuss results and implications of the simultaneous/contemporaneous X-ray (using Swift XRT) and GeV (using *Fermi*-LAT) observations with VERITAS observations at TeV energies.

4.5.1 X-ray versus TeV Energies

The MAGIC telescope had first seen a correlation between X-ray and TeV fluxes in 2009 (*140*). From 6 overlapping observations with XMM Newton and 4 overlapping observations with Swift XRT, a correlation analysis was performed, deriving a Pearson correlation coefficient $r = 0.81^{+0.06}_{-0.21}$ from the entire data set. The correlation between TeV flux and X-ray flux (Figure 4.8, left) is well fit with a straight line function (seen as a solid black line on the plot) of the form,

$$\frac{F(0.3-10keV)}{10^{-12}\ erg\ cm^{-2}\ s^{-1}} = 12.2 + 0.71 \times \left[\frac{N(E>300GeV)}{10^{-12}\ \gamma s\ cm^{-2}\ s^{-1}} \right] \tag{4.3}$$

[§]https://fermi.gsfc.nasa.gov/ssc/data/analysis/user/

A similar correlation study done by VERITAS during the TeV outburst of 2011 with Swift XRT data did not reproduce the results from MAGIC Collaboration. X-ray fluxes from Swift XRT versus TeV fluxes from VERITAS (Figure 4.8, right) produced a Pearson correlation coefficient $r = 0.36 \pm 0.32$, consistent with unrelated datasets (*137*). At this point, it could not be ruled out whether the single-orbit MAGIC/XMM-Newton/Swift XRT correlation was a random coincidence or a one-time event. X-ray fluxes from LS I $+61^\circ$ 303 have a large intrinsic variability of $\sim$ 25% on hourly scales and may have significantly changed during the several hours of observations that were required by MAGIC to achieve reliable detections of the VHE flux. Hence, large uncertainties of VHE fluxes prevented this correlation to be firmly established.

The VERITAS measurement of the correlation between X-ray and VHE gamma-ray emission began in 2014 observing season, which was also the year when an exceptional flaring episode occurred in the VHE regime (*176*) (*139*). During this season, the highest VHE flux was recorded from LS I $+61^\circ$ 303 was observed $F_{TeV}(> 300\ GeV) = (37.726 \pm 3.9769) \times 10^{-12} \gamma s\ \mathrm{cm}^{-2}\ \mathrm{s}^{-1}$, nearly 30% of the flux from Crab Nebula with a corresponding X-ray flux of $2.8^{+0.6}_{-0.4} \times 10^{-11}$ erg $\mathrm{cm}^{-2}\,\mathrm{s}^{-1}$. A Pearson correlation coefficient of $r = 0.80^{+0.14}_{-0.38}$ was calculated from 12 simultaneous/contemporaneous observations jointly performed in 2014 by Swift XRT and VERITAS (*176*). During the 2015 - 2016 and 2016 - 2017 observing seasons, 4 and 3 joint VERITAS / Swift XRT observations were added to this data set, respectively, bringing the total to 19 simultaneous/contemporaneous X-ray/TeV observations. A plot of the entire VHE gamma-ray data set against the X-ray data set is seen in Figure 4.9. Here the data points from 2014 are in blue, the data points for 2015 in green, and the data points for 2016 in red. The plot also has data points from the MAGIC correlation plot (data points from the plot on the left in Figure 4.8) in yellow. The TeV/X-ray correlation is undoubtedly seen now over 7(8) orbits observed by VERITAS/VM (both VERITAS and MAGIC referred to VM from now on) spanning over multiple years.

The straight line fitted to the 19 joint VERITAS /Swift XRT observations has the form

$$\frac{F(0.3-10keV)}{10^{-12}\ erg\ cm^{-2}\ s^{-1}} = 12.36 + 0.5602 \times \left[\frac{N(E>300GeV)}{10^{-12}\ \gamma s\ cm^{-2}\ s^{-1}}\right] \tag{4.4}$$

The slope and intercept are 0.5951 and $13.46 \times 10^{-12} \gamma s\ \mathrm{cm}^{-2}\ \mathrm{s}^{-1}$respectively considering all VERITAS (19 data pairs) and MAGIC (10 data pairs) observations, well within errors of

the fitted parameters derived from the first correlation seen by MAGIC during the single orbit in 2007. The Pearson correlation for the joint VERITAS and Swift XRT data between 2014 - 2016 is $r = 0.756$ with a p value of 1.796×10^{-3} where p value is the probability that a $|r|$ larger than the calculated value would be produced from independent X-ray and TeV fluxes. Including the 10 XMM Newton / Swift XRT and MAGIC simultaneous observations improves the Pearson correlation coefficient to $r = 0.773$ with the p value of 8.916×10^{-7}.

Large uncertainties of flux value call for a further robust test for the strength of the correlation, which is done using the *z-Transformed Discrete Correlation Function* (ZDCF) (*177*). ZDCF determines the 68% confidence level intervals for the correlation coefficient from unevenly sampled data. The Fisher z-transform is calculated for the Pearson correlation coefficient as follows:

$$z := \frac{1}{2} ln \Big[\frac{1+r}{1-r} \Big] = arctanh(r) \tag{4.5}$$

Considering z to be normally distributed for the fluxes in TeV and X-ray independent of each other the standard error of z can be calculated by $1/\sqrt{N-3}$ where N is the number of observations. The confidence interval for z can be calculated as

$$z'_{\pm} = z \pm (criterion\ z) \times (standard\ deviation) \tag{4.6}$$

where criterion z corresponds to the desired confidence level (e.g., 1.96 for 95% confidence interval, 0.9945 for a 68% confidence interval). The limit $z'_{\pm}$ is converted back to the upper and lower bounds of the correlation coefficient using:

$$r_{\pm} = \frac{exp(2z) - 1}{exp(2z) + 1} = tanh(z'_{\pm}) \tag{4.7}$$

Using ZDCF for 68% confidence level interval on the VERITAS TeV data and the corresponding Swift X-ray data the uncertainties of the Pearson correlation coefficient is calculated to be $r = 0.756^{+0.09}_{-0.13}$. Extending the data set to include the MAGIC fluxes with corresponding XMM-Newton / Swift XRT X-ray, ZDCF for 68% confidence level interval gives $r = 0.773^{+0.07}_{-0.09}$. The uncertainties in the value of the correlation coefficient are significantly reduced compared to both the previous values found in MAGIC data (*140*) and VERITAS data (*176*).

The strong correlation seen between X-ray data (0.3-10keV) and VHE gamma rays ($>$ 300GeV) suggests that a common particle population may be responsible for both

the X-ray and TeV flared emission. Since VHE fluxes are from phases near the apastron passage (VHE flux is expected to suffer maximum absorption just before periastron (*178*)) where absorption is minimum coupled with unabsorbed X-ray fluxes, models suggesting variable absorption mechanisms for this correlation can be ruled out. The leptonic model, where synchrotron radiation from high-energy electrons produces X-ray photons which up-scatter low energy stellar photons to TeV energies via IC processes, is preferred over the hadronic model. The hadronic model proposes the X-ray emitting $e^{\pm}$ and TeV photons are produced by the same proton population (for details of the argument see (*140*) and references therein).

4.5.2 GeV Versus TeV Energies

The consistent all-sky monitoring capabilities of *Fermi*-LAT present an unprecedented opportunity for multiwavelength observations of LS I $+61^{\circ}$ 303 at GeV gamma-ray energies. All VERITAS observations since 2014 have been used to construct a plot of TeV fluxes against GeV fluxes shown in Figure 4.10 with 28 observations for 2014 - 2015 season in cyan, 17 observations for 2015 - 2016 season in black, and 10 observations for 2016 - 2017 observations in red. The GeV and TeV fluxes are found to be independent of each other. The Pearson correlation coefficient for the 55 pairs of observations from VERITAS and *Fermi*-LAT was $r = -0.0255$ with a p-value of 0.85 (i.e., 85% probability that other independent data sets may show higher correlation than this data set). Previous correlation studies between GeV and TeV gamma rays have yielded similar conclusion, the emission from these two wavebands are uncorrelated (*137*). The origin of the TeV emission and GeV emission can be said with reasonable certainty to be from two different physical processes, potentially driven by independent particle populations. This hypothesis can be further examined by studying the joint GeV-TeV spectral energy distribution, as described in the next section.

4.6 GeV-TeV Joint Spectral Energy Distribution

The joint spectral energy distribution (SED) constructed using data from the 2014 - 2015 VERITAS observing season and the overlapping *Fermi*-LAT monitoring is shown in Figure 4.11. The SED extends from 100 MeV to 10 TeV and shows two distinct features.

Fermi-LAT data are fitted with a power law with exponential cutoff and VERITAS data fit well with a power law. The first feature is an exponential cutoff in the energy spectrum seen at the GeV energy range. The second is the simple power-law fit to the data in TeV energy range where there is no apparent break seen upto 15 TeV. In the SED, the emission seen by *Fermi*-LAT is disconnected from that seen by VERITAS, evident from the lack of emission seen in the 1-200 GeV energy range. The disconnected spectrum reinforces the possibility of seperate particle populations producing GeV and TeV emission that is seen by *Fermi*-LAT and VERITAS , respectively.

The spectral shape of the GeV emission with distinct cutoff at few GeV is typical of *Fermi*-LAT detected pulsars(*7*). Similar behaviour is also exhibited by TeV binaries PSR B1259-63 (hosting a ms pulsar) (*35*) and LS 5039 (*179*). The HE emission in pulsar binary systems are modelled to be contributions from the magnetospheric radiations whereas the VHE emission may be from IC up-scattered stellar photons driven by synchrotron X-ray photons originating from fast moving electrons in the magnetic field of the pulsar. These features are also seen broadly in the model SED for LS I $+61^{\circ}$ 303 shown in the bottom panel of Figure 3.6 where the the emission detected by *Fermi*-LAT and EGRET (i.e., GeV emission) are on the falling edge of the synchrotron emission bump and the TeV is driven by IC processes.

4.7 Discussion

Previous long-term multifrequency observations from LS I $+61^{\circ}$ 303 were unable to find the X-ray/TeV correlation, seen by MAGIC in 2007. The persistant correlation is now seen over multiple orbits spanning several years. Despite the presence of significant gaps between observations, the correlation is constant and cannot be simply dismissed as a coincidence. A single leptonic population could produce the correlated X-ray/TeV emission and the energy losses may be dominated by adiabatic processes (*180*). The rapidly simultaneous variations of fluxes in both TeV and X-ray wavelengths indicates a common mechanism that affects the IC and synchrotron mechanisms that produce the respective emissions.

We hypothesize, the magneto-hydrodynamical processes in the acceleration and emission regions modulate the number of emitting particles via dominant adiabatic losses

giving rise to the correlated X-ray and TeV emissions (the number of injected particles assumed constant). The hydrodynamical processes may be related to the interaction of pulsar wind or the microquasar jet with the stellar wind of the Be star. The observed X-ray photon index of 1.58 supports a model of dominant adiabatic losses (shocked plasma suffer adiabatic losses as it expands).

Studying the X-ray light curves in detail and sampling the entire orbit could point towards orbital dependencies of the model. The IC emission produced by upscattering stellar photons by energetic leptons (which are also producing the X-rays via synchrotron) would be subjected to further modulation by the changes in seed photon density along the orbit as well as interaction angles due to geometrical orientation of the orbit. The phases corresponding to observations that established the correlation between X-ray and TeV emissions are close to apastron. In these phases, the CO is $> 7\ R_\star$ (upper-limit derived from Hα observations) away from the optical star, beyond the radius of direct photon-photon absorption and pair creation effects from stellar optical/UV photons. The X-ray fluxes are also de-absorbed hence any absorption effects can be neglected. The correlated X-ray and TeV fluxes is not an artifact of variable absorption towards the source and hints to be an intrinsic property of the system supporting the leptonic one zone model (*140*, *180*).

The noncorrelation seen in the GeV/TeV data sets during three consecutive seasons of highly active states of LS I $+61^\circ$ 303 strongly confirms the theory that there are two different parent particle populations driving the emission at the respective energy levels. The GeV spectra of the source is quite stable over different parts of the orbit and fits a power-law with exponential cutoff at 4-6 GeV. However, the GeV modulation reduced significantly resulting a flatter lightcurve during years 2009-2010 when LS I $+61^\circ$ 303 was detected in only a low flux state below 5% of Crab Nebula at TeV.

The GeV emission from LS I $+61^\circ$ 303 is key to understanding the energetics of the system and testing the neutron star colliding wind model. The similarity of the spectrum to *Fermi*-LAT pulsar which also shows exponential cutoff are consistant with the magnetospheric origin for the HE emission (*97*). The emitted gamma-ray luminosity (L_γ) is related to the pulsar's spin down luminosity ($\dot{E}$) as $\eta_\gamma = L_\gamma/\dot{E}$ where η_γ is the gamma-ray efficiency. For $\dot{E} > 10^{34}$ erg s^{-1}, $\eta_\gamma \simeq 0.034(\dot{E}/10^{36}\ \text{erg}\ s^{-1})^{-1/2}$ from *Fermi*-LAT observations of pulsars (*7*). Solving for $\dot{E}$ we get $\dot{E} \simeq L_\gamma^2/(1.156 \times 10^{33})$ erg cm^{-2} s^{-1}. Using phase

averaged values from *Fermi*-LAT observation of LS I $+61^\circ$ 303 (*97*) assuming traditional models like polar cap, a spin down luminosity of $\dot{E} \simeq 2 \times 10^{35}$ erg $s^{-1}$is obtained which complements the NS model described in Section 3.2.2. However, if more sophisticated recent pulsar models like slot-gap or outer-gap models are used, it would result in a much more energetic pulsar with $\dot{E} \simeq 3 \times 10^{37}$ erg s^{-1}. Considering an alternate IC mode of production for observed *Fermi*-LAT flux, the spin-down luminosity is still found to be of the order of 10^{37} erg s^{-1}. This is because the efficiency between the spin-down luminosity and observed IC luminosity is 1-10%, considering the later to be of the order 10^{35}erg s^{-1}. Either way, such an energetic pulsar wind could not be contained by the comparatively feeble Be star wind, contradicting the elongated shape of radio emission seen around orbit interpreted as the cometary tail of pulsar wind (*122*). For more details on the one-zone model, origin of correlated X-ray/VHE emission from LS I $+61^\circ$ 303 , and details on the energy budget of the system, see (*180*).

Some evidence of coupling between thermal and nonthermal emission coming from LS I $+61^\circ$ 303 has been found (*181*). The orbital noncorrelation between HE and VHE emission and the cutoff in HE spectrum are reminiscent of multiple nonthermal emission regions along the orbit. The constant X-ray and TeV quiescent emission seen around the entire orbit (the later is a recent discovery by VERITAS, see Section 3.4.3 for details) could share a common origin with the GeV emission. Extensive simultaneous GeV/TeV data sampled evenly around the entire orbit is essential to test this theory. The observed correlation also raises additional questions regarding long term steady overall behaviour of the source. Further long term multiwavelength monitoring of LS I $+61^\circ$ 303 is necessary to unravel the true nature of this exceptional TeV binary.

Table 4.1: VERITAS observation results from days with simultaneous/contemporaneous Swift observations.

MJD	Orbital Phase (ϕ)	N_{ON}	N_{OFF}	Significance (σ)	Exposure [hours]	Flux $\times 10^{-12}$ cm^{-2} s^{-1}
56948	0.595	128.0	363.0	15.1392	1.5014	37.726 ± 3.9769
56950	0.671	7.0	84.0	-1.0641	1.0008	-1.6681 ± 1.3941
56951	0.708	11.0	231.0	-0.4923	1.001	-0.9062 ± 1.7602
56952	0.746	10.0	207.0	-0.4633	1.001	-0.8164 ± 1.6862
56954	0.821	10.0	247.0	-1.0115	1.000	-1.8669 ± 1.6795
56960	0.048	11.0	213.0	-0.2202	1.001	-0.3959 ± 1.7619
56975	0.614	116.0	295.0	15.0297	1.80	28.334 ± 3.0755
56976	0.652	65.0	251.0	9.3832	1.2842	20.169 ± 3.2105
56983	0.916	10.0	102.0	1.6023	0.6517	3.3747 ± 2.4826
57001	0.595	17.0	226.0	1.1520	1.3897	1.7646 ± 1.6733
57002	0.633	72.0	463.0	7.1537	2.6517	9.3552 ± 1.7350
57003	0.671	77.0	412.0	8.5128	2.2558	12.480 ± 2.0376
57359	0.107	20.0	233.0	1.7762	1.5008	2.3187 ± 1.4827
57365	0.333	28.0	285.0	2.6863	1.5008	3.8993 ± 1.7115
57367	0.409	34.0	195.0	5.3706	1.2172	9.0826 ± 2.3083
57394	0.428	10.0	130.0	0.9278	1.0006	1.3392 ± 1.5840
57667	0.731	11.0	58.0	3.0645	0.4503	9.5565 ± 4.2551
57670	0.844	37.0	303.0	3.7950	2.0011	5.5329 ± 1.7878
57692	0.675	66.0	274.0	8.8178	1.5008	21.077 ± 3.4628

Table 4.2: Swift observation results from days with simultaneous/contemporaneous VERITAS observations.

MJD	n_H $[cm^{-2}]$	Photon Index	Flux(Observed) [erg cm^{-2} s^{-1}]	Flux(Unabsorbed) [erg cm^{-2} s^{-1}]	W-stat(dof)	Spectrum Exposure
56948	1.1 (+0.4, -0.3) $\times 10^{22}$	1.64 (+0.32, -0.29)	1.87 (+0.28, -0.24)$\times 10^{-11}$	2.8 (+0.6, -0.4)$\times 10^{-11}$	188.19 (252)	1.4 ks
56950	4.9 (+4.6, -3.0) $\times 10^{21}$	1.8 (+0.6, -0.5)	4.4 (+1.5, -1.1)$\times 10^{-12}$	6.3 (+3.2, -1.4)$\times 10^{-12}$	65.53 (69)	990 s
56951	7 (+6, -4) $\times 10^{21}$	1.8 (+0.7, -0.6)	5.0 (+1.9, -1.3) $\times 10^{-12}$	7.7 (+5.1, -1.9) $\times 10^{-12}$	47.22 (65)	777 s
56952	6 (+4, -3) $\times 10^{21}$	1.6 (+0.5, -0.5)	7.2 (+2.3, -1.7) $\times 10^{-12}$	9.61 (+2.92, -1.00) $\times 10^{-12}$	69.49 (83)	867 s
56954	7 (+8, -5) $\times 10^{21}$	1.5 (+0.7, -0.6)	7.4 (+2.7, -1.9) $\times 10^{-12}$	9.8 (+5.4, -2.2) $\times 10^{-12}$	64.27 (75)	997 s
56960	1.3 (+0.9, -0.7) $\times 10^{22}$	1.8 (+0.6, -0.6)	7.3 (+2.4, -1.7) $\times 10^{-12}$	1.2 (+1.0, -0.3) $\times 10^{-11}$	67.84 (75)	792 s
56975	9.4 (+3.6, -2.9) $\times 10^{21}$	1.31 (+0.28, -0.27)	2.6 (+0.4, -0.3) $\times 10^{-11}$	3.3 (+0.4, -0.4) $\times 10^{-11}$	228.00 (249)	1.2 ks
56976	10 (+4, -4) $\times 10^{21}$	1.6 (+0.4, -0.3)	1.74 (+0.32, -0.27) $\times 10^{-11}$	2.5 (+0.6, -0.4) $\times 10^{-11}$	163.58 (179)	1.1 ks
56983	1.8 (+1.7, -1.1) $\times 10^{22}$	1.8 (+0.9, -0.8)	5.5 (+2.2, -1.5) $\times 10^{-12}$	1.00 (+1.80, -0.32) $\times 10^{-11}$	50.25 (65)	1.1 ks
57001	7.4 (+2.4, -2.0) $\times 10^{21}$	1.69 (+0.27, -0.25)	1.02 (+0.15, -0.13) $\times 10^{-11}$	1.48 (+0.23, -0.17) $\times 10^{-11}$	199.76 (251)	2.3 ks
57002	7.6 (+2.4, -2.1) $\times 10^{21}$	1.48 (+0.24, -0.23)	1.67 (+0.22, -0.19) $\times 10^{-11}$	2.22 (+0.26, -0.22) $\times 10^{-11}$	253.45 (290)	1.9 ks
57003	10 (+4, -3) $\times 10^{21}$	1.5 (+0.3, -0.3)	1.73 (+0.31, -0.26) $\times 10^{-11}$	2.4 (+0.5, -0.3) $\times 10^{-11}$	139.31 (182)	1.6 ks
57359	1.0 (+0.6, -0.5) $\times 10^{22}$	1.7 (+0.5, -0.5)	1.14 (+0.28, -0.22) $\times 10^{-11}$	1.8 (+0.8, -0.4) $\times 10^{-11}$	139.25 (131)	847 s
57365	1.0 (+0.6, -0.5) $\times 10^{22}$	1.5 (+0.5, -0.4)	1.27 (+0.30, -0.24) $\times 10^{-11}$	1.8 (+0.6, -0.3) $\times 10^{-11}$	131.61 (131)	935 s
57367	9.0 (+3.6, -2.9) $\times 10^{21}$	1.7 (+0.3, -0.3)	2.3 (+0.4, -0.3) $\times 10^{-11}$	3.5 (+0.8, -0.5) $\times 10^{-11}$	146.50 (209)	892 s
57394	1.4 (+0.7, -0.6) $\times 10^{22}$	2.1 (+0.6, -0.5)	9.6 (+2.6, -1.9) $\times 10^{-12}$	2.05 (+1.84, -0.59) $\times 10^{-11}$	93.22 (107)	952 s
57667	8.5 (+2.9, -2.4) $\times 10^{21}$	1.69 (+0.29, -0.27)	1.40 (+0.21, -0.18) $\times 10^{-11}$	2.10 (+0.37, -0.25) $\times 10^{-11}$	206.64 (254)	1.8 ks
57670	6 (+6, -4) $\times 10^{21}$	1.8 (+0.7, -0.6)	1.5 (+0.7, -0.5) $\times 10^{-11}$	2.28 (+1.77, -0.62) $\times 10^{-11}$	28.94 (44)	183 s
57692	6.8 (+2.0, -1.7) $\times 10^{21}$	1.49 (+0.21, -0.20)	1.96 (+0.23, -0.21) $\times 10^{-11}$	2.59 (+0.26, -0.23) $\times 10^{-11}$	255.17 (316)	2.0 ks

Table 4.3: VERITAS and *Fermi*-LAT fluxes from days with simultaneous/contemporaneous observations.

MJD	TeV σ	VERITAS Exposure [h]	TeV Flux $\times 10^{-12}$cm^{-2} s^{-1}	GeV TS	GeV Flux erg $\times 10^{-7}$cm^{-2} s^{-1}
56946	-0.8917	0.3667	-2.7930 ± 2.7014	39.3579	13.016 ± 4.03678
56947	5.7767	0.4167	25.476 ± 6.5120	23.9469	7.37863 ± 3.35214
56948	15.1392	1.5014	37.726 ± 3.9769	36.9712	12.6358 ± 2.8403
56950	-1.0641	1.0008	-1.6681 ± 1.3941	31.8364	7.48912 ± 2.23225
56951	-0.4923	1.0014	-0.9062 ± 1.7602	64.4964	8.62771 ± 2.06657
56952	-0.4633	1.0011	-0.8164 ± 1.6862	52.3382	7.95481 ± 2.15084
56954	-1.0115	1.0006	-1.8669 ± 1.6795	81.9682	8.43275 ± 2.13209
56956	0.5065	1.0022	0.9484 ± 1.9531	61.8789	10.3691 ± 2.47355
56958	1.5452	1.0011	2.9556 ± 2.1561	103.277	11.5665 ± 2.20102
56960	-0.2202	1.0019	-0.3959 ± 1.7619	50.9073	8.45153 ± 2.03931
56962	1.1900	1.0006	2.3166 ± 2.1393	43.6225	7.40235 ± 2.00704
56973	0.5101	0.4333	1.5388 ± 3.2201	93.2558	13.7919 ± 2.46687
56974	4.8963	0.6003	14.695 ± 4.2170	19.3283	7.32326 ± 2.39571
56975	15.0297	1.8008	28.334 ± 3.0755	35.6897	6.04558 ± 2.25179
56976	9.3832	1.2842	20.169 ± 3.2105	67.961	12.9565 ± 2.75557
56977	1.5334	1.0514	2.7602 ± 2.0272	50.3058	7.38712 ± 2.0181
56979	0.1354	1.0028	0.2333 ± 1.7456	17.0323	4.25996 ± 2.33683
56981	3.1159	1.0031	5.7007 ± 2.3036	42.5527	6.43335 ± 2.37689
56982	0.5101	0.5014	1.6722 ± 3.4992	18.04	5.32402 ± 2.14404
56983	1.6023	0.6517	3.3747 ± 2.4826	9.00907	1.85209 ± 1.50792
56985	2.4736	0.9514	4.5828 ± 2.2547	23.1218	6.67882 ± 2.41048
56987	0.6310	1.0033	1.0666 ± 1.7894	31.8193	3.41986 ± 1.11873
56989	1.7928	1.0036	3.4011 ± 2.1729	18.4071	7.16264 ± 2.72658

Table 4.3 Continued.

MJD	TeV σ	VERITAS Exposure [h]	TeV Flux $\times 10^{-12}$cm^{-2} s^{-1}	GeV TS	GeV Flux erg $\times 10^{-7}$cm^{-2} s^{-1}
57000	0.9060	0.2311	3.8064 ± 5.1860	116.41	13.2283 ± 2.07601
57001	1.1520	1.3897	1.7646 ± 1.6733	289.533	21.2102 ± 6.01358
57002	7.1537	2.6517	9.3552 ± 1.7350	145.632	13.8446 ± 2.0196
57003	8.5128	2.2558	12.480 ± 2.0376	96.3997	9.9035 ± 1.93467
57032	0.4804	1.0036	0.6441 ± 1.4139	104.237	11.9034 ± 2.11813
57357	1.2940	0.5003	2.8939 ± 2.6198	88.5167	9.98989 ± 2.08934
57358	1.2590	1.0006	2.1927 ± 1.9312	100.347	11.2242 ± 2.00568
57359	1.7762	1.5008	2.3187 ± 1.4827	86.3393	7.22655 ± 1.94516
57362	0.1058	1.4508	0.1382 ± 1.3175	40.7662	10.2474 ± 2.22325
57364	3.2991	1.0006	6.1700 ± 2.3472	25.8754	5.89893 ± 1.95065
57365	2.6863	1.5008	3.8993 ± 1.7115	86.4681	10.0443 ± 1.95704
57367	5.3706	1.2172	9.0826 ± 2.3083	26.8343	5.76999 ± 2.00579
57370	4.2194	0.9839	8.2777 ± 2.7236	99.3662	11.9947 ± 2.05661
57372	10.0104	1.5008	16.913 ± 2.5987	108.982	9.27361 ± 1.81722
57385	0.0905	0.4000	0.2209 ± 2.4744	54.6948	8.65939 ± 1.94128
57387	1.0165	0.1667	4.3547 ± 5.1891	94.6219	10.7741 ± 2.09971
57389	0.2462	1.5008	0.2827 ± 1.1730	107.493	14.7048 ± 2.45031
57391	-0.1739	1.2231	-0.2284 ± 1.2920	74.5	14.8411 ± 2.46729
57394	0.9278	1.0006	1.3392 ± 1.5840	121.164	13.2743 ± 2.42736
57397	2.3423	1.0006	3.7498 ± 1.9518	81.0215	9.46253 ± 1.87989
57399	11.2134	1.5008	19.757 ± 2.8042	52.2824	7.79415 ± 1.82215
57401	9.2757	1.5008	16.297 ± 2.6199	45.9802	5.1781 ± 1.60235
57662	-0.0837	1.5008	-0.1398 ± 1.6585	82.4059	10.0034 ± 2.23514
57663	-0.5736	0.8619	-1.0910 ± 1.7626	64.388	12.0106 ± 2.31521
57665	8.4191	1.5008	16.927 ± 2.8721	94.8711	11.0587 ± 2.07711
57667	3.1423	0.4503	10.119 ± 4.3158	75.55	8.7188 ± 1.94002
57670	3.2261	2.0011	4.5498 ± 1.6757	24.5753	2.91231 ± 1.24556

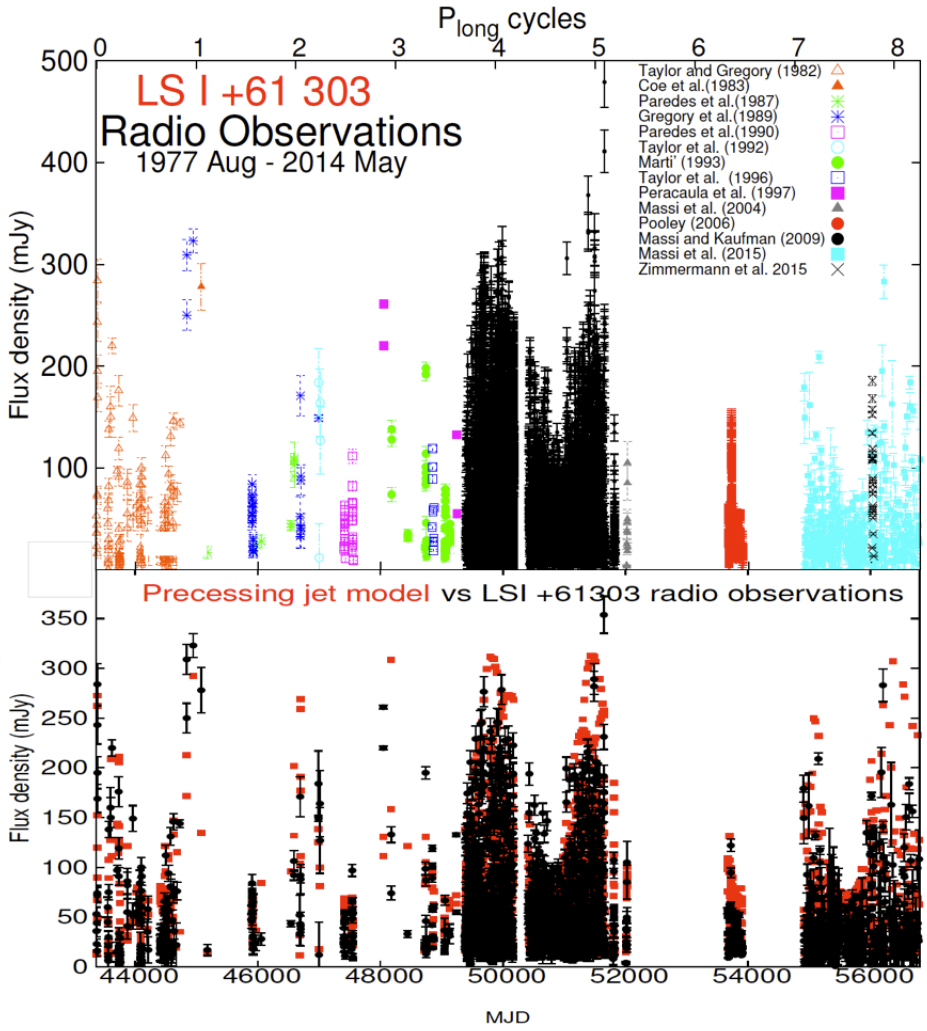

Figure 4.1: *Top:* Radio Observations of LS I $+61^{\circ}$ 303 spaning 36.8 years covering nearly 8 superorbital periods. *Bottom:* The same 36.8 years of radio data fitted with model of microquasar with precessing jets (red points). Figures reproduced from (*106*).

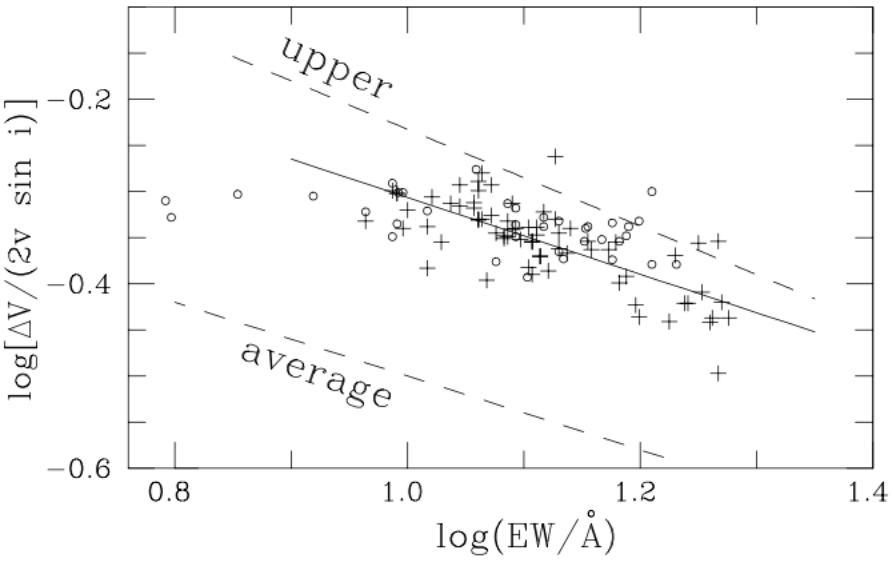

Figure 4.2: Plot of $log(\Delta V/2v\ sini)$ versus EW (Hα) for LS I +61° 303 . Dashed lines depict average behavior and upper limits for Be stars clearly pointing at above averrage disc densities for LS I +61° 303 . Plot reproduced from (*169*).

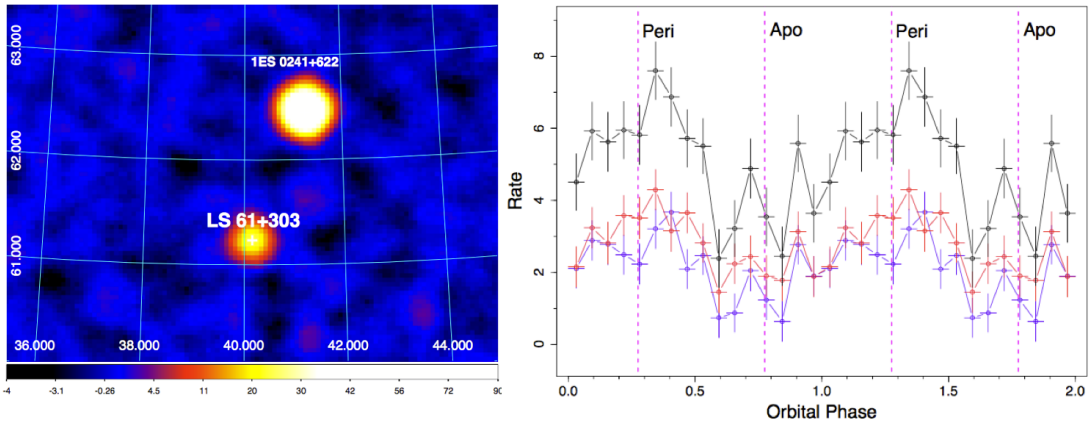

Figure 4.3: *Left:* Skymap image of LS I +61° 303 in the 15-150keV energy range from Swift/BAT *Right:* Phase folded Swift/BAT lightcurve in three energy ranges, 15-35keV in red, 35-150kev in blue, and 15-150keV in black. Figures reproduced from (*173*).

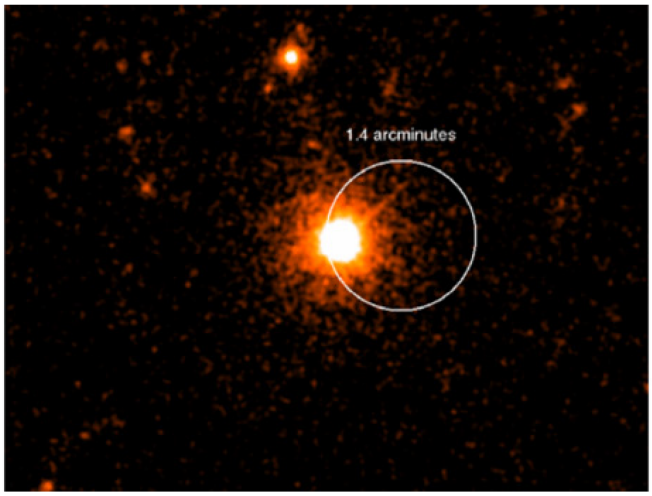

Figure 4.4: Swift XRT image of LS I $+61^{\circ}$ 303 using 165 ks of data overlaid with Swift/BAT error circle of the magnetar-like short burst event, figure reproduced from (*143*).

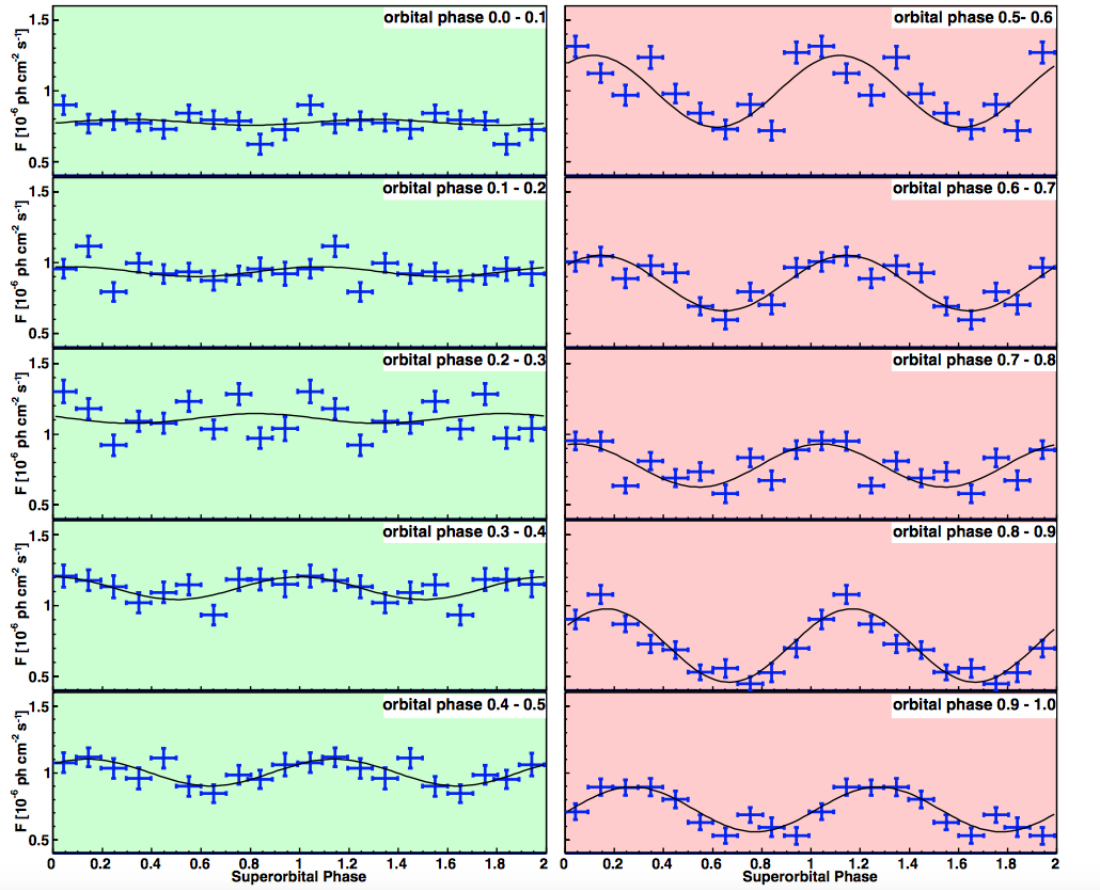

Figure 4.5: Superorbital variability of GeV flux $>$ 100MeV is seen at individual phases covering apastron passage ($\phi = 0.5 - 1.0$). Solid black line in each panel is a sinusoidal fit to the data from *Fermi*-LAT with a fixed period of 1667 days. Figure reproduced from (*162*).

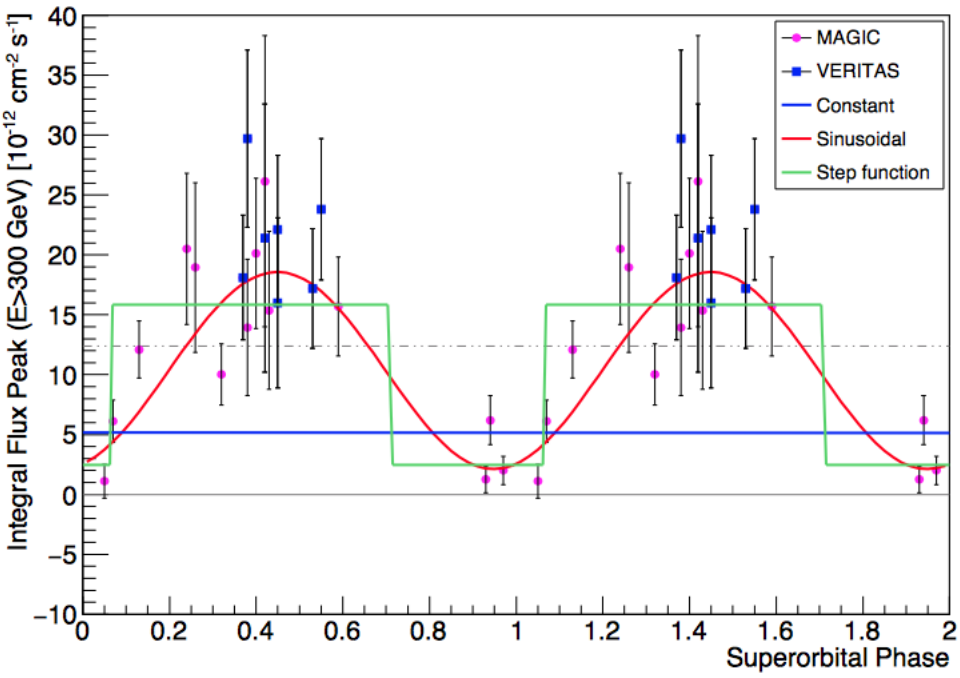

Figure 4.6: Superorbital variability seen at TeV wavelengths on phase range $\phi = 0.5 - 0.7$ when folded with 1667 days period figure reproduced from (*163*).

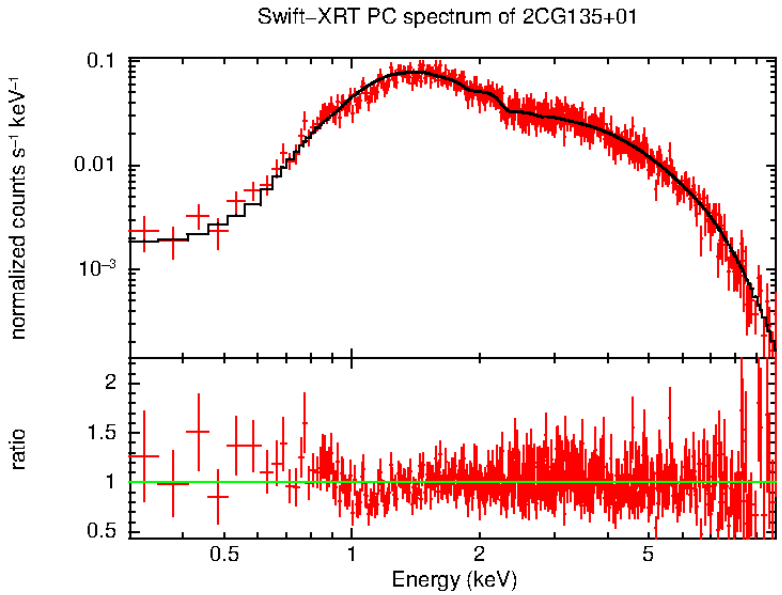

Figure 4.7: X-ray spectrum obtained from all Swift observations from October 2014 to December 2016. Photon Index for the 109.ks data set is 1.58 ± 0.04 and average unabsorbed flux of $(1.69 \pm 0.03) \times 10^{-11}$ erg cm^{-2} s^{-1}with a reduced χ^2 of 0.96.

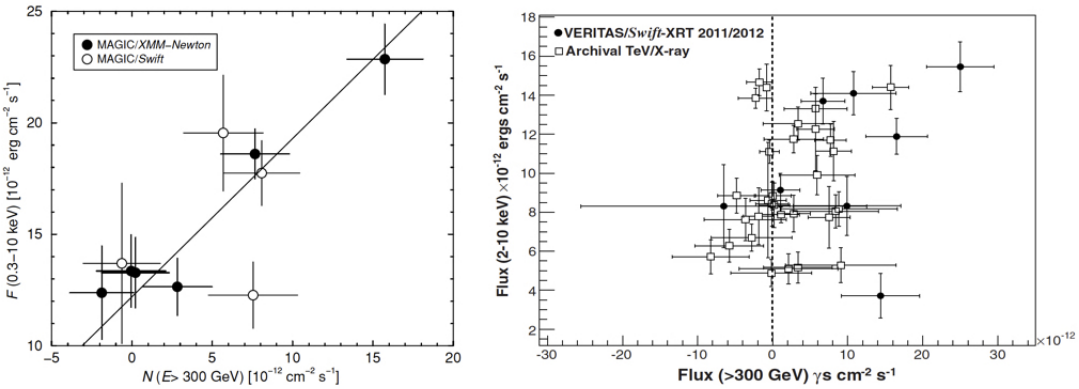

Figure 4.8: *Left:* Correlation at the level $r = 0.81^{+0.06}_{-0.21}$ seen by MAGIC in 2007 data using 10 simultaneous observations with XMM Newton and Swift XRT, figure reproduced from (*140*). *Right* Uncorrelated X-ray and TeV flux with correlation coefficient $r = 0.36 \pm 0.32$ seen from simultaneous Swift XRT and VERITAS observations, figure reproduced from (*137*).

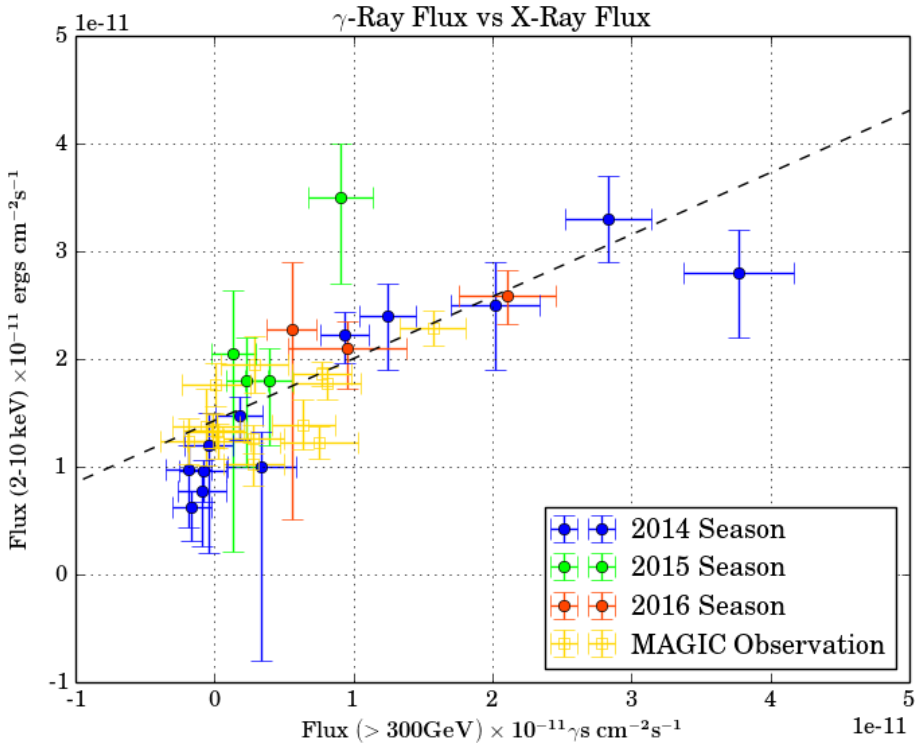

Figure 4.9: TeV(VERITAS) vs X-ray(Swift XRT) fluxes, Pearson correlation coefficient $r = 0.756^{+0.09}_{-0.13}$ for the datasets.

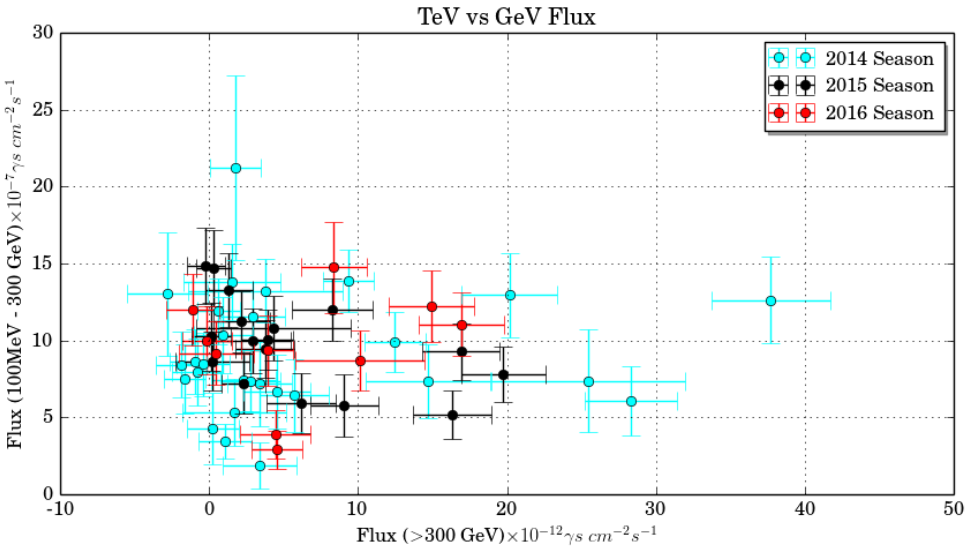

Figure 4.10: TeV (VERITAS) vs GeV(*Fermi*-LAT) Fluxes, Pearson Correlation coefficient $r = -0.0255^{0.13}_{-0.14} \pm 0.7131$ for the datasets.

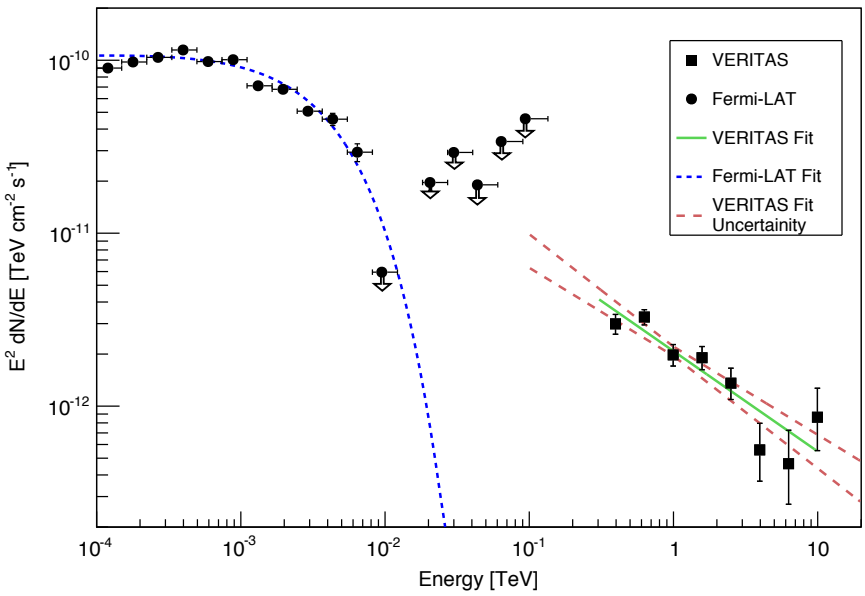

Figure 4.11: Spectral Energy Distribution (SED) from 100MeV to 10TeV.

CHAPTER 5

SS433: THE ELUSIVE MICROQUASAR SYSTEM

The SS433 high-mass X-ray binary system has been studied extensively in radio, optical, X-ray, and gamma-ray energy ranges. In spite of decades of observations and theoretical modeling, this unique system still poses many questions, especially in the high-energy range. It has been predicted to be a strong source of gamma-ray emission based on the interaction of its powerful precessing jets with the surrounding interstellar medium. Previous generation IACTs like HEGRA had placed upper limits on this system with the anticipation that the current generation of IACTs like VERITAS and MAGIC would be better equipped to detect TeV emission. In this chapter, a detailed description of this unique HMXB system harboring a microquasar will be given. Results of VERITAS observations of SS433 between 2009 and 2012 will be presented along with a discussion of the implications of these results.

5.1 SS433, the Microquasar

Object 433 from the from Stephenson and Sanduleak Catalog (1977) was identified as a variable nonthermal radio (*182*) and variable X-ray source (*183*). The hydrogen and neutral helium emission lines were identified to be extensively Doppler shifted to the red and blue by many thousands of km/s (*184*, *185*). This was explained in (*184*, *186*, *187*) that the shift in H and HE I lines are due to oppositely directed bipolar jets of gas that are precessing. This significant discovery spurred several decades of theory, observations, and modeling of the SS433 system.

SS433 a eclipsing binary system consisting of a super-giant $\sim$A7Ib star (*188*) of mass $30M_{\odot}$ and an accreting blackhole of mass $9M_{\odot}$ in an 13.082 day orbit (*189*). It is located in the galactic plane; the position of its optical counter part is at RA: $19^{h}11^{m}49^{s}$ Dec: $+4^{\circ}58'48''$ with corresponding galactic coordinate is (l, b) = (39.700, 2.252) at an estimated

distance of $5.5 \pm 0.2kpc$ (*190*). The most fascinating aspect of the SS433 system are its dual jets which excite the surrounding W50 nebula.

W50 closely resembles a supernova remnant and is extended along the jet precessional axis with SS433 in the center with lobes in eastern and western directions. The radio morphology of the W50 nebula and its surrounding is seen in Figure 5.1, the central magenta star is the location of SS433 with bright lobes in the eastern and western directions. The central blackhole accretes matter and gives rise to these relativistic jets (bulk speeds of 0.26c) which precess with a period of $\sim$ 162.50 days along an axis which is approximately at 78° with the line of sight. In addition to their precessional motion, the jets undergo small amplitude so-called nutational oscillations with a period of 6.28 days, which is half the synodic orbital period, $P_{orb} = 13.082$ days. The nutational nodding of the jets and accretion disk is due to periodic tidal perturbations of the disk by the gravitational field of the donor star (*191*) or to perturbations of the accretion flow. For quick reference of the reader the parameters of SS433 are listed in Table 5.1 with a schematic representation in Figure 5.2

Using different observational methods guided by radiation mechanisms, distance from the source, etc., the X-ray jets, the optical jets, and radio jets can be identified. The X-ray jets are short but radio emission can be seen along almost the entire extent of the optical jet. The jets of SS433 are unique not only because of their extent and interaction with the W50 nebula but also because of their baryonic content. It is the only known system where hadrons are accelerated in the jets along with leptons (*192*) making it a unique laboratory to study the production of gamma rays via proton-proton interaction (relativistic hadrons interaction with cold ions within the jets).

5.1.1 Radio Observations

The central source in the SS433 system radiates 1 Jy at centimeter wavelengths. This bright radio star's emission is mostly nonthermal in origin. The bulk of the synchrotron radio emission appears about $\sim 10^{15}$ cm from the central source (*193*) which is also the location of maximum optical line emissions from the jet. The radio emission from the jet fades away beyond a distance of 10^{17} cm and reappears at $\sim 10^{20}$ cm where intense X-ray emission is also observed (*194*).This is referred to as the 'ears' or lobes of the W50 nebula.

Relativistic electrons are continuously generated and travel along the jet producing the synchrotron radio emission. The jets are termed 'heavy' due to the constituent $e^- p^+$ plasma propagating at low relativistic speeds of 0.26c without significant deceleration. The relativistic particles are supposedly accelerated in shock waves during interactions between the jets and gas flowing from the accretion disk. The heavy jets are what makes SS433 a unique system among microquasars.

Long-term monitoring of SS433 has revealed the variable nature of the system (*195*). The radio jets show both quiescent and active states, where powerful overlapping flares are seen during the later lasting 30-90 days (*193*). The radio flux varies with a 6.29-day nutational period but is not modulated by the orbital or precessional period. During a flaring episode, the internal structure of the radio jets are altered and may show up as a one-sided jet. The asymmetry of the ejection and the interaction of the jet with the surrounding gas from the disk wind and absorption of radio emission by this gas may be the driving factors for the radio structures seen during the flare, occurring due to perturbation in the jet activity. Radio image of SS433 from VLA is shown in Figure 5.3.

5.1.2 X-ray Observations

SS433 has been intensively studied in X-ray wavelengths since 1979 and an excellent review of early observations is available in (*196*). A short chronological summary of observations from the various instruments is discussed in this section. It will help in the understanding the motivation to observe this peculiar source at higher energies. The *Einstein Observatory* was first among many to observe SS433 extensively and revealed it to be a variable X-ray source. Due to the observatory's limited energy resolution, it was a challenge determining whether the emission was thermal or nonthermal in nature. Symmetric X-ray structures extending 10^{20} cm from the central bright source was also discovered by *Einstein Observatory* which later is now believed to be formed due to the interaction of the jets and the surrounding medium. The discoverers suggested synchrotron and a more plausible thermal emission mechanisms for lobes (*197*). Finer resolution was achieved with the advent of *EXOSAT*, a Doppler-shifted FeXXV Kα emission line was found in *EXOSAT* GSPC X-ray spectra of SS433 which was moving in accordance with the jet precession period ($\sim P_{pr}$)(*198*). This proved the X-rays originated in the jets and were thermal in

origin. Only one X-ray emission line was found in the spectrum and it was assumed that X-ray emitting zone of the receding jet was obscured by the accretion disk constraining the size of the jet $\leq 10^{12}$ cm. Data from *ROSAT* were used to conduct detailed spectroscopic studies of the eastern and western lobes (*194*, *199*). A *ROSAT* PSPC image of the eastern and western jet termination regions are shown in the two panels of Figure 5.4 While the X-ray lobes of the eastern jet coincided with the radio ear, there was no such coincident X-ray emission from the western radio ear. The large-scale asymmetries in eastern and western jets were explained by the nonuniform expansion of the W50 supernova remnant into the inhomogeneous ISM. Softer spectrum in regions w1 and w2 of the western jet was attributed to breaking of the jet and pushing the radio ear further into the denser medium towards the galactic plane whereas the eastern ear was towards a lower density of confining matter, away from the galactic plane.

ASCA found many more moving emission lines of Si, S, Ar, Ca, Fe, and Ni (*200*), confirmed the visibility of both approaching and receding jets and suggested them to be longer than previously thought. The spectrum of X-ray regions adjacent to SS433 had a harder spectrum than those farther away in the lobes (*201*). The authors suggested that the emission in the lobes were likely from synchrotron electrons accelerated by the shock which led to the first predictions of ultra-high-energy gamma rays extending up to TeV energies from the lobes. The authors in (*202*) made a detailed study of the western lobe of SS433 with *Chandra* and preferred a nonthermal approach in explaining the emission and the corresponding derived values for N_H, synchrotron energies and lifetimes were in agreement with those seen previously by *ROSAT* and *ASCA*.

Clear precessional variability was seen n 18-60 keV hard X-ray energy range by *INTEGRAL*. The precessional lightcurve for eclipsed $(0.95 < \phi_{orb} < 1.05)$ and uneclipsed $(0.2 < \phi_{orb} < 0.8)$ states are shown in Figure 5.5 which shows the maximum flux to be 5-7 times greater than the minimum flux. This variability was found to be stable over several precessional periods (*188*).

5.2 High-Energy Emission from SS433

This section outlines the models predicting gamma-ray emission from different parts of the SS433 system and a summary of observations that has been conducted n the HE and

VHE wavelengths.

5.2.1 Production of Gamma Rays in Jets of SS433

Reynoso model predicts emission of gamma rays from the jets of SS433 where gamma rays would be produced close to the black hole, visible during certain phases when absorption is minimum by the disk (*188*). The model describes protons accelerated to 3.4×10^6 GeV in the jets at shocks produced by collisions of plasma outflows with different bulk velocities. Applying the conservation equation in the shock frame, the upstream velocity would be greater than the downstream velocity and the two regions may be regarded as two converging flows. The first-order Fermi acceleration processes would produce a power-law particle spectrum. The proton-proton interactions would then produce secondary gamma rays and neutrinos.

The gamma rays would be subject to various absorption mechanisms. The primary source of absorption would be the star when it eclipses the blackhole for $\sim$ 2 days once every 13 days. A second absorption feature would correspond to interactions between gamma rays and nucleons from the extended disk. At higher energies, the $\gamma\gamma$ interactions would become dominant where UV photon and mid-IR photons would heavily attenuate those photon $\geq$ 50 GeV and $\geq$ 500 GeV, respectively (*203*)

Favorable observation window for SS433 according to the Reynoso model would be for phase $\phi \geq 0.91$ and $\phi \leq 0.09$ when the extended disk is open maximum open in Earth's direction, the expected fluxes are shown in Figure 5.6. In this phase, the gamma rays would be minimally affected by absorption by the thick equatorial disk. A conservative estimate of the half opening angle 30° gives optimal detectability window of $\sim$ 29 days. If the half opening angle is smaller than the assumption then the observational window would be wider.

5.2.2 Production of Gamma Rays from Microquasar Interaction with ISM

The *Bordas* model is based on an analytical jet/medium interaction structures in radio galaxies (*204*). This model assumes two oppositely directed conical jets emerging from the central blackhole. The ejected material in the jets decelerates when its mass becomes equal to the swept-up ISM. Two shocks are formed at the tip, one propagating forward into the ISM (bow-shock) and the other inward back into the jet material (reverse shock). Matter crossing back in the reverse shock inflates the cocoon which protects the jets from any disruptions and a third confinement shock is formed in the jet where the pressure is equal to that of the cocoon. The different aspects of the model are represented as a diagram in Figure 5.7.

Electrons are accelerated by the shocks along the jets by first or Fermi acceleration processes. They could reach energies 2-10 TeV in the shell region where synchrotron emission is the dominant radiative process. Similarly, synchrotron emission would also dominate in the cocoon region where electrons could be accelerated up to 100 TeV. In the reconfinement region, both synchrotron emission and IC emission could equally contribute for electrons accelerated up to 10 TeV.

Based on conservative estimates of various parameters of the model like the age of the microquasar, distance, density of ISM, kinetic power of the jet, and the nonthermal luminosity fraction, the authors in (*205*) estimates the flux below detectable level of current IACTs ($\sim 10^{-15} ergs^{-1} cm^{-2}$ above 100 GeV). It is to be noted that the selected parameters may be too conservative and the authors have only accounted for the leptonic component. The powerful jets of SS433 have been proven to have a hadronic component which is likely to produce gamma rays in the jet termination region.

5.2.3 HE Observations

Using 5 years of data from *Fermi*-LAT a significant emission region was associated with SS433 (*205*). The point-like emission region had a significance of 7.3σ with a 3σ positional accuracy at a 99% confidence level. A TS map of the $5^\circ \times 5^\circ$ is shown in Figure 5.8 with a diamond marking the optical position of SS433.

Due to the lack of any plausible high-energy counterpart and predicted nonthermal activity from SS433 the significant emission region was associated with SS433. It is to be

noted the authors mention the best-fit position to the emission at R.A. = 287°.65, Dec. = 4°.72, which is 0°.41 away from the nominal position of SS433, with a 1σ error circle of 0°.15. A steady flux of $\phi_\gamma = 2.4 \pm 0.3 \times 10^{-8} \gamma s\ cm^2\ s^1$ was calculated above 200MeV from the entire 5 year dataset.

The spectral energy distribution of the *Fermi*-LAT flux shown in Figure 5.9 is fitted with IC, relativistic bremsstrahlung and proton-plasma interaction emission but, none of these models fit the data below 250 MeV. Besides exploring the possibility of gamma-ray emission from the jet base and interaction of the jet with the W50 nebula, authors have also speculated the W50 nebula itself as the source of gamma rays, similar to observed TeV emitting supernova remnants like IC443.

5.2.4 VHE Observations

The HEGRA IACT-System observed a region of diameter 4.0° centered on SS433 between 1998 and 2001 (*206*). HEGRA was unable to detect SS433 or any part of the jet using a total of 109.9 h of data that were acquired during this period. A 99% confidence U.L. on flux was placed on various regions of the SS433 system which are listed in Table 5.2. They also calculated a lower limit on the postshocked magnetic field in the e3 region $\geq 19 \mu G$.

The CANGAROO II telescope was also unable to detect SS433 with 85.2h (ON source) and 80.8h (OFF source) with data recorded between 2001 and 2002 (*207*). They derived upper limits from fluxes at 99% confidence level at regions p1, p2, and p3 (all locations in the western jet) to be $1.5 \times 10^{12}, 1.3 \times 10^{12}$, and $7.9 \times 10^{13}\ cm^2\ sec^1$, respectively, for $E_{th} >$ 0.85 TeV. Most recently, MAGIC and H.E.S.S. also conducted joint campaigns on SS433 but also failed to detect any significant emission (*208*). The available MAGIC skymap of the SS433 system is seen in Figure 5.10

5.3 VERITAS Observations

VERITAS archival data had a total of $\sim$ 90 h of data within a 1.5° offset from SS433. The data were recorded mostly between September 2007 and July 2012. There were also few h of data that were acquired during Target of Opportunity observations following a GRB. The later was discarded due to poor weather conditions. The data recorded between September 2007 and July 2012 are from two different epochs V4 and V5 of the instrument's

operation. From the V4 epoch, 10.4 h of data, recorded between September 2007 - July 2008 has been already analyzed and no significant emission was detected from the source , although the author in (*209*) found a 4.9σ pretrials significance in the w2 interaction region. The $\sim$ 72 h data used here are from V5 epoch collected September 2009 - July 2012. SS433 is located in a busy gamma-ray neighborhood with the extended MGRO J1908+06 only a few degrees away at R.A.: $19^h07^m54^s$ Dec.: $+06^\circ16'07''$. The telescopes wobbled around a central location in the sky between SS433 and MGRO J1908+06 to accommodate both the sources in the field of view (FoV), maximizing observation for both the sources. Table 5.3 provides a summary the VERITAS observations used in this work.

5.4 Data Analysis

SS433 lies in a complex region close to the galactic plane. Not only is the source extended in the sky over $2^\circ \times 2^\circ$, it lies close to the extended MGRO J1906+08 source. A number of regions on interest (ROI) has been selected for analysis from the exposure around this region, listed in Table 5.4.

The ROI have been selected based on previous observations in this region and guided by predictions of gamma-ray production from different regions of SS433. The *Bordas Model*, places a maximum limit on energies of electron at $\sim$ 10TeV producing HE emission through synchrotron and IC radiative channels in the jet reconfinement region, close to the central engine. This makes the region around the blackhole a logical choice for the search of TeV gamma rays. According to the *Bordas Model* the western region (referred to as w2 in (*199*)) of the W50 remnant is also plausible site for gamma-ray production via interactions between relativistic jet particles and the remnant shell. As mentioned in 5.1.2, strong nonthermal emission arise in this region with the regions of strongest emission tracing out the helical precession of the flowing jet into the W50 environment (*202*). The helical jets are seen from a *Chandra* image shown Figure 5.11.

Three regions in the eastern jet are defined as e1, e2, and e3 based on (*199*) of which e3 is the region where the 'radio' ear coincides with X-ray emission. The X-ray emission from e3 has competing models of thermal bremsstrahlung interpretation (due to limited energy resolution of ROSAT and ASCA (*199*)) and nonthermal synchrotron emission (supported by strong spatial radio/X-ray correlation (*194*, *210*)). Since the e3 region has been

investigated previously by HEGRA IACT (*206*) and a reasonable upper limit was already placed (Table 5.2), this work concentrates on other two regions, e1 and e2 in the eastern jet. These two regions are also of interest due to their strong nonthermal X-ray fluxes. The regions are shown in Figure 5.12 which is a *ROSAT* PSPC image focusing on the eastern jet of SS433.

Archival VERITAS data for these 4 ROI for the analysis presented here. A specialized Boosted Decision Tree (BDT) technique was employed for the analysis of the data. The BDT technique has shown substantial improvement in source detection significances over the standard technique, retaining more gamma rays during the γ/hadron seperation step (*85*). This technique improves sensitivity especially for faint gamma-ray sources. The cuts used are harder from the standard cuts for higher energy threshold due to large zenith angle observations. To improve performance on weaker sources, specialized hard-weak BDT cuts were used that are less restrictive than hard BDT cuts. Hard-weak cuts allow recovery of a better gamma-ray rate while maintaining low background rates compared the the more restrictive hard BDT cuts.

The orientation between the jets and the extended disk may play a role in source visibility. It may result in detectability only during certain precessional phases when the the gamma rays originating at the base of the jets will travel to the without having to pass through the equatorial disk (*203*, *211*). The predicted phase for gamma-ray detectability is most likely is between $\phi \geq 0.91$ and $\phi \leq 0.09$ where $\phi_0 = JD2443507.47$ is defined as when the disk is maximum open to the observer (*188*). The precessional phase has been binned into 5 bins with width of 0.2 starting with phase $\phi = 0.1$.

The ring background method (see (*91*) for details) has been used to estimate the background of cosmic rays, night sky background, noise, etc. A bright extended TeV source MGRO J1908+06 is within the field of view in the data and has been excluded while performing background estimation. All of the selected ROI have also been excluded from the background estimation.

5.5 Results

The entire data from VERITAS comprise, of mainly two epochs V4 and V5. The V4 epoch was before the relocation of T1. Some V5 data were previously analyzed focusing

on the central SS433 source and w2 of the western jet (*209*). In the current analysis on V5 data from 2009 to 2012, no significant gamma-ray emission is found from SS433 central blackhole, w2, e1, or e2. The skymap at the location of SS433 BH is seen in Figure 5.13 with radio contours overlaid in green. A 99% flux upper limit calculated at the location is $2.29 \times 10^{-13}\gamma\ cm^{-2}s^{-1}$ above 600 GeV (analysis threshold). It is to be noted the hole in the radio contour on the eastern part is the location of eastern jet ROI e1 and e2. The 99% flux upper limits from each of the phases at the location of the BH is summarized in Table 5.5 as well as for the entire data set.

The western jet had received special attention in (*209*) because of the the strong non-thermal emission coming from this region as seen in (*202*) with the regions of strongest emission tracing out the helical precession of the flowing jet into the W50 environment. Theoretical predictions for GeV/TeV emission from the w2 interaction point are extremely promising in the *Bordas model*. During VERITAS observations, the initial part of the data were collected by wobbling around w2 and later around a central location between SS433 and MGRO J1908+06 (to maximise joint visibility of both these sources). The 4.9σ pre-trials excess calculated by (*209*) at the location of w2 with standard hard cuts for a point source analyzing $\sim$ 19 h of data are no longer seen with $\sim$ 71 h data from the V5 epoch using BDT hard-weak cuts for a point source. A 99% confidence level flux upper limit of $2.66 \times 10^{-13}\gamma s\ cm^{-2}s^{-1}$ is calculated at w2 from the entire data set. Phase-based upper limits for w2 are also calculated and summarized in Table 5.6 respectively. The skymap shown in Figure 5.14, is overlaid with X-ray contours from ROSAT/ASCA in green with the PSF around w2 marked in black.

The X-ray emission from e1 and e2 regions in the eastern jet are harder than e3 (*199*) which made them a more suitable candidate to expect gamma-ray radiations. Both power-law and Raymond-Smith thermal models were well fit to the spectra from e1 and e2 but the high temperature obtained from the thermal bremsstrahlung model could not be constrained by *ROSAT*. The analysis of ASCA observation suggested nonthermal origins of the X-ray in absence of emission lines, coupled with electron energies of 50TeV (implying 1-2keV photon energies) the model was able to explain the harden photon index required ot fit ROSAT data. On a first glance the gamma-ray skymap also shows a warm spot at e1 and e2 seen in Figure 5.15 and Figure 5.16 but they fall short of the required signifi-

cance 5σ to claim a detection. Nevertheless, flux estimate of 5.68×10^{-13} γ cm^{-2} s^{-1}and 4.21×-13 γ cm^{-2} s^{-1}from the e1 and e2 regions could still be accurate if the future IACTs like CTA detect them. In Table 5.7 and Table 5.8, the results for a 99% confidence level upperlimit for e1 and e2 along with phase-based upper limits are summed up.

The upperlimits from each of the phases for individual ROI are shown in Figure 5.17. The same color scheme red - SS433 BH, green - w2, magenta - e1, cyan - e2 upper limits for the entire data is shown to the *Reynoso* model along with exposure hours in each phase. The limits placed by VERITAS are much lower than predicted by *Reynoso* model and the HEGRA collaboration. This indicates that SS433 may not be as luminous as thought previously. The *Bordas* model may have estimated the flux of SS433 correctly at $\sim 10^{-15}\, cm^{-2}\, s^{-1}$.

5.6 Discussion

VERITAS observations of SS433 BH, w2, e1, and e2 positions do not provide evidence of any significant gamma-ray emission, although the e1 region shows 3.7σ significance. No claim of discovery is made from any of the regions as they are below the conventionally accepted detection level of 5σ. No significant emission has been made previously by other IACTs although the upperlimits placed by HEGRA above 800GeV has been able to constrain the lower limit of the magnetic field to $19\mu G$ at e3 based on the model in (*212*). The upperlimits calculated from the VERITAS data for the different ROIs are shown in Figure 5.18. Authors in (*203*) proposed a few mechanism contributing to the opacity of gamma-ray propagation from SS433 (*203*).

The primary source of absorption would be the star when it eclipses the blackhole for $\sim$ 2 days once every 13 days. Gamma rays would be attenuated significantly by interaction with lower energy photons coming from the star and its disk by producing e^+e^- pairs via $\gamma\gamma$ annihilation processes. The optical depth would be given by

$$d\tau_{\gamma\gamma} = (1 - \hat{e}_\gamma \cdot \hat{e}_{ph}) n_{ph}\, \sigma_{\gamma\gamma}\, d\rho_\gamma\, dE\, dcos\theta'\, d\phi' \tag{5.1}$$

where the $\hat{e}_\gamma$ direction of gamma ray with energy E_γ travelling a distance of $d\rho_\gamma$ in the photon field, $\hat{e}_{ph}$ direction of soft photon from star or disk with energy E at angles θ' and ϕ', $\sigma_{\gamma\gamma}$ is the cross section of the $\gamma\gamma$ interaction. The interaction cross section $\sigma_{\gamma\gamma}$ depends on the energies E_γ, E, mass and classical radius of the electron. The low-energy photons

are contributed by both the extended disk (mid-IR and UV photons) and the companion star itself and the interaction cross section for each of these components contribute to $\sigma_{\gamma\gamma}$

A second absorption mechanism would be due to interaction of the gamma-ray photons with the matter(nucleons) in the system comming from the the star and the disk, photo producing pions. The cross section for these γN as derived in (*213*) is given by

$$\sigma_{\gamma N} = \begin{cases} 340\mu b & 200MeV < E_\gamma < 500MeV \text{ (for single pion channel)} \\ 120\mu b & E_\gamma \geq 500MeV \text{ (for multipion channel)} \end{cases} \tag{5.2}$$

According to the *Reynoso* model, gamma rays are produced via pp interaction. The model assumes the jets to be dominated by cold protons which act as targets for relativistic protons accelerated at internal shocks. Using the HEGRA upper limit for SS433 > 0.8 TeV the *Reynoso* model calculates a maximum value for $q_{rel} < 2.9 \times 10^{-4}$, fraction of the total kinetic energy of the jet carried by the relativistic protons (free parameter of the model). Using VERITAS upper limits, q_{rel} can be further constrained to maximum value of $\sim 0.9 \times 10^{-4}$. Recently claimed detection of SS433 with *Fermi*-LAT shows idiosyncratic spectral energy distribution which peaks at $\sim$ 250 MeV and extending up to merely $\sim$ 800 GeV (*205*). This spectral behaviour suggests that the maximum electron energies previously projected from nonthermal X-ray emission are an overestimate and they would only be accelerated to few GeV instead of tens of TeV. The origin of the GeV emission is also ambiguous due to poor angular resolution of *Fermi*-LAT above $\sim 1.5^\circ$ at energies $\sim$ 300 MeV. No variability is seen in the *Fermi*-LAT data suggesting the emission may be originating in the outskirts of the binary system since otherwise it would be subject to strong phase dependent absorption effects (*203*).

The nondetection of SS433 by VERITAS may be indicative of a lower intrinsic luminosity at high energies or that the gamma ray may be produced too deep in the nebula and suffer strong attenuation high enough to hinder detection. SS433 is a promising site for hadronic gamma-ray production accompanied by neutrinos (*102*, *214*) . Neutrinos are unaffected by absorption mechanism like gamma rays and if observatories like IceCube detect them, it would be a smoking gun for gamma-ray production via hadronic processes in SS433. The assumptions made by the *Bordas model* predicts gamma-ray flux in the order of 10^{-15}. In the future CTA observations may offer the best opportunity to detect gamma-ray emission from faint sources like SS433.

Table 5.1: Parameters of SS433 system (values are from (*188*, *189*, *215*).)

M_{BH}	$9M_{\odot}$	Mass of the blackhole
M_{OS}	$30M_{\odot}$	Mass of the optical star
i	$78.83 \pm 0.10^{\circ}$	Inclination angle of the precessional axis
θ	$19.85 \pm 0.17^{\circ}$	Half opening angle of the precession cone traced out by the jet
β	0.2602 ± 0.0013	Velocity of the jet in unit of c
P_{pr}	$162^{d}.50$	Precessional period of accretion disk and jet
P_{orb}	$13^{d}.082$	Orbital period of the eclipsing star
P_{nut}	$6^{d}.29$	Nutation Period
t_0	MJD 43506.97	Time at which precessional phase is at $\phi(0)$ for maximum opening of the disk.

Table 5.2: Upper limits of SS433 system calculated by HEGRA.

Source	Exposure[h]	$E_{threshold}$[TeV]	$\phi_C^{99\%}U$	$\phi_{flux}^{99\%}$
SS433 e1	72.0	0.8	0.023	6.18
SS433 e2	73.1	0.8	0.034	9.18
SS433 e3	68.8	0.8	0.032	8.96
SS433	96.3	0.7	0.032	8.93
SS433 w1	104.9	0.7	0.024	6.65
SS433 w2	100.7	0.7	0.031	9.00
SS433 knot2	103.0	0.7	0.020	5.55
SS433 knot3	100.4	0.7	0.023	6.59

Table 5.3: VERITAS observations of SS433.

Year	Exposure [h]	No. of Runs	Camera Offset (°)	Mean Elevation (°)
2009	9.33	27	0.7-1.0	59
2010	10.5	37	0.7-0.8	60
2011	26.11	88	0.05-1.1	61.2
2012	25.23	79	0.7-1.5	62.4
Total	71.17	231	0.06-1.5	61

Table 5.4: Regions of interest (RoI) in the SS433 system.

Location	R.A.	Dec	RoI
SS433	$19^h11^m49^s$	$+04°58'48''$	0.25°
w2	$19^h09^m45^s$	$+05°03'00''$	0.25°
e1	$19^h13^m33.67^s$	$+04°56'57.56''$	0.25°
e2	$19^h14^m11.22^s$	$+04°56'57.56''$	0.25°

Table 5.5: Upper limits at location of SS433 blackhole.

Phase	N_{ON}	N_{OFF}	σ	99% UL
0.1-0.3	52	586	0.2	4.12e-13
0.3-0.5	62	731	-0.1	3.39e-13
0.5-0.7	35	357	0.7	7.95e-13
0.7-0.9	22	231	0.3	7.90e-13
0.9-1.1	25	282	0.0	5.70e-13
All	196	2195	0.4	2.29e-13

Table 5.6: Upper limits at location of w2 (western jet).

Phase	N_{ON}	N_{OFF}	σ	99% UL
0.1-0.3	57	821	0.6	4.36e-13
0.3-0.5	69	1080	0.0	3.16e-13
0.5-0.7	42	546	1.1	8.07e-13
0.7-0.9	31	325	2.0	1.17e-12
0.9-1.1	26	463	-0.6	4.05e-13
All	225	3245	1.2	2.66e-13

Table 5.7: Upper limits at location of e1 (eastern jet).

Phase	N_{ON}	N_{OFF}	σ	99% UL
0.1-0.3	49	563	1.1	6.22e-13
0.3-0.5	68	583	2.6	8.54e-13
0.5-0.7	36	278	2.5	1.45e-12
0.7-0.9	23	218	1.6	1.40e-12
0.9-1.1	23	280	0.5	7.97e-13
All	199	1925	3.7	5.68e-13

Table 5.8: Upper limits at location of e2 (eastern jet).

Phase	N_{ON}	N_{OFF}	σ	99% UL
0.1-0.3	39	427	-0.1	4.47e-13
0.3-0.5	61	435	3.0	1.03e-12
0.5-0.7	21	231	0.2	7.79e-13
0.7-0.9	15	172	-0.1	9.23e-13
0.9-1.1	17	172	0.4	7.77e-13
All	153	1442	1.8	4.21e-13

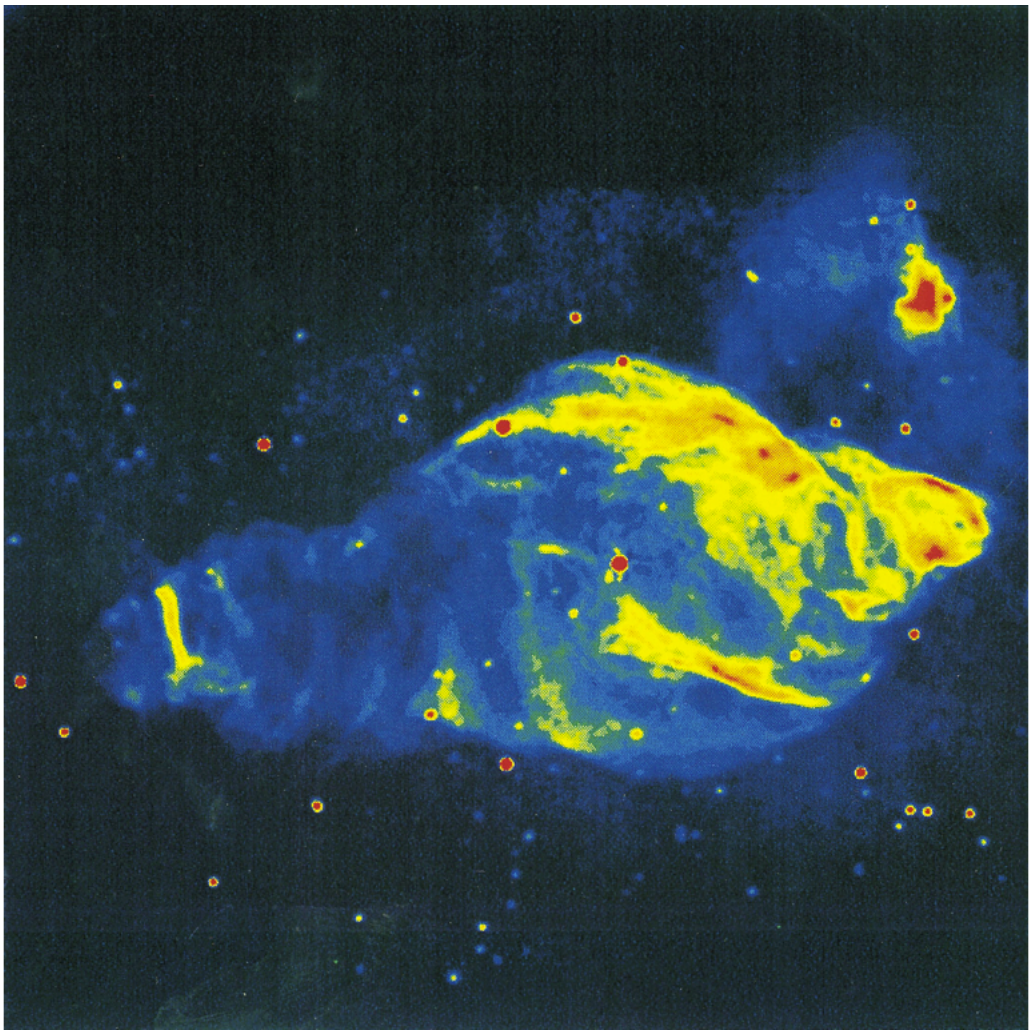

Figure 5.1: W50 nebula and its surrounding with the microquasar SS433 in center (pseudocolor). This is a composite image from 58 different pointings by Very Large Array at the National Radio Astronomy Observatory, reproduced from (*210*).

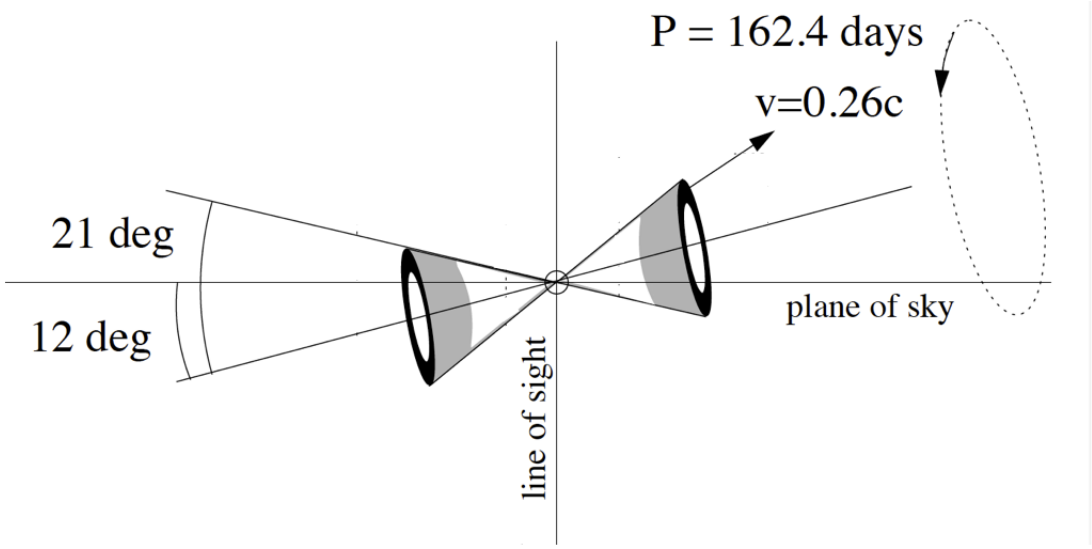

Figure 5.2: Schematic diagram of the precessional jet geometry of SS433, figure reproduced from (*192*).

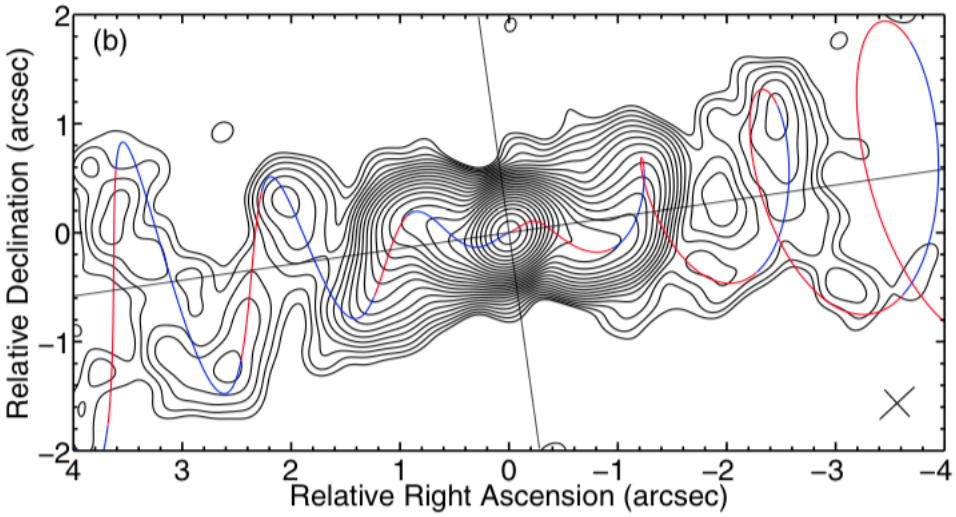

Figure 5.3: VLA image of SS433 from data were recorded in July 2007. C-band uniformly weighted images of total intensity. Contours are in steps of $\sqrt{2}$. The kinematic model of the jets is overlayed on the figure with blue and red line segments representing the retreating and oncoming jet material, respectively. Figure is adapted from (*216*), detailed information about contour levels, map noise, etc., is found therein.

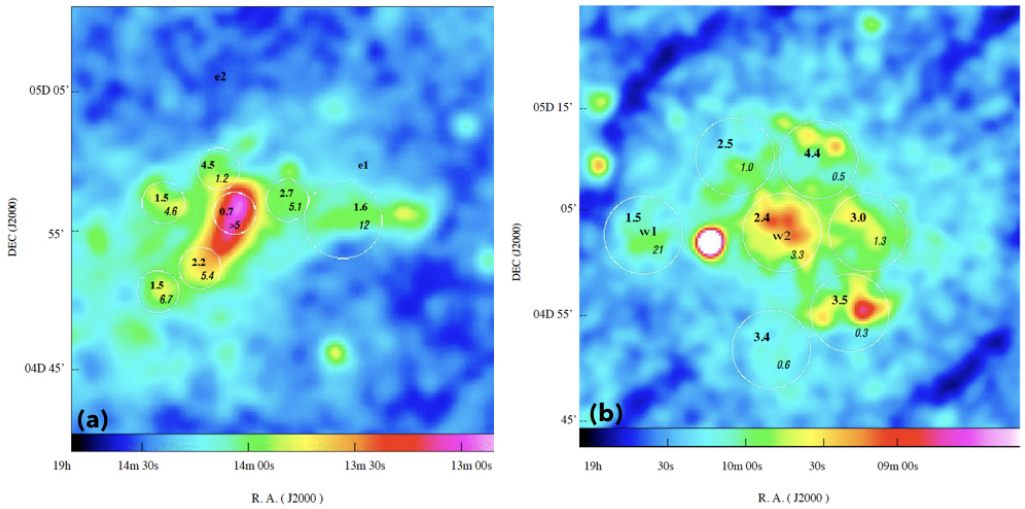

Figure 5.4: (a)*ROSAT* PSPC image of the eastern lobe of SS433 system. Regions e1(of radius $\sim 3.5'$) and e2(of radius $\sim 2.0'$) are labeled. (b) *ROSAT* PSPC image of the western lobe of SS433 system. Bright X-ray source at RA:$19^h10^m13^s$ and dec:$+5^\circ2'14''$ is independent of the system. The regions w1 and w2 are centered at 19′ and 31″ west of SS433 are labeled. Figures reproduced from (*199*).

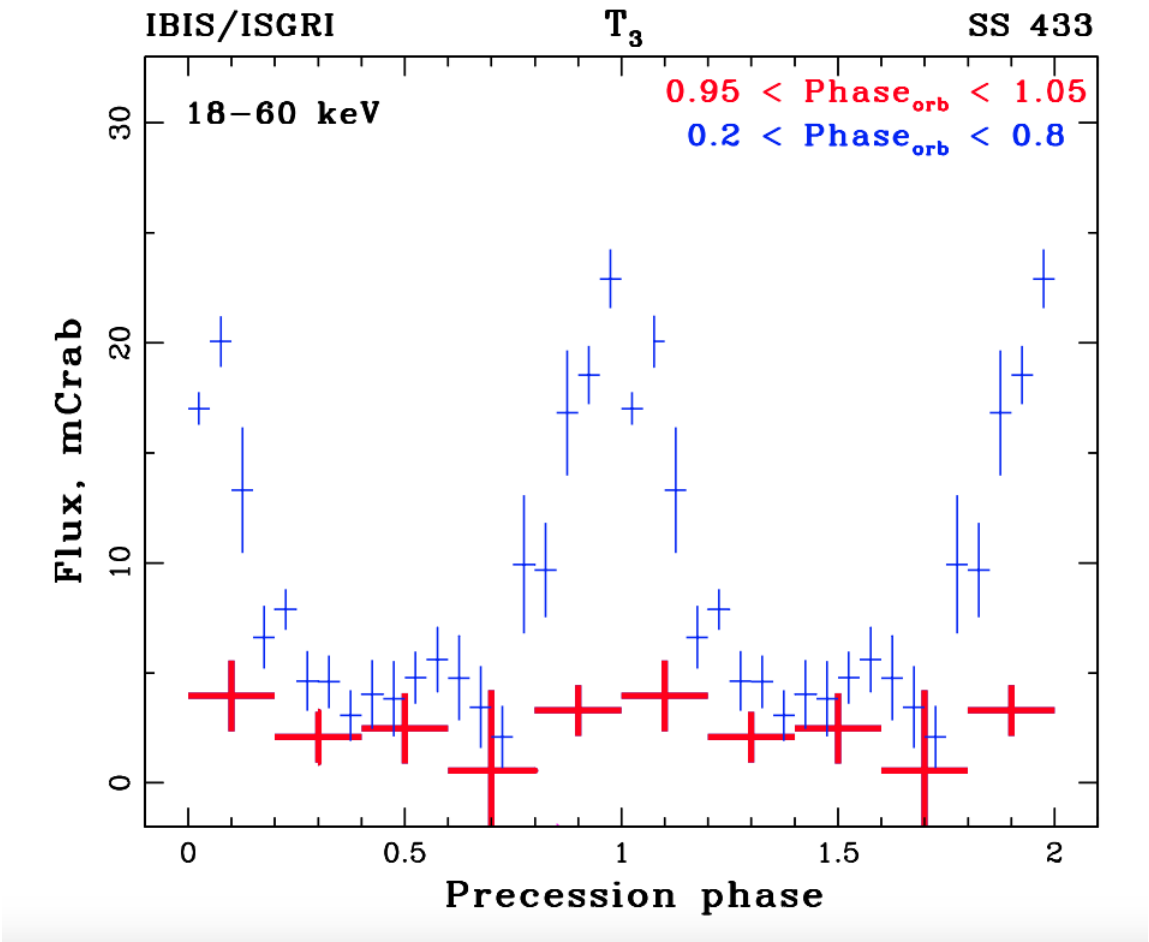

Figure 5.5: Light curve from INTEGRAL in 18-60 keV energy range. Red crosses representing flux when the system is out primary orbital eclipse, blue crosses when inside eclipses. Figure reproduced from (*188*).

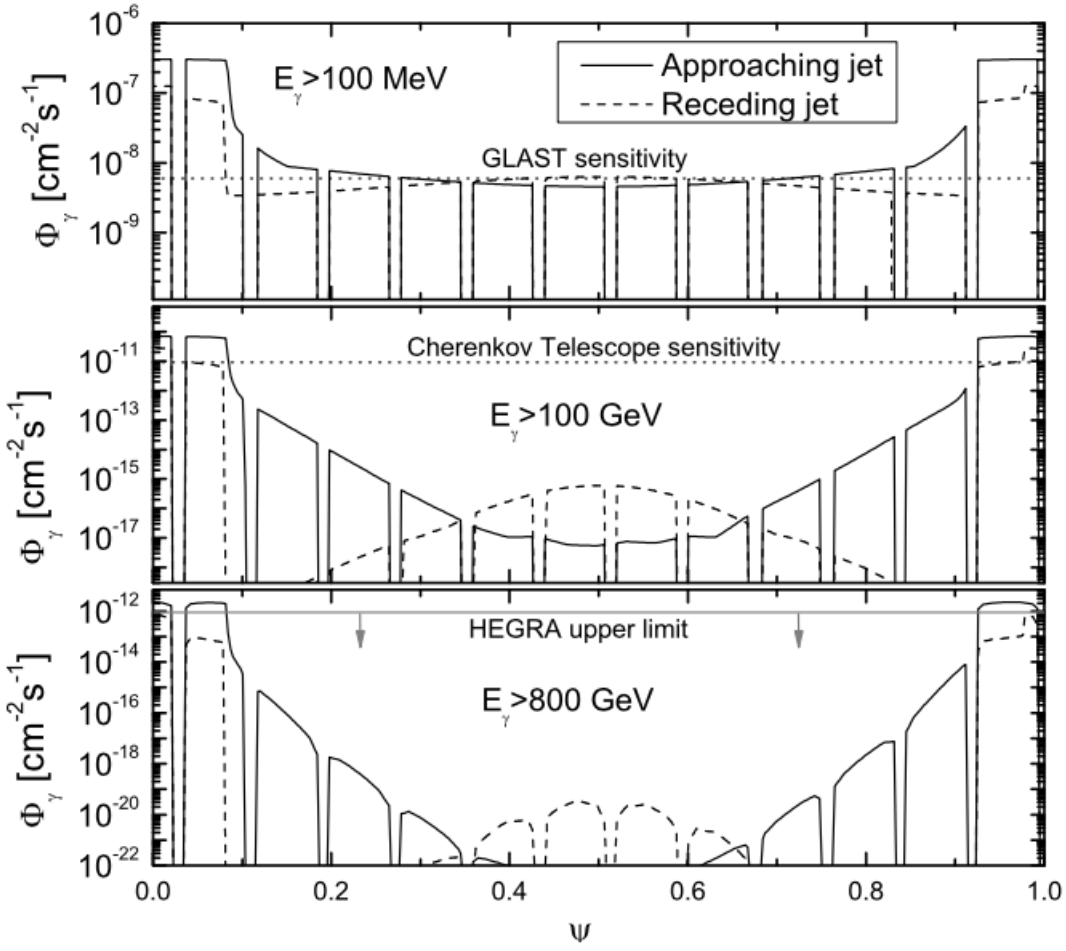

Figure 5.6: Predicted gamma-ray flux observable at earth as a function of precessional phase of the jet. Top panel for *Fermi*-LAT energy range 100 $MeV < E_\gamma < 300\ GeV$, middle panel for current generation IACTs like VERITAS and MAGIC for $E_\gamma > 100 GeV$, and bottom panel for previous generation IACTs like HEGRA for $E_\gamma > 800 GeV$. Figure reproduced from (*211*).

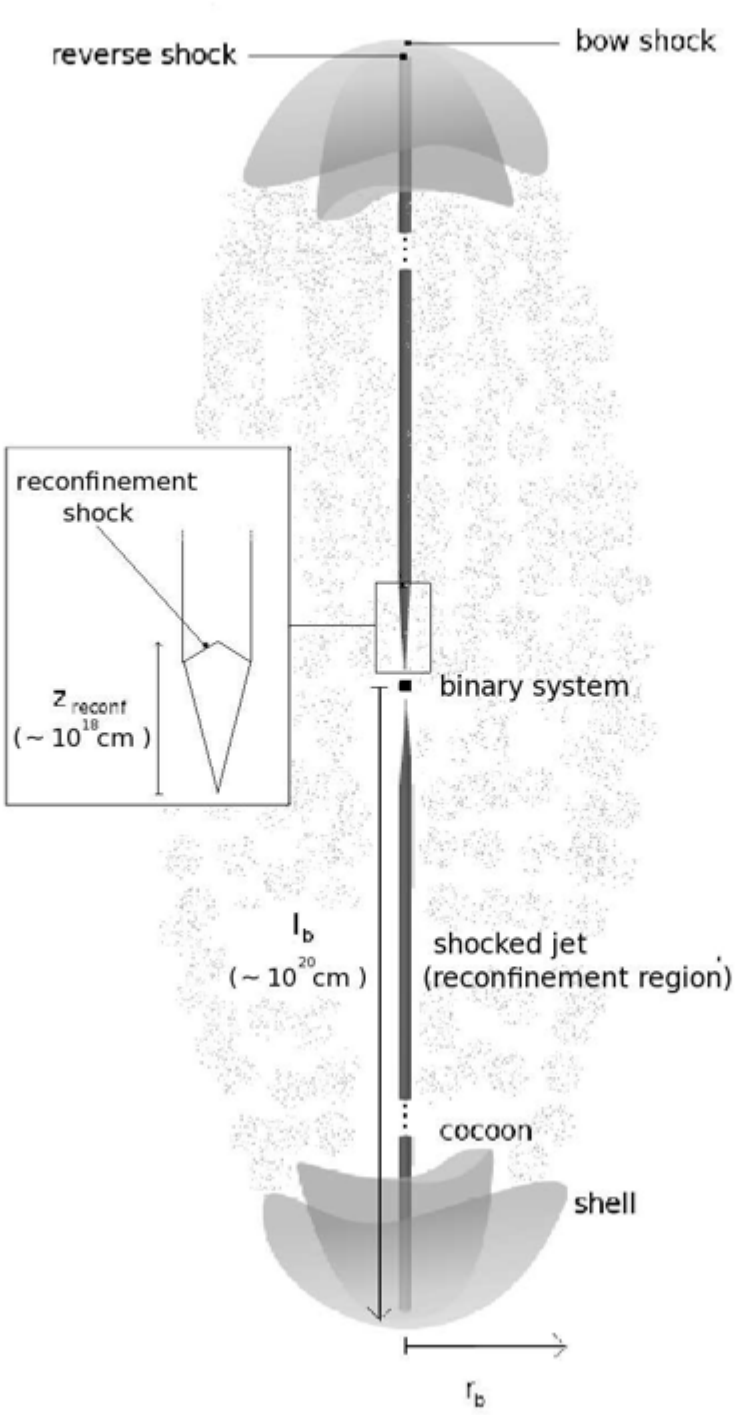

Figure 5.7: Diagram of the Bordas model (not-to-scale) depicting the three zones discussed in the text. Figure reproduced from (*204*).

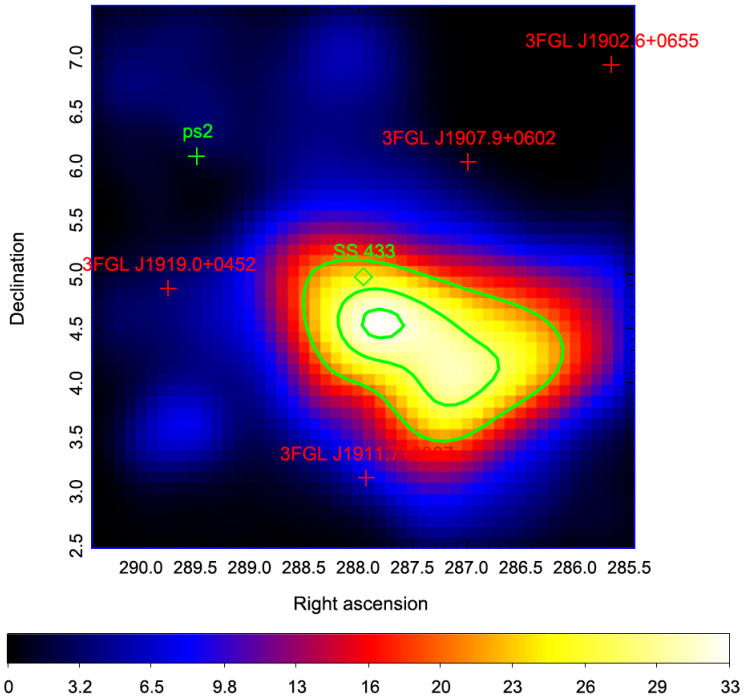

Figure 5.8: Test Significance (TS) map of around the the optical position of SS433 using data from *Fermi*-LAT . Bright sources from 3FGL catalog excluded from background. Contours correspond to 68%, 95%, and 99% positional accuracy. Colorbar represents TS value. Figure reproduced from (*205*).

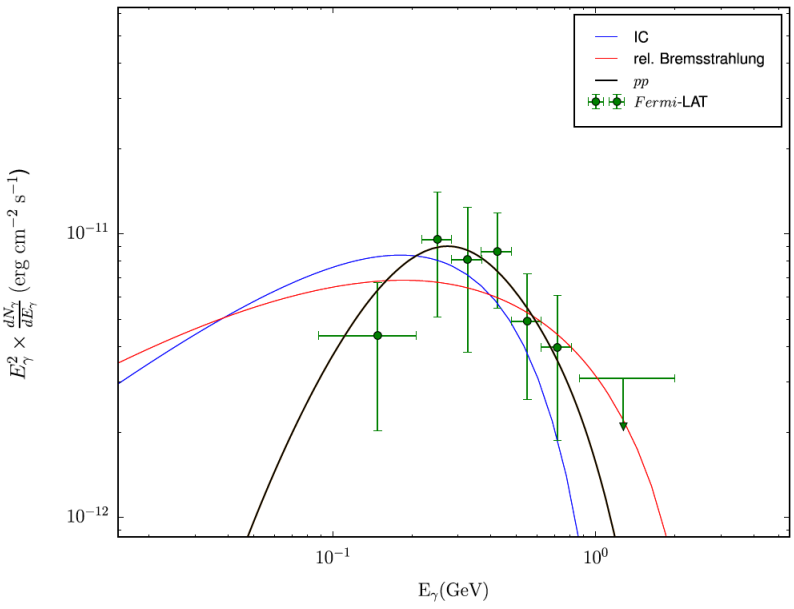

Figure 5.9: Spectral energy distribution of data from *Fermi*-LAT. Models depicting gamma-ray production through IC(blue), relativistic bremsstrahlung(red) and proton-plasma interaction (black) processes are depicted. Figure reproduced from (*205*).

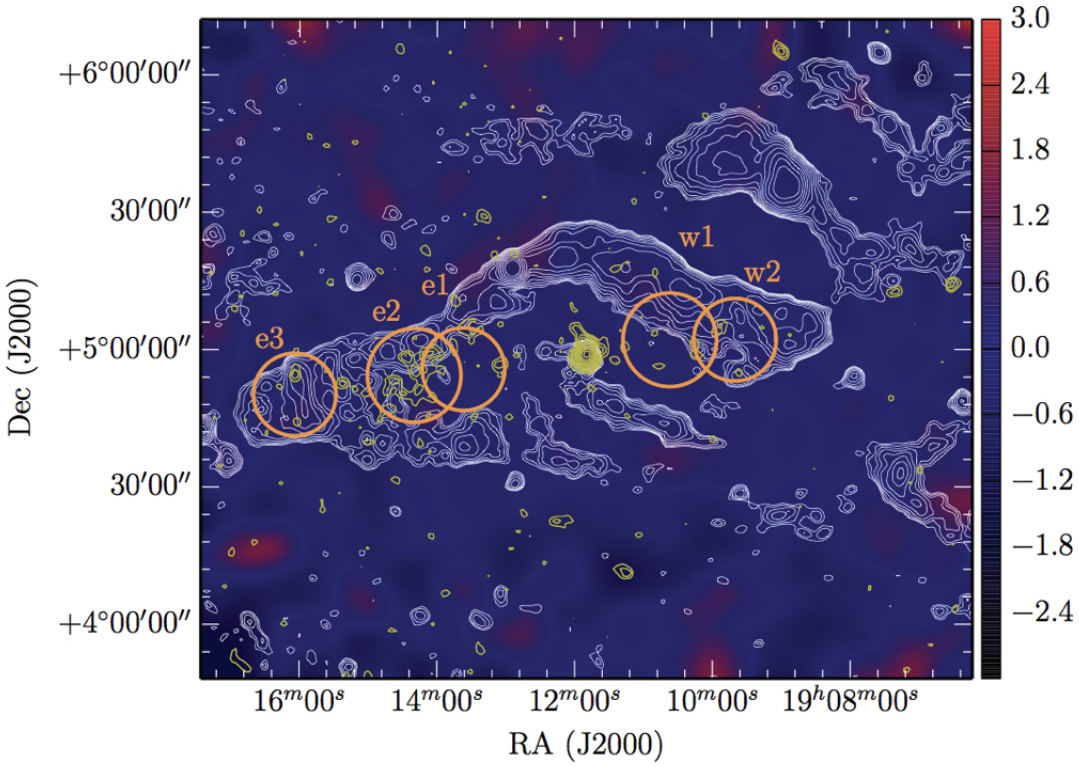

Figure 5.10: Skymap from MAGIC of SS433/W50 system above energy threshold of 0.25TeV. Jet interaction regions w1, w2, and e1, e2, e3 are marked with GB6 4.85GHz radio contours in white and ROSAT broadband X-ray contours in yellow. Figure reproduced from (*208*), see reference therein for details on radio and x-ray contours.

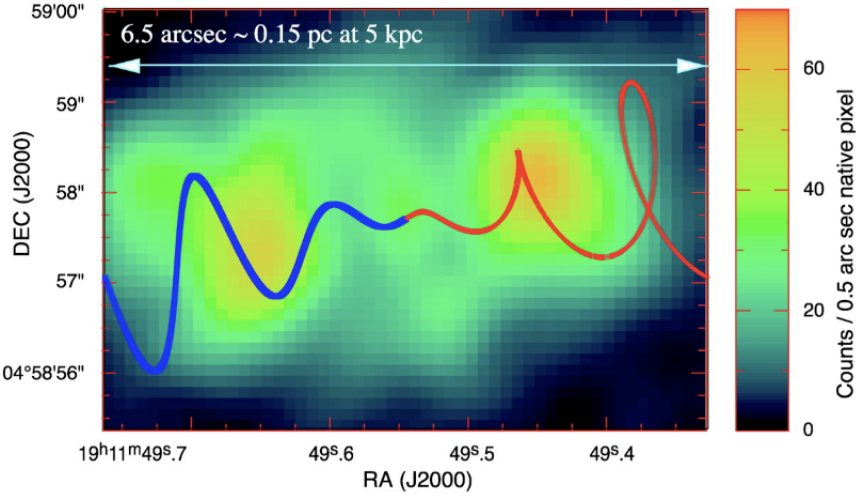

Figure 5.11: The red and blue shifted hadronic X-ray jets of SS433 shown in *Chandra* observations between 0.8-10 keV. It is from these jets that gamma-ray emission is expected to be modulated as a function of the precessional phase ϕ (Figure reproduced from (*192*).

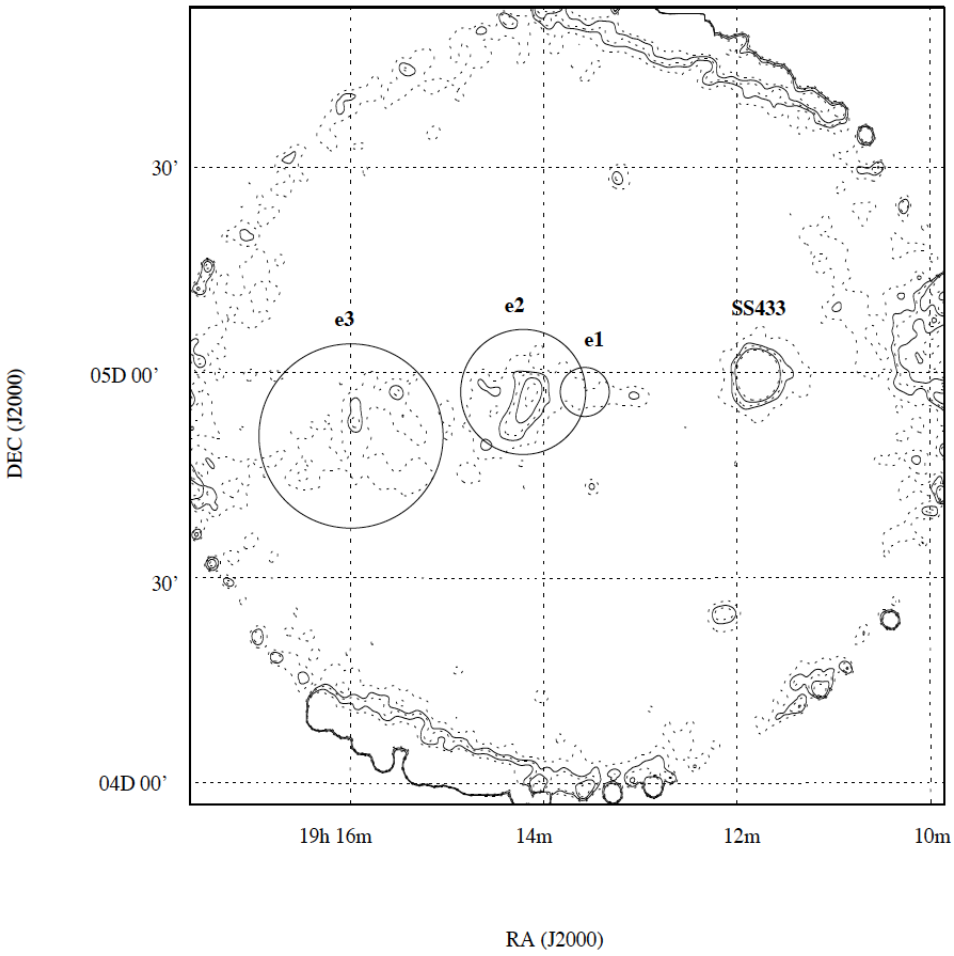

Figure 5.12: *ROSAT* PSPC contour plot of the eastern lobe in energy range 0.1-2.4 keV. The regions e1 e2 and e3 are centered at 24′,35′, and 60′ from SS433. These same ROI are used in the analysis of VERITAS data later. Figure reproduced from (*199*).

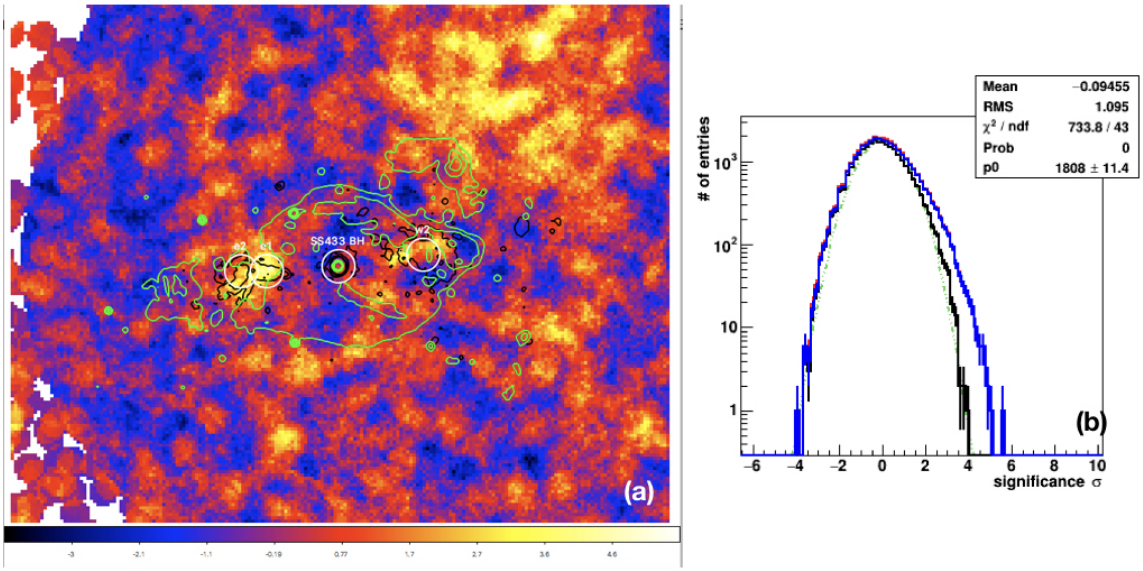

Figure 5.13: (a) Skymap of SS433 region with radio contour overlayed in green and location of blackhole marked. Significance at location is 0.4σ (b) Significance distribution at location of SS433 BH.

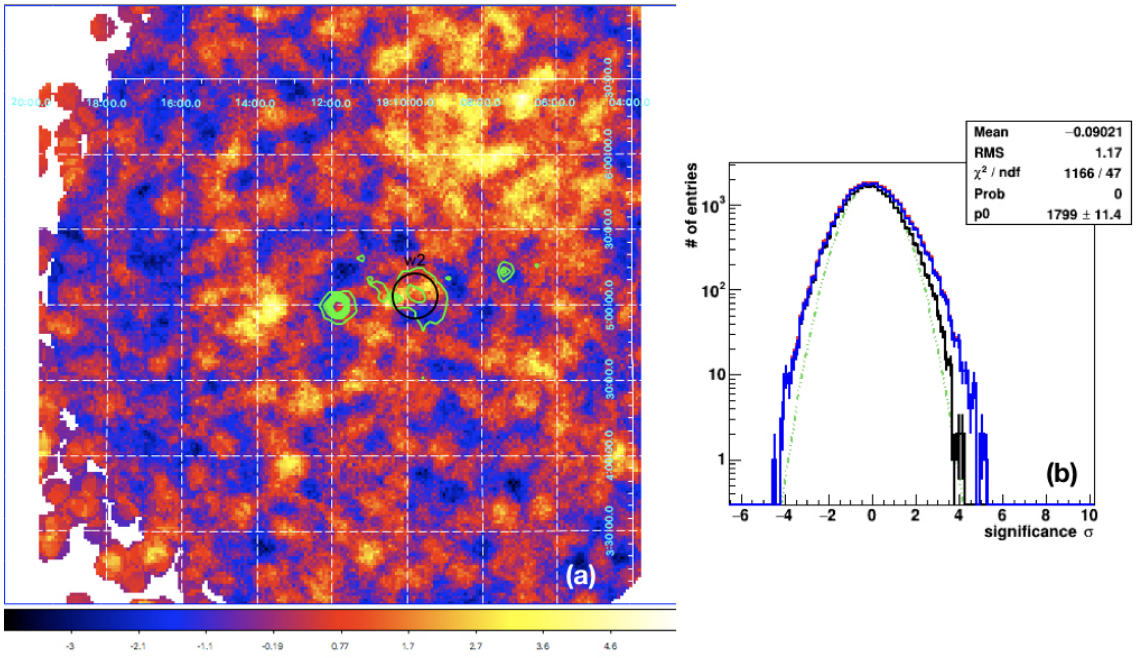

Figure 5.14: (a) Skymap of SS433 region with X-ray contour overlayed in green and location of w2 (in western jet) marked. Significance at location is 1.2σ (b) Significance distribution at w2 location.

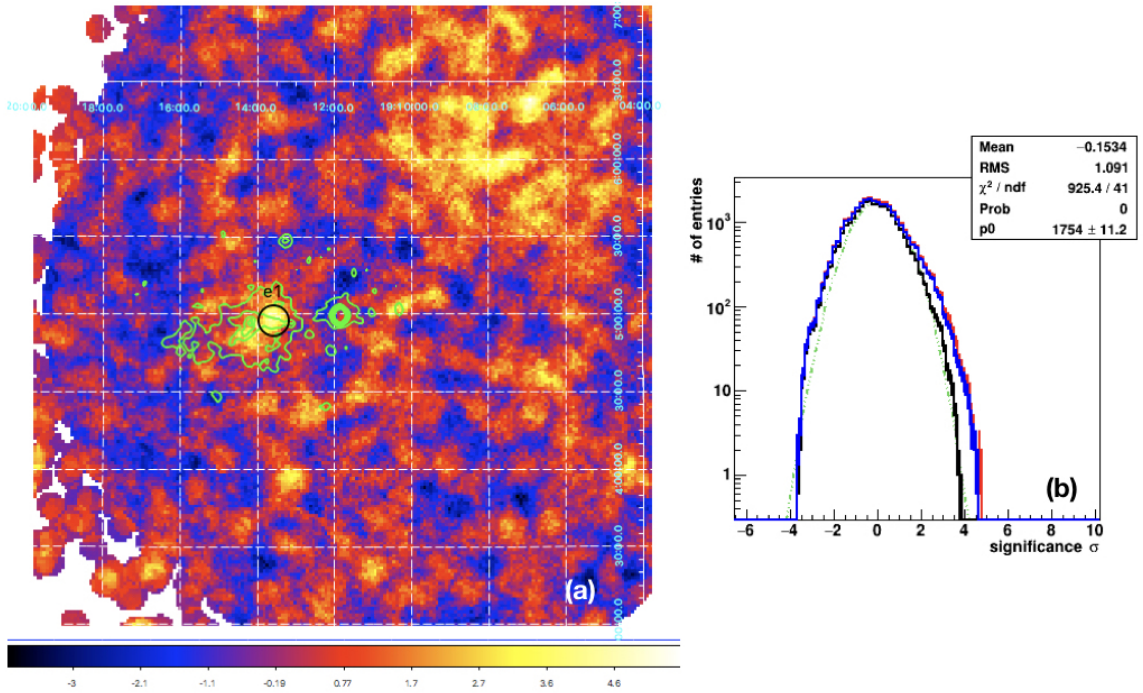

Figure 5.15: (a) Skymap of SS433 region with X-ray contour overlayed in green and location of e1 (in eastern jet) marked. Significance at location is 3.7σ (b) Significance distribution at e1 location.

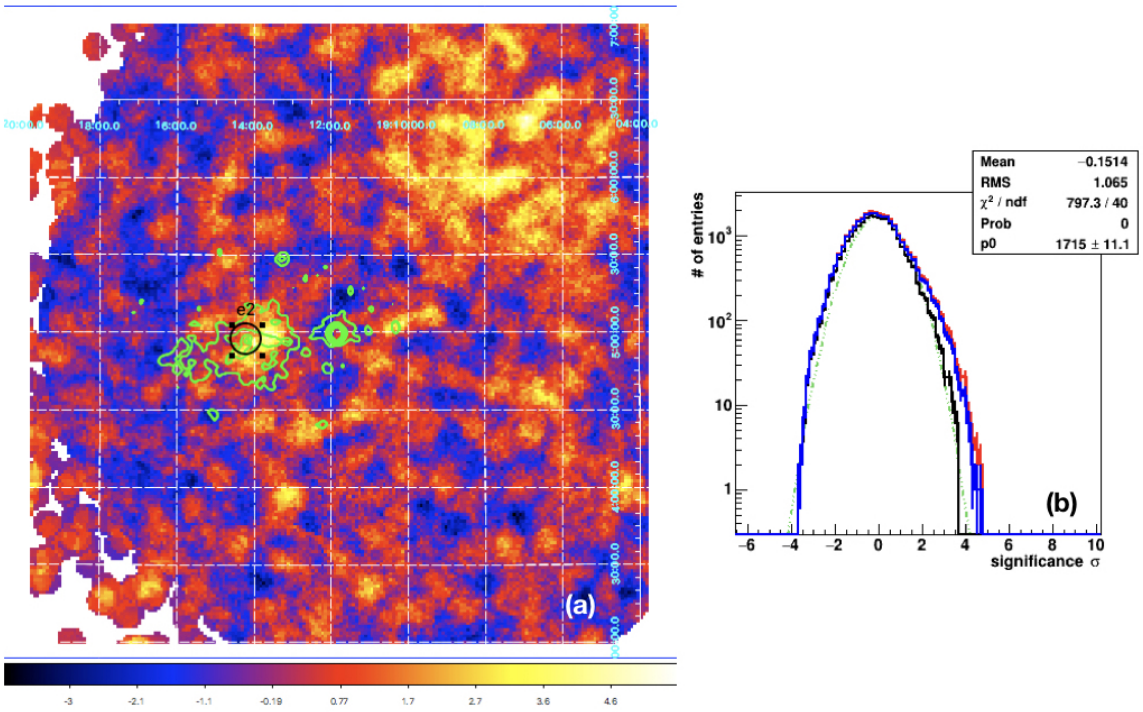

Figure 5.16: (a) Skymap of SS433 region with X-ray contour overlayed in green and location of e1 (in eastern jet) marked. Significance at location is 1.8σ (b) Significance distribution at e2 location.

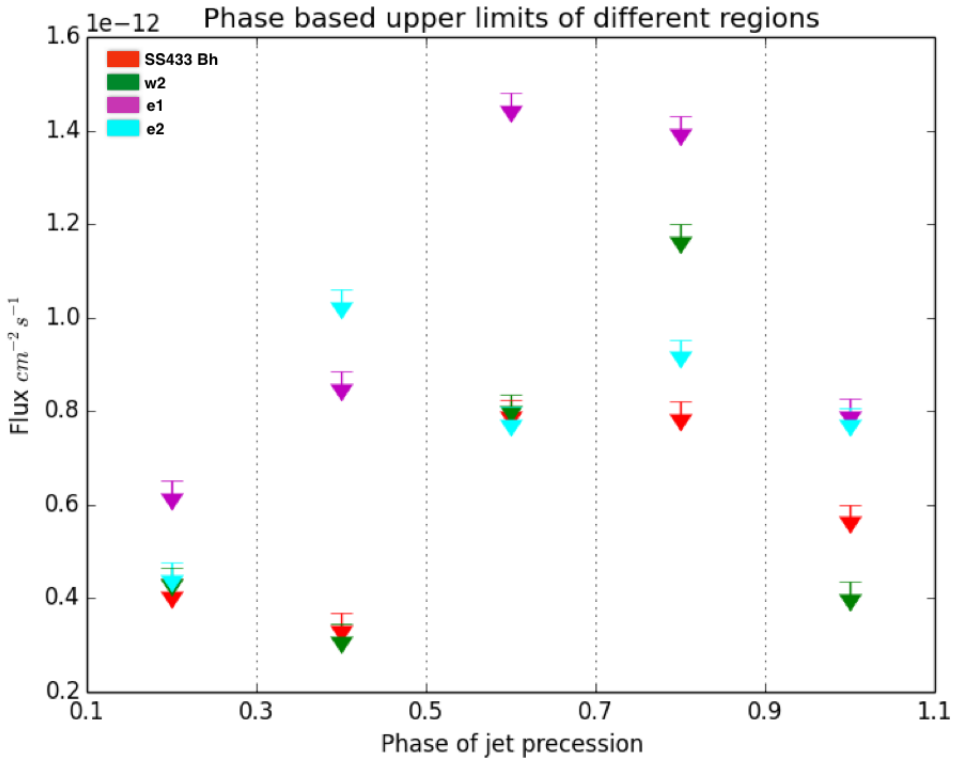

Figure 5.17: 99% confidence level flux upper limits for different phases of the SS433 system for the defined ROI.

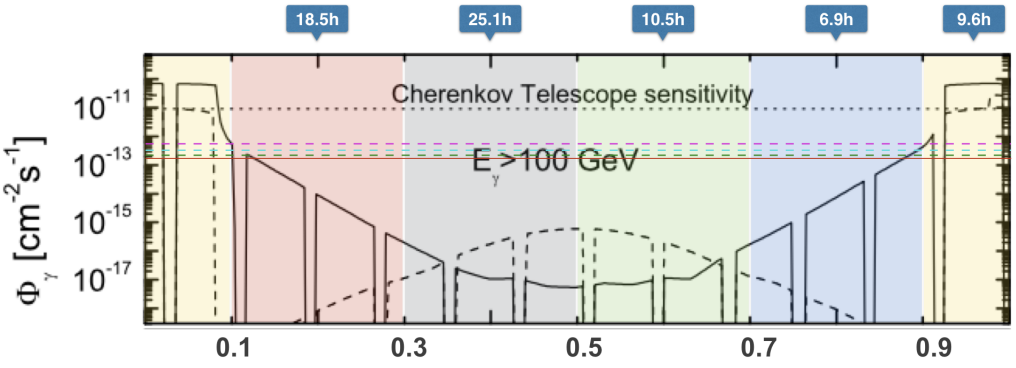

Figure 5.18: 99% confidence level flux upper limits for different ROI with same color scheme as before for the SS433 system.

CHAPTER 6

CONCLUSION

Many X-ray binaries have now also been detected at higher energies ($>$ 100 GeV), expanding our knowledge about sources that are capable of such efficient particle acceleration. Although predictions have been made that tens of gamma-ray binaries should be detected at TeV energies, only 6 have been discovered by the current generation of IACTs in their search over the past 13 years. The striking scarcity of TeV binaries warrants the need for better estimates of their population. Studying the currently known system will help constrain energetics of these systems and discern the conditions necessary for the formation of them in the first place. Comprehensive models exist for both microquasars and neutron stars as companions to massive optical stars in TeV binaries. While observations of PSR B1259-63 have confirmed that a pulsar in binary association with a Be star is capable of producing TeV emission, the same cannot be said for a microquasar binary systems. High-mass X-ray binaries which host microquasars like Cyg X-3, Cyg X-1, and SS433 are yet to be detected at TeV energies.

In this work, using 10 years of VERITAS observational data, new aspects of the LS I $+61^\circ$ 303 TeV binary system are discovered. Although different features of the binary can be explained by both the NS model and μQ model neither models comprehensively satisfy all the observational traits.

- Regular TeV outbursts continue from LS I $+61^\circ$ 303 near apastron phases $\phi_{0.55} - \phi_{0.65}$ seen during 2014, 2015 and 2016 observing seasons. The VHE spectrum during the outburst is stable with a spectral index of $(-2.5) \sim (-2.6)$. Exceptional TeV outbursts were observed from LS I $+61^\circ$ 303 during October to November, 2014 with fluxes $>$ 30% of the constant Crab Nebula flux. Photons with energy $>$ 10 TeV from the binary and a lack of spectral cutoff are indicative of particles with energies $\geq$ 10 TeV. Magnetic field $B \leq 0.03$ G for 10 TeV electrons and $B \leq 0.02$ G for 20

TeV electron at apastron are calculated using conservative estimates of the emission region (*139*).

- TeV flux variability is on a nightly scale. Significance flux differences from data recorded on consecutive nights were found for multiple pairs of observations at a $> 3\sigma$ level. Variability at a significance 5.15σ for one observational pair (the first two nights during October 2014 outburst) and the sharp transitions from flux upper limits to significantly detected fluxes over the course of 24 h during TeV outbursts are strongly suggestive of short-term variability in TeV at nightly timescales. The nightly variability assist in constraining the size of TeV emitting regions, i.e., the size of possible 'clumps' in the wind for pulsar binary models (*120*, *137*, *139*). Based on the X-ray variability seen on shorter times scales $\sim$ 100 s, the size of the emission region could be constrained to $< c\Delta t = 6 \times 10^{10}$ (*175*). Detection of such short variabilities are not possibile by current generation of IACTs which have longer integration timescales for a nominal detection of LS I $+61^{\circ}$ 303 .

- Clear correlation is seen between X-ray and TeV fluxes obtained from contemporaneous/simultaneous observation by Swift XRT and VERITAS . A Pearson correlation coefficient of $r = 0.756^{+0.09}_{-0.13}$ is calculated for the 20 pairs of observation that were sampled from 7 different orbits spanning over 3 observational seasons. Previously, a similar correlation was found during a single orbit in 2007 (in MAGIC, XMM-Newton, and Swift XRT data (*140*)). Straight line fits both sets of data had similar slopes and intercepts. The persistent correlation between X-ray and TeV fluxes strongly hints at a single parent particle population driving the emission in both these wavebands and they originate in the same locality of the binary system. The NS colliding wind model (*120*) where particles are accelerated at the shock front is preferred over the μQ model. The accelerated particle emits synchrotron X-rays and via synchrotron self-Compton processes low-energy photons from the surrounding medium are upscattered to TeV energies. The TeV/X-ray correlation could constrain the size of the emitting region to 10% of the orbital separation to a range of radii between $\sim 3 \times 10^{11}$ cm (at periastron) and $\sim 9 \times 10^{11}$ cm (at apastron) if the one-sove emitter in located close to the compact object (*180*). Some authors have argued that the VHE/X-ray

correlation seen by MAGIC was indicative of a local physical condition and cannot be established as steady overall behaviour (*217*). VERITAS observations have safely ruled out any such doubts by not only establishing persistant correlation between TeV/X-ray wavelengths over multiple orbits, but also by confirming the trend of the correlated fluxes that was seen previously by MAGIC.

- No correlation is found when comparing the TeV and GeV fluxes from the same UTC dates when LS I $+61^\circ$ 303 was observed by VERITAS and *Fermi*-LAT. The broad spectral energy distribution extending from MeV to TeV range had two distinct features. The observations for *Fermi*-LAT fitted well to a power-law with exponential cutoff. The exponential cutoff was at $\sim$ 4 GeV. The TeV part of the spectrum, using observations from VERITAS was a simple power-law. In all *Fermi*-LAT pulsars, an exponential cutoff to the power-law is seen in the 1-10 GeV range and the emission hypothesized to be curvature radiation in the outer pulsar magnetosphere (*7*). If LS I $+61^\circ$ 303 hosts a neutron star (pulsar whose beamed polar radiation is pointed away from earth), the noncorrelation between GeV and TeV radiation would be expected since they originate in two different particle populations in two different locations of the system. The GeV radiation from the outer magnetosphere of the pulsar and the TeV from the bow shock created by colliding stellar winds of the neutron star and the Be star. The GeV-TeV noncorrelation can also be explained in the framework of the NS flip-flop model (*143*). The pulsar's spin-down energy converted to HE gamma rays were assumed to be the origin of the observed GeV emission, whereas the TeV emission was attributed to the interaction of the Be star's wind with the strong 'Ejector' pulsar outflow.

- A quiescent TeV emission is now detected for the first time from LS I $+61^\circ$ 303 almost throughout its entire orbit. Besides the TeV outburst seen near apastron, the phase binned lightcurve shows a hint of elevated flux near periastron. The flip-flop pulsar model where the compact star switches between its propeller (at periastron) and ejector (at apastron) regimes could fit well with this behavior.

- Spectral study was performed in three different parts of the orbit, apastron passage where $0.5 < \phi_{apastron} < 0.8$, before periastron where $\phi_{BPeri} > 0.8$ & $\phi_{BPeri} < 0.2$

and after periastron $0.2 < \phi_{APeri} < 0.5$. The spectral index for $\phi_{apastron}$ and ϕ_{APeri} were $\sim$ 2.6 but that for ϕ_{BPeri} was about $\sim$ 2.8. Similar to LS 5039 where a cutoff is seen when the compact star is eclipsed by outflowing matter (*37*), LS I $+61^{\circ}$ 303 also changes its spectral behavior at superior conjunction passage. A softer spectral index is indicative of absorption of the higher energy photons which is also commonly seen in AGNs. The softer spectrum extends up to 3 TeV beyond which there could be a spectral cutoff but it cannot be confirmed due to low statistics. Greater absorption of photons in the higher end of the energy spectrum could be used to better model the geometry of the orbit, which would lead to better mass estimates for the compact star.

Both the μQ and binary pulsar model have their own merits, but neither model fully explains LS I $+61^{\circ}$ 303 . While the μQ model is able to predict the various temporal features of the system like rise times of X-ray and TeV emission and superorbital period from the astronomical beat phenomenon (*105*), it falls short on some key features that should be observable for an accreting blackhole. Thermal X-ray spectrum shows no evidence of accretion occurring in LS I $+61^{\circ}$ 303 and the this μQ models inability to accurately describe the observed high-energy spectrum is a severe shortcoming (*120*). The absence of pulsed emission from LS I $+61^{\circ}$ 303 fuels the debate in favor of the μQ model. The pulsar wind binary on the other hand predicts the broad band spectral behaviour relatively better (*120*). The changing morphology of a pulsar tail pointed away from the BE star observed in radio wavelength also supports the NS model (*122*). The recent discovery of superorbital modulation at TeV energies has refueled the pulsar flip-flop model (*163*). However there are valid concerns that a slow equatorial stellar wind would overcome an energetic pulsar wind and shape it into a cometary tail (*104*). A magnetar like outburst observed by *Swift* from the direction of LS I $+61^{\circ}$ 303 could even imply the presence of a magnetar in a binary system, a first of its kind (*143*).

The search for TeV emission from gamma-ray binary candidate SS433 was also performed using $\sim$ 70 h of VERITAS data. The region where the hadronic jets of the microquasar terminate in the interstellar medium are hotbeds of particle acceleration; emission at other wavelengths have been observed and TeV emission is predicted. The location of the blackhole, two locations in the eastern jet (e1 and e2) and one location at the western

jet (w2) have been searched for TeV emission. A hint of emission may be existent at e1 but detection is not claimed since the significance is $< 5\sigma$. For all 4 locations, the 99% flux upper limits are calculated. According to the *Reynoso* model, TeV emission is expected to be significantly absorbed except during certain phases of the jet's precession for the maximum accretion disc opening angle. VHE emission has been searched at the above mentioned 4 locations during relevant phases of maximum disc opening angle. No significant VHE gamma-ray emission is detected for the pertinent phases and the 99% flux upper limits have been calculated for them.

It is clear that the simple models are unable to adequately define a complex systems like LS I $+61^{\circ}$ 303 or SS433. Microquasar binaries may have much lower intrinsic gamma-ray fluxes which make them hard to detect. It took almost 7 years of *Fermi*-LAT data to get a weak detection of SS433. More sensitive next generation telescopes like CTA may provide definitive answers to the open questions posed by these unique systems (*218*). With CTA sensitivity it might be possible to detect TeV variability on $\sim$ 1000 s timescales and probe deeper into the acceleration mechanisms and the dynamical mechanisms underlying the VHE emission, which is a crucial step in understanding the apparently erratic variability.

REFERENCES

(1) Guo, F.; Li, H.; Daughton, W.; Liu, Y.-H. Formation of Hard Power Laws in the Energetic Particle Spectra Resulting from Relativistic Magnetic Reconnection. *Phys. Rev. Lett.* **2014**, *113*, 155005.

(2) Rieger, F. M.; Duffy, P. Particle Acceleration in Astrophysical Shear Flows. *Chin. J. Astron. Astrophys.* **2005**, *5*, 195.

(3) Tajima, T.; Dawson, J. M. Laser Electron Accelerator. *Phys. Rev. Lett.* **1979**, *43*, 267–270.

(4) Lorenz, E.; Wagner, R. Very High-Energy Gamma-Ray Astronomy. A 23-year Success Story in High-Energy Astroparticle Physics. *Eur. Phys. J. H* **2012**, *37*, 459–513.

(5) Longair, M. S. *High Energy Astrophysics*, 3rd ed.; Cambridge University Press: Cambridge, UK, 2011.

(6) Blumenthal, G. R.; Gould, R. J. Bremsstrahlung, Synchrotron Radiation, and Compton Scattering of High-Energy Electrons Traversing Dilute Gases. *Rev. Mod. Phys.* **1970**, *42*, 237–271.

(7) Abdo, A. A.; Ackermann, M.; Ajello, M.; Atwood, W. B.; Axelsson, M.; Baldini, L.; Ballet, J.; Barbiellini, G.; Baring, M. G.; Bastieri, D.; Baughman, B. M.; Bechtol, K.; Bellazzini, R.; Berenji, B.; Blandford, R. D.; Bloom, E. D.; Bonamente, E.; Borgland, A. W.; Bregeon, J.; Brez, A.; Brigida, M.; Bruel, P.; Burnett, T. H.; Buson, S.; Caliandro, G. A.; Cameron, R. A.; Camilo, F.; Caraveo, P. A.; Casandjian, J. M.; Cecchi, C.; elik, .; Charles, E.; Chekhtman, A.; Cheung, C. C.; Chiang, J.; Ciprini, S.; Claus, R.; Cognard, I.; Cohen-Tanugi, J.; Cominsky, L. R.; Conrad, J.; Corbet, R.; Cutini, S.; den Hartog, P. R.; Dermer, C. D.; de Angelis, A.; de Luca, A.; de Palma, F.; Digel, S. W.; Dormody, M.; do Couto e Silva, E.; Drell, P. S.; Dubois, R.; Dumora, D.; Espinoza, C.; Farnier, C.; Favuzzi, C.; Fegan, S. J.; Ferrara, E. C.; Focke, W. B.; Fortin, P.; Frailis, M.; Freire, P. C. C.; Fukazawa, Y.; Funk, S.; Fusco, P.; Gargano, F.; Gasparrini, D.; Gehrels, N.; Germani, S.; Giavitto, G.; Giebels, B.; Giglietto, N.; Giommi, P.; Giordano, F.; Glanzman, T.; Godfrey, G.; Gotthelf, E. V.; Grenier, I. A.; Grondin, M.-H.; Grove, J. E.; Guillemot, L.; Guiriec, S.; Gwon, C.; Hanabata, Y.; Harding, A. K.; Hayashida, M.; Hays, E.; Hughes, R. E.; Jackson, M. S.; Jhannesson, G.; Johnson, A. S.; Johnson, R. P.; Johnson, T. J.; Johnson, W. N.; Johnston, S.; Kamae, T.; Kanbach, G.; Kaspi, V. M.; Katagiri, H.; Kataoka, J.; Kawai, N.; Kerr, M.; Kndlseder, J.; Kocian, M. L.; Kramer, M.; Kuss, M.; Lande, J.; Latronico, L.; Lemoine-Goumard, M.; Livingstone, M.; Longo, F.; Loparco, F.; Lott, B.; Lovellette, M. N.; Lubrano, P.; Lyne, A. G.; Madejski, G. M.; Makeev, A.; Manchester, R. N.; Marelli, M.; Mazziotta, M. N.; McConville, W.; McEnery, J. E.; McGlynn, S.; Meurer, C.; Michelson, P. F.; Mineo, T.; Mitthumsiri, W.; Mizuno, T.; Moiseev, A. A.; Monte, C.; Monzani, M. E.; Morselli, A.; Moskalenko, I. V.; Murgia, S.; Nakamori, T.; Nolan, P. L.; Norris, J. P.; Noutsos, A.; Nuss, E.; Ohsugi, T.; Omodei, N.; Orlando, E.; Ormes, J. F.;

Ozaki, M.; Paneque, D.; Panetta, J. H.; Parent, D.; Pelassa, V.; Pepe, M.; Pesce-Rollins, M.; Piron, F.; Porter, T. A.; Rain, S.; Rando, R.; Ransom, S. M.; Ray, P. S.; Razzano, M.; Rea, N.; Reimer, A.; Reimer, O.; Reposeur, T.; Ritz, S.; Rodriguez, A. Y.; Romani, R. W.; Roth, M.; Ryde, F.; Sadrozinski, H. F.-W.; Sanchez, D.; Sander, A.; Parkinson, P. M. S.; Scargle, J. D.; Schalk, T. L.; Sellerholm, A.; Sgr, C.; Siskind, E. J.; Smith, D. A.; Smith, P. D.; Spandre, G.; Spinelli, P.; Stappers, B. W.; Starck, J.-L.; Striani, E.; Strickman, M. S.; Strong, A. W.; Suson, D. J.; Tajima, H.; Takahashi, H.; Takahashi, T.; Tanaka, T.; Thayer, J. B.; Thayer, J. G.; Theureau, G.; Thompson, D. J.; Thorsett, S. E.; Tibaldo, L.; Tibolla, O.; Torres, D. F.; Tosti, G.; Tramacere, A.; Uchiyama, Y.; Usher, T. L.; Etten, A. V.; Vasileiou, V.; Venter, C.; Vilchez, N.; Vitale, V.; Waite, A. P.; Wang, P.; Wang, N.; Watters, K.; Weltevrede, P.; Winer, B. L.; Wood, K. S.; Ylinen, T.; Ziegler, M. The First Fermi Large Area Telescope Catalog of Gamma-Ray Pulsars. *Astrophys. J., Suppl. Ser.* **2010**, *187*, 460.

(8) Olive, K.; Group, P. D. Review of Particle Physics. *Chin. Phys. C* **2014**, *38*, 090001.

(9) Halzen, F. IceCube in the Era of Multimessenger Astrophysics. *Mod. Phys. Lett. A* **2017**, *32*, 1730010.

(10) Dubus, G. Gamma-Ray Binaries and Related Systems. *Astron. Astrophys. Rev.* **2013**, *21*, 64.

(11) Bodaghee, A.; Tomsick, J. A.; Pottschmidt, K.; Rodriguez, J.; Wilms, J.; Pooley, G. G. Gamma-Ray Observations of the Microquasars Cygnus X-1, Cygnus X-3, GRS 1915+105, and GX 339-4 with the Fermi Large Area Telescope. *Astrophys. J.* **2013**, *775*, 98.

(12) Sabatini, S.; Tavani, M.; Coppi, P.; Pooley, G.; Del Santo, M.; Campana, R.; Chen, A.; Evangelista, Y.; Piano, G.; Bulgarelli, A.; Cattaneo, P. W.; Colafrancesco, S.; Del Monte, E.; Giuliani, A.; Giusti, M.; Longo, F.; Morselli, A.; Pellizzoni, A.; Pilia, M.; Striani, E.; Trifoglio, M.; Vercellone, S. Gamma-Ray Observations of Cygnus X-1 above 100 MeV in the Hard and Soft States. *Astrophys. J.* **2013**, *766*, 83.

(13) Piano, G.; Tavani, M.; Vittorini, V.; Trois, A.; Giuliani, A.; Bulgarelli, A.; Evangelista, Y.; Coppi, P.; Del Monte, E.; Sabatini, S.; Striani, E.; Donnarumma, I.; Hannikainen, D.; Koljonen, K. I. I.; McCollough, M.; Pooley, G.; Trushkin, S.; Zanin, R.; Barbiellini, G.; Cardillo, M.; Cattaneo, P. W.; Chen, A. W.; Colafrancesco, S.; Feroci, M.; Fuschino, F.; Giusti, M.; Longo, F.; Morselli, A.; Pellizzoni, A.; Pittori, C.; Pucella, G.; Rapisarda, M.; Rappoldi, A.; Soffitta, P.; Trifoglio, M.; Vercellone, S.; Verrecchia, F. The AGILE Monitoring of Cygnus X-3: Transient Gamma-Ray Emission and Spectral Constraints. *Astron. Astrophys.* **2012**, *545*, A110.

(14) Fermi LAT Collaboration,; Abdo, A. A.; Ackermann, M.; Ajello, M.; Axelsson, M.; Baldini, L.; Ballet, J.; Barbiellini, G.; Bastieri, D.; Baughman, B. M.; Bechtol, K.; Bellazzini, R.; Berenji, B.; Blandford, R. D.; Bloom, E. D.; Bonamente, E.; Borgland, A. W.; Brez, A.; Brigida, M.; Bruel, P.; Burnett, T. H.; Buson, S.; Caliandro, G. A.; Cameron, R. A.; Caraveo, P. A.; Casandjian, J. M.; Cecchi, C.; Çelik, Ö.; Chaty, S.; Cheung, C. C.; Chiang, J.; Ciprini, S.; Claus, R.; Cohen-Tanugi, J.; Cominsky, L. R.; Conrad, J.; Corbel, S.; Corbet, R.; Dermer, C. D.; de Palma, F.; Digel, S. W.; do Couto e Silva, E.; Drell, P. S.; Dubois, R.; Dubus, G.; Dumora, D.; Farnier, C.; Favuzzi, C.;

Fegan, S. J.; Focke, W. B.; Fortin, P.; Frailis, M.; Fusco, P.; Gargano, F.; Gehrels, N.; Germani, S.; Giavitto, G.; Giebels, B.; Giglietto, N.; Giordano, F.; Glanzman, T.; Godfrey, G.; Grenier, I. A.; Grondin, M.-H.; Grove, J. E.; Guillemot, L.; Guiriec, S.; Hanabata, Y.; Harding, A. K.; Hayashida, M.; Hays, E.; Hill, A. B.; Hjalmarsdotter, L.; Horan, D.; Hughes, R. E.; Jackson, M. S.; Jóhannesson, G.; Johnson, A. S.; Johnson, T. J.; Johnson, W. N.; Kamae, T.; Katagiri, H.; Kawai, N.; Kerr, M.; Knödlseder, J.; Kocian, M. L.; Koerding, E.; Kuss, M.; Lande, J.; Latronico, J.; Lemoine-Goumard, M.; Longo, F.; Loparco, F.; Lott, B.; Lovellette, M. N.; Lubrano, P.; Madejski, G. M.; Makeev, A.; Marchand, L.; Marelli, M.; Max-Moerbeck, W.; Mazziotta, M. N.; McColl, N.; McEnery, J. E.; Meurer, C.; Michelson, P. F.; Migliari, S.; Mitthumsiri, W.; Mizuno, T.; Monte, C.; Monzani, M. E.; Morselli, A.; Moskalenko, I. V.; Murgia, S.; Nolan, P. L.; Norris, J. P.; Nuss, E.; Ohsugi, T.; Omodei, N.; Ong, R. A.; Ormes, J. F.; Paneque, D.; Parent, D.; Pelassa, V.; Pepe, M.; Pesce-Rollins, M.; Piron, F.; Pooley, G.; Porter, T. A.; Pottschmidt, K.; Rainò, S.; Rando, R.; Ray, P. S.; Razzano, M.; Rea, N.; Readhead, A.; Reimer, A.; Reimer, O.; Richards, J. L.; Rochester, L. S.; Rodriguez, J.; Rodriguez, A. Y.; Romani, R. W.; Ryde, F.; Sadrozinski, H. F.-W.; Sander, A.; Saz Parkinson, P. M.; Sgrò, C.; Siskind, E. J.; Smith, D. A.; Smith, P. D.; Spinelli, P.; Starck, J.-L.; Stevenson, M.; Strickman, M. S.; Suson, D. J.; Takahashi, H.; Tanaka, T.; Thayer, J. B.; Thompson, D. J.; Tibaldo, L.; Tomsick, J. A.; Torres, D. F.; Tosti, G.; Tramacere, A.; Uchiyama, Y.; Usher, T. L.; Vasileiou, V.; Vilchez, N.; Vitale, V.; Waite, A. P.; Wang, P.; Wilms, J.; Winer, B. L.; Wood, K. W.; Ylinen, T.; Ziegler, M. Modulated High-Energy Gamma-Ray Emission from the Microquasar Cygnus X-3. *Science* **2009**, *326*, 1512.

(15) Zdziarski, A. A.; Maitra, C.; Frankowski, A.; Skinner, G. K.; Misra, R. Energy-dependent Orbital Modulation of X-rays and Constraints on Emission of the Jet in Cyg X-3. *Mon. Not. R. Astron. Soc.* **2012**, *426*, 1031–1042.

(16) Stawarz, Ł.; Aharonian, F.; Kataoka, J.; Ostrowski, M.; Siemiginowska, A.; Sikora, M. Dynamics and High-Energy Emission of the Flaring HST-1 Knot in the M 87 Jet. *Mon. Not. R. Astron. Soc.* **2006**, *370*, 981–992.

(17) Albert, J.; Aliu, E.; Anderhub, H.; Antoranz, P.; Armada, A.; Baixeras, C.; Barrio, J. A.; Bartko, H.; Bastieri, D.; Becker, J. K.; Bednarek, W.; Berger, K.; Bigongiari, C.; Biland, A.; Bock, R. K.; Bordas, P.; Bosch-Ramon, V.; Bretz, T.; Britvitch, I.; Camara, M.; Carmona, E.; Chilingarian, A.; Coarasa, J. A.; Commichau, S.; Contreras, J. L.; Cortina, J.; Costado, M. T.; Curtef, V.; Danielyan, V.; Dazzi, F.; De Angelis, A.; Delgado, C.; de los Reyes, R.; De Lotto, B.; Domingo-Santamaría, E.; Dorner, D.; Doro, M.; Errando, M.; Fagiolini, M.; Ferenc, D.; Fernández, E.; Firpo, R.; Flix, J.; Fonseca, M. V.; Font, L.; Fuchs, M.; Galante, N.; García-López, R. J.; Garczarczyk, M.; Gaug, M.; Giller, M.; Goebel, F.; Hakobyan, D.; Hayashida, M.; Hengstebeck, T.; Herrero, A.; Höhne, D.; Hose, J.; Hsu, C. C.; Jacon, P.; Jogler, T.; Kosyra, R.; Kranich, D.; Kritzer, R.; Laille, A.; Lindfors, E.; Lombardi, S.; Longo, F.; López, J.; López, M.; Lorenz, E.; Majumdar, P.; Maneva, G.; Mannheim, K.; Mansutti, O.; Mariotti, M.; Martínez, M.; Mazin, D.; Merck, C.; Meucci, M.; Meyer, M.; Miranda, J. M.; Mirzoyan, R.; Mizobuchi, S.; Moralejo, A.; Nieto, D.; Nilsson, K.; Ninkovic, J.; Oña-Wilhelmi, E.; Otte, N.; Oya, I.; Panniello, M.; Paoletti, R.; Paredes, J. M.; Pasanen, M.; Pascoli, D.; Pauss, F.; Pegna, R.; Persic, M.; Peruzzo, L.; Piccioli, A.; Prandini, E.; Puchades, N.; Raymers, A.; Rhode, W.; Ribó, M.; Rico, J.; Rissi, M.; Robert, A.;

Rügamer, S.; Saggion, A.; Saito, T.; Sánchez, A.; Sartori, P.; Scalzotto, V.; Scapin, V.; Schmitt, R.; Schweizer, T.; Shayduk, M.; Shinozaki, K.; Shore, S. N.; Sidro, N.; Sillanpää, A.; Sobczynska, D.; Stamerra, A.; Stark, L. S.; Takalo, L.; Temnikov, P.; Tescaro, D.; Teshima, M.; Torres, D. F.; Turini, N.; Vankov, H.; Vitale, V.; Wagner, R. M.; Wibig, T.; Wittek, W.; Zandanel, F.; Zanin, R.; Zapatero, J. Very High Energy Gamma-Ray Radiation from the Stellar Mass Black Hole Binary Cygnus X-1. *Astrophys. J. Lett.* **2007**, *665*, L51–L54.

(18) Zanin, R.; Fernández-Barral, A.; de Oña Wilhelmi, E.; Aharonian, F.; Blanch, O.; Bosch-Ramon, V.; Galindo, D. Gamma Rays Detected from Cygnus X-1 with Likely Jet Origin. *Astron. Astrophys.* **2016**, *596*, A55.

(19) Guenette, R.; VERITAS Collaboration, VERITAS Observations of X-ray Binaries. 31st. International Cosmic Ray Conference, Łódź, Poland. 2009.

(20) RICO, J. Search for VHE Signals from Microquasars with MAGIC. 32nd International Cosmic Ray Conference, Beijing, China. 2011; p 177.

(21) Dickinson, H.; Latham, I.; Chadwick, P. A Search for VHE γ-ray Binaries in the H.E.S.S. Galactic Plane Scan. 30th. International Cosmic Ray Conference, Merida, Yucatán. 2007; pp 637–640.

(22) Dubus, G. Gamma-Ray Emission from Binaries in Context. *C. R. Phys.* **2015**, *16*, 661–673.

(23) Lyne, A. G.; Stappers, B. W.; Keith, M. J.; Ray, P. S.; Kerr, M.; Camilo, F.; Johnson, T. J. The Binary Nature of PSR J2032+4127. *Mon. Not. R. Astron. Soc.* **2015**, *451*, 581–587.

(24) Ho, W. C. G.; Ng, C.-Y.; Lyne, A. G.; Stappers, B. W.; Coe, M. J.; Halpern, J. P.; Johnson, T. J.; Steele, I. A. Multiwavelength Monitoring and X-ray Brightening of Be X-ray Binary PSR J2032+4127/MT91 213 On Its Approach to Periastron. *Mon. Not. R. Astron. Soc.* **2017**, *464*, 1211–1219.

(25) Aliu, E.; Aune, T.; Behera, B.; Beilicke, M.; Benbow, W.; Berger, K.; Bird, R.; Buckley, J. H.; Bugaev, V.; Cardenzana, J. V.; Cerruti, M.; Chen, X.; Ciupik, L.; Connolly, M. P.; Cui, W.; Duke, C.; Dumm, J.; Errando, M.; Falcone, A.; Federici, S.; Feng, Q.; Finley, J. P.; Fortin, P.; Fortson, L.; Furniss, A.; Galante, N.; Gillanders, G. H.; Griffin, S.; Griffiths, S. T.; Grube, J.; Gyuk, G.; Hanna, D.; Holder, J.; Hughes, G.; Humensky, T. B.; Kaaret, P.; Kargaltsev, O.; Kertzman, M.; Khassen, Y.; Kieda, D.; Krawczynski, H.; Lang, M. J.; Madhavan, A. S.; Maier, G.; Majumdar, P.; McCann, A.; Moriarty, P.; Mukherjee, R.; Nieto, D.; O'Faoláin de Bhróithe, A.; Ong, R. A.; Otte, A. N.; Pandel, D.; Perkins, J. S.; Pohl, M.; Popkow, A.; Prokoph, H.; Quinn, J.; Ragan, K.; Rajotte, J.; Reyes, L. C.; Reynolds, P. T.; Richards, G. T.; Roache, E.; Sembroski, G. H.; Skole, C.; Staszak, D.; Telezhinsky, I.; Theiling, M.; Tucci, J. V.; Tyler, J.; Varlotta, A.; Vincent, S.; Wakely, S. P.; Weekes, T. C.; Weinstein, A.; Welsing, R.; Williams, D. A.; Zitzer, B. Observations of the Unidentified Gamma-Ray Source TeV J2032+4130 by VERITAS. *Astrophys. J.* **2014**, *783*, 16.

(26) Albert, J.; Aliu, E.; Anderhub, H.; Antoranz, P.; Baixeras, C.; Barrio, J. A.; Bartko, H.; Bastieri, D.; Becker, J. K.; Bednarek, W.; Berger, K.; Bigongiari, C.; Biland, A.;

Bock, R. K.; Bonnoli, G.; Bordas, P.; Bosch-Ramon, V.; Bretz, T.; Britvitch, I.; Camara, M.; Carmona, E.; Chilingarian, A.; Commichau, S.; Contreras, J. L.; Cortina, J.; Costado, M. T.; Curtef, V.; Dazzi, F.; De Angelis, A.; Delgado, C.; de los Reyes, R.; Domingo-Santamaría, E.; De Lotto, B.; De Maria, M.; De Sabata, F.; Dorner, D.; Doro, M.; Errando, M.; Fagiolini, M.; Ferenc, D.; Fernández, E.; Firpo, R.; Fonseca, M. V.; Font, L.; Galante, N.; García-López, R. J.; Garczarczyk, M.; Gaug, M.; Goebel, F.; Hayashida, M.; Herrero, A.; Höhne, D.; Hose, J.; Hsu, C. C.; Huber, S.; Jogler, T.; Kosyra, R.; Kranich, D.; Laille, A.; Leonardo, E.; Lindfors, E.; Lombardi, S.; Longo, F.; López, M.; Lorenz, E.; Majumdar, P.; Maneva, G.; Mankuzhiyil, N.; Mannheim, K.; Mariotti, M.; Martínez, M.; Mazin, D.; Merck, C.; Meucci, M.; Meyer, M.; Miranda, J. M.; Mirzoyan, R.; Mizobuchi, S.; Moralejo, A.; Nieto, D.; Nilsson, K.; Ninkovic, J.; Oña-Wilhelmi, E.; Otte, N.; Oya, I.; Panniello, M.; Paoletti, R.; Paredes, J. M.; Pasanen, M.; Pascoli, D.; Pauss, F.; Pegna, R.; Persic, M.; Peruzzo, L.; Piccioli, A.; Prandini, E.; Puchades, N.; Raymers, A.; Rhode, W.; Ribó, M.; Rico, J.; Rissi, M.; Robert, A.; Rügamer, S.; Saggion, A.; Saito, T. Y.; Sánchez, A.; Sartori, P.; Scalzotto, V.; Scapin, V.; Schmitt, R.; Schweizer, T.; Shayduk, M.; Shinozaki, K.; Shore, S. N.; Sidro, N.; Sillanpää, A.; Sobczynska, D.; Spanier, F.; Stamerra, A.; Stark, L. S.; Takalo, L.; Temnikov, P.; Tescaro, D.; Teshima, M.; Torres, D. F.; Turini, N.; Vankov, H.; Venturini, A.; Vitale, V.; Wagner, R. M.; Wittek, W.; Zandanel, F.; Zanin, R.; Zapatero, J. MAGIC Observations of the Unidentified γ-Ray Source TeV J2032+4130. *Astrophys. J. Lett.* **2008**, *675*, L25.

(27) Abdo, A. A.; Ackermann, M.; Ajello, M.; Atwood, W. B.; Baldini, L.; Ballet, J.; Barbiellini, G.; Bastieri, D.; Bechtol, K.; Bellazzini, R.; Berenji, B.; Blandford, R. D.; Bloom, E. D.; Bonamente, E.; Borgland, A. W.; Bouvier, A.; Brandt, T. J.; Bregeon, J.; Brez, A.; Brigida, M.; Bruel, P.; Buehler, R.; Burnett, T. H.; Buson, S.; Caliandro, G. A.; Cameron, R. A.; Caraveo, P. A.; Carrigan, S.; Casandjian, J. M.; Cecchi, C.; Çelik, Ö.; Charles, E.; Chaty, S.; Chekhtman, A.; Cheung, C. C.; Chiang, J.; Ciprini, S.; Claus, R.; Cohen-Tanugi, J.; Conrad, J.; Corbel, S.; Corbet, R.; DeCesar, M. E.; den Hartog, P. R.; Dermer, C. D.; de Palma, F.; Digel, S. W.; Donato, D.; do Couto e Silva, E.; Drell, P. S.; Dubois, R.; Dubus, G.; Dumora, D.; Favuzzi, C.; Fegan, S. J.; Ferrara, E. C.; Fortin, P.; Frailis, M.; Fuhrmann, L.; Fukazawa, Y.; Funk, S.; Fusco, P.; Gargano, F.; Gasparrini, D.; Gehrels, N.; Germani, S.; Giglietto, N.; Giordano, F.; Giroletti, M.; Glanzman, T.; Godfrey, G.; Grenier, I. A.; Grondin, M.-H.; Grove, J. E.; Guiriec, S.; Hadasch, D.; Harding, A. K.; Hayashida, M.; Hays, E.; Healey, S. E.; Hill, A. B.; Horan, D.; Hughes, R. E.; Itoh, R.; Jean, P.; Jóhannesson, G.; Johnson, A. S.; Johnson, R. P.; Johnson, T. J.; Johnson, W. N.; Kamae, T.; Katagiri, H.; Kataoka, J.; Kerr, M.; Knödlseder, J.; Koerding, E.; Kuss, M.; Lande, J.; Latronico, L.; Lee, S.-H.; Lemoine-Goumard, M.; Llena Garde, M.; Longo, F.; Loparco, F.; Lott, B.; Lovellette, M. N.; Lubrano, P.; Makeev, A.; Mazziotta, M. N.; McConville, W.; McEnery, J. E.; Mehault, J.; Michelson, P. F.; Mizuno, T.; Moiseev, A. A.; Monte, C.; Monzani, M. E.; Morselli, A.; Moskalenko, I. V.; Murgia, S.; Nakamori, T.; Naumann-Godo, M.; Nestoras, I.; Nolan, P. L.; Norris, J. P.; Nuss, E.; Ohno, M.; Ohsugi, T.; Okumura, A.; Omodei, N.; Orlando, E.; Ormes, J. F.; Ozaki, M.; Paneque, D.; Panetta, J. H.; Parent, D.; Pelassa, V.; Pepe, M.; Pesce-Rollins, M.; Piron, F.; Porter, T. A.; Rainò, S.; Rando, R.; Ray, P. S.; Razzano, M.; Razzaque, S.; Rea, N.; Reimer, A.; Reimer, O.; Reposeur, T.; Ripken, J.; Ritz, S.; Romani, R. W.; Roth, M.; Sadrozinski, H. F.-W.; Sander, A.; Saz Parkinson, P. M.; Scargle, J. D.; Schinzel, F. K.; Sgrò, C.; Shaw, M. S.; Siskind, E. J.;

Smith, D. A.; Smith, P. D.; Sokolovsky, K. V.; Spandre, G.; Spinelli, P.; Stawarz, Ł.; Strickman, M. S.; Suson, D. J.; Takahashi, H.; Takahashi, T.; Tanaka, T.; Tanaka, Y.; Thayer, J. B.; Thayer, J. G.; Thompson, D. J.; Tibaldo, L.; Torres, D. F.; Tosti, G.; Tramacere, A.; Uchiyama, Y.; Usher, T. L.; Vandenbroucke, J.; Vasileiou, V.; Vilchez, N.; Vitale, V.; Waite, A. P.; Wallace, E.; Wang, P.; Winer, B. L.; Wolff, M. T.; Wood, K. S.; Yang, Z.; Ylinen, T.; Ziegler, M.; Maehara, H.; Nishiyama, K.; Kabashima, F.; Bach, U.; Bower, G. C.; Falcone, A.; Forster, J. R.; Henden, A.; Kawabata, K. S.; Koubsky, P.; Mukai, K.; Nelson, T.; Oates, S. R.; Sakimoto, K.; Sasada, M.; Shenavrin, V. I.; Shore, S. N.; Skinner, G. K.; Sokoloski, J.; Stroh, M.; Tatarnikov, A. M.; Uemura, M.; Wahlgren, G. M.; Yamanaka, M. Gamma-Ray Emission Concurrent with the Nova in the Symbiotic Binary V407 Cygni. *Science* **2010**, *329*, 817–821.

(28) Ackermann, M.; Ajello, M.; Albert, A.; Baldini, L.; Ballet, J.; Barbiellini, G.; Bastieri, D.; Bellazzini, R.; Bissaldi, E.; Blandford, R. D.; Bloom, E. D.; Bottacini, E.; Brandt, T. J.; Bregeon, J.; Bruel, P.; Buehler, R.; Buson, S.; Caliandro, G. A.; Cameron, R. A.; Caragiulo, M.; Caraveo, P. A.; Cavazzuti, E.; Charles, E.; Chekhtman, A.; Cheung, C. C.; Chiang, J.; Chiaro, G.; Ciprini, S.; Claus, R.; Cohen-Tanugi, J.; Conrad, J.; Corbel, S.; D'Ammando, F.; de Angelis, A.; den Hartog, P. R.; de Palma, F.; Dermer, C. D.; Desiante, R.; Digel, S. W.; Di Venere, L.; do Couto e Silva, E.; Donato, D.; Drell, P. S.; Drlica-Wagner, A.; Favuzzi, C.; Ferrara, E. C.; Focke, W. B.; Franckowiak, A.; Fuhrmann, L.; Fukazawa, Y.; Fusco, P.; Gargano, F.; Gasparrini, D.; Germani, S.; Giglietto, N.; Giordano, F.; Giroletti, M.; Glanzman, T.; Godfrey, G.; Grenier, I. A.; Grove, J. E.; Guiriec, S.; Hadasch, D.; Harding, A. K.; Hayashida, M.; Hays, E.; Hewitt, J. W.; Hill, A. B.; Hou, X.; Jean, P.; Jogler, T.; Jóhannesson, G.; Johnson, A. S.; Johnson, W. N.; Kerr, M.; Knödlseder, J.; Kuss, M.; Larsson, S.; Latronico, L.; Lemoine-Goumard, M.; Longo, F.; Loparco, F.; Lott, B.; Lovellette, M. N.; Lubrano, P.; Manfreda, A.; Martin, P.; Massaro, F.; Mayer, M.; Mazziotta, M. N.; McEnery, J. E.; Michelson, P. F.; Mitthumsiri, W.; Mizuno, T.; Monzani, M. E.; Morselli, A.; Moskalenko, I. V.; Murgia, S.; Nemmen, R.; Nuss, E.; Ohsugi, T.; Omodei, N.; Orienti, M.; Orlando, E.; Ormes, J. F.; Paneque, D.; Panetta, J. H.; Perkins, J. S.; Pesce-Rollins, M.; Piron, F.; Pivato, G.; Porter, T. A.; Rainò, S.; Rando, R.; Razzano, M.; Razzaque, S.; Reimer, A.; Reimer, O.; Reposeur, T.; Saz Parkinson, P. M.; Schaal, M.; Schulz, A.; Sgrò, C.; Siskind, E. J.; Spandre, G.; Spinelli, P.; Stawarz, Ł.; Suson, D. J.; Takahashi, H.; Tanaka, T.; Thayer, J. G.; Thayer, J. B.; Thompson, D. J.; Tibaldo, L.; Tinivella, M.; Torres, D. F.; Tosti, G.; Troja, E.; Uchiyama, Y.; Vianello, G.; Winer, B. L.; Wolff, M. T.; Wood, D. L.; Wood, K. S.; Wood, M.; Charbonnel, S.; Corbet, R. H. D.; De Gennaro Aquino, I.; Edlin, J. P.; Mason, E.; Schwarz, G. J.; Shore, S. N.; Starrfield, S.; Teyssier, F.; Fermi-LAT Collaboration, Fermi Establishes Classical Novae as a Distinct Class of Gamma-Ray Sources. *Science* **2014**, *345*, 554–558.

(29) Aliu, E.; Archambault, S.; Arlen, T.; Aune, T.; Beilicke, M.; Benbow, W.; Bouvier, A.; Bradbury, S. M.; Buckley, J. H.; Bugaev, V.; Byrum, K.; Cannon, A.; Cesarini, A.; Ciupik, L.; Collins-Hughes, E.; Connolly, M. P.; Cui, W.; Decerprit, G.; Dickherber, R.; Duke, C.; Dumm, J.; Dwarkadas, V. V.; Errando, M.; Falcone, A.; Feng, Q.; Finley, J. P.; Finnegan, G.; Fortson, L.; Furniss, A.; Galante, N.; Gall, D.; Godambe, S.; Griffin, S.; Grube, J.; Gyuk, G.; Hanna, D.; Holder, J.; Huan, H.; Hughes, G.; Humensky, T. B.; Kaaret, P.; Karlsson, N.; Kertzman, M.; Khassen, Y.; Kieda, D.; Krawczynski, H.; Krennrich, F.; Lang, M. J.; Lee, K.; Maier, G.; Majumdar, P.; McArthur, S.; Mc-

Cann, A.; Millis, J.; Moriarty, P.; Mukherjee, R.; Nuñez, P. D.; Ong, R. A.; Orr, M.; Otte, A. N.; Pandel, D.; Park, N.; Perkins, J. S.; Pohl, M.; Prokoph, H.; Quinn, J.; Ragan, K.; Reyes, L. C.; Reynolds, P. T.; Roache, E.; Rose, H. J.; Ruppel, J.; Saxon, D. B.; Schroedter, M.; Sembroski, G. H.; Skole, C.; Smith, A. W.; Staszak, D.; Telezhinsky, I.; Tešić, G.; Theiling, M.; Thibadeau, S.; Tsurusaki, K.; Tyler, J.; Varlotta, A.; Vincent, S.; Vivier, M.; Wakely, S. P.; Ward, J. E.; Weekes, T. C.; Weinstein, A.; Weisgarber, T.; Welsing, R.; Williams, D. A.; Zitzer, B. VERITAS Observations of the Nova in V407 Cygni. *Astrophys. J.* **2012**, *754*, 77.

(30) Tavani, M.; Sabatini, S.; Pian, E.; Bulgarelli, A.; Caraveo, P.; Viotti, R. F.; Corcoran, M. F.; Giuliani, A.; Pittori, C.; Verrecchia, F.; Vercellone, S.; Mereghetti, S.; Argan, A.; Barbiellini, G.; Boffelli, F.; Cattaneo, P. W.; Chen, A. W.; Cocco, V.; D'Ammando, F.; Costa, E.; DeParis, G.; Del Monte, E.; Di Cocco, G.; Donnarumma, I.; Evangelista, Y.; Ferrari, A.; Feroci, M.; Fiorini, M.; Froysland, T.; Fuschino, F.; Galli, M.; Gianotti, F.; Labanti, C.; Lapshov, I.; Lazzarotto, F.; Lipari, P.; Longo, F.; Marisaldi, M.; Mastropietro, M.; Morelli, E.; Moretti, E.; Morselli, A.; Pacciani, L.; Pellizzoni, A.; Perotti, F.; Piano, G.; Picozza, P.; Pilia, M.; Porrovecchio, G.; Pucella, G.; Prest, M.; Rapisarda, M.; Rappoldi, A.; Rubini, A.; Soffitta, P.; Trifoglio, M.; Trois, A.; Vallazza, E.; Vittorini, V.; Zambra, A.; Zanello, D.; Santolamazza, P.; Giommi, P.; Colafrancesco, S.; Antonelli, L. A.; Salotti, L. Detection of Gamma-Ray Emission from the Eta-Carinae Region. *Astrophys. J. Lett.* **2009**, *698*, L142–L146.

(31) Eichler, D.; Usov, V. Particle Acceleration and Nonthermal Radio Emission in Binaries of Early-Type Stars. *Astrophys. J.* **1993**, *402*, 271–279.

(32) Tavani, M.; Arons, J. Theory of High-Energy Emission from the Pulsar/Be Star System PSR 1259-63. I. Radiation Mechanisms and Interaction Geometry. *Astrophys. J.* **1997**, *477*, 439–464.

(33) Chernyakova, M.; Neronov, A.; Lutovinov, A.; Rodriguez, J.; Johnston, S. XMM-Newton Observations of PSR B1259-63 Near the 2004 Periastron Passage. *Mon. Not. R. Astron. Soc.* **2006**, *367*, 1201–1208.

(34) Khangulyan, D.; Hnatic, S.; Aharonian, F.; Bogovalov, S. TeV Light Curve of PSR B1259-63/SS2883. *Mon. Not. R. Astron. Soc.* **2007**, *380*, 320–330.

(35) Abdo, A. A.; Ackermann, M.; Ajello, M.; Allafort, A.; Ballet, J.; Barbiellini, G.; Bastieri, D.; Bechtol, K.; Bellazzini, R.; Berenji, B.; Blandford, R. D.; Bonamente, E.; Borgland, A. W.; Bregeon, J.; Brigida, M.; Bruel, P.; Buehler, R.; Buson, S.; Caliandro, G. A.; Cameron, R. A.; Camilo, F.; Caraveo, P. A.; Cecchi, C.; Charles, E.; Chaty, S.; Chekhtman, A.; Chernyakova, M.; Cheung, C. C.; Chiang, J.; Ciprini, S.; Claus, R.; Cohen-Tanugi, J.; Cominsky, L. R.; Corbel, S.; Cutini, S.; D'Ammando, F.; de Angelis, A.; den Hartog, P. R.; de Palma, F.; Dermer, C. D.; Digel, S. W.; Silva, E. d. C. e.; Dormody, M.; Drell, P. S.; Drlica-Wagner, A.; Dubois, R.; Dubus, G.; Dumora, D.; Enoto, T.; Espinoza, C. M.; Favuzzi, C.; Fegan, S. J.; Ferrara, E. C.; Focke, W. B.; Fortin, P.; Fukazawa, Y.; Funk, S.; Fusco, P.; Gargano, F.; Gasparrini, D.; Gehrels, N.; Germani, S.; Giglietto, N.; Giommi, P.; Giordano, F.; Giroletti, M.; Glanzman, T.; Godfrey, G.; Grenier, I. A.; Grondin, M.-H.; Grove, J. E.; Grundstrom, E.; Guiriec, S.; Gwon, C.; Hadasch, D.; Harding, A. K.; Hayashida, M.; Hays, E.; Jóhannesson, G.; Johnson, A. S.; Johnson, T. J.; Johnston, S.; Kamae, T.;

Katagiri, H.; Kataoka, J.; Keith, M.; Kerr, M.; Knödlseder, J.; Kramer, M.; Kuss, M.; Lande, J.; Lee, S.-H.; Lemoine-Goumard, M.; Longo, F.; Loparco, F.; Lovellette, M. N.; Lubrano, P.; Manchester, R. N.; Marelli, M.; Mazziotta, M. N.; Michelson, P. F.; Mitthumsiri, W.; Mizuno, T.; Moiseev, A. A.; Monte, C.; Monzani, M. E.; Morselli, A.; Moskalenko, I. V.; Murgia, S.; Nakamori, T.; Naumann-Godo, M.; Neronov, A.; Nolan, P. L.; Norris, J. P.; Noutsos, A.; Nuss, E.; Ohsugi, T.; Okumura, A.; Omodei, N.; Orlando, E.; Paneque, D.; Parent, D.; Pesce-Rollins, M.; Pierbattista, M.; Piron, F.; Porter, T. A.; Possenti, A.; Rainò, S.; Rando, R.; Ray, P. S.; Razzano, M.; Razzaque, S.; Reimer, A.; Reimer, O.; Reposeur, T.; Ritz, S.; Sadrozinski, H. F.-W.; Scargle, J. D.; Sgrò, C.; Shannon, R.; Siskind, E. J.; Smith, P. D.; Spandre, G.; Spinelli, P.; Strickman, M. S.; Suson, D. J.; Takahashi, H.; Tanaka, T.; Thayer, J. G.; Thayer, J. B.; Thompson, D. J.; Thorsett, S. E.; Tibaldo, L.; Tibolla, O.; Torres, D. F.; Tosti, G.; Troja, E.; Uchiyama, Y.; Usher, T. L.; Vandenbroucke, J.; Vasileiou, V.; Vianello, G.; Vitale, V.; Waite, A. P.; Wang, P.; Winer, B. L.; Wolff, M. T.; Wood, D. L.; Wood, K. S.; Yang, Z.; Ziegler, M.; Zimmer, S. Discovery of High-energy Gamma-Ray Emission from the Binary System PSR B1259-63/LS 2883 around Periastron with Fermi. *Astrophys. J. Lett.* **2011**, *736*, L11.

(36) Aharonian, F.; Akhperjanian, A. G.; Aye, K.-M.; Bazer-Bachi, A. R.; Beilicke, M.; Benbow, W.; Berge, D.; Berghaus, P.; Bernlöhr, K.; Boisson, C.; Bolz, O.; Borrel, V.; Braun, I.; Breitling, F.; Brown, A. M.; Gordo, J. B.; Chadwick, P. M.; Chounet, L.-M.; Cornils, R.; Costamante, L.; Degrange, B.; Dickinson, H. J.; Djannati-Ataï, A.; Drury, L. O.; Dubus, G.; Emmanoulopoulos, D.; Espigat, P.; Feinstein, F.; Fleury, P.; Fontaine, G.; Fuchs, Y.; Funk, S.; Gallant, Y. A.; Giebels, B.; Gillessen, S.; Glicenstein, J. F.; Goret, P.; Hadjichristidis, C.; Hauser, M.; Heinzelmann, G.; Henri, G.; Hermann, G.; Hinton, J. A.; Hofmann, W.; Holleran, M.; Horns, D.; Jacholkowska, A.; de Jager, O. C.; Khélifi, B.; Komin, N.; Konopelko, A.; Latham, I. J.; Le Gallou, R.; Lemière, A.; Lemoine-Goumard, M.; Leroy, N.; Lohse, T.; Marcowith, A.; Martin, J.-M.; Martineau-Huynh, O.; Masterson, C.; McComb, T. J. L.; de Naurois, M.; Nolan, S. J.; Noutsos, A.; Orford, K. J.; Osborne, J. L.; Ouchrif, M.; Panter, M.; Pelletier, G.; Pita, S.; Pühlhofer, G.; Punch, M.; Raubenheimer, B. C.; Raue, M.; Raux, J.; Rayner, S. M.; Reimer, A.; Reimer, O.; Ripken, J.; Rob, L.; Rolland, L.; Rowell, G.; Sahakian, V.; Saugé, L.; Schlenker, S.; Schlickeiser, R.; Schuster, C.; Schwanke, U.; Siewert, M.; Sol, H.; Spangler, D.; Steenkamp, R.; Stegmann, C.; Tavernet, J.-P.; Terrier, R.; Théoret, C. G.; Tluczykont, M.; Vasileiadis, G.; Venter, C.; Vincent, P.; Völk, H. J.; Wagner, S. J. Discovery of Very High Energy Gamma Rays Associated with an X-ray Binary. *Science* **2005**, *309*, 746–749.

(37) Mariaud, C.; Bordas, P.; Aharonian, F.; Boettcher, M.; Dubus, G.; de Naurois, M.; Romoli, C.; V. Zabalza for the H. E. S. S. Collaboration, VHE Observations of the Gamma-Ray Binary system LS 5039 with H.E.S.S. 2015, arXiv:astro-ph.HE/1509.05791. arXiv.org e-Print archive. https://arxiv.org/abs/1509.05791 (accessed May 30, 2017).

(38) Aharonian, F.; Anchordoqui, L.; Khangulyan, D.; Montaruli, T. Microquasar LS 5039: A TeV Gamma-Ray Emitter and a Potential TeV Neutrino Source. J. of Phys. Conf. Ser., Zaragoza, Spain. 2006; pp 408–415.

(39) Aharonian, F. A.; Akhperjanian, A. G.; Bazer-Bachi, A. R.; Behera, B.; Beilicke, M.; Benbow, W.; Berge, D.; Bernlöhr, K.; Boisson, C.; Bolz, O.; Borrel, V.; Braun, I.;

Brion, E.; Brown, A. M.; Bühler, R.; Büsching, I.; Boutelier, T.; Carrigan, S.; Chadwick, P. M.; Chounet, L.-M.; Coignet, G.; Cornils, R.; Costamante, L.; Degrange, B.; Dickinson, H. J.; Djannati-Ataï, A.; Domainko, W.; O'C. Drury, L.; Dubus, G.; Egberts, K.; Emmanoulopoulos, D.; Espigat, P.; Farnier, C.; Feinstein, F.; Fiasson, A.; Förster, A.; Fontaine, G.; Funk, S.; Funk, S.; Füßling, M.; Gallant, Y. A.; Giebels, B.; Glicenstein, J. F.; Glück, B.; Goret, P.; Hadjichristidis, C.; Hauser, D.; Hauser, M.; Heinzelmann, G.; Henri, G.; Hermann, G.; Hinton, J. A.; Hoffmann, A.; Hofmann, W.; Holleran, M.; Hoppe, S.; Horns, D.; Jacholkowska, A.; de Jager, O. C.; Kendziorra, E.; Kerschhaggl, M.; Khélifi, B.; Komin, N.; Kosack, K.; Lamanna, G.; Latham, I. J.; Le Gallou, R.; Lemière, A.; Lemoine-Goumard, M.; Lohse, T.; Martin, J. M.; Martineau-Huynh, O.; Marcowith, A.; Masterson, C.; Maurin, G.; McComb, T. J. L.; Moulin, E.; de Naurois, M.; Nedbal, D.; Nolan, S. J.; Noutsos, A.; Olive, J.-P.; Orford, K. J.; Osborne, J. L.; Panter, M.; Pedaletti, G.; Pelletier, G.; Petrucci, P.-O.; Pita, S.; Pühlhofer, G.; Punch, M.; Ranchon, S.; Raubenheimer, B. C.; Raue, M.; Rayner, S. M.; Reimer, O.; Ripken, J.; Rob, L.; Rolland, L.; Rosier-Lees, S.; Rowell, G.; Ruppel, J.; Sahakian, V.; Santangelo, A.; Saugé, L.; Schlenker, S.; Schlickeiser, R.; Schröder, R.; Schwanke, U.; Schwarzburg, S.; Schwemmer, S.; Shalchi, A.; Sol, H.; Spangler, D.; Steenkamp, R.; Stegmann, C.; Superina, G.; Tam, P. H.; Tavernet, J.-P.; Terrier, R.; Tluczykont, M.; van Eldik, C.; Vasileiadis, G.; Venter, C.; Vialle, J. P.; Vincent, P.; Völk, H. J.; Wagner, S. J.; Ward, M.; Moriguchi, Y.; Fukui, Y. Discovery of a Point-like Very-High-Energy γ-ray Source in Monoceros. *Astron. Astrophys.* **2007**, *469*, L1–L4.

(40) Caliandro, G. A.; Hill, A. B.; Torres, D. F.; Hadasch, D.; Ray, P.; Abdo, A.; Hessels, J. W. T.; Ridolfi, A.; Possenti, A.; Burgay, M.; Rea, N.; Tam, P. H. T.; Dubois, R.; Dubus, G.; Glanzman, T.; Jogler, T. The Missing GeV γ-ray Binary: Searching for HESS J0632+057 with Fermi-LAT. *Mon. Not. R. Astron. Soc.* **2013**, *436*, 740–749.

(41) Mori, M.; Kawachi, A.; Nagataki, S.; Naito, T. Fermi-LAT Study of Two Gamma-Ray Binaries, HESS J0632+057 and AGL J2241+4454. 2013, arXiv:astro-ph.HE/1303.1606. arXiv.org e-Print archive. https://arxiv.org/abs/1303.1606 (accessed May 30, 2017).

(42) Maier, G. VHE Observations of the Binary Candidate HESS J0632+057 with H.E.S.S. and VERITAS. 32nd International Cosmic Ray Conference, Beijing, China. 2011; p 79.

(43) Aleksić, J.; Alvarez, E. A.; Antonelli, L. A.; Antoranz, P.; Asensio, M.; Backes, M.; Barres de Almeida, U.; Barrio, J. A.; Bastieri, D.; Becerra González, J.; Bednarek, W.; Berger, K.; Bernardini, E.; Biland, A.; Blanch, O.; Bock, R. K.; Boller, A.; Bonnoli, G.; Borla Tridon, D.; Bosch-Ramon, V.; Bretz, T.; Cañellas, A.; Carmona, E.; Carosi, A.; Colin, P.; Colombo, E.; Contreras, J. L.; Cortina, J.; Cossio, L.; Covino, S.; Da Vela, P.; Dazzi, F.; De Angelis, A.; De Caneva, G.; De Cea del Pozo, E.; De Lotto, B.; Delgado Mendez, C.; Diago Ortega, A.; Doert, M.; Domínguez, A.; Dominis Prester, D.; Dorner, D.; Doro, M.; Eisenacher, D.; Elsaesser, D.; Ferenc, D.; Fonseca, M. V.; Font, L.; Fruck, C.; García López, R. J.; Garczarczyk, M.; Garrido Terrats, D.; Giavitto, G.; Godinović, N.; González Muñoz, A.; Gozzini, S. R.; Hadasch, D.; Häfner, D.; Herrero, A.; Hildebrand, D.; Hose, J.; Hrupec, D.; Huber, B.; Jankowski, F.; Jogler, T.; Kadenius, V.; Kellermann, H.; Klepser, S.; Krähenbühl, T.; Krause, J.; La Barbera, A.; Lelas, D.; Leonardo, E.; Lewandowska, N.; Lindfors, E.; Lombardi, S.; López, M.; López-Coto, R.; López-Oramas, A.; Lorenz, E.;

Makariev, M.; Maneva, G.; Mankuzhiyil, N.; Mannheim, K.; Maraschi, L.; Mariotti, M.; Martínez, M.; Mazin, D.; Meucci, M.; Miranda, J. M.; Mirzoyan, R.; Moldón, J.; Moralejo, A.; Munar-Adrover, P.; Niedzwiecki, A.; Nieto, D.; Nilsson, K.; Nowak, N.; Orito, R.; Paiano, S.; Paneque, D.; Paoletti, R.; Pardo, S.; Paredes, J. M.; Partini, S.; Perez-Torres, M. A.; Persic, M.; Pilia, M.; Pochon, J.; Prada, F.; Prada Moroni, P. G.; Prandini, E.; Puerto Gimenez, I.; Puljak, I.; Reichardt, I.; Reinthal, R.; Rhode, W.; Ribó, M.; Rico, J.; Rügamer, S.; Saggion, A.; Saito, K.; Saito, T. Y.; Salvati, M.; Satalecka, K.; Scalzotto, V.; Scapin, V.; Schultz, C.; Schweizer, T.; Shore, S. N.; Sillanpää, A.; Sitarek, J.; Snidaric, I.; Sobczynska, D.; Spanier, F.; Spiro, S.; Stamatescu, V.; Stamerra, A.; Steinke, B.; Storz, J.; Strah, N.; Sun, S.; Surić, T.; Takalo, L.; Takami, H.; Tavecchio, F.; Temnikov, P.; Terzić, T.; Tescaro, D.; Teshima, M.; Tibolla, O.; Torres, D. F.; Treves, A.; Uellenbeck, M.; Vogler, P.; Wagner, R. M.; Weitzel, Q.; Zabalza, V.; Zandanel, F.; Zanin, R. Detection of VHE γ-Rays from HESS J0632+057 during the 2011 February X-Ray Outburst with the MAGIC Telescopes. *Astrophys. J. Lett.* **2012**, *754*, L10.

(44) Aliu, E.; Archambault, S.; Aune, T.; Behera, B.; Beilicke, M.; Benbow, W.; Berger, K.; Bird, R.; Bouvier, A.; Buckley, J. H.; Bugaev, V.; Byrum, K.; Cerruti, M.; Chen, X.; Ciupik, L.; Connolly, M. P.; Cui, W.; Duke, C.; Dumm, J.; Errando, M.; Falcone, A.; Federici, S.; Feng, Q.; Finley, J. P.; Fortin, P.; Fortson, L.; Furniss, A.; Galante, N.; Gillanders, G. H.; Griffin, S.; Griffiths, S. T.; Grube, J.; Gyuk, G.; Hanna, D.; Holder, J.; Hughes, G.; Humensky, T. B.; Kaaret, P.; Kertzman, M.; Khassen, Y.; Kieda, D.; Krawczynski, H.; Krennrich, F.; Lang, M. J.; Madhavan, A. S.; Maier, G.; Majumdar, P.; McCann, A.; Moriarty, P.; Mukherjee, R.; Nieto, D.; de Bhrithe, A. O.; Ong, R. A.; Otte, A. N.; Park, N.; Perkins, J. S.; Pohl, M.; Popkow, A.; Prokoph, H.; Quinn, J.; Ragan, K.; Rajotte, J.; Reyes, L. C.; Reynolds, P. T.; Richards, G. T.; Roache, E.; Rousselle, J.; Sembroski, G. H.; Sheidaei, F.; Skole, C.; Smith, A. W.; Staszak, D.; Stroh, M.; Telezhinsky, I.; Theiling, M.; Tucci, J. V.; Tyler, J.; Varlotta, A.; Vincent, S.; Wakely, S. P.; Weinstein, A.; Welsing, R.; Williams, D. A.; Zajczyk, A.; Zitzer, B.; Collaboration, T. V.; Abramowski, A.; Aharonian, F.; Benkhali, F. A.; Akhperjanian, A. G.; Angner, E.; Anton, G.; Balenderan, S.; Balzer, A.; Barnacka, A.; Becherini, Y.; Tjus, J. B.; Bernlhr, K.; Birsin, E.; Bissaldi, E.; Biteau, J.; Bttcher, M.; Boisson, C.; Bolmont, J.; Bordas, P.; Brucker, J.; Brun, F.; Brun, P.; Bulik, T.; Carrigan, S.; Casanova, S.; Cerruti, M.; Chadwick, P. M.; Chalme-Calvet, R.; Chaves, R. C. G.; Cheesebrough, A.; Chrtien, M.; Colafrancesco, S.; Cologna, G.; Conrad, J.; Couturier, C.; Dalton, M.; Daniel, M. K.; Davids, I. D.; Degrange, B.; Deil, C.; deWilt, P.; Dickinson, H. J.; Djannati-Ata, A.; Domainko, W.; Drury, L. O.; Dubus, G.; Dutson, K.; Dyks, J.; Dyrda, M.; Edwards, T.; Egberts, K.; Eger, P.; Espigat, P.; Farnier, C.; Fegan, S.; Feinstein, F.; Fernandes, M. V.; Fernandez, D.; Fiasson, A.; Fontaine, G.; Frster, A.; Fssling, M.; Gajdus, M.; Gallant, Y. A.; Garrigoux, T.; Giavitto, G.; Giebels, B.; Glicenstein, J. F.; Grondin, M.-H.; Grudziska, M.; Hffner, S.; Hahn, J.; Harris, J.; Heinzelmann, G.; Henri, G.; Hermann, G.; Hervet, O.; Hillert, A.; Hinton, J. A.; Hofmann, W.; Hofverberg, P.; Holler, M.; Horns, D.; Jacholkowska, A.; Jahn, C.; Jamrozy, M.; Janiak, M.; Jankowsky, F.; Jung, I.; Kastendieck, M. A.; Katarzyski, K.; Katz, U.; Kaufmann, S.; Khlifi, B.; Kieffer, M.; Klepser, S.; Klochkov, D.; Kluniak, W.; Kneiske, T.; Kolitzus, D.; Komin, N.; Kosack, K.; Krakau, S.; Krayzel, F.; Krger, P. P.; Laffon, H.; Lamanna, G.; Lefaucheur, J.; Lemire, A.; Lemoine-Goumard, M.; Lenain, J.-P.; Lennarz, D.; Lohse, T.; Lopatin, A.; Lu, C.-C.; Marandon, V.; Mar-

cowith, A.; Marx, R.; Maurin, G.; Maxted, N.; Mayer, M.; McComb, T. J. L.; Mhault, J.; Menzler, U.; Meyer, M.; Moderski, R.; Mohamed, M.; Moulin, E.; Murach, T.; Naumann, C. L.; de Naurois, M.; Niemiec, J.; Nolan, S. J.; Oakes, L.; Ohm, S.; de Oa Wilhelmi, E.; Opitz, B.; Ostrowski, M.; Oya, I.; Panter, M.; Parsons, R. D.; Arribas, M. P.; Pekeur, N. W.; Pelletier, G.; Perez, J.; Petrucci, P.-O.; Peyaud, B.; Pita, S.; Poon, H.; Phlhofer, G.; Punch, M.; Quirrenbach, A.; Raab, S.; Raue, M.; Reimer, A.; Reimer, O.; Renaud, M.; de los Reyes, R.; Rieger, F.; Rob, L.; Romoli, C.; Rosier-Lees, S.; Rowell, G.; Rudak, B.; Rulten, C. B.; Sahakian, V.; Sanchez, D. A.; Santangelo, A.; Schlickeiser, R.; Schssler, F.; Schulz, A.; Schwanke, U.; Schwarzburg, S.; Schwemmer, S.; Sol, H.; Spengler, G.; Spies, F.; Stawarz, .; Steenkamp, R.; Stegmann, C.; Stinzing, F.; Stycz, K.; Sushch, I.; Szostek, A.; Tavernet, J.-P.; Tavernier, T.; Taylor, A. M.; Terrier, R.; Tluczykont, M.; Trichard, C.; Valerius, K.; van Eldik, C.; Vasileiadis, G.; Venter, C.; Viana, A.; Vincent, P.; Vlk, H. J.; Volpe, F.; Vorster, M.; Wagner, S. J.; Wagner, P.; Ward, M.; Weidinger, M.; Weitzel, Q.; White, R.; Wierzcholska, A.; Willmann, P.; Wrnlein, A.; Wouters, D.; Zacharias, M.; Zajczyk, A.; Zdziarski, A. A.; Zech, A.; Zechlin, H.-S.; Collaboration, H. Long-term TeV and X-Ray Observations of the Gamma-Ray Binary HESS J0632+057. *Astrophys. J.* **2014**, *780*, 168.

(45) Maier, G.; VERITAS Collaboration, Long-term TeV Observations of the Gamma-Ray Binary HESS J0632+057 with VERITAS. 34th. International Cosmic Ray Conference,, The Hague, Netherlands. 2015; p 754.

(46) McCann, A. Discovery of Emission Above 100 GeV from The Crab Pulsar with VERITAS. Ph.D. thesis, McGill University, Montreal, Canada, 2012.

(47) Eger, P.; Laffon, H.; Bordas, P.; de Oña Whilhelmi, E.; Hinton, J.; Pühlhofer, G. Discovery of a Variable X-ray Counterpart to HESS J1832-093: A New Gamma-Ray Binary? *Mon. Not. R. Astron. Soc.* **2016**, *457*, 1753–1758.

(48) Gehrels, N.; Chincarini, G.; Giommi, P.; Mason, K. O.; Nousek, J. A.; Wells, A. A.; White, N. E.; Barthelmy, S. D.; Burrows, D. N.; Cominsky, L. R.; Hurley, K. C.; Marshall, F. E.; Mészáros, P.; Roming, P. W. A.; Angelini, L.; Barbier, L. M.; Belloni, T.; Campana, S.; Caraveo, P. A.; Chester, M. M.; Citterio, O.; Cline, T. L.; Cropper, M. S.; Cummings, J. R.; Dean, A. J.; Feigelson, E. D.; Fenimore, E. E.; Frail, D. A.; Fruchter, A. S.; Garmire, G. P.; Gendreau, K.; Ghisellini, G.; Greiner, J.; Hill, J. E.; Hunsberger, S. D.; Krimm, H. A.; Kulkarni, S. R.; Kumar, P.; Lebrun, F.; Lloyd-Ronning, N. M.; Markwardt, C. B.; Mattson, B. J.; Mushotzky, R. F.; Norris, J. P.; Osborne, J.; Paczynski, B.; Palmer, D. M.; Park, H.-S.; Parsons, A. M.; Paul, J.; Rees, M. J.; Reynolds, C. S.; Rhoads, J. E.; Sasseen, T. P.; Schaefer, B. E.; Short, A. T.; Smale, A. P.; Smith, I. A.; Stella, L.; Tagliaferri, G.; Takahashi, T.; Tashiro, M.; Townsley, L. K.; Tueller, J.; Turner, M. J. L.; Vietri, M.; Voges, W.; Ward, M. J.; Willingale, R.; Zerbi, F. M.; Zhang, W. W. The Swift Gamma-Ray Burst Mission. *Astrophys. J.* **2004**, *611*, 1005–1020.

(49) Barthelmy, S. D.; Barbier, L. M.; Cummings, J. R.; Fenimore, E. E.; Gehrels, N.; Hullinger, D.; Krimm, H. A.; Markwardt, C. B.; Palmer, D. M.; Parsons, A.; Sato, G.; Suzuki, M.; Takahashi, T.; Tashiro, M.; Tueller, J. The Burst Alert Telescope (BAT) on the SWIFT Midex Mission. *Space Sci. Rev.* **2005**, *120*, 143–164.

(50) Burrows, D. N.; Hill, J. E.; Nousek, J. A.; Kennea, J. A.; Wells, A.; Osborne, J. P.; Abbey, A. F.; Beardmore, A.; Mukerjee, K.; Short, A. D. T.; Chincarini, G.; Campana, S.; Citterio, O.; Moretti, A.; Pagani, C.; Tagliaferri, G.; Giommi, P.; Capalbi, M.; Tamburelli, F.; Angelini, L.; Cusumano, G.; Bräuninger, H. W.; Burkert, W.; Hartner, G. D. The Swift X-Ray Telescope. *Space Sci. Rev.* **2005**, *120*, 165–195.

(51) Roming, P. W. A.; Kennedy, T. E.; Mason, K. O.; Nousek, J. A.; Ahr, L.; Bingham, R. E.; Broos, P. S.; Carter, M. J.; Hancock, B. K.; Huckle, H. E.; Hunsberger, S. D.; Kawakami, H.; Killough, R.; Koch, T. S.; McLelland, M. K.; Smith, K.; Smith, P. J.; Soto, J. C.; Boyd, P. T.; Breeveld, A. A.; Holland, S. T.; Ivanushkina, M.; Pryzby, M. S.; Still, M. D.; Stock, J. The Swift Ultra-Violet/Optical Telescope. *Space Sci. Rev.* **2005**, *120*, 95–142.

(52) Atwood, W. B.; Abdo, A. A.; Ackermann, M.; Althouse, W.; Anderson, B.; Axelsson, M.; Baldini, L.; Ballet, J.; Band, D. L.; Barbiellini, G.; Bartelt, J.; Bastieri, D.; Baughman, B. M.; Bechtol, K.; Bdrde, D.; Bellardi, F.; Bellazzini, R.; Berenji, B.; Bignami, G. F.; Bisello, D.; Bissaldi, E.; Blandford, R. D.; Bloom, E. D.; Bogart, J. R.; Bonamente, E.; Bonnell, J.; Borgland, A. W.; Bouvier, A.; Bregeon, J.; Brez, A.; Brigida, M.; Bruel, P.; Burnett, T. H.; Busetto, G.; Caliandro, G. A.; Cameron, R. A.; Caraveo, P. A.; Carius, S.; Carlson, P.; Casandjian, J. M.; Cavazzuti, E.; Ceccanti, M.; Cecchi, C.; Charles, E.; Chekhtman, A.; Cheung, C. C.; Chiang, J.; Chipaux, R.; Cillis, A. N.; Ciprini, S.; Claus, R.; Cohen-Tanugi, J.; Condamoor, S.; Conrad, J.; Corbet, R.; Corucci, L.; Costamante, L.; Cutini, S.; Davis, D. S.; Decotigny, D.; DeKlotz, M.; Dermer, C. D.; de Angelis, A.; Digel, S. W.; do Couto e Silva, E.; Drell, P. S.; Dubois, R.; Dumora, D.; Edmonds, Y.; Fabiani, D.; Farnier, C.; Favuzzi, C.; Flath, D. L.; Fleury, P.; Focke, W. B.; Funk, S.; Fusco, P.; Gargano, F.; Gasparrini, D.; Gehrels, N.; Gentit, F.-X.; Germani, S.; Giebels, B.; Giglietto, N.; Giommi, P.; Giordano, F.; Glanzman, T.; Godfrey, G.; Grenier, I. A.; Grondin, M.-H.; Grove, J. E.; Guillemot, L.; Guiriec, S.; Haller, G.; Harding, A. K.; Hart, P. A.; Hays, E.; Healey, S. E.; Hirayama, M.; Hjalmarsdotter, L.; Horn, R.; Hughes, R. E.; Jhannesson, G.; Johansson, G.; Johnson, A. S.; Johnson, R. P.; Johnson, T. J.; Johnson, W. N.; Kamae, T.; Katagiri, H.; Kataoka, J.; Kavelaars, A.; Kawai, N.; Kelly, H.; Kerr, M.; Klamra, W.; Kndlseder, J.; Kocian, M. L.; Komin, N.; Kuehn, F.; Kuss, M.; Landriu, D.; Latronico, L.; Lee, B.; Lee, S.-H.; Lemoine-Goumard, M.; Lionetto, A. M.; Longo, F.; Loparco, F.; Lott, B.; Lovellette, M. N.; Lubrano, P.; Madejski, G. M.; Makeev, A.; Marangelli, B.; Massai, M. M.; Mazziotta, M. N.; McEnery, J. E.; Menon, N.; Meurer, C.; Michelson, P. F.; Minuti, M.; Mirizzi, N.; Mitthumsiri, W.; Mizuno, T.; Moiseev, A. A.; Monte, C.; Monzani, M. E.; Moretti, E.; Morselli, A.; Moskalenko, I. V.; Murgia, S.; Nakamori, T.; Nishino, S.; Nolan, P. L.; Norris, J. P.; Nuss, E.; Ohno, M.; Ohsugi, T.; Omodei, N.; Orlando, E.; Ormes, J. F.; Paccagnella, A.; Paneque, D.; Panetta, J. H.; Parent, D.; Pearce, M.; Pepe, M.; Perazzo, A.; Pesce-Rollins, M.; Picozza, P.; Pieri, L.; Pinchera, M.; Piron, F.; Porter, T. A.; Poupard, L.; Rain, S.; Rando, R.; Rapposelli, E.; Razzano, M.; Reimer, A.; Reimer, O.; Reposeur, T.; Reyes, L. C.; Ritz, S.; Rochester, L. S.; Rodriguez, A. Y.; Romani, R. W.; Roth, M.; Russell, J. J.; Ryde, F.; Sabatini, S.; Sadrozinski, H. F.-W.; Sanchez, D.; Sander, A.; Sapozhnikov, L.; Parkinson, P. M. S.; Scargle, J. D.; Schalk, T. L.; Scolieri, G.; Sgr, C.; Share, G. H.; Shaw, M.; Shimokawabe, T.; Shrader, C.; Sierpowska-Bartosik, A.; Siskind, E. J.; Smith, D. A.; Smith, P. D.; Spandre, G.; Spinelli, P.; Starck, J.-L.; Stephens, T. E.; Strickman, M. S.; Strong, A. W.; Suson, D. J.; Tajima, H.; Takahashi, H.; Takahashi, T.; Tanaka, T.; Tenze, A.; Tether, S.;

Thayer, J. B.; Thayer, J. G.; Thompson, D. J.; Tibaldo, L.; Tibolla, O.; Torres, D. F.; Tosti, G.; Tramacere, A.; Turri, M.; Usher, T. L.; Vilchez, N.; Vitale, V.; Wang, P.; Watters, K.; Winer, B. L.; Wood, K. S.; Ylinen, T.; Ziegler, M. The Large Area Telescope on the Fermi Gamma-Ray Space Telescope Mission. *Astrophys. J.* **2009**, *697*, 1071–1102.

(53) Meegan, C.; Lichti, G.; Bhat, P. N.; Bissaldi, E.; Briggs, M. S.; Connaughton, V.; Diehl, R.; Fishman, G.; Greiner, J.; Hoover, A. S.; van der Horst, A. J.; von Kienlin, A.; Kippen, R. M.; Kouveliotou, C.; McBreen, S.; Paciesas, W. S.; Preece, R.; Steinle, H.; Wallace, M. S.; Wilson, R. B.; Wilson-Hodge, C. The Fermi Gamma-Ray Burst Monitor. *Astrophys. J.* **2009**, *702*, 791–804.

(54) Acero, F.; Ackermann, M.; Ajello, M.; Albert, A.; Atwood, W. B.; Axelsson, M.; Baldini, L.; Ballet, J.; Barbiellini, G.; Bastieri, D.; Belfiore, A.; Bellazzini, R.; Bissaldi, E.; Blandford, R. D.; Bloom, E. D.; Bogart, J. R.; Bonino, R.; Bottacini, E.; Bregeon, J.; Britto, R. J.; Bruel, P.; Buehler, R.; Burnett, T. H.; Buson, S.; Caliandro, G. A.; Cameron, R. A.; Caputo, R.; Caragiulo, M.; Caraveo, P. A.; Casandjian, J. M.; Cavazzuti, E.; Charles, E.; Chaves, R. C. G.; Chekhtman, A.; Cheung, C. C.; Chiang, J.; Chiaro, G.; Ciprini, S.; Claus, R.; Cohen-Tanugi, J.; Cominsky, L. R.; Conrad, J.; Cutini, S.; D'Ammando, F.; de Angelis, A.; DeKlotz, M.; de Palma, F.; Desiante, R.; Digel, S. W.; Di Venere, L.; Drell, P. S.; Dubois, R.; Dumora, D.; Favuzzi, C.; Fegan, S. J.; Ferrara, E. C.; Finke, J.; Franckowiak, A.; Fukazawa, Y.; Funk, S.; Fusco, P.; Gargano, F.; Gasparrini, D.; Giebels, B.; Giglietto, N.; Giommi, P.; Giordano, F.; Giroletti, M.; Glanzman, T.; Godfrey, G.; Grenier, I. A.; Grondin, M.-H.; Grove, J. E.; Guillemot, L.; Guiriec, S.; Hadasch, D.; Harding, A. K.; Hays, E.; Hewitt, J. W.; Hill, A. B.; Horan, D.; Iafrate, G.; Jogler, T.; Jóhannesson, G.; Johnson, R. P.; Johnson, A. S.; Johnson, T. J.; Johnson, W. N.; Kamae, T.; Kataoka, J.; Katsuta, J.; Kuss, M.; La Mura, G.; Landriu, D.; Larsson, S.; Latronico, L.; Lemoine-Goumard, M.; Li, J.; Li, L.; Longo, F.; Loparco, F.; Lott, B.; Lovellette, M. N.; Lubrano, P.; Madejski, G. M.; Massaro, F.; Mayer, M.; Mazziotta, M. N.; McEnery, J. E.; Michelson, P. F.; Mirabal, N.; Mizuno, T.; Moiseev, A. A.; Mongelli, M.; Monzani, M. E.; Morselli, A.; Moskalenko, I. V.; Murgia, S.; Nuss, E.; Ohno, M.; Ohsugi, T.; Omodei, N.; Orienti, M.; Orlando, E.; Ormes, J. F.; Paneque, D.; Panetta, J. H.; Perkins, J. S.; Pesce-Rollins, M.; Piron, F.; Pivato, G.; Porter, T. A.; Racusin, J. L.; Rando, R.; Razzano, M.; Razzaque, S.; Reimer, A.; Reimer, O.; Reposeur, T.; Rochester, L. S.; Romani, R. W.; Salvetti, D.; Sánchez-Conde, M.; Saz Parkinson, P. M.; Schulz, A.; Siskind, E. J.; Smith, D. A.; Spada, F.; Spandre, G.; Spinelli, P.; Stephens, T. E.; Strong, A. W.; Suson, D. J.; Takahashi, H.; Takahashi, T.; Tanaka, Y.; Thayer, J. G.; Thayer, J. B.; Thompson, D. J.; Tibaldo, L.; Tibolla, O.; Torres, D. F.; Torresi, E.; Tosti, G.; Troja, E.; Van Klaveren, B.; Vianello, G.; Winer, B. L.; Wood, K. S.; Wood, M.; Zimmer, S.; Fermi-LAT Collaboration, Fermi Large Area Telescope Third Source Catalog. *Astrophys. J., Suppl. Ser.* **2015**, *218*, 23.

(55) Holder, J. Atmospheric Cherenkov Gamma-Ray Telescopes. 2015, arXiv:astro-ph.HE/1510.05675. arXiv.org e-Print archive. https://arxiv.org/abs/1510.05675 (accessed May 30, 2017).

(56) Bernlöhr, K.; Carrol, O.; Cornils, R.; Elfahem, S.; Espigat, P.; Gillessen, S.; Heinzelmann, G.; Hermann, G.; Hofmann, W.; Horns, D.; Jung, I.; Kankanyan, R.; Katona, A.; Khelifi, B.; Krawczynski, H.; Panter, M.; Punch, M.; Rayner, S.; Rowell, G.; Tluczykont, M.; van Staa, R. The Optical System of the H.E.S.S. Imaging

Atmospheric Cherenkov Telescopes. Part I: Layout and Components of the System. *Astropart. Phys.* **2003**, *20*, 111–128.

(57) Cornils, R.; Gillessen, S.; Jung, I.; Hofmann, W.; Beilicke, M.; Bernlöhr, K.; Carrol, O.; Elfahem, S.; Heinzelmann, G.; Hermann, G.; Horns, D.; Kankanyan, R.; Katona, A.; Krawczynski, H.; Panter, M.; Rayner, S.; Rowell, G.; Tluczykont, M.; van Staa, R. The Optical System of the H.E.S.S. Imaging Atmospheric Cherenkov Telescopes. Part II: Mirror Alignment and Point Spread Function. *Astropart. Phys.* **2003**, *20*, 129–143.

(58) Becherini, Y.; Punch, M.; H. E. S. S. Collaboration, Performance of HESS-II in Multi-telescope Mode with a Multivariate Analysis. 5th International Meeting on High Energy Gamma-Ray Astronomy, Heidelberg, Germany, July. 2012; pp 741–744.

(59) Aharonian, F.; Akhperjanian, A. G.; Bazer-Bachi, A. R.; Beilicke, M.; Benbow, W.; Berge, D.; Bernlöhr, K.; Boisson, C.; Bolz, O.; Borrel, V.; Braun, I.; Breitling, F.; Brown, A. M.; Chadwick, P. M.; Chounet, L.-M.; Cornils, R.; Costamante, L.; Degrange, B.; Dickinson, H. J.; Djannati-Ataï, A.; Drury, L. O.; Dubus, G.; Emmanoulopoulos, D.; Espigat, P.; Feinstein, F.; Fontaine, G.; Fuchs, Y.; Funk, S.; Gallant, Y. A.; Giebels, B.; Gillessen, S.; Glicenstein, J. F.; Goret, P.; Hadjichristidis, C.; Hauser, M.; Heinzelmann, G.; Henri, G.; Hermann, G.; Hinton, J. A.; Hofmann, W.; Holleran, M.; Horns, D.; Jacholkowska, A.; de Jager, O. C.; Khélifi, B.; Komin, N.; Konopelko, A.; Latham, I. J.; Le Gallou, R.; Lemière, A.; Lemoine-Goumard, M.; Leroy, N.; Lohse, T.; Martin, J. M.; Martineau-Huynh, O.; Marcowith, A.; Masterson, C.; McComb, T. J. L.; de Naurois, M.; Nolan, S. J.; Noutsos, A.; Orford, K. J.; Osborne, J. L.; Ouchrif, M.; Panter, M.; Pelletier, G.; Pita, S.; Pühlhofer, G.; Punch, M.; Raubenheimer, B. C.; Raue, M.; Raux, J.; Rayner, S. M.; Reimer, A.; Reimer, O.; Ripken, J.; Rob, L.; Rolland, L.; Rowell, G.; Sahakian, V.; Saugé, L.; Schlenker, S.; Schlickeiser, R.; Schuster, C.; Schwanke, U.; Siewert, M.; Sol, H.; Spangler, D.; Steenkamp, R.; Stegmann, C.; Tavernet, J.-P.; Terrier, R.; Théoret, C. G.; Tluczykont, M.; Vasileiadis, G.; Venter, C.; Vincent, P.; Völk, H. J.; Wagner, S. J. The H.E.S.S. Survey of the Inner Galaxy in Very High Energy Gamma Rays. *Astrophys. J.* **2006**, *636*, 777–797.

(60) Ahnen, M. L.; Ansoldi, S.; Antonelli, L. A.; Antoranz, P.; Babic, A.; Banerjee, B.; Bangale, P.; de Almeida, U. B.; Barrio, J. A.; Bednarek, W.; Bernardini, E.; Biasuzzi, B.; Biland, A.; Blanch, O.; Bonnefoy, S.; Bonnoli, G.; Borracci, F.; Bretz, T.; Carmona, E.; Carosi, A.; Chatterjee, A.; Clavero, R.; Colin, P.; Colombo, E.; Contreras, J. L.; Cortina, J.; Covino, S.; Vela, P. D.; Dazzi, F.; Angelis, A. D.; Lotto, B. D.; de Oa Wilhelmi, E.; Mendez, C. D.; Pierro, F. D.; Prester, D. D.; Dorner, D.; Doro, M.; Einecke, S.; Glawion, D. E.; Elsaesser, D.; Fernndez-Barral, A.; Fidalgo, D.; Fonseca, M. V.; Font, L.; Frantzen, K.; Fruck, C.; Galindo, D.; Lpez, R. J. G.; Garczarczyk, M.; Terrats, D. G.; Gaug, M.; Giammaria, P.; Godinovi, N.; Muoz, A. G.; Guberman, D.; Hahn, A.; Hanabata, Y.; Hayashida, M.; Herrera, J.; Hose, J.; Hrupec, D.; Hughes, G.; Idec, W.; Kodani, K.; Konno, Y.; Kubo, H.; Kushida, J.; Barbera, A. L.; Lelas, D.; Lindfors, E.; Lombardi, S.; Lpez, M.; Lpez-Coto, R.; Lpez-Oramas, A.; Lorenz, E.; Majumdar, P.; Makariev, M.; Mallot, K.; Maneva, G.; Manganaro, M.; Mannheim, K.; Maraschi, L.; Marcote, B.; Mariotti, M.; Martnez, M.; Mazin, D.; Menzel, U.; Miranda, J. M.; Mirzoyan, R.; Moralejo, A.; Moretti, E.; Nakajima, D.; Neustroev, V.; Niedzwiecki, A.; Rosillo, M. N.; Nilsson, K.; Nishijima, K.; Noda, K.; Orito, R.;

Overkemping, A.; Paiano, S.; Palacio, J.; Palatiello, M.; Paneque, D.; Paoletti, R.; Paredes, J. M.; Paredes-Fortuny, X.; Persic, M.; Poutanen, J.; Moroni, P. G. P.; Prandini, E.; Puljak, I.; Rhode, W.; Rib, M.; Rico, J.; Garcia, J. R.; Saito, T.; Satalecka, K.; Schultz, C.; Schweizer, T.; Shore, S. N.; Sillanp, A.; Sitarek, J.; Snidaric, I.; Sobczynska, D.; Stamerra, A.; Steinbring, T.; Strzys, M.; Takalo, L.; Takami, H.; Tavecchio, F.; Temnikov, P.; Terzi, T.; Tescaro, D.; Teshima, M.; Thaele, J.; Torres, D. F.; Toyama, T.; Treves, A.; Verguilov, V.; Vovk, I.; Ward, J. E.; Will, M.; Wu, M. H.; Zanin, R.; Collaboration, M.; Ajello, M.; Baldini, L.; Barbiellini, G.; Bastieri, D.; Gonzlez, J. B.; Bellazzini, R.; Bissaldi, E.; Blandford, R. D.; Bonino, R.; Bregeon, J.; Bruel, P.; Buson, S.; Caliandro, G. A.; Cameron, R. A.; Caragiulo, M.; Caraveo, P. A.; Cavazzuti, E.; Chiang, J.; Chiaro, G.; Ciprini, S.; DAmmando, F.; de Palma, F.; Desiante, R.; Venere, L. D.; Domnguez, A.; Fusco, P.; Gargano, F.; Gasparrini, D.; Giglietto, N.; Giordano, F.; Giroletti, M.; Grenier, I. A.; Guiriec, S.; Hays, E.; Hewitt, J. W.; Jogler, T.; Kuss, M.; Larsson, S.; Li, J.; Li, L.; Longo, F.; Loparco, F.; Lovellette, M. N.; Lubrano, P.; Maldera, S.; Mayer, M.; Mazziotta, M. N.; McEnery, J. E.; Mirabal, N.; Mizuno, T.; Monzani, M. E.; Morselli, A.; Moskalenko, I. V.; Nuss, E.; Ojha, R.; Ohsugi, T.; Omodei, N.; Orlando, E.; Perkins, J. S.; Pesce-Rollins, M.; Piron, F.; Pivato, G.; Porter, T. A.; Raino, S.; Rando, R.; Razzano, M.; Reimer, A.; Reimer, O.; Sgro, C.; Siskind, E. J.; Spada, F.; Spandre, G.; Spinelli, P.; Tajima, H.; Takahashi, H.; Thayer, J. B.; Thompson, D. J.; Troja, E.; Wood, K. S.; Collaboration, F.-L.; Balokovic, M.; Berdyugin, A.; Carraminana, A.; Carrasco, L.; Chavushyan, V.; Ramazani, V. F.; Feige, M.; Haarto, S.; Haeusner, P.; Hovatta, T.; Kania, J.; Klamt, J.; Lhteenmki, A.; Leon-Tavares, J.; Lorey, C.; Pacciani, L.; Porras, A.; Recillas, E.; Reinthal, R.; Tornikoski, M.; Wolfert, D.; Zottmann, N. Very High Energy γ-Rays from the Universe's Middle Age: Detection of the z = 0.940 Blazar PKS 1441+25 with MAGIC. *Astrophys. J. Lett.* **2015**, *815*, L23.

(61) Aliu, E.; Anderhub, H.; Antonelli, L. A.; Antoranz, P.; Backes, M.; Baixeras, C.; Barrio, J. A.; Bartko, H.; Bastieri, D.; Becker, J. K.; Bednarek, W.; Berger, K.; Bernardini, E.; Bigongiari, C.; Biland, A.; Bock, R. K.; Bonnoli, G.; Bordas, P.; Bosch-Ramon, V.; Bretz, T.; Britvitch, I.; Camara, M.; Carmona, E.; Chilingarian, A.; Commichau, S.; Contreras, J. L.; Cortina, J.; Costado, M. T.; Covino, S.; Curtef, V.; Dazzi, F.; De Angelis, A.; De Cea del Pozo, E.; de los Reyes, R.; De Lotto, B.; De Maria, M.; De Sabata, F.; Delgado Mendez, C.; Dominguez, A.; Dorner, D.; Doro, M.; Elsässer, D.; Errando, M.; Fagiolini, M.; Ferenc, D.; Fernandez, E.; Firpo, R.; Fonseca, M. V.; Font, L.; Galante, N.; Garcia Lopez, R. J.; Garczarczyk, M.; Gaug, M.; Goebel, F.; Hadasch, D.; Hayashida, M.; Herrero, A.; Höhne, D.; Hose, J.; Hsu, C. C.; Huber, S.; Jogler, T.; Kranich, D.; La Barbera, A.; Laille, A.; Leonardo, E.; Lindfors, E.; Lombardi, S.; Longo, F.; Lopez, M.; Lorenz, E.; Majumdar, P.; Maneva, G.; Mankuzhiyil, N.; Mannheim, K.; Maraschi, L.; Mariotti, M.; Martinez, M.; Mazin, D.; Meucci, M.; Meyer, M.; Miranda, J. M.; Mirzoyan, R.; Moles, M.; Moralejo, A.; Nieto, D.; Nilsson, K.; Ninkovic, J.; Otte, N.; Oya, I.; Paoletti, R.; Paredes, J. M.; Pasanen, M.; Pascoli, D.; Pauss, F.; Pegna, R. G.; Perez-Torres, M. A.; Persic, M.; Peruzzo, L.; Piccioli, A.; Prada, F.; Prandini, E.; Puchades, N.; Raymers, A.; Rhode, W.; Ribó, M.; Rico, J.; Rissi, M.; Robert, A.; Rügamer, S.; Saggion, A.; Saito, T. Y.; Salvati, M.; Sanchez-Conde, M.; Sartori, P.; Satalecka, K.; Scalzotto, V.; Scapin, V.; Schweizer, T.; Shayduk, M.; Shinozaki, K.; Shore, S. N.; Sidro, N.; Sierpowska-Bartosik, A.; Sillanpää, A.; Sobczynska, D.; Spanier, F.; Stamerra, A.; Stark, L. S.;

Takalo, L.; Tavecchio, F.; Temnikov, P.; Tescaro, D.; Teshima, M.; Tluczykont, M.; Torres, D. F.; Turini, N.; Vankov, H.; Venturini, A.; Vitale, V.; Wagner, R. M.; Wittek, W.; Zabalza, V.; Zandanel, F.; Zanin, R.; Zapatero, J.; de Jager, O. C.; de Ona Wilhelmi, E.; MAGIC Collaboration, Observation of Pulsed γ-Rays Above 25 GeV from the Crab Pulsar with MAGIC. *Science* **2008**, *322*, 1221.

(62) Ahnen, M. L.; Ansoldi, S.; Antonelli, L. A.; Antoranz, P.; Arcaro, C.; Babic, A.; Banerjee, B.; Bangale, P.; Barres de Almeida, U.; Barrio, J. A.; Becerra González, J.; Bednarek, W.; Bernardini, E.; Berti, A.; Biasuzzi, B.; Biland, A.; Blanch, O.; Bonnefoy, S.; Bonnoli, G.; Borracci, F.; Bretz, T.; Buson, S.; Carosi, A.; Chatterjee, A.; Clavero, R.; Colin, P.; Colombo, E.; Contreras, J. L.; Cortina, J.; Covino, S.; Da Vela, P.; Dazzi, F.; De Angelis, A.; De Lotto, B.; de Oña Wilhelmi, E.; Di Pierro, F.; Doert, M.; Domínguez, A.; Dominis Prester, D.; Dorner, D.; Doro, M.; Einecke, S.; Eisenacher Glawion, D.; Elsaesser, D.; Engelkemeier, M.; Fallah Ramazani, V.; Fernández-Barral, A.; Fidalgo, D.; Fonseca, M. V.; Font, L.; Frantzen, K.; Fruck, C.; Galindo, D.; García López, R. J.; Garczarczyk, M.; Garrido Terrats, D.; Gaug, M.; Giammaria, P.; Godinović, N.; Gora, D.; Guberman, D.; Hadasch, D.; Hahn, A.; Hayashida, M.; Herrera, J.; Hose, J.; Hrupec, D.; Hughes, G.; Idec, W.; Kodani, K.; Konno, Y.; Kubo, H.; Kushida, J.; La Barbera, A.; Lelas, D.; Lindfors, E.; Lombardi, S.; Longo, F.; López, M.; López-Coto, R.; Majumdar, P.; Makariev, M.; Mallot, K.; Maneva, G.; Manganaro, M.; Mannheim, K.; Maraschi, L.; Marcote, B.; Mariotti, M.; Martínez, M.; Mazin, D.; Menzel, U.; Miranda, J. M.; Mirzoyan, R.; Moralejo, A.; Moretti, E.; Nakajima, D.; Neustroev, V.; Niedzwiecki, A.; Nievas Rosillo, M.; Nilsson, K.; Nishijima, K.; Noda, K.; Nogués, L.; Paiano, S.; Palacio, J.; Palatiello, M.; Paneque, D.; Paoletti, R.; Paredes, J. M.; Paredes-Fortuny, X.; Pedaletti, G.; Peresano, M.; Perri, L.; Persic, M.; Poutanen, J.; Prada Moroni, P. G.; Prandini, E.; Puljak, I.; Garcia, J. R.; Reichardt, I.; Rhode, W.; Ribó, M.; Rico, J.; Saito, T.; Satalecka, K.; Schroeder, S.; Schweizer, T.; Shore, S. N.; Sillanpää, A.; Sitarek, J.; Snidaric, I.; Sobczynska, D.; Stamerra, A.; Strzys, M.; Surić, T.; Takalo, L.; Tavecchio, F.; Temnikov, P.; Terzić, T.; Tescaro, D.; Teshima, M.; Torres, D. F.; Toyama, T.; Treves, A.; Vanzo, G.; Verguilov, V.; Vovk, I.; Ward, J. E.; Will, M.; Wu, M. H.; Zanin, R.; Desiante, R. Detection of Very High Energy Gamma-Ray Emission from the Gravitationally Lensed Blazar QSO B0218+357 with the MAGIC Telescopes. *Astron. Astrophys.* **2016**, *595*, A98.

(63) Abeysekara, A. U.; Aguilar, J. A.; Aguilar, S.; Alfaro, R.; Almaraz, E.; Álvarez, C.; Álvarez-Romero, J. d. D.; Álvarez, M.; Arceo, R.; Arteaga-Velázquez, J. C.; Badillo, C.; Barber, A.; Baughman, B. M.; Bautista-Elivar, N.; Belmont, E.; Benítez, E.; Ben-Zvi, S. Y.; Berley, D.; Bernal, A.; Bonamente, E.; Braun, J.; Caballero-Lopez, R.; Cabrera, I.; Carramiñana, A.; Carrasco, L.; Castillo, M.; Chambers, L.; Conde, R.; Condreay, P.; Cotti, U.; Cotzomi, J.; D'Olivo, J. C.; de la Fuente, E.; De León, C.; Delay, S.; Delepine, D.; DeYoung, T.; Diaz, L.; Diaz-Cruz, L.; Dingus, B. L.; Duvernois, M. A.; Edmunds, D.; Ellsworth, R. W.; Fick, B.; Fiorino, D. W.; Flandes, A.; Fraija, N. I.; Galindo, A.; García-Luna, J. L.; García-Torales, G.; Garfias, F.; González, L. X.; González, M. M.; Goodman, J. A.; Grabski, V.; Gussert, M.; Guzmán-Ceron, C.; Hampel-Arias, Z.; Harris, T.; Hays, E.; Hernandez-Cervantes, L.; Hüntemeyer, P. H.; Imran, A.; Iriarte, A.; Jimenez, J. J.; Karn, P.; Kelley-Hoskins, N.; Kieda, D.; Langarica, R.; Lara, A.; Lauer, R.; Lee, W. H.; Linares, E. C.; Linnemann, J. T.; Longo, M.; Luna-García, R.; Martínez, H.; Martínez, J.; Martínez, L. A.; Martínez, O.; Martínez-Castro, J.; Martos, M.; Matthews, J.; McEnery, J. E.; Medina-Tanco, G.; Mendoza-

Torres, J. E.; Miranda-Romagnoli, P. A.; Montaruli, T.; Moreno, E.; Mostafa, M.; Napsuciale, M.; Nava, J.; Nellen, L.; Newbold, M.; Noriega-Papaqui, R.; Oceguera-Becerra, T.; Olmos Tapia, A.; Orozco, V.; Pérez, V.; Pérez-Pérez, E. G.; Perkins, J. S.; Pretz, J.; Ramirez, C.; Ramírez, I.; Rebello, D.; Rentería, A.; Reyes, J.; Rosa-González, D.; Rosado, A.; Ryan, J. M.; Sacahui, J. R.; Salazar, H.; Salesa, F.; Sandoval, A.; Santos, E.; Schneider, M.; Shoup, A.; Silich, S.; Sinnis, G.; Smith, A. J.; Sparks, K.; Springer, W.; Suárez, F.; Suarez, N.; Taboada, I.; Tellez, A. F.; Tenorio-Tagle, G.; Tepe, A.; Toale, P. A.; Tollefson, K.; Torres, I.; Ukwatta, T. N.; Valdes-Galicia, J.; Vanegas, P.; Vasileiou, V.; Vázquez, O.; Vázquez, X.; Villaseñor, L.; Wall, W.; Walters, J. S.; Warner, D.; Westerhoff, S.; Wisher, I. G.; Wood, J.; Yodh, G. B.; Zaborov, D.; Zepeda, A. On the Sensitivity of the HAWC Observatory to Gamma-Ray Bursts. *Astropart. Phys.* **2012**, *35*, 641–650.

(64) HAWC Collaboration,; Abeysekara, A. U.; Alfaro, R.; Alvarez, C.; Álvarez, J. D.; Arceo, R.; Arteaga-Velázquez, J. C.; Ayala Solares, H. A.; Barber, A. S.; Baughman, B. M.; Bautista-Elivar, N.; Belmont, E.; BenZvi, S. Y.; Berley, D.; Bonilla Rosales, M.; Braun, J.; Caballero-Lopez, R. A.; Caballero-Mora, K. S.; Carramiñana, A.; Castillo, M.; Cotti, U.; Cotzomi, J.; de la Fuente, E.; De León, C.; DeYoung, T.; Diaz Hernandez, R.; Díaz-Vélez, J. C.; Dingus, B. L.; DuVernois, M. A.; Ellsworth, R. W.; Fernandez, A.; Fiorino, D. W.; Fraija, N.; Galindo, A.; Garfias, F.; González, L. X.; González, M. M.; Goodman, J. A.; Grabski, V.; Gussert, M.; Hampel-Arias, Z.; Hui, C. M.; Hüntemeyer, P.; Imran, A.; Iriarte, A.; Karn, P.; Kieda, D.; Kunde, G. J.; Lara, A.; Lauer, R. J.; Lee, W. H.; Lennarz, D.; León Vargas, H.; Linares, E. C.; Linnemann, J. T.; Longo, M.; Luna-GarcIa, R.; Marinelli, A.; Martinez, H.; Martinez, O.; Martínez-Castro, J.; Matthews, J. A. J.; Miranda-Romagnoli, P.; Moreno, E.; Mostafá, M.; Nava, J.; Nellen, L.; Newbold, M.; Noriega-Papaqui, R.; Oceguera-Becerra, T.; Patricelli, B.; Pelayo, R.; Pérez-Pérez, E. G.; Pretz, J.; Rivière, C.; Rosa-González, D.; Salazar, H.; Salesa, F.; Sanchez, F. E.; Sandoval, A.; Santos, E.; Schneider, M.; Silich, S.; Sinnis, G.; Smith, A. J.; Sparks, K.; Springer, R. W.; Taboada, I.; Toale, P. A.; Tollefson, K.; Torres, I.; Ukwatta, T. N.; Villaseñor, L.; Weisgarber, T.; Westerhoff, S.; Wisher, I. G.; Wood, J.; Yodh, G. B.; Younk, P. W.; Zaborov, D.; Zepeda, A.; Zhou, H. The HAWC Gamma-Ray Observatory: Design, Calibration, and Operation. 2013, arXiv:astro-ph.HE/1310.0074. arXiv.org e-Print archive. https://arxiv.org/abs/1310.0074 (accessed May 30, 2017.

(65) Abeysekara, A. U.; Albert, A.; Alfaro, R.; Alvarez, C.; Álvarez, J. D.; Arceo, R.; Arteaga-Velázquez, J. C.; Ayala Solares, H. A.; Barber, A. S.; Baughman, B.; Bautista-Elivar, N.; Becerra Gonzalez, J.; Becerril, A.; Belmont-Moreno, E.; BenZvi, S. Y.; Berley, D.; Bernal, A.; Braun, J.; Brisbois, C.; Caballero-Mora, K. S.; Capistrán, T.; Carramiñana, A.; Casanova, S.; Castillo, M.; Cotti, U.; Cotzomi, J.; Coutiño de León, S.; de la Fuente, E.; De León, C.; Diaz Hernandez, R.; Dingus, B. L.; DuVernois, M. A.; Díaz-Vélez, J. C.; Ellsworth, R. W.; Engel, K.; Fiorino, D. W.; Fraija, N.; García-González, J. A.; Garfias, F.; Gerhardt, M.; González Muñoz, A.; González, M. M.; Goodman, J. A.; Hampel-Arias, Z.; Harding, J. P.; Hernandez, S.; Hernandez-Almada, A.; Hinton, J.; Hui, C. M.; Hüntemeyer, P.; Iriarte, A.; Jardin-Blicq, A.; Joshi, V.; Kaufmann, S.; Kieda, D.; Lara, A.; Lauer, R. J.; Lee, W. H.; Lennarz, D.; León Vargas, H.; Linnemann, J. T.; Longinotti, A. L.; Raya, G. L.; Luna-García, R.; López-Coto, R.; Malone, K.; Marinelli, S. S.; Martinez, O.; Martinez-Castellanos, I.; Martínez-Castro, J.; Martínez-Huerta, H.; Matthews, J. A.; Miranda-

Romagnoli, P.; Moreno, E.; Mostafá, M.; Nellen, L.; Newbold, M.; Nisa, M. U.; Noriega-Papaqui, R.; Pelayo, R.; Pretz, J.; Pérez-Pérez, E. G.; Ren, Z.; Rho, C. D.; Rivière, C.; Rosa-González, D.; Rosenberg, M.; Ruiz-Velasco, E.; Salazar, H.; Salesa Greus, F.; Sandoval, A.; Schneider, M.; Schoorlemmer, H.; Sinnis, G.; Smith, A. J.; Springer, R. W.; Surajbali, P.; Taboada, I.; Tibolla, O.; Tollefson, K.; Torres, I.; Ukwatta, T. N.; Vianello, G.; Villaseñor, L.; Weisgarber, T.; Westerhoff, S.; Wisher, I. G.; Wood, J.; Yapici, T.; Younk, P. W.; Zepeda, A.; Zhou, H. The 2HWC HAWC Observatory Gamma-Ray Catalog. *Astrophys. J.* **2017**, *843*, 40.

(66) CTA Consortium., Introducing the CTA Concept. *Astropart. Phys.* **2013**, *43*, 3–18.

(67) Jelley, J. V.; Porter, N. A. Čerenkov Radiation from the Night Sky, and its Application to γ-Ray Astronomy. *Q. J. R. Astron. Soc.* **1963**, *4*, 275.

(68) Braun, I.; Commichau, S. C.; Rissi, M.; Backes, M.; Biland, A.; Bretz, T.; Britvitch, I.; Commichau, V.; von Gunten, H.; Hildebrand, D.; Horisberger, U.; Kranich, D.; Lorenz, E.; Lustermann, W.; Mannheim, K.; Neise, D.; Pauss, F.; Pohl, M.; Renker, D.; Rhode, W.; Röser, U.; Straumann, U.; Viertel, G. First Avalanche-Photodiode Camera Test (FACT): A Novel Camera Using G-APDs for the Observation of Very High-Energy γ-rays with Cherenkov Telescopes. *Nucl. Instrum. Methods Phys. Res., Sect. A* **2009**, *610*, 400–403.

(69) Hillas, A. M. Cherenkov Light Images of EAS Produced by Primary Gamma. 19th. International Cosmic Ray Conference, La Jolla, United States. 1985.

(70) Maier, G.; Acciari, V. A.; Amini, R.; Blaylock, G.; Bradbury, S. M.; Buckley, J. H.; Bugaev, V.; Butt, Y.; Byrum, K. L.; Celik, O.; Cesarini, A.; Ciupik, L.; Chow, Y. C. K.; Cogan, P.; Colin, P.; Cui, W.; Daniel, M. K.; Dowdall, C.; Dowkontt, P.; Duke, C.; Ergin, T.; Falcone, A. D.; Fegan, D. J.; Fegan, S. J.; Finley, J. P.; Fotin, P.; Fortson, L. F.; Gall, D.; Gibbs, K.; Gillanders, G.; Grube, J.; Guenette, R.; Gyuk, G.; Hall, J.; Hanna, D.; Hays, E.; Holder, J.; Horan, D.; Hughes, S. B.; Hui, C. M.; Humensky, T. B.; Imran, A.; Kaaret, P.; Kenny, G. E.; Kertzman, M.; Kieda, D.; Kildea, J.; Konopelko, A.; Krawczynski, H.; Krennrich, F.; Lang, M. J.; LeBohec, S.; Lee, K.; Manseri, H.; McCann, A.; McCutcheron, M.; Millis, J.; Moriarty, P.; Mukherjee, R.; Nagai T.,; Niemiec, J.; Ogden, P. A.; Ong, R. A.; Pandel, D.; Perkins, J. S.; Pizlo, F.; Pohl, M.; Quinn, J.; Ragan, K.; Reynolds, P. T.; Roache, E.; Rose, H. J.; Schroedter, M.; Sembroski, G. H.; Smith, A. W.; Steele, D.; Swordy, S. P.; Syson, A.; Toner, J. A.; Valcarcel, L.; Vassiliev, V. V.; Wagner, R.; Wakely, S. P.; Ward, J. E.; Weeks, T. C.; Weinstein, A.; White, R. J.; Williams, D. A.; Wissel, S. A.; Wood, M.; Zitzer, B. VERITAS: Status and Latest Results. 30th. International Cosmic Ray Conference, Merida, Yucatán. 2007; pp 1457–1460.

(71) Park, N.; VERITAS Collaboration, Performance of the VERITAS Experiment. 34th. International Cosmic Ray Conference,, The Hague, Netherlands. 2015; p 771.

(72) Perkins, J. S.; Maier, G.; VERITAS Collaboration, VERITAS Telescope 1 Relocation: Details and Improvements. AAS/High Energy Astrophysics Division #11. 2010; p 719.

(73) Kieda, D. Status of the VERITAS Upgrade. 32nd International Cosmic Ray Conference, Beijing, China. 2011; p 14.

(74) D. B. Kieda for the VERITAS Collaboration, The Gamma Ray Detection Sensitivity of the Upgraded VERITAS Observatory. 2013, arXiv:astro-ph.HE/1308.4849. arXiv.org e-Print archive. https://arxiv.org/abs/1308.4849 (accessed May 30, 2017.

(75) Zitzer, B.; VERITAS Collaboration, The VERITAS Upgraded Telescope-Level Trigger Systems: Technical Details and Performance Characterization. 2013, arXiv:astro-ph.HE/1307.8360. arXiv.org e-Print archive. https://arxiv.org/abs/1307.8360 (accessed May 30, 2017.

(76) Archambault, S.; Archer, A.; Benbow, W.; Bird, R.; Bourbeau, E.; Bouvier, A.; Buchovecky, M.; Bugaev, V.; Cardenzana, J. V.; Cerruti, M.; Ciupik, L.; Connolly, M. P.; Cui, W.; Daniel, M. K.; Errando, M.; Falcone, A.; Feng, Q.; Finley, J. P.; Fleischhack, H.; Fortson, L.; Furniss, A.; Gillanders, G. H.; Griffin, S.; Hanna, D.; Hervet, O.; Holder, J.; Hughes, G.; Humensky, T. B.; Hütten, M.; Johnson, C. A.; Kaaret, P.; Kar, P.; Kertzman, M.; Kieda, D.; Krause, M.; Lang, M. J.; Lin, T. T. Y.; Maier, G.; McArthur, S.; Moriarty, P.; Mukherjee, R.; Nieto, D.; O'Brien, S.; Ong, R. A.; Otte, A. N.; Park, N.; Pohl, M.; Popkow, A.; Pueschel, E.; Quinn, J.; Ragan, K.; Reynolds, P. T.; Richards, G. T.; Roache, E.; Rulten, C.; Sadeh, I.; Sembroski, G. H.; Shahinyan, K.; Staszak, D.; Telezhinsky, I.; Trepanier, S.; Wakely, S. P.; Weinstein, A.; Wilcox, P.; Williams, D. A.; Zitzer, B. Gamma-Ray Observations Under Bright Moonlight with VERITAS. *Astropart. Phys.* **2017**, *91*, 34–43.

(77) Krennrich, F.; Bond, I. H.; Boyle, P. J.; Bradbury, S. M.; Buckley, J. H.; Carter-Lewis, D.; Celik, O.; Cui, W.; Daniel, M.; D'Vali, M.; de la Calle Perez, I.; Duke, C.; Falcone, A.; Fegan, D. J.; Fegan, S. J.; Finley, J. P.; Fortson, L. F.; Gaidos, J.; Gammell, S.; Gibbs, K.; Gillanders, G. H.; Grube, J.; Hall, J.; Hall, T. A.; Hanna, D.; Hillas, A. M.; Holder, J.; Horan, D.; Jarvis, A.; Jordan, M.; Kenny, G. E.; Kertzman, M.; Kieda, D.; Kildea, J.; Knapp, J.; Kosack, K.; Krawczynski, H.; Lang, M. J.; LeBohec, S.; Linton, E.; Lloyd-Evans, J.; Milovanovic, A.; Moriarty, P.; Müller, D.; Nagai, T.; Nolan, S.; Ong, R. A.; Pallassini, R.; Petry, D.; Power-Mooney, B.; Quinn, J.; Quinn, M.; Ragan, K.; Rebillot, P.; Reynolds, P. T.; Rose, H. J.; Schroedter, M.; Sembroski, G.; Swordy, S. P.; Syson, A.; Vassiliev, V. V.; Walker, G.; Wakely, S. P.; Weekes, T. C.; Zweerink, J. VERITAS: the Very Energetic Radiation Imaging Telescope Array System. *New Astron. Rev.* **2004**, *48*, 345–349.

(78) Winston, R. Light Collection within the Framework of Geometrical Optics∗. *J. Opt. Soc. Am.* **1970**, *60*, 245–247.

(79) Otte, N. Upgrade of VERITAS with High Efficiency Photomultipliers. 32nd International Cosmic Ray Conference, Beijing, China. 2011; p 247.

(80) Weinstein, A. The VERITAS Trigger System. 30th. International Cosmic Ray Conference, Merida, Yucatán. 2007; pp 1539–1542.

(81) Hays, E. VERITAS Data Acquisition. 30th. International Cosmic Ray Conference, Merida, Yucatán. 2007; pp 1543–1546.

(82) Wakely, S. P.; Cui, W.; Pizlo, F.; Nolan, S.; Quinn, J.; Ozlem, C.; Ong, R. VERITAS Data Acquisition and Analysis Systems. 28th. International Cosmic Ray Conference, Tsukuba, Japan. 2003; p 2839.

(83) Weekes, T. C.; Cawley, M. F.; Fegan, D. J.; Gibbs, K. G.; Hillas, A. M.; Kowk, P. W.; Lamb, R. C.; Lewis, D. A.; Macomb, D.; Porter, N. A.; Reynolds, P. T.; Vacanti, G. Observation of TeV Gamma Rays from the Crab Nebula Using the Atmospheric Cherenkov Imaging Technique. *Astrophys. J.* **1989**, *342*, 379–395.

(84) Aharonian, F. A.; Akhperjanian, A. G.; Barrio, J. A.; Bernlöhr, K.; Bojahr, H.; Contreras, J. L.; Cortina, J.; Daum, A.; Deckers, T.; Fonseca, V.; Gonzalez, J. C.; Heinzelmann, G.; Hemberger, M.; Hermann, G.; Heß, M.; Heusler, A.; Hofmann, W.; Hohl, H.; Horns, D.; Ibarra, A.; Kankanyan, R.; Kirstein, O.; Köhler, C.; Konopelko, A.; Kornmeyer, H.; Kranich, D.; Krawczynski, H.; Lampeitl, H.; Lindner, A.; Lorenz, E.; Magnussen, N.; Meyer, H.; Mirzoyan, R.; Moralejo, A.; Padilla, L.; Panter, M.; Petry, D.; Plaga, R.; Plyasheshnikov, A.; Prahl, J.; Pühlhofer, G.; Rauterberg, G.; Renault, C.; Rhode, W.; Sahakian, V.; Samorski, M.; Schmele, D.; Schröder, F.; Stamm, W.; Völk, H. J.; Wiebel-Sooth, B.; Wiedner, C.; Willmer, M.; Wirth, H. The Temporal Characteristics of the TeV Gamma-radiation from MKN 501 in 1997. I. Data from the Stereoscopic Imaging Atmospheric Cherenkov Telescope System of HEGRA. *Astron. Astrophys.* **1999**, *342*, 69–86.

(85) Krause, M.; Pueschel, E.; Maier, G. Improved γ-Hadron Separation for the Detection of Faint γ-ray Sources Using Boosted Decision Trees. *Astropart. Phys.* **2017**, *89*, 1–9.

(86) Li, T.-P.; Ma, Y.-Q. Analysis Methods for Results in Gamma-Ray Astronomy. *Astrophys. J.* **1983**, *272*, 317–324.

(87) Aharonian, F.; Akhperjanian, A. G.; Bazer-Bachi, A. R.; Beilicke, M.; Benbow, W.; Berge, D.; Bernlöhr, K.; Boisson, C.; Bolz, O.; Borrel, V.; Braun, I.; Breitling, F.; Brown, A. M.; Bühler, R.; Büsching, I.; Carrigan, S.; Chadwick, P. M.; Chounet, L.-M.; Cornils, R.; Costamante, L.; Degrange, B.; Dickinson, H. J.; Djannati-Ataï, A.; O'C. Drury, L.; Dubus, G.; Egberts, K.; Emmanoulopoulos, D.; Espigat, P.; Feinstein, F.; Ferrero, E.; Fiasson, A.; Fontaine, G.; Funk, S.; Funk, S.; Gallant, Y. A.; Giebels, B.; Glicenstein, J. F.; Goret, P.; Hadjichristidis, C.; Hauser, D.; Hauser, M.; Heinzelmann, G.; Henri, G.; Hermann, G.; Hinton, J. A.; Hofmann, W.; Holleran, M.; Horns, D.; Jacholkowska, A.; de Jager, O. C.; Khélifi, B.; Komin, N.; Konopelko, A.; Kosack, K.; Latham, I. J.; Le Gallou, R.; Lemière, A.; Lemoine-Goumard, M.; Lohse, T.; Martin, J. M.; Martineau-Huynh, O.; Marcowith, A.; Masterson, C.; McComb, T. J. L.; de Naurois, M.; Nedbal, D.; Nolan, S. J.; Noutsos, A.; Orford, K. J.; Osborne, J. L.; Ouchrif, M.; Panter, M.; Pelletier, G.; Pita, S.; Pühlhofer, G.; Punch, M.; Raubenheimer, B. C.; Raue, M.; Rayner, S. M.; Reimer, A.; Reimer, O.; Ripken, J.; Rob, L.; Rolland, L.; Rowell, G.; Sahakian, V.; Saugé, L.; Schlenker, S.; Schlickeiser, R.; Schwanke, U.; Sol, H.; Spangler, D.; Spanier, F.; Steenkamp, R.; Stegmann, C.; Superina, G.; Tavernet, J.-P.; Terrier, R.; Théoret, C. G.; Tluczykont, M.; van Eldik, C.; Vasileiadis, G.; Venter, C.; Vincent, P.; Völk, H. J.; Wagner, S. J.; Ward, M. Observations of the Crab Nebula with H.E.S.S. *Astron. Astrophys.* **2006**, *457*, 899–915.

(88) Smith, A. Multiwavelength Observations of the TeV Binary LS I $+61^\circ$ 303 . Ph.D. thesis, The University of Leeds, West Yorkshire, England, 2008.

(89) de Naurois, M.; Mazin, D. Ground-Based Detectors in Very-High-Energy Gamma-Ray Astronomy. *C. R. Phys.* **2015**, *16*, 610–627.

(90) LeBohec, S.; Duke, C.; Jordan, P. Minimal Stereoscopic Analysis for Imaging Atmospheric Cherenkov Telescope Arrays. *Astropart. Phys.* **2005**, *24*, 26–31.

(91) Berge, D.; Funk, S.; Hinton, J. Background Modelling in Very-High-Energy γ-ray Astronomy. *Astron. Astrophys.* **2007**, *466*, 1219–1229.

(92) Casares, J.; Ribas, I.; Paredes, J. M.; Martí, J.; Allende Prieto, C. Orbital Parameters of the Microquasar LS I $+61^\circ$ 303 . *Mon. Not. R. Astron. Soc.* **2005**, *360*, 1105–1109.

(93) Taylor, A. R.; Gregory, P. C. Periodic Radio Emission from LS I $+61^\circ$ 303 . *Astrophys. J.* **1982**, *255*, 210–216.

(94) Hutchings, J. B.; Crampton, D. Spectroscopy of the Unique Degenerate Binary Star LS I $+61^\circ$ 303 . *Publ. Astron. Soc. Pac.* **1981**, *93*, 486–489.

(95) Gregory, P. C. Bayesian Analysis of Radio Observations of the Be X-Ray Binary LS I $+61^\circ$ 303 . *Astrophys. J.* **2002**, *575*, 427–434.

(96) Paredes, J. M.; Marti, J.; Peracaula, M.; Ribo, M. Evidence of X-ray Periodicity in LS I $+61^\circ$ 303 . *Astron. Astrophys.* **1997**, *320*, L25–L28.

(97) Abdo, A. A.; Ackermann, M.; Ajello, M.; Atwood, W. B.; Axelsson, M.; Baldini, L.; Ballet, J.; Barbiellini, G.; Bastieri, D.; Baughman, B. M.; Bechtol, K.; Bellazzini, R.; Berenji, B.; Blandford, R.; Bloom, E. D.; Bonamente, E.; Borgland, A. W.; Bregeon, J.; Brez, A.; Brigida, M.; Bruel, P.; Burnett, T. H.; Caliandro, G. A.; Cameron, R. A.; Caraveo, P. A.; Casandjian, J. M.; Cavazzuti, E.; Cecchi, C.; Çelik, Ö.; Charles, E.; Chaty, S.; Chekhtman, A.; Cheung, C. C.; Chiang, J.; Ciprini, S.; Claus, R.; Cohen-Tanugi, J.; Cominsky, L. R.; Conrad, J.; Corbel, S.; Corbet, R.; Cutini, S.; Dermer, C. D.; de Angelis, A.; de Luca, A.; de Palma, F.; Digel, S. W.; Dormody, M.; do Couto e Silva, E.; Drell, P. S.; Dubois, R.; Dubus, G.; Dumora, D.; Farnier, C.; Favuzzi, C.; Fegan, S. J.; Focke, W. B.; Frailis, M.; Fukazawa, Y.; Funk, S.; Fusco, P.; Gargano, F.; Gasparrini, D.; Gehrels, N.; Germani, S.; Giebels, B.; Giglietto, N.; Giordano, F.; Glanzman, T.; Godfrey, G.; Grenier, I. A.; Grondin, M.-H.; Grove, J. E.; Guillemot, L.; Guiriec, S.; Hanabata, Y.; Harding, A. K.; Hayashida, M.; Hays, E.; Hill, A. B.; Hughes, R. E.; Jóhannesson, G.; Johnson, A. S.; Johnson, R. P.; Johnson, T. J.; Johnson, W. N.; Kamae, T.; Katagiri, H.; Kataoka, J.; Kawai, N.; Kerr, M.; Knödlseder, J.; Kocian, M. L.; Kuehn, F.; Kuss, M.; Lande, J.; Larsson, S.; Latronico, L.; Longo, F.; Loparco, F.; Lott, B.; Lovellette, M. N.; Lubrano, P.; Madejski, G. M.; Makeev, A.; Marelli, M.; Mazziotta, M. N.; McEnery, J. E.; Meurer, C.; Michelson, P. F.; Mitthumsiri, W.; Mizuno, T.; Monte, C.; Monzani, M. E.; Morselli, A.; Moskalenko, I. V.; Murgia, S.; Nolan, P. L.; Nuss, E.; Ohsugi, T.; Okumura, A.; Omodei, N.; Orlando, E.; Ormes, J. F.; Paneque, D.; Panetta, J. H.; Parent, D.; Pelassa, V.; Pepe, M.; Pesce-Rollins, M.; Piron, F.; Porter, T. A.; Rainò, S.; Rando, R.; Ray, P. S.; Razzano, M.; Rea, N.; Reimer, A.; Reimer, O.; Reposeur, T.; Ritz, S.; Rochester, L. S.; Rodriguez, A. Y.; Romani, R. W.; Ryde, F.; Sadrozinski, H. F.-W.; Sanchez, D.; Sander, A.; Saz Parkinson, P. M.; Scargle, J. D.; Sgrò, C.; Shaw, M. S.; Sierpowska-Bartosik, A.; Siskind, E. J.; Smith, D. A.; Smith, P. D.; Spandre, G.; Spinelli, P.; Striani, E.; Strickman, M. S.; Suson, D. J.; Tajima, H.; Takahashi, H.; Takahashi, T.; Tanaka, T.; Thayer, J. B.; Thayer, J. G.; Thompson, D. J.; Tibaldo, L.; Torres, D. F.; Tosti, G.; Tramacere, A.; Uchiyama, Y.; Usher, T. L.; Vasileiou, V.;

Vilchez, N.; Vitale, V.; Waite, A. P.; Wang, P.; Winer, B. L.; Wood, K. S.; Ylinen, T.; Ziegler, M. Fermi LAT Observations of LS I $+61^\circ$ 303 : First Detection of an Orbital Modulation in GeV Gamma Rays. *Astrophys. J. Lett.* **2009**, *701*, L123–L128.

(98) Albert, J.; Aliu, E.; Anderhub, H.; Antoranz, P.; Armada, A.; Asensio, M.; Baixeras, C.; Barrio, J. A.; Bartelt, M.; Bartko, H.; Bastieri, D.; Bavikadi, S. R.; Bednarek, W.; Berger, K.; Bigongiari, C.; Biland, A.; Bisesi, E.; Bock, R. K.; Bordas, P.; Bosch-Ramon, V.; Bretz, T.; Britvitch, I.; Camara, M.; Carmona, E.; Chilingarian, A.; Ciprini, S.; Coarasa, J. A.; Commichau, S.; Contreras, J. L.; Cortina, J.; Curtef, V.; Danielyan, V.; Dazzi, F.; De Angelis, A.; de los Reyes, R.; De Lotto, B.; Domingo-Santamaría, E.; Dorner, D.; Doro, M.; Errando, M.; Fagiolini, M.; Ferenc, D.; Fernández, E.; Firpo, R.; Flix, J.; Fonseca, M. V.; Font, L.; Fuchs, M.; Galante, N.; Garczarczyk, M.; Gaug, M.; Giller, M.; Goebel, F.; Hakobyan, D.; Hayashida, M.; Hengstebeck, T.; Höhne, D.; Hose, J.; Hsu, C. C.; Isar, P. G.; Jacon, P.; Kalekin, O.; Kosyra, R.; Kranich, D.; Laatiaoui, M.; Laille, A.; Lenisa, T.; Liebing, P.; Lindfors, E.; Lombardi, S.; Longo, F.; López, J.; López, M.; Lorenz, E.; Lucarelli, F.; Majumdar, P.; Maneva, G.; Mannheim, K.; Mansutti, O.; Mariotti, M.; Martínez, M.; Mase, K.; Mazin, D.; Merck, C.; Meucci, M.; Meyer, M.; Miranda, J. M.; Mirzoyan, R.; Mizobuchi, S.; Moralejo, A.; Nilsson, K.; Oña-Wilhelmi, E.; Orduña, R.; Otte, N.; Oya, I.; Paneque, D.; Paoletti, R.; Paredes, J. M.; Pasanen, M.; Pascoli, D.; Pauss, F.; Pavel, N.; Pegna, R.; Persic, M.; Peruzzo, L.; Piccioli, A.; Poller, M.; Pooley, G.; Prandini, E.; Raymers, A.; Rhode, W.; Ribó, M.; Rico, J.; Riegel, B.; Rissi, M.; Robert, A.; Romero, G. E.; Rügamer, S.; Saggion, A.; Sánchez, A.; Sartori, P.; Scalzotto, V.; Scapin, V.; Schmitt, R.; Schweizer, T.; Shayduk, M.; Shinozaki, K.; Shore, S. N.; Sidro, N.; Sillanpää, A.; Sobczynska, D.; Stamerra, A.; Stark, L. S.; Takalo, L.; Temnikov, P.; Tescaro, D.; Teshima, M.; Tonello, N.; Torres, A.; Torres, D. F.; Turini, N.; Vankov, H.; Vitale, V.; Wagner, R. M.; Wibig, T.; Wittek, W.; Zanin, R.; Zapatero, J. Variable Very-High-Energy Gamma-Ray Emission from the Microquasar LS I $+61^\circ$ 303 . *Science* **2006**, *312*, 1771–1773.

(99) Acciari, V. A.; Beilicke, M.; Blaylock, G.; Bradbury, S. M.; Buckley, J. H.; Bugaev, V.; Butt, Y.; Byrum, K. L.; Celik, O.; Cesarini, A.; Ciupik, L.; Chow, Y. C. K.; Cogan, P.; Colin, P.; Cui, W.; Daniel, M. K.; Duke, C.; Ergin, T.; Falcone, A. D.; Fegan, S. J.; Finley, J. P.; Fortin, P.; Fortson, L. F.; Gall, D.; Gibbs, K.; Gillanders, G. H.; Grube, J.; Guenette, R.; Hanna, D.; Hays, E.; Holder, J.; Horan, D.; Hughes, S. B.; Hui, C. M.; Humensky, T. B.; Kaaret, P.; Kieda, D. B.; Kildea, J.; Konopelko, A.; Krawczynski, H.; Krennrich, F.; Lang, M. J.; LeBohec, S.; Lee, K.; Maier, G.; McCann, A.; McCutcheon, M.; Millis, J.; Moriarty, P.; Mukherjee, R.; Nagai, T.; Ong, R. A.; Pandel, D.; Perkins, J. S.; Pizlo, F.; Pohl, M.; Quinn, J.; Ragan, K.; Reynolds, P. T.; Rose, H. J.; Schroedter, M.; Sembroski, G. H.; Smith, A. W.; Steele, D.; Swordy, S. P.; Toner, J. A.; Valcarcel, L.; Vassiliev, V. V.; Wagner, R.; Wakely, S. P.; Ward, J. E.; Weekes, T. C.; Weinstein, A.; White, R. J.; Williams, D. A.; Wissel, S. A.; Wood, M.; Zitzer, B. VERITAS Observations of the γ-Ray Binary LS I $+61^\circ$ 303 . *Astrophys. J.* **2008**, *679*, 1427–1432.

(100) Apparao, K. M. V. Optical and Infrared Modulation in the Be-star/X-ray Source LS I $+61^\circ$ 303 . *Astron. Astrophys.* **1999**, *348*, 843–845.

(101) Bosch-Ramon, V.; Paredes, J. M.; Romero, G. E.; Ribó, M. The Radio to TeV Orbital Variability of the Microquasar LS I $+61^\circ$ 303 . *Astron. Astrophys.* **2006**, *459*, L25–L28.

(102) Romero, G. E.; Torres, D. F.; Kaufman Bernadó, M. M.; Mirabel, I. F. Hadronic Gamma-Ray Emission from Windy Microquasars. *Astron. Astrophys.* **2003**, *410*, L1–L4.

(103) Romero, G. E.; Christiansen, H. R.; Orellana, M. Hadronic High-Energy Gamma-Ray Emission from the Microquasar LS I +61° 303 . *Astrophys. J.* **2005**, *632*, 1093–1098.

(104) Romero, G. E.; Okazaki, A. T.; Orellana, M.; Owocki, S. P. Accretion vs. Colliding Wind Models for the Gamma-Ray Binary LS I +61° 303 : an Assessment. *Astron. Astrophys.* **2007**, *474*, 15–22.

(105) Jaron, F.; Torricelli-Ciamponi, G.; Massi, M. Understanding the Periodicities in Radio and GeV Emission from LS I +61° 303 . *Astron. Astrophys.* **2016**, *595*, A92.

(106) Massi, M.; Torricelli-Ciamponi, G. Origin of the Long-term Modulation of Radio Emission of LS I +61° 303 . *Astron. Astrophys.* **2016**, *585*, A123.

(107) Massi, M.; Ribó, M.; Paredes, J. M.; Garrington, S. T.; Peracaula, M.; Martí, J. Hints for a Fast Precessing Relativistic Radio Jet in LS I +61° 303 . *Astron. Astrophys.* **2004**, *414*, L1–L4.

(108) Massi, M.; Ros, E.; Zimmermann, L. VLBA Images of the Precessing Jet of LS I +61° 303 . *Astron. Astrophys.* **2012**, *540*, A142.

(109) Massi, M.; Jaron, F. Long-term Periodicity in LS I +61° 303 as Beat Frequency between Orbital and Precessional Rate. *Astron. Astrophys.* **2013**, *554*, A105.

(110) Ray, P. S.; Foster, R. S.; Waltman, E. B.; Tavani, M.; Ghigo, F. D. Long-Term Flux Monitoring of LS I +61° 303 at 2.25 and 8.3 GHz. *Astrophys. J.* **1997**, *491*, 381–387.

(111) Massi, M.; Torricelli-Ciamponi, G. Intrinsic Physical Properties and Doppler Boosting Effects in LS I +61° 303 . *Astron. Astrophys.* **2014**, *564*, A23.

(112) Larwood, J. On the Precession of Accretion Discs in X-ray Binaries. *Mon. Not. R. Astron. Soc.* **1998**, *299*, L32–l36.

(113) Massi, M.; Kaufman Bernadó, M. Radio Spectral Index Analysis and Classes of Ejection in LS I +61° 303 . *Astrophys. J.* **2009**, *702*, 1179–1189.

(114) Massi, M. The Two-Peak Model of LS I +61° 303 : Radio Spectral Index Analysis. *Mem. Soc. Astron. Ital.* **2011**, *82*, 77.

(115) Cañellas, A.; Joshi, B. C.; Paredes, J. M.; Ishwara-Chandra, C. H.; Moldón, J.; Zabalza, V.; Martí, J.; Ribó, M. Search for Radio Pulsations in LS I +61° 303 . *Astron. Astrophys.* **2012**, *543*, A122.

(116) Maraschi, L.; Treves, A. A Model for LS I +61° 303 . *Mon. Not. R. Astron. Soc.* **1981**, *194*, 1P–5P.

(117) Harrison, F. A.; Ray, P. S.; Leahy, D. A.; Waltman, E. B.; Pooley, G. G. Simultaneous X-Ray and Radio Monitoring of the Unusual Binary LS I +61° 303 : Measurements of the Light Curve and High-Energy Spectrum. *Astrophys. J.* **2000**, *528*, 454–461.

(118) Sierpowska, A.; Bednarek, W. γ-rays from Cascades in Close Massive Binaries Containing Energetic Pulsars. *Mon. Not. R. Astron. Soc.* **2005**, *356*, 711–726.

(119) Dubus, G. Gamma-Ray Binaries and Related System. *Astron. Astrophys.* **2006**, *456*, 801–817.

(120) Zdziarski, A. A.; Neronov, A.; Chernyakova, M. A Compact Pulsar Wind Nebula Model of the γ-ray-loud Binary LS I $+61^\circ$ 303 . *Mon. Not. R. Astron. Soc.* **2010**, *403*, 1873–1886.

(121) Li, J.; Torres, D. F.; Zhang, S.; Chen, Y.; Hadasch, D.; Ray, P. S.; Kretschmar, P.; Rea, N.; Wang, J. Long-term X-Ray Monitoring of LS I $+61^\circ$ 303 : Analysis of Spectral Variability and Flares. *Astrophys. J.* **2011**, *733*, 89.

(122) Dhawan, V.; Mioduszewski, A.; Rupen, M. LS I $+61^\circ$ 303 is a Be-Pulsar Binary, Not a Microquasar. VI Microquasar Workshop: Microquasars and Beyond, Como, Italy. 2006; p 52.1.

(123) Zamanov, R.; Martí, J.; García-Hernández, M. T. Mass of the Compact Object in the Be/Gamma-Ray Binaries LS I $+61^\circ$ 303 and MWC 148. *Bulgarian Astronom. J.* **2017**, *27*, 57.

(124) Özel, F.; Psaltis, D.; Narayan, R.; Santos Villarreal, A. On the Mass Distribution and Birth Masses of Neutron Stars. *Astrophys. J.* **2012**, *757*, 55.

(125) Chamel, N.; Haensel, P.; Zdunik, J. L.; Fantina, A. F. On the Maximum Mass of Neutron Stars. *Int. J. Mod. Phys. E* **2013**, *22*, 1330018.

(126) Vila, G. S.; Pepe, C.; Romero, G. E. Spectral Energy Distribution, Radio Maps and Polarization of Cygnus X-1: A Lepto-Hadronic Model. *Boletin de la Asociacion Argentina de Astronomia La Plata Argentina* **2016**, *58*, 240–242.

(127) Neronov, A.; Chernyakova, M. Radio-to-TeV γ-ray Emission from PSR B1259-63. *Astrophys. Space Sci.* **2007**, *309*, 253–259.

(128) Barthelmy, S. D.; Baumgartner, W.; Cummings, J.; Gehrels, N.; Markwardt, C.; Sakamoto, T.; Godet, O.; Evans, P.; Osborne, J.; Beardmore, A. P.; Kennea, J.; Falcone, A.; Burrows, D.; Campana, S.; de Pasquale, M. Swift-BAT/-XRT Refined Analysis on Trigger 324362 (LS I $+61^\circ$ 303). *GRB Coordinates Network* **2008**, *8215*.

(129) de Pasquale, M.; Barthelmy, S. D.; Baumgartner, W. H.; Gehrels, N.; Gronwall, C.; Kennea, J. A.; Mao, J.; Markwardt, C. B.; Tagliaferri, G. Swift Trigger 324362 (LS I $+61^\circ$ 303 ?). *GRB Coordinates Network* **2008**, *8209*.

(130) Dubus, G.; Giebels, B. Swift BAT Detection of a SGR-like Burst from LS I $+61^\circ$ 303 . *The Astronomer's Telegram* **2008**, *1715*.

(131) Gavriil, F. P.; Gonzalez, M. E.; Gotthelf, E. V.; Kaspi, V. M.; Livingstone, M. A.; Woods, P. M. Magnetar-Like Emission from the Young Pulsar in Kes 75. *Science* **2008**, *319*, 1802.

(132) Negueruela, I. Be/X-ray Binaries: An Observational Approach. Massive Stars in Interactive Binaries. 2007; p 477.

(133) Belczynski, K.; Ziolkowski, J. On the Apparent Lack of Be X-Ray Binaries with Black Holes. *Astrophys. J.* **2009**, *707*, 870–877.

(134) Tauris, T. M.; van den Heuvel, E. P. J. *Compact stellar X-ray sources*; Cambridge University Press: Cambridge, UK, 2006; pp 623–665.

(135) Gies, D. R. Glimpses of Be Binary Evolution. IAU Colloq. 175: The Be Phenomenon in Early-Type Stars. 2000; p 668.

(136) Acciari, V. A.; Aliu, E.; Arlen, T.; Aune, T.; Beilicke, M.; Benbow, W.; Bradbury, S. M.; Buckley, J. H.; Bugaev, V.; Byrum, K.; Cannon, A.; Cesarini, A.; Ciupik, L.; Collins-Hughes, E.; Connolly, M. P.; Cui, W.; Dickherber, R.; Duke, C.; Errando, M.; Falcone, A.; Finley, J. P.; Finnegan, G.; Fortson, L.; Furniss, A.; Galante, N.; Gall, D.; Gillanders, G. H.; Godambe, S.; Griffin, S.; Grube, J.; Guenette, R.; Gyuk, G.; Hanna, D.; Holder, J.; Hughes, G.; Hui, C. M.; Humensky, T. B.; Kaaret, P.; Karlsson, N.; Kertzman, M.; Kieda, D.; Krawczynski, H.; Krennrich, F.; Lang, M. J.; LeBohec, S.; Maier, G.; Majumdar, P.; McArthur, S.; McCann, A.; Moriarty, P.; Mukherjee, R.; Ong, R. A.; Orr, M.; Otte, A. N.; Park, N.; Perkins, J. S.; Pohl, M.; Prokoph, H.; Quinn, J.; Ragan, K.; Reyes, L. C.; Reynolds, P. T.; Roache, E.; Rose, H. J.; Ruppel, J.; Saxon, D. B.; Schroedter, M.; Sembroski, G. H.; Senturk, G. D.; Smith, A. W.; Staszak, D.; Tešić, G.; Theiling, M.; Thibadeau, S.; Tsurusaki, K.; Varlotta, A.; Vassiliev, V. V.; Vincent, S.; Vivier, M.; Wakely, S. P.; Ward, J. E.; Weekes, T. C.; Weinstein, A.; Weisgarber, T.; Williams, D. A.; Zitzer, B. VERITAS Observations of the TeV Binary LS I $+61^\circ$ 303 During 2008-2010. *Astrophys. J.* **2011**, *738*, 3.

(137) Aliu, E.; Archambault, S.; Behera, B.; Berger, K.; Beilicke, M.; Benbow, W.; Bird, R.; Bouvier, A.; Bugaev, V.; Cerruti, M.; Chen, X.; Ciupik, L.; Connolly, M. P.; Cui, W.; Dumm, J.; Falcone, A.; Federici, S.; Feng, Q.; Finley, J. P.; Fortin, P.; Fortson, L.; Furniss, A.; Galante, N.; Gillanders, G. H.; Griffin, S.; Griffiths, S. T.; Grube, J.; Gyuk, G.; Hanna, D.; Holder, J.; Hughes, G.; Humensky, T. B.; Kaaret, P.; Kertzman, M.; Khassen, Y.; Kieda, D.; Krennrich, F.; Lang, M. J.; Maier, G.; Majumdar, P.; McArthur, S.; McCann, A.; Moriarty, P.; Mukherjee, R.; O'Faoláin de Bhróithe, A.; Ong, R. A.; Otte, A. N.; Park, N.; Perkins, J. S.; Pohl, M.; Popkow, A.; Prokoph, H.; Quinn, J.; Ragan, K.; Rajotte, J.; Ratliff, G.; Reynolds, P. T.; Richards, G. T.; Roache, E.; Sembroski, G. H.; Sheidaei, F.; Skole, C.; Smith, A. W.; Staszak, D.; Telezhinsky, I.; Tyler, J.; Varlotta, A.; Vincent, S.; Wakely, S. P.; Weekes, T. C.; Weinstein, A.; Welsing, R.; Zajczyk, A.; Zitzer, B. Multiwavelength Observations of the TeV Binary LS I $+61^\circ$ 303 with VERITAS, Fermi-LAT, and Swift/XRT during a TeV Outburst. *Astrophys. J.* **2013**, *779*, 88.

(138) Khangulyan, D.; Aharonian, F.; Bosch-Ramon, V. On the Formation of TeV Radiation in LS 5039. *Mon. Not. R. Astron. Soc.* **2008**, *383*, 467–478.

(139) Archambault, S.; Archer, A.; Aune, T.; Barnacka, A.; Benbow, W.; Bird, R.; Buchovecky, M.; Buckley, J. H.; Bugaev, V.; Byrum, K.; Cardenzana, J. V.; Cerruti, M.; Chen, X.; Ciupik, L.; Collins-Hughes, E.; Connolly, M. P.; Cui, W.; Dickinson, H. J.; Dumm, J.; Eisch, J. D.; Falcone, A.; Feng, Q.; Finley, J. P.; Fleischhack, H.; Flinders, A.; Fortin, P.; Fortson, L.; Furniss, A.; Gillanders, G. H.; Griffin, S.; Grube, J.; Gyuk, G.; Hütten, M.; Håkansson, N.; Hanna, D.; Holder, J.; Humensky, T. B.; Johnson, C. A.; Kaaret, P.; Kar, P.; Kelley-Hoskins, N.; Kertzman, M.;

Khassen, Y.; Kieda, D.; Krause, M.; Krennrich, F.; Kumar, S.; Lang, M. J.; Maier, G.; McArthur, S.; McCann, A.; Meagher, K.; Millis, J.; Moriarty, P.; Mukherjee, R.; Nieto, D.; O'Brien, S.; O'Faoláin de Bhróithe, A.; Ong, R. A.; Otte, A. N.; Pandel, D.; Park, N.; Pelassa, V.; Pohl, M.; Popkow, A.; Pueschel, E.; Quinn, J.; Ragan, K.; Reynolds, P. T.; Richards, G. T.; Roache, E.; Rousselle, J.; Rulten, C.; Santander, M.; Sembroski, G. H.; Shahinyan, K.; Smith, A. W.; Staszak, D.; Telezhinsky, I.; Tucci, J. V.; Tyler, J.; Vincent, S.; Wakely, S. P.; Weiner, O. M.; Weinstein, A.; Wilhelm, A.; Williams, D. A.; Zitzer, B. Exceptionally Bright TeV Flares from the Binary LS I +61° 303 . *Astrophys. J. Lett.* **2016**, *817*, L7.

(140) Anderhub, H.; Antonelli, L. A.; Antoranz, P.; Backes, M.; Baixeras, C.; Balestra, S.; Barrio, J. A.; Bastieri, D.; Becerra González, J.; Becker, J. K.; Bednarek, W.; Berger, K.; Bernardini, E.; Biland, A.; Blanch Bigas, O.; Bock, R. K.; Bonnoli, G.; Bordas, P.; Borla Tridon, D.; Bosch-Ramon, V.; Bose, D.; Braun, I.; Bretz, T.; Britzger, D.; Camara, M.; Carmona, E.; Carosi, A.; Colin, P.; Commichau, S.; Contreras, J. L.; Cortina, J.; Costado, M. T.; Covino, S.; Dazzi, F.; De Angelis, A.; de Cea del Pozo, E.; De los Reyes, R.; De Lotto, B.; De Maria, M.; De Sabata, F.; Delgado Mendez, C.; Domínguez, A.; Dominis Prester, D.; Dorner, D.; Doro, M.; Elsaesser, D.; Errando, M.; Ferenc, D.; Fernández, E.; Firpo, R.; Fonseca, M. V.; Font, L.; Galante, N.; García López, R. J.; Garczarczyk, M.; Gaug, M.; Godinovic, N.; Goebel, F.; Hadasch, D.; Herrero, A.; Hildebrand, D.; Höhne-Mönch, D.; Hose, J.; Hrupec, D.; Hsu, C. C.; Jogler, T.; Klepser, S.; Kranich, D.; La Barbera, A.; Laille, A.; Leonardo, E.; Lindfors, E.; Lombardi, S.; Longo, F.; López, M.; Lorenz, E.; Majumdar, P.; Maneva, G.; Mankuzhiyil, N.; Mannheim, K.; Maraschi, L.; Mariotti, M.; Martínez, M.; Mazin, D.; Meucci, M.; Miranda, J. M.; Mirzoyan, R.; Miyamoto, H.; Moldón, J.; Moles, M.; Moralejo, A.; Nieto, D.; Nilsson, K.; Ninkovic, J.; Orito, R.; Oya, I.; Paoletti, R.; Paredes, J. M.; Pasanen, M.; Pascoli, D.; Pauss, F.; Pegna, R. G.; Perez-Torres, M. A.; Persic, M.; Peruzzo, L.; Prada, F.; Prandini, E.; Puchades, N.; Puljak, I.; Reichardt, I.; Rhode, W.; Ribó, M.; Rico, J.; Rissi, M.; Robert, A.; Rügamer, S.; Saggion, A.; Saito, T. Y.; Salvati, M.; Sánchez-Conde, M.; Satalecka, K.; Scalzotto, V.; Scapin, V.; Schweizer, T.; Shayduk, M.; Shore, S. N.; Sidro, N.; Sierpowska-Bartosik, A.; Sillanpää, A.; Sitarek, J.; Sobczynska, D.; Spanier, F.; Spiro, S.; Stamerra, A.; Stark, L. S.; Suric, T.; Takalo, L.; Tavecchio, F.; Temnikov, P.; Tescaro, D.; Teshima, M.; Torres, D. F.; Turini, N.; Vankov, H.; Wagner, R. M.; Zabalza, V.; Zandanel, F.; Zanin, R.; Zapatero, J.; MAGIC Collaboration,; Falcone, A.; Vetere, L.; Gehrels, N.; Trushkin, S.; Dhawan, V.; Reig, P. Correlated X-Ray and Very High Energy Emission in the Gamma-Ray Binary LS I +61° 303 . *Astrophys. J. Lett.* **2009**, *706*, L27–L32.

(141) Albert, J.; Aliu, E.; Anderhub, H.; Antonelli, L. A.; Antoranz, P.; Backes, M.; Baixeras, C.; Barrio, J. A.; Bartko, H.; Bastieri, D.; Becker, J. K.; Bednarek, W.; Berger, K.; Bernardini, E.; Bigongiari, C.; Biland, A.; Bock, R. K.; Bonnoli, G.; Bordas, P.; Bosch-Ramon, V.; Bretz, T.; Britvitch, I.; Camara, M.; Carmona, E.; Chilingarian, A.; Commichau, S.; Contreras, J. L.; Cortina, J.; Costado, M. T.; Covino, S.; Curtef, V.; Dazzi, F.; DeAngelis, A.; DeCea del Pozo, E.; de los Reyes, R.; DeLotto, B.; DeMaria, M.; DeSabata, F.; Delgado Mendez, C.; Dominguez, A.; Dorner, D.; Doro, M.; Errando, M.; Fagiolini, M.; Ferenc, D.; Fernández, E.; Firpo, R.; Fonseca, M. V.; Font, L.; Galante, N.; García López, R. J.; Garczarczyk, M.; Gaug, M.; Goebel, F.; Hayashida, M.; Herrero, A.; Höhne, D.; Hose, J.; Hsu, C. C.; Huber, S.; Jogler, T.;

Kranich, D.; La Barbera, A.; Laille, A.; Leonardo, E.; Lindfors, E.; Lombardi, S.; Longo, F.; López, M.; Lorenz, E.; Majumdar, P.; Maneva, G.; Mankuzhiyil, N.; Mannheim, K.; Maraschi, L.; Mariotti, M.; Martínez, M.; Mazin, D.; Meucci, M.; Meyer, M.; Miranda, J. M.; Mirzoyan, R.; Mizobuchi, S.; Moles, M.; Moralejo, A.; Nieto, D.; Nilsson, K.; Ninkovic, J.; Otte, N.; Oya, I.; Panniello, M.; Paoletti, R.; Paredes, J. M.; Pasanen, M.; Pascoli, D.; Pauss, F.; Pegna, R. G.; Perez-Torres, M. A.; Persic, M.; Peruzzo, L.; Piccioli, A.; Prada, F.; Prandini, E.; Puchades, N.; Raymers, A.; Rhode, W.; Ribó, M.; Rico, J.; Rissi, M.; Robert, A.; Rügamer, S.; Saggion, A.; Saito, T. Y.; Salvati, M.; Sanchez-Conde, M.; Sartori, P.; Satalecka, K.; Scalzotto, V.; Scapin, V.; Schmitt, R.; Schweizer, T.; Shayduk, M.; Shinozaki, K.; Shore, S. N.; Sidro, N.; Sierpowska-Bartosik, A.; Sillanpää, A.; Sobczynska, D.; Spanier, F.; Stamerra, A.; Stark, L. S.; Takalo, L.; Tavecchio, F.; Temnikov, P.; Tescaro, D.; Teshima, M.; Tluczykont, M.; Torres, D. F.; Turini, N.; Vankov, H.; Venturini, A.; Vitale, V.; Wagner, R. M.; Wittek, W.; Zabalza, V.; Zandanel, F.; Zanin, R.; Zapatero, J. Periodic Very High Energy γ-Ray Emission from LS I $+61^\circ$ 303 Observed with the MAGIC Telescope. *Astrophys. J.* **2009**, *693*, 303–310.

(142) Aleksić, J.; Alvarez, E. A.; Antonelli, L. A.; Antoranz, P.; Asensio, M.; Backes, M.; Barrio, J. A.; Bastieri, D.; Becerra González, J.; Bednarek, W.; Berdyugin, A.; Berger, K.; Bernardini, E.; Biland, A.; Blanch, O.; Bock, R. K.; Boller, A.; Bonnoli, G.; Borla Tridon, D.; Bosch-Ramon, V.; Braun, I.; Bretz, T.; Cañellas, A.; Carmona, E.; Carosi, A.; Colin, P.; Colombo, E.; Contreras, J. L.; Cortina, J.; Cossio, L.; Covino, S.; Dazzi, F.; De Angelis, A.; De Caneva, G.; De Cea del Pozo, E.; De Lotto, B.; Delgado Mendez, C.; Diago Ortega, A.; Doert, M.; Domínguez, A.; Dominis Prester, D.; Dorner, D.; Doro, M.; Elsaesser, D.; Ferenc, D.; Fonseca, M. V.; Font, L.; Fruck, C.; García López, R. J.; Garczarczyk, M.; Garrido, D.; Giavitto, G.; Godinović, N.; Hadasch, D.; Häfner, D.; Herrero, A.; Hildebrand, D.; Höhne-Mönch, D.; Hose, J.; Hrupec, D.; Huber, B.; Jogler, T.; Kellermann, H.; Klepser, S.; Krähenbühl, T.; Krause, J.; La Barbera, A.; Lelas, D.; Leonardo, E.; Lindfors, E.; Lombardi, S.; López, A.; López, M.; Lorenz, E.; Makariev, M.; Maneva, G.; Mankuzhiyil, N.; Mannheim, K.; Maraschi, L.; Mariotti, M.; Martínez, M.; Mazin, D.; Meucci, M.; Miranda, J. M.; Mirzoyan, R.; Miyamoto, H.; Moldón, J.; Moralejo, A.; Munar-Adrover, P.; Nieto, D.; Nilsson, K.; Orito, R.; Oya, I.; Paneque, D.; Paoletti, R.; Pardo, S.; Paredes, J. M.; Partini, S.; Pasanen, M.; Pauss, F.; Perez-Torres, M. A.; Persic, M.; Peruzzo, L.; Pilia, M.; Pochon, J.; Prada, F.; Prada Moroni, P. G.; Prandini, E.; Puljak, I.; Reichardt, I.; Reinthal, R.; Rhode, W.; Ribó, M.; Rico, J.; Rügamer, S.; Saggion, A.; Saito, K.; Saito, T. Y.; Salvati, M.; Satalecka, K.; Scalzotto, V.; Scapin, V.; Schultz, C.; Schweizer, T.; Shayduk, M.; Shore, S. N.; Sillanpää, A.; Sitarek, J.; Sobczynska, D.; Spanier, F.; Spiro, S.; Stamerra, A.; Steinke, B.; Storz, J.; Strah, N.; Surić, T.; Takalo, L.; Takami, H.; Tavecchio, F.; Temnikov, P.; Terzić, T.; Tescaro, D.; Teshima, M.; Tibolla, O.; Torres, D. F.; Treves, A.; Uellenbeck, M.; Vankov, H.; Vogler, P.; Wagner, R. M.; Weitzel, Q.; Zabalza, V.; Zandanel, F.; Zanin, R. Detection of the γ-Ray Binary LS I $+61^\circ$ 303 in a Low-flux State at Very High Energy γ-Rays with the MAGIC Telescopes in 2009. *Astrophys. J.* **2012**, *746*, 80.

(143) Torres, D. F.; Rea, N.; Esposito, P.; Li, J.; Chen, Y.; Zhang, S. A Magnetar-like Event from LS I $+61^\circ$ 303 and Its Nature as a Gamma-Ray Binary. *Astrophys. J.* **2012**, *744*, 106.

(144) Pringle, J. E.; Rees, M. J. Accretion Disc Models for Compact X-Ray Sources. *Astron. Astrophys.* **1972**, *21*, 1.

(145) Basko, M. M.; Sunyaev, R. A. The Import of the Alfven Surface for the X-ray Pulse Formation in Accreting Pulsars. *Soviet Astron.* **1976**, *20*, 537.

(146) Cui, W. Evidence for "Propeller" Effects in X-Ray Pulsars GX 1+4 and GRO J1744-28. *Astrophys. J. Lett.* **1997**, *482*, L163–L166.

(147) Rea, N. Deep Search for the Pulsars Powering the TeV Emission of LS I $+61^\circ$ 303 and LS 5039. Chandra Proposal, 2008.

(148) Tavani, M.; Hermsen, W.; van Dijk, R.; Strickman, M.; Zhang, S. N.; Foster, R. S.; Ray, P. S.; Mattox, J.; Ulmer, M.; Purcell, W.; Coe, M. Monitoring the Gamma-Ray Source 2CG 135+1 and the Radio star LS I $+61^\circ$ 303 . *Astron. Astrophys., Suppl. Ser.* **1996**, *120*, 243–248.

(149) Zamanov, R.; Marti, J.; Marziani, P. Be/X-ray Binary LS I $+61^\circ$ 303 in Terms of Ejector-Propeller Model. The Second National Conference on Astrophysics of Compact Objects. 2001; p 50.

(150) Zamanov, R. K. An Ejector-Propeller Model for LSI +61 303. *Mon. Not. R. Astron. Soc.* **1995**, *272*, 308–310.

(151) Chernyakova, M.; Neronov, A.; Molkov, S.; Malyshev, D.; Lutovinov, A.; Pooley, G. Superorbital Modulation of X-Ray Emission from Gamma-Ray Binary LS I $+61^\circ$ 303 . *Astrophys. J. Lett.* **2012**, *747*, L29.

(152) Xing, Y.; Wang, Z.; Takata, J. Superorbital modulation at GeV energies in the gamma-ray binary LS I +61 303. 2017, arXiv:astro-ph.HE/1704.02091. arXiv.org e-Print archive. https://arxiv.org/abs/1704.02091 (accessed May 30, 2017).

(153) Papitto, A.; Torres, D. F.; Rea, N. Possible Changes of State and Relevant Timescales for a Neutron Star in LS I $+61^\circ$ 303 . *Astrophys. J.* **2012**, *756*, 188.

(154) Rea, N.; Torres, D. F.; van der Klis, M.; Jonker, P. G.; Méndez, M.; Sierpowska-Bartosik, A. Deep Chandra Observations of TeV Binaries - I. LS I $+61^\circ$ 303 . *Mon. Not. R. Astron. Soc.* **2010**, *405*, 2206–2214.

(155) Marcote, B.; Ribó, M.; Paredes, J. M.; Ishwara-Chandra, C. H.; Swinbank, J. D.; Broderick, J. W.; Markoff, S.; Fender, R.; Wijers, R. A. M. J.; Pooley, G. G.; Stewart, A. J.; Bell, M. E.; Breton, R. P.; Carbone, D.; Corbel, S.; Eislöffel, J.; Falcke, H.; Grießmeier, J.-M.; Kuniyoshi, M.; Pietka, M.; Rowlinson, A.; Serylak, M.; van der Horst, A. J.; van Leeuwen, J.; Wise, M. W.; Zarka, P. Orbital and Superorbital Variability of LS I $+61^\circ$ 303 at Low Radio Frequencies with GMRT and LOFAR. *Mon. Not. R. Astron. Soc.* **2016**, *456*, 1791–1802.

(156) Marti, J.; Paredes, J. M. Modelling of LS I $+61^\circ$ 303 from Near Infrared Data. *Astron. Astrophys.* **1995**, *298*, 151.

(157) Mendelson, H.; Mazeh, T. Discovery of a 26.5-day Optical Periodicity of LS I $+61^\circ$ 303 . *Mon. Not. R. Astron. Soc.* **1989**, *239*, 733–740.

(158) McSwain, M. V.; Grundstrom, E. D.; Gies, D. R.; Ray, P. S. Hα Emission Variability in the γ-ray Binary LS I $+61^\circ$ 303 . *Astrophys. J.* **2010**, *724*, 379–385.

(159) Paredes, J. M.; Marti, J.; Peracaula, M.; Ribo, M. Evidence of X-ray Periodicity in LS I $+61^\circ$ 303 . *Astron. Astrophys.* **1997**, *320*, L25–L28.

(160) Hadasch, D. Results from the Binaries LS I $+61^\circ$ 303 and LS 5039 after 2.5 Years of Fermi Monitoring. International Journal of Modern Physics Conference Series. 2012; pp 61–66.

(161) Li, J.; Torres, D. F.; Zhang, S.; Hadasch, D.; Rea, N.; Caliandro, G. A.; Chen, Y.; Wang, J. Unveiling the Super-Orbital Modulation of LS I $+61^\circ$ 303 in X-rays. Feeding Compact Objects: Accretion on All Scales. 2013; pp 255–256.

(162) Ackermann, M.; Ajello, M.; Ballet, J.; Barbiellini, G.; Bastieri, D.; Bellazzini, R.; Bonamente, E.; Brandt, T. J.; Bregeon, J.; Brigida, M.; Bruel, P.; Buehler, R.; Buson, S.; Caliandro, G. A.; Cameron, R. A.; Caraveo, P. A.; Casandjian, J. M.; Cavazzuti, E.; Cecchi, C.; Chekhtman, A.; Chiang, J.; Chiaro, G.; Ciprini, S.; Claus, R.; Cohen-Tanugi, J.; Cominsky, L. R.; Conrad, J.; Cutini, S.; Dalton, M.; D'Ammando, F.; de Angelis, A.; den Hartog, P. R.; de Palma, F.; Dermer, C. D.; Digel, S. W.; Di Venere, L.; Drell, P. S.; Dubois, R.; Favuzzi, C.; Fegan, S. J.; Ferrara, E. C.; Focke, W. B.; Franckowiak, A.; Funk, S.; Fusco, P.; Gargano, F.; Gasparrini, D.; Germani, S.; Giglietto, N.; Giordano, F.; Giroletti, M.; Glanzman, T.; Godfrey, G.; Grenier, I. A.; Guiriec, S.; Hadasch, D.; Hanabata, Y.; Harding, A. K.; Hayashida, M.; Hays, E.; Hill, A. B.; Horan, D.; Hughes, R. E.; Jogler, T.; Jóhannesson, G.; Johnson, A. S.; Johnson, T. J.; Kawano, T.; Kerr, M.; Knödlseder, J.; Kuss, M.; Lande, J.; Larsson, S.; Latronico, L.; Lemoine-Goumard, M.; Li, J.; Longo, F.; Lovellette, M. N.; Lubrano, P.; Mayer, M.; Mazziotta, M. N.; McEnery, J. E.; Michelson, P. F.; Mizuno, T.; Monzani, M. E.; Morselli, A.; Moskalenko, I. V.; Murgia, S.; Nemmen, R.; Nuss, E.; Ohsugi, T.; Okumura, A.; Orienti, M.; Orlando, E.; Ormes, J. F.; Paneque, D.; Papitto, A.; Perkins, J. S.; Pesce-Rollins, M.; Piron, F.; Pivato, G.; Rainò, S.; Rando, R.; Razzano, M.; Rea, N.; Reimer, A.; Reimer, O.; Scargle, J. D.; Schulz, A.; Sgrò, C.; Siskind, E. J.; Spandre, G.; Spinelli, P.; Takahashi, H.; Thayer, J. G.; Thayer, J. B.; Tinivella, M.; Torres, D. F.; Tosti, G.; Troja, E.; Uchiyama, Y.; Usher, T. L.; Vandenbroucke, J.; Vasileiou, V.; Vianello, G.; Vitale, V.; Werner, M.; Winer, B. L.; Wood, K. S. Associating Long-term γ-Ray Variability with the Superorbital Period of LS I $+61^\circ$ 303 . *Astrophys. J. Lett.* **2013**, *773*, L35.

(163) Ahnen, M. L.; Ansoldi, S.; Antonelli, L. A.; Antoranz, P.; Babic, A.; Banerjee, B.; Bangale, P.; Barres de Almeida, U.; Barrio, J. A.; Becerra González, J.; Bednarek, W.; Bernardini, E.; Biasuzzi, B.; Biland, A.; Blanch, O.; Bonnefoy, S.; Bonnoli, G.; Borracci, F.; Bretz, T.; Buson, S.; Carosi, A.; Chatterjee, A.; Clavero, R.; Colin, P.; Colombo, E.; Contreras, J. L.; Cortina, J.; Covino, S.; Da Vela, P.; Dazzi, F.; De Angelis, A.; De Lotto, B.; de Oña Wilhelmi, E.; Delgado Mendez, C.; Di Pierro, F.; Domínguez, A.; Dominis Prester, D.; Dorner, D.; Doro, M.; Einecke, S.; Eisenacher Glawion, D.; Elsaesser, D.; Fernández-Barral, A.; Fidalgo, D.; Fonseca, M. V.; Font, L.; Frantzen, K.; Fruck, C.; Galindo, D.; García López, R. J.; Garczarczyk, M.; Garrido Terrats, D.; Gaug, M.; Giammaria, P.; Godinović, N.; González Muñoz, A.; Gora, D.; Guberman, D.; Hadasch, D.; Hahn, A.; Hanabata, Y.; Hayashida, M.; Herrera, J.; Hose, J.; Hrupec, D.; Hughes, G.; Idec, W.; Kodani, K.; Konno, Y.;

Kubo, H.; Kushida, J.; La Barbera, A.; Lelas, D.; Lindfors, E.; Lombardi, S.; Longo, F.; López, M.; López-Coto, R.; López-Oramas, A.; Majumdar, P.; Makariev, M.; Mallot, K.; Maneva, G.; Manganaro, M.; Mannheim, K.; Maraschi, L.; Marcote, B.; Mariotti, M.; Martínez, M.; Mazin, D.; Menzel, U.; Miranda, J. M.; Mirzoyan, R.; Moralejo, A.; Moretti, E.; Nakajima, D.; Neustroev, V.; Niedzwiecki, A.; Nievas Rosillo, M.; Nilsson, K.; Nishijima, K.; Noda, K.; Orito, R.; Overkemping, A.; Paiano, S.; Palacio, J.; Palatiello, M.; Paneque, D.; Paoletti, R.; Paredes, J. M.; Paredes-Fortuny, X.; Pedaletti, G.; Persic, M.; Poutanen, J.; Prada Moroni, P. G.; Prandini, E.; Puljak, I.; Rhode, W.; Ribó, M.; Rico, J.; Rodriguez Garcia, J.; Saito, T.; Satalecka, K.; Schultz, C.; Schweizer, T.; Shore, S. N.; Sillanpää, A.; Sitarek, J.; Snidaric, I.; Sobczynska, D.; Stamerra, A.; Steinbring, T.; Strzys, M.; Takalo, L.; Takami, H.; Tavecchio, F.; Temnikov, P.; Terzić, T.; Tescaro, D.; Teshima, M.; Thaele, J.; Torres, D. F.; Toyama, T.; Treves, A.; Verguilov, V.; Vovk, I.; Ward, J. E.; Will, M.; Wu, M. H.; Zanin, R.; MAGIC Collaboration,; Casares, J.; Herrero, A. Super-Orbital Variability of LS I $+61^\circ$ 303 at TeV Energies. *Astron. Astrophys.* **2016**, *591*, A76.

(164) Gregory, P. C.; Taylor, A. R. New Highly Variable Radio Source, Possible Counterpart of Gamma-Ray Source CG135+1. *Nature* **1978**, *272*, 704–706.

(165) Hermsen, W.; Swanenburg, B. N.; Bignami, G. F.; Boella, G.; Buccheri, R.; Scarsi, L.; Kanbach, G.; Mayer-Hasselwander, H. A.; Masnou, J. L.; Paul, J. A. New High Energy Gamma-Ray Sources Observed by COS B. *Nature* **1977**, *269*, 494.

(166) Frail, D. A.; Hjellming, R. M. Distance and Total Column Density to the Periodic Radio Star LS I $+61^\circ$ 303 . *Astron. J.* **1991**, *101*, 2126–2130.

(167) Paredes, J. M.; Figueras, F. Detection of Optical Variability of LS I $+61^\circ$ 303 . *Astron. Astrophys.* **1986**, *154*, L30–L32.

(168) Taylor, A. R.; Gregory, P. C. Two-frequency Radio Spectra During an Outburst of the Periodic Radio Star LS I $+61^\circ$ 303 . *Astrophys. J.* **1984**, *283*, 273–278.

(169) Zamanov, R. K.; Martí, J.; Paredes, J. M.; Fabregat, J.; Ribó, M.; Tarasov, A. E. Evidence of Hα Periodicities in LS I $+61^\circ$ 303 . *Astron. Astrophys.* **1999**, *351*, 543–550.

(170) Bignami, G. F.; Caraveo, P. A.; Lamb, R. C.; Markert, T. H.; Paul, J. A. Einstein X-ray Identification of the Variable Radio Star LS I $+61^\circ$ 303 . *Astrophys. J. Lett.* **1981**, *247*, L85–L88.

(171) Goldoni, P.; Mereghetti, S. X-ray Observations of the Peculiar Be star LS I $+61^\circ$ 303 . *Astron. Astrophys.* **1995**, *299*, 751.

(172) Li, J.; Torres, D. F.; Zhang, S. Spectral Analysis in Orbital/Superorbital Phase Space and Hints of Superorbital Variability in the Hard X-Rays of LS I $+61^\circ$ 303 . *Astrophys. J. Lett.* **2014**, *785*, L19.

(173) D'Aì, A.; Cusumano, G.; La Parola, V.; Segreto, A.; Mineo, T. Temporal Features of LS I $+61^\circ$ 303 in Hard X-rays from the Swift/BAT Survey Data. *Mon. Not. R. Astron. Soc.* **2016**, *456*, 1955–1959.

(174) Albert, J.; Aliu, E.; Anderhub, H.; Antoranz, P.; Backes, M.; Baixeras, C.; Barrio, J. A.; Bartko, H.; Bastieri, D.; Becker, J. K.; Bednarek, W.; Berger, K.; Bigongiari, C.;

Biland, A.; Bock, R. K.; Bonnoli, G.; Bordas, P.; Bosch-Ramon, V.; Bretz, T.; Britvitch, I.; Camara, M.; Carmona, E.; Chilingarian, A.; Commichau, S.; Contreras, J. L.; Cortina, J.; Costado, M. T.; Curtef, V.; Dazzi, F.; De Angelis, A.; de los Reyes, R.; De Lotto, B.; De Maria, M.; De Sabata, F.; Delgado Mendez, C.; Dorner, D.; Doro, M.; Errando, M.; Fagiolini, M.; Ferenc, D.; Fernández, E.; Firpo, R.; Fonseca, M. V.; Font, L.; Galante, N.; García López, R. J.; Garczarczyk, M.; Gaug, M.; Goebel, F.; Hayashida, M.; Herrero, A.; Höhne, D.; Hose, J.; Hsu, C. C.; Huber, S.; Jogler, T.; Kosyra, R.; Kranich, D.; Laille, A.; Leonardo, E.; Lindfors, E.; Lombardi, S.; Longo, F.; López, M.; Lorenz, E.; Majumdar, P.; Maneva, G.; Mankuzhiyil, N.; Mannheim, K.; Mariotti, M.; Martínez, M.; Mazin, D.; Merck, C.; Meucci, M.; Meyer, M.; Miranda, J. M.; Mirzoyan, R.; Mizobuchi, S.; Moles, M.; Moralejo, A.; Nieto, D.; Nilsson, K.; Ninkovic, J.; Oña-Wilhelmi, E.; Otte, N.; Oya, I.; Panniello, M.; Paoletti, R.; Paredes, J. M.; Pasanen, M.; Pascoli, D.; Pauss, F.; Pegna, R. G.; Pérez-Torres, M. A.; Persic, M.; Peruzzo, L.; Piccioli, A.; Prada, F.; Prandini, E.; Puchades, N.; Raymers, A.; Rhode, W.; Ribó, M.; Rico, J.; Rissi, M.; Robert, A.; Rügamer, S.; Saggion, A.; Saito, T. Y.; Sánchez, A.; Sánchez-Conde, M. A.; Sartori, P.; Scalzotto, V.; Scapin, V.; Schmitt, R.; Schweizer, T.; Shayduk, M.; Shinozaki, K.; Shore, S. N.; Sidro, N.; Sillanpää, A.; Sobczynska, D.; Spanier, F.; Stamerra, A.; Stark, L. S.; Takalo, L.; Temnikov, P.; Tescaro, D.; Teshima, M.; Torres, D. F.; Turini, N.; Vankov, H.; Venturini, A.; Vitale, V.; Wagner, R. M.; Wittek, W.; Zandanel, F.; Zanin, R.; Zapatero, J.; MAGIC Collaboration,; Guerrero, M. A.; Alberdi, A.; Paragi, Z.; Muxlow, T. W. B.; Diamond, P. Multiwavelength (Radio, X-Ray, and γ-Ray) Observations of the γ-Ray Binary LS I $+61^\circ$ 303 . *Astrophys. J.* **2008**, *684*, 1351–1358.

(175) Smith, A.; Kaaret, P.; Holder, J.; Falcone, A.; Maier, G.; Pandel, D.; Stroh, M. Long-Term X-Ray Monitoring of the TeV Binary LS I $+61^\circ$ 303 With the Rossi X-Ray Timing Explorer. *Astrophys. J.* **2009**, *693*, 1621–1627.

(176) Kar, P.; VERITAS Collaboration, Long-term VERITAS Monitoring of LS I $+61^\circ$ 303 in Conjunction with X-ray, and GeV Observation Campaigns. 34th. International Cosmic Ray Conference,, The Hague, Netherlands. 2015; p 818.

(177) Alexander, T. Is AGN Variability Correlated with Other AGN Properties? ZDCF Analysis of Small Samples of Sparse Light Curves. Astronomical Time Series. 1997; p 163.

(178) Dubus, G. Gamma-Ray Absorption in Massive X-ray Binaries. *Astron. Astrophys.* **2006**, *451*, 9–18.

(179) Abdo, A. A.; Ackermann, M.; Ajello, M.; Atwood, W. B.; Axelsson, M.; Baldini, L.; Ballet, J.; Barbiellini, G.; Bastieri, D.; Baughman, B. M.; Bechtol, K.; Bellazzini, R.; Berenji, B.; Blandford, R. D.; Bloom, E. D.; Bonamente, E.; Borgland, A. W.; Bregeon, J.; Brez, A.; Brigida, M.; Bruel, P.; Burnett, T. H.; Buson, S.; Caliandro, G. A.; Cameron, R. A.; Caraveo, P. A.; Casandjian, J. M.; Cavazzuti, E.; Cecchi, C.; Çelik, Ö.; Chaty, S.; Chekhtman, A.; Cheung, C. C.; Chiang, J.; Ciprini, S.; Claus, R.; Cohen-Tanugi, J.; Cominsky, L. R.; Conrad, J.; Corbel, S.; Corbet, R.; Cutini, S.; Dermer, C. D.; de Angelis, A.; de Palma, F.; Digel, S. W.; Silva, E. d. C. e.; Drell, P. S.; Dubois, R.; Dubus, G.; Dumora, D.; Farnier, C.; Favuzzi, C.; Fegan, S. J.; Focke, W. B.; Fortin, P.; Frailis, M.; Fukazawa, Y.; Funk, S.; Fusco, P.; Gargano, F.; Gasparrini, D.; Gehrels, N.;

Germani, S.; Giebels, B.; Giglietto, N.; Giordano, F.; Glanzman, T.; Godfrey, G.; Grenier, I. A.; Grondin, M.-H.; Grove, J. E.; Guillemot, L.; Guiriec, S.; Hanabata, Y.; Harding, A. K.; Hayashida, M.; Hays, E.; Hill, A. B.; Horan, D.; Hughes, R. E.; Jackson, M. S.; Jóhannesson, G.; Johnson, A. S.; Johnson, T. J.; Johnson, W. N.; Kamae, T.; Katagiri, H.; Kataoka, J.; Kawai, N.; Kerr, M.; Knödlseder, J.; Kocian, M. L.; Kuehn, F.; Kuss, M.; Lande, J.; Larsson, S.; Latronico, L.; Lemoine-Goumard, M.; Longo, F.; Loparco, F.; Lott, B.; Lovellette, M. N.; Lubrano, P.; Madejski, G. M.; Makeev, A.; Marelli, M.; Mazziotta, M. N.; McEnery, J. E.; Meurer, C.; Michelson, P. F.; Mitthumsiri, W.; Mizuno, T.; Moiseev, A. A.; Monte, C.; Monzani, M. E.; Morselli, A.; Moskalenko, I. V.; Murgia, S.; Nolan, P. L.; Norris, J. P.; Nuss, E.; Ohsugi, T.; Omodei, N.; Orlando, E.; Ormes, J. F.; Ozaki, M.; Paneque, D.; Panetta, J. H.; Parent, D.; Pelassa, V.; Pepe, M.; Pesce-Rollins, M.; Piron, F.; Porter, T. A.; Rainò, S.; Rando, R.; Ray, P. S.; Razzano, M.; Rea, N.; Reimer, A.; Reimer, O.; Reposeur, T.; Ritz, S.; Rochester, L. S.; Rodriguez, A. Y.; Romani, R. W.; Roth, M.; Ryde, F.; Sadrozinski, H. F.-W.; Sanchez, D.; Sander, A.; Saz Parkinson, P. M.; Scargle, J. D.; Sgrò, C.; Sierpowska-Bartosik, A.; Siskind, E. J.; Smith, D. A.; Smith, P. D.; Spandre, G.; Spinelli, P.; Strickman, M. S.; Suson, D. J.; Tajima, H.; Takahashi, H.; Takahashi, T.; Tanaka, T.; Tanaka, Y.; Thayer, J. B.; Thompson, D. J.; Tibaldo, L.; Torres, D. F.; Tosti, G.; Tramacere, A.; Uchiyama, Y.; Usher, T. L.; Vasileiou, V.; Venter, C.; Vilchez, N.; Vitale, V.; Waite, A. P.; Wallace, E.; Wang, P.; Winer, B. L.; Wood, K. S.; Ylinen, T.; Ziegler, M. Fermi/LAT Observations of LS 5039. *Astrophys. J. Lett.* **2009**, *706*, L56–L61.

(180) Zabalza, V.; Paredes, J. M.; Bosch-Ramon, V. On the Origin of Correlated X-ray/VHE Emission from LS I $+61^\circ$ 303 . *Astron. Astrophys.* **2011**, *527*, A9.

(181) Paredes-Fortuny, X.; Ribó, M.; Bosch-Ramon, V.; Casares, J.; Fors, O.; Núñez, J. Evidence of Coupling Between the Thermal and Nonthermal Emission in the Gamma-Ray binary LS I $+61^\circ$ 303 . *Astron. Astrophys.* **2015**, *575*, L6.

(182) Feldman, P. A.; Purton, C. R.; Stiff, T.; Kwok, S. H-alpha-Emission Object SS 433. *Int. Astron. Union Circ.* **1978**, *3258*.

(183) Marshall, F. E.; Mushotzky, R. F.; Boldt, E. A.; Holt, S. S.; Serlemitsos, P. J. X-Ray Emission from SS 433. *Int. Astron. Union Circ.* **1978**, *3314*.

(184) Margon, B.; Grandi, S. A.; Stone, R. P. S.; Ford, H. C. Enormous Periodic Doppler Shifts in SS 433. *Astrophys. J. Lett.* **1979**, *233*, L63–L68.

(185) Margon, B.; Ford, H. C.; Katz, J. I.; Kwitter, K. B.; Ulrich, R. K.; Stone, R. P. S.; Klemola, A. The Bizarre Spectrum of SS 433. *Astrophys. J. Lett.* **1979**, *230*, L41–L45.

(186) Milgrom, M. On the Interpretation of the Large Variations in the Line Positions in SS433. *Astron. Astrophys.* **1979**, *76*, L3–L6.

(187) Fabian, A. C.; Rees, M. J. SS 433 - A Double Jet in Action. *Mon. Not. R. Astron. Soc.* **1979**, *187*, 13P–16P.

(188) Cherepashchuk, A. M.; Sunyaev, R. A.; Molkov, S. V.; Antokhina, E. A.; Postnov, K. A.; Bogomazov, A. I. INTEGRAL Observations of SS433: System's Parameters and Nutation of Supercritical Accretion Disc. *Mon. Not. R. Astron. Soc.* **2013**, *436*, 2004–2013.

(189) Cherepashchuk, A. M.; Sunyaev, R. A.; Fabrika, S. N.; Postnov, K. A.; Molkov, S. V.; Barsukova, E. A.; Antokhina, E. A.; Irsmambetova, T. R.; Panchenko, I. E.; Seifina, E. V.; Shakura, N. I.; Timokhin, A. N.; Bikmaev, I. F.; Sakhibullin, N. A.; Aslan, Z.; Khamitov, I.; Pramsky, A. G.; Sholukhova, O.; Gnedin, Y. N.; Arkharov, A. A.; Larionov, V. M. INTEGRAL Observations of SS433: Results of a Coordinated Campaign. *Astron. Astrophys.* **2005**, *437*, 561–573.

(190) Blundell, K. M.; Bowler, M. G. Symmetry in the Changing Jets of SS 433 and Its True Distance from Us. *Astrophys. J. Lett.* **2004**, *616*, L159–L162.

(191) Katz, J. I.; Anderson, S. F.; Grandi, S. A.; Margon, B. Nodding Motions of Accretion Rings and Disks - A Short-term Period in SS 433. *Astrophys. J.* **1982**, *260*, 780–793.

(192) Migliari, S.; Fender, R.; Méndez, M. Iron Emission Lines from Extended X-ray Jets in SS 433: Reheating of Atomic Nuclei. *Science* **2002**, *297*, 1673–1676.

(193) Vermeulen, R. C.; Murdin, P. G.; van den Heuvel, E. P. J.; Fabrika, S. N.; Wagner, B.; Margon, B.; Hutchings, J. B.; Schilizzi, R. T.; van Kerkwijk, M. H.; van den Hoek, L. B.; Ott, E.; Angebault, L. P.; Miley, G. K.; D'Odorico, S.; Borisov, N. Monitoring of Very Rapid Changes in the Optical Spectrum of SS 433 in May/June 1987. *Astron. Astrophys.* **1993**, *270*, 204–222.

(194) Brinkmann, W.; Aschenbach, B.; Kawai, N. ROSAT Observations of the W 50/SS 433 System. *Astron. Astrophys.* **1996**, *312*, 306–316.

(195) Bursov, N. N.; Trushkin, S. A. Multifrequency Observations of a Recent Radio Flare in SS 433. *Astron. Lett.* **1995**, *21*, 145–148.

(196) Margon, B. Observations of SS 433. *Annu. Rev. Astron. Astrophys.* **1984**, *22*, 507–536.

(197) Watson, M. G.; Willingale, R.; Grindlay, J. E.; Seward, F. D. The X-ray Lobes of SS 433. *Astrophys. J.* **1983**, *273*, 688–696.

(198) Watson, M. G.; Stewart, G. C.; King, A. R.; Brinkmann, W. Doppler-shifted X-ray Line Emission from SS433. *Mon. Not. R. Astron. Soc.* **1986**, *222*, 261–271.

(199) Safi-Harb, S.; Ögelman, H. ROSAT and ASCA Observations of W50 Associated with the Peculiar Source SS 433. *Astrophys. J.* **1997**, *483*, 868–881.

(200) Kotani, T.; Kawai, N.; Aoki, T.; Doty, J.; Matsuoka, M.; Mitsuda, K.; Nagase, F.; Ricker, G.; White, N. E. Discovery of the Double Doppler-shifted Emission-line Systems in the X-ray Spectrum of SS 433. *Publ. Astron. Soc. Jpn.* **1994**, *46*, L147–L150.

(201) Yamauchi, S.; Kawai, N.; Aoki, T. A Nonthermal X-ray Spectrum from the Supernova Remnant W 50. *Publ. Astron. Soc. Jpn.* **1994**, *46*, L109–L113.

(202) Moldowan, A.; Safi-Harb, S. Chandra and RXTE study of the Western Lobe of W50 and Galactic Microquasar SS 433. *J. R. Astron. Soc. Can* **2005**, *99*, 141.

(203) Reynoso, M. M.; Christiansen, H. R.; Romero, G. E. Gamma-Ray Absorption in the Microquasar SS433. *Astropart. Phys.* **2008**, *28*, 565–572.

(204) Bordas, P.; Bosch-Ramon, V.; Paredes, J. M.; Perucho, M. Nonthermal Emission from Microquasar/ISM Interaction. *Astron. Astrophys.* **2009**, *497*, 325–334.

(205) Bordas, P.; Yang, R.; Kafexhiu, E.; Aharonian, F. Detection of Persistent Gamma-Ray Emission Toward SS433/W50. *Astrophys. J. Lett.* **2015**, *807*, L8.

(206) Aharonian, F.; Akhperjanian, A.; Beilicke, M.; Bernlöhr, K.; Börst, H.-G.; Bojahr, H.; Bolz, O.; Coarasa, T.; Contreras, J.; Cortina, J.; Denninghoff, S.; Fonseca, V.; Girma, M.; Götting, N.; Heinzelmann, G.; Hermann, G.; Heusler, A.; Hofmann, W.; Horns, D.; Jung, I.; Kankanyan, R.; Kestel, M.; Kohnle, A.; Konopelko, A.; Kranich, D.; Lampeitl, H.; Lopez, M.; Lorenz, E.; Lucarelli, F.; Mang, O.; Mazin, D.; Meyer, H.; Mirzoyan, R.; Moralejo, A.; Oña-Wilhelmi, E.; Panter, M.; Plyasheshnikov, A.; Pühlhofer, G.; de Los Reyes, R.; Rhode, W.; Ripken, J.; Rowell, G. P.; Sahakian, V.; Samorski, M.; Schilling, M.; Siems, M.; Sobzynska, D.; Stamm, W.; Tluczykont, M.; Vitale, V.; Völk, H. J.; Wiedner, C. A.; Wittek, W. TeV Gamma-Ray Observations of SS-433 and a Survey of the Surrounding Field with the HEGRA IACT-System. *Astron. Astrophys.* **2005**, *439*, 635–643.

(207) Hayashi, S.; Kajino, F.; Naito, T.; Asahara, A.; Bicknell, G. V.; Clay, R. W.; Doi, Y.; Edwards, P. G.; Enomoto, R.; Gunji, S.; Hara, S.; Hara, T.; Hattori, T.; Itoh, C.; Kabuki, S.; Katagiri, H.; Kawachi, A.; Kifune, T.; Ksenofontov, L. T.; Kubo, H.; Kurihara, T.; Kurosaka, R.; Kushida, J.; Matsubara, Y.; Miyashita, Y.; Mizumoto, Y.; Mori, M.; Mori, H.; Muraishi, H.; Muraki, Y.; Nakase, T.; Nishida, D.; Nishijima, K.; Ohishi, M.; Okumura, K.; Patterson, J. R.; Protheroe, R. J.; Sakamoto, N.; Sakurazawa, K.; Swaby, D. L.; Tanimori, T.; Tanimura, H.; Thornton, G.; Tokanai, F.; Tsuchiya, K.; Uchida, T.; Watanabe, S.; Yamaoka, T.; Yanagita, S.; Yoshida, T.; Yoshikoshi, T. Search for VHE Gamma Rays from SS433/W50 with the CANGAROO-II Telescope. *Astropart. Phys.* **2009**, *32*, 112–119.

(208) Bednarek, W.; Blanch, O.; Cortina, J.; de Oña Wilhelmi, E.; Hadasch, D.; López-Coto, R.; López-Oramas, A.; Munar-Adrover, P.; Paredes, J. M.; Pérez-Torres, M. A.; Ribó, M.; Sitarek, J.; Torres, D. F.; Zanin, R. MAGIC VHE Gamma-Ray Observations of Binary Systems. 6th International Symposium on High Energy Gamma-Ray Astronomy, Heidelberg, Germany, July 11-15. 2016; p 040016.

(209) Guenette, R. VERITAS Observations of Galactic Compact Objects. Ph.D. thesis, McGill University, Montreal, Canada, 2010.

(210) Dubner, G. M.; Holdaway, M.; Goss, W. M.; Mirabel, I. F. A High-Resolution Radio Study of the W50-SS 433 System and the Surrounding Medium. *Astron. J.* **1998**, *116*, 1842–1855.

(211) Reynoso, M. M.; Romero, G. E.; Christiansen, H. R. Production of Gamma Rays and Neutrinos in the Dark Jets of the Microquasar SS433. *Mon. Not. R. Astron. Soc.* **2008**, *387*, 1745–1754.

(212) Aharonian, F. A.; Atoyan, A. M. Gamma Rays from Galactic Sources with Relativistic Jets. *New Astron. Rev.* **1998**, *42*, 579–584.

(213) Atoyan, A. M.; Dermer, C. D. Neutral Beams from Blazar Jets. *Astrophys. J.* **2003**, *586*, 79–96.

(214) Christiansen, H. R.; Orellana, M.; Romero, G. E. High-energy Neutrino Emission from X-ray Binaries. *Phys. Rev. D* **2006**, *73*, 063012.

(215) Margon, B.; Anderson, S. F. Ten Years of SS 433 Kinematics. *Astrophys. J.* **1989**, *347*, 448–454.

(216) Roberts, D. H.; Wardle, J. F. C.; Lipnick, S. L.; Selesnick, P. L.; Slutsky, S. Structure and Magnetic Fields in the Precessing Jet System SS 433. I. Multifrequency Imaging from 1998. *Astrophys. J.* **2008**, *676*, 584–593.

(217) Torres, D. F.; Zhang, S.; Li, J.; Rea, N.; Caliandro, G. A.; Hadasch, D.; Chen, Y.; Wang, J.; Ray, P. S. Variability in the Orbital Profiles of the X-ray Emission of the γ-ray Binary LS I $+61^\circ$ 303 . *Astrophys. J. Lett.* **2010**, *719*, L104–L108.

(218) Paredes, J. M.; Bednarek, W.; Bordas, P.; Bosch-Ramon, V.; De Cea del Pozo, E.; Dubus, G.; Funk, S.; Hadasch, D.; Khangulyan, D.; Markoff, S.; Moldón, J.; Munar-Adrover, P.; Nagataki, S.; Naito, T.; de Naurois, M.; Pedaletti, G.; Reimer, O.; Ribó, M.; Szostek, A.; Terada, Y.; Torres, D. F.; Zabalza, V.; Zdziarski, A. A.; CTA Consortium, Binaries With the Eyes of CTA. *Astropart. Phys.* **2013**, *43*, 301–316.